



HAL
open science

Development of the differential method associated with the Fast Fourier Factorization for the modelization of photonic device: from complex optical diffraction grating to guided integrated optic structure

Habib Mohamad

► **To cite this version:**

Habib Mohamad. Development of the differential method associated with the Fast Fourier Factorization for the modelization of photonic device: from complex optical diffraction grating to guided integrated optic structure. Optics / Photonic. Université Grenoble Alpes [2020-..], 2020. English. NNT: 2020GRALT032 . tel-03102609

HAL Id: tel-03102609

<https://theses.hal.science/tel-03102609>

Submitted on 7 Jan 2021

HAL is a multi-disciplinary open access archive for the deposit and dissemination of scientific research documents, whether they are published or not. The documents may come from teaching and research institutions in France or abroad, or from public or private research centers.

L'archive ouverte pluridisciplinaire **HAL**, est destinée au dépôt et à la diffusion de documents scientifiques de niveau recherche, publiés ou non, émanant des établissements d'enseignement et de recherche français ou étrangers, des laboratoires publics ou privés.



THÈSE

Pour obtenir le grade de

DOCTEUR DE L'UNIVERSITÉ GRENOBLE ALPES

Spécialité : OPTIQUE ET RADIOFREQUENCES

Arrêté ministériel : 25 mai 2016

Présentée par

Habib MOHAMAD

Thèse dirigée par **Alain MORAND**
et codirigée par **Pierre BENECH**, Professeur

préparée au sein du **Laboratoire Institut de Microélectronique, Electromagnétisme et Photonique - Laboratoire d'hyperfréquences et de caractérisation** dans l'**École Doctorale Electronique, Electrotechnique, Automatique, Traitement du Signal (EEATS)**

développement de la méthode différentielle associée à la Fast Fourier Factorization pour la photonique : étude de réseaux diffractifs complexes et modélisation de structures en optique intégrée.

Development of the differential method associated with the Fast Fourier Factorization for the modelization of photonic device: from complex optical diffraction grating to guided integrated optic structure

Thèse soutenue publiquement le **16 octobre 2020**, devant le jury composé de :

Monsieur Alain MORAND

MCF, Université Grenoble Alpes - IMEP-LAHC, Directeur de thèse

Monsieur Olivier GAUTHIER-LAFAYE

Directeur de recherche, CNRS-Laboratoire d'analyse et d'architecture des systèmes (LAAS-CNRS), Rapporteur

Monsieur Gérard GRANET

Professeur des Universités, Université Clermont Auvergne - Institut Pascal, Rapporteur

Monsieur Pierre BENECH

Professeur des Universités, Grenoble INP - IMEP-LAHC, Co-directeur de thèse

Monsieur Frédéric GARET

Professeur des Universités, Université Savoie Mont Blanc - IMEP-LAHC, Président du jury

Madame Nadège COURJAL

Maître de conférences, Université de Franche-Comté, Examinatrice

Abstract

Nowadays to design photonic devices, it is important to have reliable and efficient simulation tools. In fact, if exploiting the technological grids of the design parameters is considered possible for the simple devices, its cost in terms of number of tests becomes an obstacle to the optimization of the structures. Therefore, it is essential to develop fully vectorial simulations, with complex or/and real refractive indices materials, to guarantee that all the propagation modes (guided, radiated and evanescent modes) are taken into account. The simulations of the structures with high contrast refractive index (Silicon photonics for example) or structures using metallic layer and generating plasmonic modes or sub-wavelength structures like metamaterials are a set of examples that requires the use of these tools. These methods can be differentiated by their used calculation algorithm: calculation in the frequency domain by finite differences or finite elements, Fourier based methods, or calculation in the temporal domain with the finite difference method... For example, the FDTD has become in the recent years a reference tool in the domain of silicon photonics. However, almost all these methods are not necessarily optimal. They can be distinguishable by the required numerical resources, particularly in terms of the used memory, the execution time, the take into account of the boundary conditions, the discretization of the structure, or their workspace domain (spectral or spatial) ... Over the last fifteen years, the group involved with the development of electromagnetic tools in the laboratory (IMEP-Lahc), headed towards the development of RCWA based numerical tools to simulate and design the optical response of diffractive and guided optic structures. However, this last method as the FDTD can generate approximations inducing inaccuracies or an increase in the numerical resources used for certain configurations (memory, execution time...). The objective of this thesis is to develop a more general tool aiming to reduce these imperfections while retaining the possibility of using it on a multitude of photonics applications (diffractive optics, guided optics, etc.). My choice fell on the differential method which is widely used for the study of diffraction gratings. This method can be more efficient than the RCWA but it also has limitations especially for the simulation of periodic structures with complex profile in TM polarization. Since the 2000s, the association of a new module called FFF (Fast Fourier Factorization) has solved this problem and opened up new possibilities for this method. After

a general introduction, the differential method associated with the FFF is presented in detail. Then, a simple and fast solution which makes the use of this method with metals having a purely real and negative permittivity is proposed and solve the problem of divergence faced before. Consequently, a complete study of a dielectric diffractive structure visual security applications is subsequently detailed. Moreover, the developed code of the DM-FFF is integrated in neural networks algorithm for optimal modeling and design of visual security structures. Finally, to meet the condition of generalizing the method for the different photonic structures (guided and diffractive), a coordinate transform inspired from the aperiodic FMM was implemented in the algorithm of the DM-FFF transforming the last one into an aperiodic method for the simulation of 2D integrated optical structures for complex, non-isotropic and non-magnetic materials. The decomposition of the propagation of eigenmode basis can provide access to information which are not directly provided by the FDTD for example (guided modes, radiated modes . . .). More precise, faster and more rigorous results were obtained compared to a-FMM especially in TM polarization with curvilinear profiles such as the case of cylindrical structures.

Acknowledgements

This Ph.D. thesis is the output of the effort and support of several people to whom I am extremely grateful.

First and foremost, I wish to convey my profound and sincerest gratitude to my supervisors Doctor Alain MORAND and Professor Pierre BENECH for their valuable and insightful guidance. I accomplished a lot from their vast professional vision and scientific wisdom. It has been a real honor and privilege to have been your student.

Many thanks go to Professor Gérard Granet and Doctor Olivier Gauthier-Lafeye for accepting to review my manuscript and to Professor Frédéric Garet and Doctor Nadège Courjal for being the examiners during my defense.

Thanks to Professor Jean-François ROUX and Doctor Olivier Jacquin for accepting being the jury of the CSI of my PhD.

This 3-year Ph.D. journey would not have been possible without the financial support of the French National Agency of Research (ANR), to whom I am sincerely grateful.

Thanks to Aude and Gregory for training me on all the fabrication processes and characterization benches. Aude, thanks for your kindness and your help in the cleanroom. Gregory, thanks for your availability and will to help whenever I needed help in the characterization platforms.

Thanksto all the ODISSEA project partners! special thanks go to Sylvain Blaize for the scientific discussions and helps and for Soukaina for providing me the results calculated by the MC-grating software, and for depositing the grating layers on the waveguide samples.

Special thanks to the researcher of the Photo group in IMEP-LahC for their kindness and for the scientific meetings which increased my knowledge in the photonics domain: Davide, Elise, Jean-Emmanuel, Lionel, Julein... Thank you!

Thanks to all the administrative people of the laboratory! Annaïck , Fabienne, Isabelle, Dahlila, , Valérie, Brigitte.

Special thank goes to the sweetest Rachelle for her endless support and encouragement to finish the writing of my thesis especially during the lock-down period.

Many thanks go to Doctor Hamza Issa who encouraged me to come to France and pursue the master degree in Grenoble.

I would like to acknowledge my friends for supporting me throughout my Ph.D. and making my experience cheerful. I thank Mohamad Awad, Ali Al-Shakoush, Latifa, Ahmad, Haitham, Nisrine, Ali Azim, Victoria, Kassem, Ali Al Takech, Firas, Jalal, Mohamad Wehbi, Thibauld, Robert, Angeliki, Andres Lopez, Miltiadis, Fransesco, Nhu-Huan, and all other friends for being nice company.

I would like to express my truest gratitude and humility to my parents, Fatima (my sister) and Mahdi (my brother), for their unequivocal love, support, and all their sacrifices they made. However, they deserve every bit of credit for my success. I am perpetually indebted to them forever.

Table of contents

List of figures	vii
List of tables	xv
1 General Introduction	1
1.1 Objectives and Motivation	1
1.2 Overview of the popular electromagnetic methods	4
Nomenclature	1
I Electromagnetic Numerical Tools for the diffraction of light by periodic structures	9
2 Electromagnetism applied to 1D diffraction gratings	11
2.1 The basics of diffraction gratings	11
2.2 Maxwell's equations formalism: Transient regime	13
2.3 Maxwell's equations in the harmonics regime	14
2.4 The decomposition into TE and TM polarization	15
2.4.1 Introduction	15
2.4.2 Polarization of the field exciting the diffraction grating	16
2.5 Fourier expansion of the field	17
2.5.1 The general form of the field outside the modulated zone in TE polarization	18
2.5.2 TM polarization	19
3 Principles of the Differential Method associated with Fast Fourier Factorization	21
3.1 The differential Theory in TM polarization	21

TABLE OF CONTENTS

3.1.1	The classical Differential method: the transient equations of the electric and the magnetic fields inside the modulated zone	21
3.1.2	The harmonic Fields equations inside the modulated zone	22
3.1.3	Harmonic propagation equations	25
3.1.4	FFF associated to the differential theory in TM polarization	27
3.1.5	Fields outside the modulated zone	33
3.2	Formulation of the differential theory in TE polarization	35
3.2.1	Fields inside the modulated zone	35
3.2.2	Field outside the modulated zone	37
3.3	Numerical integration of the matrix differential system	38
3.3.1	The Runge-Kutta integration algorithm	39
3.3.2	Runge-Kutta algorithm applied to the Differential theory in Fourier space	40
3.4	The linear relation that links the modulated region with the homogeneous zones	41
3.5	Use of the Shooting Method	42
3.5.1	Defining the initial conditions	42
3.5.2	The transition from the stationary fields into the forward and backward representation of the fields	43
3.5.3	T-matrix of a given section	45
3.6	Scattering Matrix algorithm (S-Matrix)	46
3.6.1	Introduction	46
3.6.2	Definition of the S-Matrix	47
3.6.3	The total S-matrix of the entire structure	48
3.7	The intensities of the diffracted order	50
3.8	RCWA extracted from the differential theory	52
3.9	Conclusion	53
4	DM-FFF: Validation and comparison with other electromagnetic computational methods	55
4.1	Validation of the methods	55
4.1.1	Introduction	55
4.1.2	Numerical validation	56
4.2	The DM-FFF compared to other electromagnetic computational methods . .	61
4.2.1	Introduction	61
4.2.2	Sinusoidal Metallic Grating	62
4.2.3	Discontinuous structure: A Trapezoidal metallic grating as an example	68
4.3	Conclusion	71

5	The differential theory and the lossless permittivity metals: Problem and solution	73
5.1	Definition of the problem	73
5.2	Implementation of Graded Index Layer (GIL) at the metal-dielectric interface with pure negative and real permittivity metallic gratings	75
5.3	Application of the GIL on a triangular metallic grating with quasi-real negative permittivity	77
5.4	Conclusion	81
6	DM-FFF applied to visual security structures: A full study	83
6.1	Introduction	83
6.2	Spectrum to color transformation	84
6.3	All dielectric structures as a reflection visual security device	86
6.3.1	Geometry of the structure	86
6.3.2	The impact of the buffer layer on the chromatic response of the structure	87
6.3.3	Impact of the period on the chromatic response of the structure	90
6.3.4	Impact of varying the amplitude of the grating A	91
6.3.5	Impact of the incident angle θ_{inc}	93
6.4	Use of the DM-FFF for the inverse tailoring of structural color	96
6.5	Conclusion	98
II	Electromagnetic Numerical Tools for the propagation of light in guided structures	99
7	DM-FFF applied to optical guided structures: Theoretical interpretation	101
7.1	Introduction	101
7.2	Modelisation of integrated optics structures using the DM-FFF	103
7.2.1	Illustration of the problem	103
7.2.2	Perfectly Matched Layer as non-linear complex coordinate transformation	104
7.3	Formulation of the aperiodic DM-FFF (a-DM-FFF)	108
7.3.1	Propagation equation in TM polarization	108
7.3.2	Propagation equation in TE polarization	109
7.3.3	Input/Output Ψ as an equivalent guided zone	111

TABLE OF CONTENTS

7.3.4	The use of a transition matrix that directly links the amplitude of the eigen modes with the stationary harmonic vectors	116
7.4	Validation of the method	119
7.4.1	TE polarization	119
7.4.2	TM polarization	121
7.5	Conclusion	122
8	A-DM-FFF compared to the a-FMM: Application on complex shaped photonic guided structures	125
8.1	Application of the a-DM-FFF on curvilinear guided reflector	125
8.1.1	Geometry of the structure	125
8.1.2	TM polarization: Dielectric high contrast index structure	126
8.1.3	TM polarization: Metallic 2D pillar	129
8.1.4	TE polarization	131
8.1.5	Conclusion	132
8.2	Application of the a-DM-FFF on resonant cavities: Microdisk resonators as examples	133
8.2.1	Introduction	133
8.2.2	Problem of doublet resonances	133
8.2.3	Microdisk cavities excited by plane waves	136
8.2.4	Microdisk-guide coupling	142
8.3	Conclusion	152
III	Experimental results of Bragg grating filters	155
9	Fabrication and Characterization of Bragg Reflection filters associated with ion-exchanged waveguides	157
9.1	Principles of Bragg grating waveguide used as wavelength filter	157
9.2	Ion Exchanged waveguides principle	159
9.2.1	Principle of ion exchange	159
9.2.2	Description and Fabrication of optical waveguides	160
9.2.3	Characterization of the guides	161
9.3	Roll to roll Grating with ion exchanged waveguide: direct interaction	166
9.4	Roll to roll Grating with ion exchanged waveguide: Hybridization by MEMO	170
9.4.1	Hybridization process	170
9.4.2	Simulated results	171

TABLE OF CONTENTS

9.4.3 Spectral analysis	171
9.5 Conclusion	174
10 Conclusion and Perspectives	175
10.1 Conclusion	175
10.2 Perspectives	177
References	179
Appendix A The multiplication of two Fourier series: Toeplitz matrix formulation	189
Appendix B The normal of the surface for the different used geometries.	191
B.1 Rectangular Profile	191
B.2 Sinusoidal Profile	191
B.3 Trapezoidal or triangular Profile	192
B.4 Curvilinear profile	192
Appendix C Test ECH mask datasheet	194
Appendix D List of Publications	196
D.1 Journal Publications	196
D.2 Oral contributions in international conferences	196
D.3 Oral Contributions in French National conferences	197
Résumé	199

List of figures

1.1	(a) The wings of blue Morpho butterflies like Morpho menelaus show strong blue iridescence. (b) A TEM image of the cross-section of the Morpho sulkowskyi ground scale reveal the “Christmas tree” like structure responsible for the famous blue iridescence.	3
2.1	Geometrical representation of 1D sinusoidal diffraction grating. An incident plane wave on a periodic structure induces the diffraction of different transmitted or reflected orders.	12
2.2	Representation of the TE and TM polarization	16
2.3	Sinusoidal modulated zone illuminated with a monochromatic and linear polarized plane wave and the electromagnetic field components respectively for \vec{E} and \vec{H} in a cartesian space for (a) TE polarization (b) TM polarization.	17
3.1	Two numerical solutions	26
3.2	Grating geometry and notations of a lamellar grating illuminated with a TM polarized plane wave.	27
3.3	Two numerical solutions	29
3.4	Unit cell of sinusoidal grating profile. $f(x)$ is the function of the profile and N_x , N_z represent the normal distribution of the profile with respect to the x -axis and the z -axis respectively.	31
3.5	The modulated zone of a unit cell of a sinusoidal grating. The discretization step is D_z where each discretized layer is represented by its T-Matrix.	39
3.6	A unit cell of periodic sinusoidal grating. The propagation in the homogeneous layers are calculated via the Ψ matrix and in the modulated zone, the propagation matrix P is a result of the recursion of the Runge-Kutta integration of the different sections.	44
3.7	Definition of T-matrix of a given section. This algorithm links the amplitude of the wave of the s^{th} layer with the amplitude of the fields of the $s - 1^{th}$ layer.	45

LIST OF FIGURES

3.8 (a) Discretized grating structure, where the horizontal lines represent actual material interfaces. The fields in each layer can be represented as a superposition of upward- and downward-propagating. (b) Definition of the S-matrix of a given s section. This algorithm links the amplitude of the incoming fields towards a given layer with the amplitude of the outgoing fields from this given layer. 47

4.1 Unit cell of a dielectric rectangular periodic grating of period $\Lambda = 1 \mu m$. The structure is illuminated from the superstrate with a monochromatic and TE or TM polarized plane wave at normal incidence and a wavelength $\lambda = 600nm$. The refractive indices of the superstrate, the modulated zone and the substrate are $n_{sup} = 1, n_c = n_{sub} = 1.5$ respectively. The wave vector is $k = \frac{2\pi}{\lambda}n_{sup}$. . . 56

4.2 The field maps of the dielectric lamellar structure using the DM-FFF and Reticolo software for (a) TM polarization (b) TE polarization. 58

4.3 Convergence of the relative error of zeroth order of transmission $|T_{0_{Reticolo}} - T_{0_{DM-FFF}}|$ with $T_{0_{Reticolo}} = 0.23283470$ for different discretization steps. . . . 58

4.4 Unit cell of a sinusoidal periodic grating of period Λ . The structure is illuminated from the superstrate by a monochromatic and polarized plane wave k at a wavelength λ . The refractive indices of the superstrate, the modulated zone and the substrate are n_{sup}, n_c and n_{sub} respectively. The wave vector $k = \frac{2\pi}{\lambda}n_{sup}$ 59

4.5 The relative error of the zeroth order of transmission T_0 of the sinusoidal dielectric structure following N with respect to T_0 for $N = 150$ of each method. With $T_{0_{N=150}} = 0.412428713, 0.412673209, 0.412406292$ for the DM-FFF, the FMM and the RCWA-FFF respectively. $D_z = 1nm$ and $N_{FFT} = 8192$ samples. 61

4.6 Unit cell of the periodic grating. The structure is illuminated with a TM polarized plane wave at $\lambda = 673.2nm$ 62

4.7 Relative error with respect to the number of harmonics N for the different methods 63

4.8 Evolution of $|E_x|$ with (a) FMM, (b) RCWA-FFF, (c) DM-FFF and (d) C-Method 64

4.9 The execution time following the truncation order N for 600 cascaded layers. 65

4.10 (a) The evolution of the minus first order of reflection following N for different sub-layers n_S (b) The execution time following the truncation order N of the DM-FFF with $D_z = 0.25nm$ and n_S layers. 67

4.11	(a) Schematic representation of a trapezoidal unit cell. The normal and the tangent to the trapezoidal region using the (b) DM-FFF, (c) FMM, (d) C-Method	68
4.12	Relative error with respect to the number of harmonics N for the different methods	69
4.13	Relative error with respect to the angle β for the different methods	70
5.1	(a) Unit cell of a trapezoidal grating of period Λ associated with the graded index layer (GIL) of thickness δ . (b) The distribution of the refractive index real part along Λ at a given position $z = z_s$ (c) The distribution of the refractive index imaginary part at a given position $z = z_s$	76
5.2	(a) Geometry of the triangular grating: gold core of thickness of 50nm, $\Lambda = 400\text{nm}$. The structure is excited from the substrate with $n_{sub} = 1.55$. (b) Unit cell of the grating with GIL of thickness δ added at the dielectric-metal interface.	77
5.3	The evolution of the zeroth order of reflection $R_{(0)}$ following N of the triangular Au grating for different discretization step D_z	78
5.4	The evolution of the zeroth order of reflection $R_{(0)}$ following N of the triangular Au grating modeled via the DM-FFF for $D_z = 1\text{nm}$ and different thicknesses δ of the graded index layer (GIL)	79
5.5	Comparison of the evolution of the zeroth order of reflection $R_{(0)}$ following N of the triangular Au grating between the four different types of modal methods: DM-FFF, RCWA-FFF, FMM, and C-Method	80
5.6	Spectrum of the zeroth order of transmission $T_{(0)}$ for the DM-FFF (with and without GIL) and the C-Method. The values of both methods are calculated for $N = 45$ and $D_z = 1\text{nm}$ is used with the DM-FFF	81
6.1	CIE 1931 color matching functions	85
6.2	CIE 1931 color space chromaticity diagram known as xy space. The outer boundary is the spectral locus with wavelengths in nm.	85
6.3	Geometry of the studied structure	87
6.4	Spectral calculation as a function of the wavelength for the grating of $\Lambda = 320\text{nm}$, $A = 200\text{nm}$ and variable T . The DM-FFF has been used for the calculation with $N = 25$ and $D_z = 1\text{nm}$	88
6.5	Color palette obtained from the numerical simulation of $R_{(0)}$ and $T_{(0)}$ at normal incidence with $\Lambda = 320\text{nm}$, $A = 200\text{nm}$ and variable T	89

LIST OF FIGURES

6.6	Spectral calculation of $R_{(0)}$ as a function of the wavelength for $A = 200nm$, $T = 80nm$ for different periods Λ	90
6.7	Color palette obtained from the numerical simulation of $R_{(0)}$ and $T_{(0)}$ at normal incidence for different values of the period Λ	91
6.8	Spectral calculation of $R_{(0)}$ as a function of the wavelength for $\Lambda = 320nm$, $T = 80nm$ for different values of A	92
6.9	The evolution of the effective refractive index following $1/\lambda$ with $T = 80nm$ and different values of A	92
6.10	Color palette obtained from the numerical simulation of $R_{(0)}$ at normal incidence for $T = 80nm$, $\Lambda = 320nm$ and different values of A in nm	93
6.11	Spectral response of the dielectric structure with $T = 80nm$, $A = 180nm$, $\Lambda = 320nm$ for different incident angles θ_{inc}	94
6.12	Band diagram of the sinusoidal GMR structure with $T = 80nm$, $A = 180nm$ and $\Lambda = 320nm$. The colored straight line represents the different incident angles θ_{inc} . The left sided spectrum belongs to the reflection spectrum of the chosen structure with $\theta_{inc} = 0^\circ$	95
6.13	Chromatic response of the final chosen structure for different incident angles θ_{inc}	95
6.14	Stages of the inversion scheme proposed to retrieve the geometrical parameters of a desired chromatic response	96
6.15	Stages of the inversion scheme proposed to retrieve the geometrical parameters of a desired chromatic response	97
7.1	Semi-infinite guided structure sandwiched between two infinite spaces (Region I and Region II) ($x \in [-\infty, +\infty]$)	103
7.2	Non linear transform for modeling a 2D infinite structure in a bounded finite space (a) Artificial periodized structure with period Λ bounded in imaginary space ($X \in [-\infty - j\infty, +\infty + j\infty]$.) after applying a complex coordinate transformation. (b) Unit cell of the artificially periodized structure bounded in ($x' \in [-\frac{\Lambda}{2}, +\frac{\Lambda}{2}]$). $q_{x'}$ represents the total thickness of the PML. $e = \Lambda - q_{x'}$ is the thickness not affected by the PML. The structure is excited with a guided mode. The input and output waveguide core refractive index is n_g . The cylindrical reflector refractive index is n_d . The superstrate and the substrate are two homogeneous zones of refractive index n_{ext}	105
7.3	Non-Linear coordinate transformation (a) the complex coordinate transformation $X = F(x')$ for $\gamma = \frac{1}{1-j}$ (b) its derivative $f(x')$ with respect to x'	106

7.4	Unit cell of the lamellar artificially periodized guided structure. The structure is excited by its fundamental TM polarized guided mode at $\lambda = 0.975\mu m$ with a period $\Lambda = 1.1\mu m$ and a total thickness of PML $q_{x'} = \lambda/2$ and $\gamma = \frac{1}{1+j}$. x' is the periodization axis, z is the propagation axis and y is considered invariant.	115
7.5	(a) The evolution of R_g with respect to the length of input waveguide H . The black dashed line represents the reference value calculated in Ref.[103] with $R_{ref} = 0.3554787$ (b) The execution time of the a-DM-FFF of the reference structure with $H = 12\mu m$, $D_z = 5nm$ and $N_{FFT} = 8192$ samples following the truncation order N	115
7.6	(a) Reflection coefficient R_g following the length of the i/o waveguides H (b) the calculation time using the new transition matrix W	119
7.7	Performance of the a-DM-FFF compared to the a-FMM for a lamellar structure as a reference in TE polarization. (a) Convergence of R_g following N (b) Relative Error $ R_g - R_{N=150} $ following N	120
7.8	Performance of the a-DM-FFF compared to the a-FMM for a lamellar structure as a reference in TM polarization. (a) Convergence of R_g following N (b) Relative Error $ R_g - R_{N=150} $ following N	122
8.1	Unit cell of the artificially periodized guided reflector	126
8.2	Convergence of the high refractive index contrast case with a dielectric cylinder rod reflector of the a-DM-FFF and the a-FMM (a) R_g following N (b) The relative error $ R - R_{N=150} $ following N	127
8.3	Evolution of the reflection coefficient error $ R_{ga-DM-FFF} - R_{ga-FMM} $ following Δn . All R_g are calculated for $N = 100, 50$ and 20 with $D_z = 5nm$ for both methods.	128
8.4	Convergence of the guided structure with metallic pillar reflector (a) R_g following N (b) The relative error $ R - R_{N=150} $ following N	130
8.5	Evolution of $ E_{x'} $ with TM polarization of the a-DM-FFF and the a-FMM for $N = 50$	131
8.6	Convergence of the guided structure excited by the fundamental TE_0 guided mode (a) dielectric structure of sec.8.1.3 with $n_d = 3.5$ and $n_{ext} = 1$ (b) metallic structure of sec.8.1.4 with $n_d = 1 + j7$ and $n_{ext} = 2.9$	132
8.7	Schematic representation of a microdisk cavity of radius R	134
8.8	Spectral response of the forced oscillation regime. In this case, the excitation is a bessel function which corresponds to the wave radiated by the microdisk. The phase matching in amplitude and phase is ensured [40].	135

LIST OF FIGURES

8.9	Schematic top view of microdisk resonator (a) Excitation by two in phase plane waves, at the resonant wavelength clockwise WGM is coupled to the disk (b) Excitation by two out of phase plane waves, at the resonant wavelength anti-clockwise WGM is coupled to the disk.	136
8.10	The zeroth order of transmission response of the excited in phase and out of phase plane waves of the microdisk with $R = 4\mu m$ (a) Using the a-DM-FFF (b) Using the a-FMM. The small subfigures represent the field map of the magnetic field $Real(H_y)$ at the resonant wavelengths with $m = 30$ (azimuthal order). The central axis belongs to the radial axis of symmetry where the in phase or out of phase excitation can be distinguished (optimum in case of the in phase excitation and zeroth in the out of phase case).	138
8.11	Normalized doublet splitting quality factor (Q_b) versus disk radius for $n_d = 2.2$ and $n_{ext} = 1$	140
8.12	Normalized doublet splitting quality factor (Q_b) versus disk radius for $n_d = 3.5$ and $n_{ext} = 1$	141
8.13	Unit cell of an artificially periodized 2D microdisk resonator associated to a bus waveguide.	142
8.14	Schematic representation of the proportional of the transmission $ 1 - T $ with respect to the disk to guide gap G	143
8.15	Spectral calculations as a function of the wavelength for different gap G between the cylinder and the guide calculated by using (a) a-DM-FFF (b) a-FMM.	146
8.16	Comparison of the quality factor evolution with the gap between the analytical method (CMT) and the 2D a-DM-FFF and the 2D a-FMM.	147
8.17	Spectral calculations as a function of the wavelength for different gap G between the cylinder and the guide calculated by using (a) a-DM-FFF (b) a-FMM.	148
8.18	(a) The evolution of the Q-factor calculated by the fitting equation following G for $n_d = 2.2$ and $n_{ext} = 1$. (b) The evolution of the doublet splitting $\Delta\lambda$ following G for the a-FMM and the a-DM-FFF.	149
8.19	The evolution of the minimum transmission intensity and the maximum reflection intensity following the gap G for the (a) a-DM-FFF (b)a-FMM. The black bars belongs to the gap where the doublet clearly appears in the spectrum.	151
9.1	Schematic representation of a Bragg filter. n_{eff} is the effective refractive index of the entire structure.	157

9.2	Schematic representation of ion exchange.	159
9.3	Optical waveguide by ion exchange fabrication process.	160
9.4	Schematic representation of the test bench of the radiation analysis	162
9.5	Radiation analysis using the SUI camera (a) Monomode waveguide with $4\mu m$ width (b) Multimode waveguide with $10\mu m$ width. The x and the y axis represent the pixels of the SUI camera.	163
9.6	Schematic representation of the test bench of the propagation loss measurement	163
9.7	Schematic representation of the test bench of the spectral analysis.	165
9.8	Spectral response of the waveguide of $4\mu m$ width using the HP 70950A optical spectrum analyzer.	165
9.9	The fabrication procedure of the grating associated to the ion exchanged waveguides sample	166
9.10	Bragg grating associated to the simulated waveguide. The ion exchanged waveguide has been replaced by an equivalent refractive index step waveguide.	167
9.11	(a) The minimum transmission in dB with respect to the transverse length of the grating (b) The transmission spectrum of the BGF with $L = 1.57cm$ and for different gaps.	168
9.12	The normalized transmission power of the ion exchanged waveguide of width $3\mu m$ associated to a surface grating of period $\Lambda = 240nm$	169
9.13	The fabrication procedures of the grating associated to the ion exchanged waveguides sample with the hybridization method	170
9.14	Schematic representation of the hybridized Bragg filter.	171
9.15	(a) The minimum transmission in dB with respect to the transverse length of the grating (b) The transmission spectrum of the BGF with $L = 1.57cm$ and for different gaps.	172
9.16	The measured transmission spectrum of the hybrid structure for different width of ion exchanged waveguides.	173
9.17	The fabricated hybridized sample. The blue horizontal lines represent the direction of the waveguides and the red vertical lines belong to the periodized grating.	173
2.1	Geometrical profile of the trapezoidal evolution.	192
2.2	Geometrical parameters of the cylindrical rod.	192

List of tables

4.1	The transmission coefficient $R(n)$ of the diffracted order -1 , and 0 of the dielectric sinusoidal grating for $N = 30$ with $D_z = 1nm$ and $n_S = 1$ for the S-matrix algorithm. The coefficients are calculated using the DM-FFF, the RCWA extracted from the differential theory, and the RCWA-FFF. The reference values are calculated by the classical FMM using Reticolo. ΔR_1 , ΔR_2 , and ΔR_3 represent the absolute relative error between the values of Reticolo from one side and the values of the DM-FFF, the RCWA, and the RCWA-FFF respectively from the other side	57
4.2	The reflection coefficient $R(n)$ of the diffracted order $-1, 0, +1$ of a dielectric sinusoidal grating for $N = 30$ with $D_z = 1nm$ and $n_S = 4$ for the S-matrix algorithm. The coefficients are calculated using the DM-FFF, the RCWA extracted from the differential theory, and the RCWA-FFF. R and T represent the total reflection and the total transmission of the all reflected orders respectively. $\Delta R_1, \Delta R_2$, and ΔR_3 represent the absolute relative error with respect to the values of the MFS and the values of the DM-FFF, the RCWA, and the RCWA-FFF respectively.	60
4.3	The minus first order of reflection transmission $R_{(-1)}$ for the metallic sinusoidal structure at $N = 10, 30, 50, 100$ using the four modal methods RCWA-FFF, DM-FFF, FMM, and C-Method	64
4.4	The zero order of transmission $T_{(0)}$ for the metallic trapezoidal structure at $N = 10, 30, 50, 100, 150$, and 200 using the four modal methods RCWA-FFF, DM-FFF, FMM, and C-Method	69
4.5	The recommended modeling method with respect to the grating profile in TM polarization with dielectric-metal interface. With HR: Highly recommended, R: recommended, NR: Not Recommended	71
6.1	Target and Retrieved Geometrical Parameters Related to the Tropical Rain Forest Depicted in Fig.6.15	98

LIST OF TABLES

7.1	R_g N = 20, 50 and 150 using the a-FMM and the a-DM-FFF of the reference structure.	114
7.2	R_g using the a-FMM and the a-DM-FFF of the reference Lamellar structure in TE polarization.	121
7.3	R_g using the a-FMM and the a-DM-FFF of the reference Lamellar structure in TM polarization.	123
8.1	R_g at N = 20, 50, 100 and 150 of the a-FMM and the a-DM-FFF for the structure with high refractive index contrast dielectric pillar.	128
8.2	R_g at N = 20, 50, 100 and 150 of the a-FMM and the a-DM-FFF for the structure with metallic pillar.	131
8.3	The resonant wavelengths with respect to the radius of the disk R for odd and even modes calculated via the a-DM-FFF and the a-FMM. $n_{ext} = 1$, $n_d = 2.2$ and all the values are calculated in μm. λ_a, m_a and Q_a represents the analytically calculated values of the resonant wavelength, the azimuthal order of this wavelength, and the quality factor of the microdisk at this wavelength respectively.	139
8.4	The resonant wavelengths with respect to the radius of the disk R for odd (in phase) and even (out of phase) modes calculated via the a-DM-FFF and the a-FMM. $n_{ext} = 1$, $n_d = 3.5$ and all the values are calculated in μm. λ_a, m_a and Q_a represents the analytically calculated values of the resonant wavelength, the azimuthal order of this wavelength, and the quality factor of the microdisk at this wavelength respectively.	140
9.1	The attenuation loss in dB/cm of the different monomode waveguides with K^+/Na^+ ion exchange at $380^\circ C$ for $8h$ and with a $NaNO_3$ flash at $350^\circ C$ for 30 mins and red laser source centered at $\lambda = 635nm$.	164

List of Abbreviations

1D	One Dimensional
2D	Two Dimensional
3D	Three Dimensional
A-DM-FFF	Aperiodic Differential Method associated with Fast Fourier Factorization
A-FMM	Aperiodic Fourier Modal Method
AMM	Analytic Modal Method
ASR	Adaptive Spatial Resolution
CIE	Commission Internationale de l'éclairage
C-Method	Chandezon Method
CMT	Coupled Mode Theory
DOVID	Diffraction Optically Variable Devices
DM	Differential Method
DM-FFF	Differential Method associated with Fast Fourier Factorization
EUROPOL	European Police Office
FDTD	Finite-Difference Time-Domain Method
FEM	Finite Element Method
FFF	Fast Fourier Factorization
FFT	Fast Fourier Transform
FMM	Fourier Modal Method
FWHM	Full Width Half Maximum
GIL	Graded Index Layer

LIST OF ABBREVIATIONS

GMR	Guided Mode Resonance
HD	High Definition
IMEP-LaHC	L'Institut de Microélectronique Electromagnétisme et Photonique et le Laboratoire d'Hyperfréquences et de Caractérisation
L2N	Laboratoire Lumière, nanomatériaux et nanotechnologies
MFS	Method of Fictitious Sources
NIR	Near Infra-Red
OHIM	Office of Harmonization in the Internal Market
RGB	Red Green Blue
RCWA	Rigorous Coupled Wave Analysis
RCWA-FFF	Rigorous Coupled Wave Analysis associated with Fast Fourier Factorization
SNOM	Near-field scanning optical microscopy
SOI	Silicon On Insulator
SPP	Surface Plasmon Polariton
SWG	Sub-Wavelength Grating
TE	Transverse Electric
TM	Transverse Magnetic
UV	Ultra-Violet
WGM	Whispering Gallery Mode
WDM	Wavelength-Division Multiplexing

Chapter 1

General Introduction

1.1 Objectives and Motivation

The study of light has been an important part of science from its beginning. Four generations have governed the evolution of optics. Starting by the conventional optics introduced by the ancient Greek, to the micro-optics, then the guided optics and recently the nano-optics known as nanophotonics. These four groups are considered as the core of optical science and forming its three branches: 1) the geometrical optics that describes the propagation of light between different medium as straight rays, and defined by the classical laws of the reflection and refraction. 2) the physical optics that deals with the light as a series of propagating electric and magnetic field oscillations. Indeed, It is particularly based on a series of four equations so called Maxwell's equations. 3) the quantum optics that studies the effect and the nature of light as quantized photons at submicroscopic levels. Owing to Maxwell, the world has witnessed a steady technological advancement in several areas. So, the light can be treated as an electromagnetic oscillations.

Nowadays, the ability to control and manipulate the optical electromagnetic waves (light) is one of the leading goals of scientists, researchers and optical engineers. Although, some natural optical systems have attracted researchers and theorists due to its important optical effects. Indeed, we live in a world full of colors. For example, if a flower re-emits all the wavelengths of the visible light, it will be white. In reverse, it is perceived as black, and in between where it absorbs and reflects some wavelengths it will have a color. However, the nature produces colors in three ways: through pigments, structural colors or bioluminescence. Consequently, the structural color has received the attention of scientists. These systems are often brightly colored, strongly iridescent and distinguished from the obvious structures and surfaces that are colored by pigmentation or bioluminescence colors. The first trials to understand the physical origin of those effects had began in the 18th century by Isaac Newton

and Robert Hook [34, 85]. They firstly observed the iridescent colors of the peacock feathers and silverfish scales. Accordingly, they correctly predicted that those colors are a result of physical structures rather pigmentation.

With the introduction of the electron microscope in the 1940's, the structural color in nature becomes a subject of study. In this context, the structural colors are categorized as either iridescent or non-iridescent. The iridescent color are thus defined as the structural colors that change with the viewing angle. On the other hand, if the color doesn't change with the change of the angle of observation, the produced color is called non-iridescent. However, from scientific point of view, the structural colors are mainly originated from a natural periodic arrangement that changes the characterizations of the incident light. To elaborate more, this physical coloration is divided into two types, the iridescent structural colors which are produced from the interference and the diffraction of light provoked by the irregularity of the structure, and the non-iridescent structural colors produced from the scattering.

Based on these observations and many other after, new ideas and new photonic structures have been inspired from the nature. The most interesting natural optical tricks is the ability of some butterflies, birds and flowers to change their colors. This interaction takes place in the presence of periodic structures. This periodic arrangement has the ability to modify and diffract the light to be transmitted, reflected or absorbed by the involved materials. Although, the size of the periodicity has to be compared to the wavelength under study. For example, a structure with periodicity of few millimeters or centimeters can control the electromagnetic wave in the microwave domain. On the other hand, the optical light (that we are interested in here) can be controlled with periodicity of tens to hundred nanometers. Moreover, the periodicity of the structure can be defined by the number of dimensions that sustain it. Thus, the light can be controlled by 1D, 2D or 3D periodic arrangements. The researchers have defined what's called "**the diffraction grating**" for the 1D arrangement. In contrast, photonic crystals are marked for 2D or 3D arrangement.

However, there are already some natural inspired fabrications and products available that have replicated the surface structure of animals or flowers, such as textiles, anti-counterfeiting technologies, optical filters, and optical security devices. In all these structures, the light behavior is ruled by Maxwell's equations. Moreover, the 1D diffraction gratings are characterized by their wide range of applications. Starting with spectroscopy, to the sensing applications and the structural color generation and not ending with the astronomy.

In a recent joint report, the European Police Office (EUROPOL) and the Office for Harmonization in the Internal Market (OHIM) pointed out the disastrous economical (200 billion USD per year) and health-related consequences of goods counterfeit. The dreadful

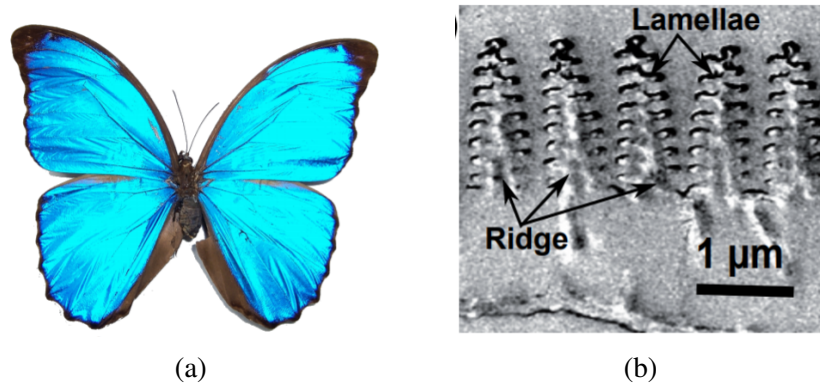


Fig. 1.1 (a) The wings of blue Morpho butterflies like *Morpho menelaus* show strong blue iridescence. (b) A TEM image of the cross-section of the *Morpho sulkowskyi* ground scale reveal the “Christmas tree” like structure responsible for the famous blue iridescence.

events that have recently happened in Europe made evident that travel and identity documents such as passports or ID cards are among the most counterfeited products. Counterfeiters have also benefit of the recent development in fabrication and characterization technologies that paradoxically, had led, to important advances in the Optical Document Security (ODS) domain. There is therefore a need for even more innovative optical security devices involving complex designs and new materials difficult, if not impossible, to fabricate without specialized laboratory equipment.

At this scale, more rigorous electromagnetic modeling methods depending on Maxwell's equations are mandatory for the computation of the interaction between the incident light and the structure. A wide range of numerical methods has been developed from many decades for the modelization of photonic structures. These methods have witnessed enormous leaps in terms of accuracy and their capabilities of modeling photonic structure following the previous years.

On the other hand, the numerical characterization and modeling of guided wave passive structures have been an interesting research topics in the last five decades. In the early 1960's, the efforts were devoted to the foundations of the waveguide theory. Twenty years later, dozens of numerical methods have been developed in order to analyze guided structures in the microwave and optical domains [25]. Nowadays, the integrated optic components are widely demanded in whispered applications. Moreover, the rapid growth in the domain of integrated optic has forced researchers and engineers to step up their efforts the development of more accurate and rigorous electromagnetic computational methods. The photonic guided structure is an open boundary device, basically composed of a waveguide core sandwiched between two homogeneous regions (superstrate and substrate). The guided structure is normally excited by one or more polarized guided mode. Thus, depending on the width of

the input waveguide and the wavelength under study, the waveguide may be considered as monomode (only one mode can propagate inside the structure) or multimode (two or more modes which can be excited).

Practically, when dealing with diffraction gratings, we talk about a plane wave excitation (TM, TE or linearly polarized waves). Moreover, the periodicity of the structure allows to deal with the problem using the Floquet-Bloch theory of periodic structures. Nevertheless, the guided optical structures share multiple commons with the periodic structures. Only two differences exist: 1) the way of excitation as the guided structure are excited by guided mode instead of plane wave, 2) the geometry of the structure itself as guided devices are considered as semi-infinite structures and not periodic arrangements (open boundary problem). Thus, to turn any electromagnetic computational method from the modelization of periodic structures into the conception of guided structures the two previous conditions must be fulfilled. Meanwhile, the first condition can be forwardly respected by changing the plane wave illumination into a guided wave excitation. In contrast, the second one should satisfy the outgoing conditions of an open structure. For that, a new concept has been introduced to some numerical methods dedicated for the modelization of the diffraction grating by associating perfectly matched layers at the boundary of each unit cell of the periodic structures by suppressing the outgoing and incoming waves from the neighboring cells [36].

1.2 Overview of the popular electromagnetic methods

Maxwell's equations are the set of equations that describe the propagation of electromagnetic waves in different medium. Therefore, the study of the interaction between electromagnetic waves and complex structures necessitates the use of numerical modeling methods. From many decades, theorists and researchers spared no effort in the development of efficient and powerful methods that tackle the problem of nano-scaled diffraction of optical wave especially when the studied structure is in the order of the incident wavelength. Two well-known approaches exist to deal with the electromagnetic diffraction problem. In the first one, Maxwell's equations are treated in time space and the other approach deals with them as a matter of spatial frequency so that in Fourier space.

For time domain, the most exploited method is the finite difference time domain method briefly known as FDTD [123]. It has been introduced by Yee in 1966 and developed over the years. Its algorithm is based on the discretization of the time and space simultaneously. Notwithstanding, its implementation is considered straightforward and simple. In contrast, due to the discretization meshes a large number of variables appears turning the algorithm

into a time consuming and memory exhausting technique. Moreover, the Finite Element Method (FEM) is also one of the leading spatial domain methods [112]. Its solution rests on the description of a global function of a global domain in terms of nodes of sub-functions in sub-domains recognized as finite element. As the FEM discretizes the domain appropriately, the advantage of this method compared to the FDTD appears with the minimization of the geometrical discretization error. Although, the meshing of Maxwell's equations leads to an algebraic system where the number of variables is proportional to the number of discretized meshes. Apparently, the FEM is considered as a powerful method. But, when complex structures are investigated, giant matrices full of zeros appear with the small meshes. However, storing this type of system is not an easy job. Consequently, in the temporal regime of Maxwell's equations, the matrices must be reorganized appropriately leading to a lack of execution time and computer memory.

Another drawback of the FEM occurs when handling with diffractive structures. At this level, the calculated electromagnetic fields suffer from singularities at the boundaries of the structures and generating the slow convergence of the method.

The other branch of methods dedicated for the study of diffraction of light by periodic structures is known as Fourier space methods. This family will be the center of the concern of this manuscript. Their algorithms are based on the projection of the electromagnetic fields on the modes of the structure. Three basic methods are the backbone of this family, the Differential Method (DM) [81], the Fourier Modal Method (FMM) also known as Rigorous Coupled Wave Analysis (RCWA) [48, 73, 75], and the Chandezon Method so-called (C-Method) [16, 56]. Indeed, the DM and the FMM share multiple common concepts.

Apparently, the study done by Tamir et al. of the interaction of electromagnetic wave with variable dielectric sinusoidal profiles in transverse electric polarization (TE) was the first step on the appearance of the FMM at the mid of 1960's [107]. Simultaneously, the same problem was addressed by Yeh and al. for the transverse magnetic polarization (TM) [124]. It appears that Burkhardt was the first theorist that reformulated the FMM in the form of truncated Eigenvalue matrix problem to study the diffraction of light for both TE and TM polarization [14]. In 1973, Kaspar has extended the work of Burkhardt to deal with complex and non-sinusoidal profiles [45]. One of the most published theory of the FMM is the paper of Peng [91]. He deduced that the FMM might be unworkable on all types of surface relief gratings. In his study, he mentioned that the regularity of a linear system doesn't assure the convergence of an infinite determinant. Therefore, he concluded that other mathematical solution must be applied for surface relief gratings to determine the characteristic solutions of the grating region. Without being up-to-date to the result of Peng, Knop was investigated, in 1978, the use of FMM on surface relief lamellar gratings

[48]. He extracted an eigenvalue problem for the TM polarization case by coupling two first-order differential equations. The qualitative leap of this method was in 1981 where Moharam and Gaylord figured out the volume gratings with inclined surface [73]. Moreover, they elaborated the use of the representation of an arbitrary structures as a succession of rectangular step index distribution known as the staircase approximation. Indeed, they also derived the eigenvalue differential equation for TE and TM polarizations [74]. Consequently, their work and all the previous other works have turned the Fourier Modal Method into the most popular tool for the modeling of diffraction gratings. In 2005, Hugonin et al. have demonstrated that applying a non-linear and complex coordinate transformation to the propagation equations of the FMM can turn the method into an aperiodic method used for the modeling of guided optical structures instead of optical periodic gratings [36]. Basically, this coordinate transformation play the role of Perfectly Matched Layers (PML) that suppress the incoming waves from the neighboring cells allowing to model artificially periodized guided structures as an open boundary semi-infinite structure.

At the same time of the appearance of FMM, the development of the Differential Method was on in full swing. We're are talking about a more rigorous method aiming to reduce the number of variables during the integration of the differential form of Maxwell's equations by dealing with the problem in the harmonic space. In case of 1D diffraction grating, the harmonic time dependence and the periodicity along the periodization axis added to the invariance with respect to a given axis help to treat the system of differential equations smoothly [15, 92]. Dating to the 70's, the first application of the DM was realized through Numerov numerical integration algorithm [80]. This integration allows the modeling of finite and infinite conductive diffraction gratings in TE and TM polarization. Although, numerical instabilities have been observed during this process especially when modeling deep grooves in TM polarization. This weakness has attracted the attention of researchers, involving in the algorithm of the DM and FMM, along 20 years without any valid interpretation. In 1996, series of papers ,introduced by Granet, Lalanne and Li, was the clue to unblock the limitations of the differential method [27, 51, 55]. The researchers referred this numerical instabilities to two reasons. The first error is due to the numerical integration process where the exponential components of the evanescent Fourier modes grow exponentially imposing numerical fluctuations. For that, the efforts was devoted to find the best mathematical solution that suit well with the integration step. Firstly the Schmidt orthogonality has been used to tackle this problem, but this method doesn't show a big impact on the stability of the method. Another solution rests on the discretized integration has not also shown its well functionality. Finally, the use of the S-Matrix algorithm has demonstrated that it is the most effective algorithm to handle this problem [54]. Despite this solution, the divergence of

the method weren't completely treated where another source of instabilities has appeared. This error is originated from the slow convergence of the Fourier series product describing the electromagnetic field at the interface of the grating especially in TM polarization. In other words, the multiplication of two discontinuous periodic functions which must give a continuous displacement field is not respected in the Fourier domain. For that, Li proposed to use what is called the 'inverse rule' [55]. Basically, these errors take place when two discontinuous periodic functions are multiplied. Therefore, the inverse rule will be applied for functions with complementary jump discontinuities along the periodization axis. This case appears, for example, in TM polarization between the incident electric field and the permittivity distribution at the surface of the modulated zone. Indeed, the same inverse rule has been applied to FMM as same instabilities was appeared during tests. At the beginning of the 21th century, a dramatic reformulation of the differential method has been applied by Popov et al. They introduced the Fast Fourier Factorization (FFF) to the propagation matrix of the Differential Method [94]. Since then, the efficiency of the method has incredibly been enhanced especially for non-lamellar gratings illuminated by TM polarized light. This reformulation allows to correctly describe the evolution of the incident field with respect to the grating's profile enabling an accurate and rigorous modeling technique for a wide class of diffraction problems.

Similarly, the C-Method is a frequency method applied on arbitrary shaped gratings. Its algorithm is based on the description of the grating's surface as continuous function [58]. After applying a coordinate transformation along the propagation axis and the periodic axis, the coefficients of Maxwell's equations become spatially dependent. In that case, the corrugation layer is replaced by a simple layer with a constant thickness and an equivalent complex permittivity.

Last but not least, the integral theory is another approach to deal with the diffraction problem. This theory is known as the integral method [70]. In that case, the fields at any point of the cartesian space is expressed as a set of integral functions. Therefore, the determination of the fields at any point of the space is reduced to the determination of the unknown functions following the periodic axis. The first use of the method featured with the perfectly conducting grating in the 1970's. At that time, the other electromagnetic methods was not adapted for such problem. But, this method is considered hard to be implemented and memory and time exhausting techniques while dealing with multi-layered diffraction gratings constituted by a stack of different refraction index.

Part I

Electromagnetic Numerical Tools for the diffraction of light by periodic structures

Chapter 2

Electromagnetism applied to 1D diffraction gratings

Basically, electromagnetism is the phenomenon of interaction of electric fields with magnetic fields. This branch of science is the fruit of works of several scientists. In 1861, James Maxwell assembled these theorems into a concise set of equations and completed their laws by a consistent and coherent model so-called Maxwell's equations. This set describes the distribution of the electric and magnetic fields and their change with respect to time. This chapter is intended to review the basics of diffraction of light, ruled by Maxwell's equations, of ideally 1D infinite periodic structure arrangements known as diffraction gratings.

2.1 The basics of diffraction gratings

'No single tool has contributed more to the progress of modern physics than the diffraction grating, especially in its reflecting form' are the opening words of a research article published in 1949 by the spectroscopist George R. Harrison. A diffraction grating is a set of closely spaced grooves or periodic arrangement. When a plane wave excites this arrangement, the diffraction of light by one of this groove interferes constructively or destructively with the light diffracted from the other grooves. Consequently, the light is split and diffracted into several plane waves (either transmitted or reflected) traveling in different directions and known as diffracted orders.

Referring to the grating's law (Eq.2.1) the x component part of the wave vector \vec{k}' issued from the grating is different from the incident wave vector \vec{k} along x . Then, diffraction angle

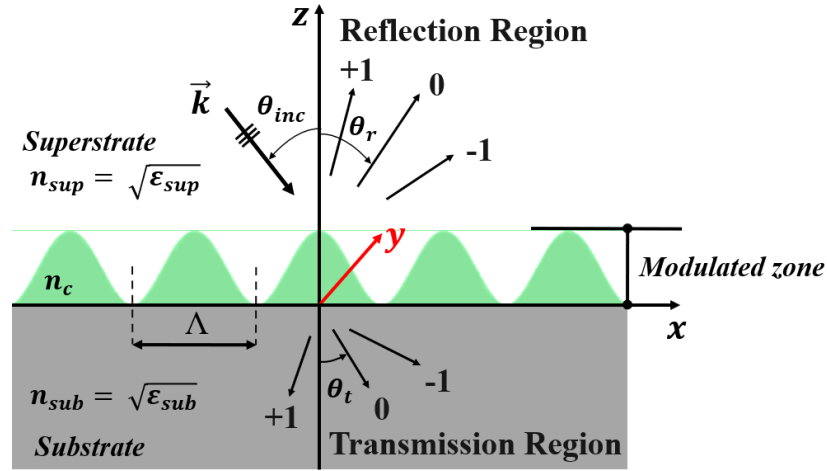


Fig. 2.1 Geometrical representation of 1D sinusoidal diffraction grating. An incident plane wave on a periodic structure induces the diffraction of different transmitted or reflected orders.

($\theta_{R/T}$) of each reflected (R) or transmitted (T) order can accurately be predicted depending on the angle of incidence θ_{inc} and the period of the grating Λ as follows,

$$k'_x = k_x + m \frac{2\pi}{\Lambda} \quad (2.1)$$

$$n_{sup/sub} \frac{2\pi}{\lambda} \sin(\theta_{r/t}) = n_{inc} \frac{2\pi}{\lambda} \sin(\theta_{inc}) + m \frac{2\pi}{\Lambda}$$

However, this equation can be expressed in a simplest form as,

$$n_{sup/sub} \sin(\theta_{r/t}) = n_{inc} \sin(\theta_{inc}) + m \frac{\lambda}{\Lambda} \quad (2.2)$$

With, $n_{sup/sub}$ and n_{inc} represent the refractive index of the superstrate layer or the substrate layer and the refractive index of the incident region respectively, and $m \in \mathbb{Z}$ is the number of the diffracted order.

On the other hand, the drop-off of a given order m occurs when the angle of incidence is chosen in a way that the refracted or transmitted plane wave is excited with grazing angle, which mathematically expressed as $\sin(\theta_{r/t}) = \pm 1$. Under this condition, the cut-off wavelength of the m^{th} diffracted order λ_m can be calculated as,

$$\lambda_m = \frac{\Lambda}{m} [\pm n_{sup/sub} - n_{inc} \sin(\theta_{inc})] \quad (2.3)$$

Aside the calculated angles and cut-off wavelengths, there is no information brought by these laws concerning the distribution of energy on each diffracted order. Although, the transmission and reflection coefficients could be expressed as Rayleigh expansions. But, calculating the efficiency of each order is not straightforward. These values depend on the incident angle, the polarization of the plane wave, the opto-geometrical dimensions of the grating and the different refractive indices of the structure. Accordingly, electromagnetic numerical methods based on Maxwell's Equations have to be developed to tackle this problem.

2.2 Maxwell's equations formalism: Transient regime

Maxwell's equations are a set of four equations where each one of them describes a fact. By combining the four laws proposed by Faraday, Ampère and Gauss and including his famous term into the Ampère law. J.Maxwell succeeded to describe correctly the interaction of electric and magnetic field as follows,

1) The Farady-Maxwell's law:

$$\vec{\nabla} \wedge \vec{\mathbf{E}} = -\frac{\partial \vec{\mathbf{B}}}{\partial t} \quad (2.4)$$

With $\vec{\mathbf{E}}$ that represents the electric field and $\vec{\mathbf{B}}$ the magnetic displacement . This equation implies that the time variation of magnetic field induces a rotation in the electric field.

2) Maxwell-Ampère's law:

$$\vec{\nabla} \wedge \vec{\mathbf{H}} = \frac{\partial \vec{\mathbf{D}}}{\partial t} + \vec{\mathbf{J}} \quad (2.5)$$

With $\vec{\mathbf{H}}$ the magnetic field, $\vec{\mathbf{D}}$ the electric displacement, and $\vec{\mathbf{J}}$ the vector of the electric current density. This equation stipulates that the rotation of the magnetic field depends on the time variation of electric field as well to the electric current.

3) Gauss's law (Electricity) :

$$\vec{\nabla} \cdot \vec{\mathbf{D}} = \rho \quad (2.6)$$

With ρ the volume density of the electric charge, this equation tells us that the electric flux through a closed surface is directly linked to the electric field induced at the surface of a defined volume. The displacement of the electric field is proportional to the electric charge density ρ .

4) Gauss's law (magnetism) :

$$\vec{\nabla} \cdot \vec{\mathbf{B}} = 0 \quad (2.7)$$

This equation indicates that the magnetic flux through a closed surface is null. There is no magnetic sources equivalent to the electric charges.

2.3 Maxwell's equations in the harmonics regime

The field time dependence is expressed following $\exp(-j\omega t)$. Therefore, a variable time dependent function $\mathbf{F}(r, t)$ can be expressed with respect to its harmonic function $F(r, \omega)$ via the Fourier transformation as ,

$$\mathbf{F}(r, t) = \int_{-\infty}^{+\infty} F(r, \omega) e^{j\omega t} d\omega \quad (2.8)$$

Hence, the set of Maxwell's equations can be expressed in its harmonic form as,

$$\begin{cases} \vec{\nabla} \wedge \vec{\mathbf{E}} &= j\omega \vec{\mathbf{B}} \\ \vec{\nabla} \wedge \vec{\mathbf{H}} &= -j\omega \vec{\mathbf{D}} + \vec{\mathbf{J}} \\ \vec{\nabla} \cdot \vec{\mathbf{D}} &= \rho \\ \vec{\nabla} \cdot \vec{\mathbf{B}} &= 0 \end{cases} \quad (2.9)$$

Under this situation, all variables are considered as complex functions following the angular frequency ω and the variable of the r space. As non-electric current sources exist in case of diffraction gratings and by considering linear, isotropic, homogeneous and non-magnetic media ($\vec{\mathbf{J}} = 0$ and $\rho = 0$), the constitutive equations that characterize this situation can be expressed as follows,

$$\vec{\mathbf{D}} = \epsilon \vec{\mathbf{E}} \quad (2.10)$$

$$\vec{\mathbf{B}} = \mu \vec{\mathbf{H}} \quad (2.11)$$

$\mu = \mu_0 \mu_r$ is the magnetic permeability with $\mu_r = 1$ (in case of non-magnetic materials), $\mu_0 = 4\pi \times 10^{-7} H/m$. $\epsilon = \epsilon_0 \epsilon_r$ where $n_r = \sqrt{\epsilon_r}$ represent the medium electric permittivity and the medium refractive index respectively. In addition, $\epsilon_0 = 8.854 \times 10^{-12} F/m$ is the permittivity of the free space . However, it is important to mention that $\epsilon(\omega)$ is a frequency dependent parameter which is linked directly to the chromatic dispersion of the involved medium.

By bearing in mind that $\vec{\nabla} \cdot (\vec{\nabla} \wedge \vec{F}) = 0$ with \vec{F} stands either for the electric field \vec{E} or the magnetic field \vec{H} , the use of Eq.(2.9), Eq.(2.10), and Eq.(2.11) leads to the simplified system of Maxwell's equations as follows,

$$\begin{cases} \vec{\nabla} \wedge \vec{E} = j\omega\mu_0\vec{H} \\ \vec{\nabla} \wedge \vec{H} = -j\omega\varepsilon\vec{E} \end{cases} \quad (2.12)$$

The projection of Eq.(2.12) on a cartesian coordinate system leads to a set of six coupled partial differential equations :

$$\left\{ \begin{array}{l} \frac{\partial E_z}{\partial y} - \frac{\partial E_y}{\partial z} = j\omega\mu_0 H_x \\ \frac{\partial E_x}{\partial z} - \frac{\partial E_z}{\partial x} = j\omega\mu_0 H_y \\ \frac{\partial E_y}{\partial x} - \frac{\partial E_x}{\partial y} = j\omega\mu_0 H_z \end{array} \right. \quad (2.13a)$$

$$\frac{\partial E_x}{\partial z} - \frac{\partial E_z}{\partial x} = j\omega\mu_0 H_y \quad (2.13b)$$

$$\frac{\partial E_y}{\partial x} - \frac{\partial E_x}{\partial y} = j\omega\mu_0 H_z \quad (2.13c)$$

$$\frac{\partial H_z}{\partial y} - \frac{\partial H_y}{\partial z} = -j\omega\varepsilon E_x \quad (2.13d)$$

$$\frac{\partial H_x}{\partial z} - \frac{\partial H_z}{\partial x} = -j\omega\varepsilon E_y \quad (2.13e)$$

$$\frac{\partial H_y}{\partial x} - \frac{\partial H_x}{\partial y} = -j\omega\varepsilon E_z \quad (2.13f)$$

2.4 The decomposition into TE and TM polarization

2.4.1 Introduction

In electromagnetic, it is important to introduce the notation of the polarization of the excited wave (direction of vibration of the EM field in the work plane). In his book, Germain Chartier has explained that the wave (light) is considered as a transversal and vectorial vibration [17]. In other words, the light is related to a vector which vibrates perpendicularly to the direction of the propagation vector. This last vector represents the vector of the the plane wave \vec{k} . In optics, the EM fields are usually decomposed into two polarizations : 1) the transverse electric polarization TE , 2) the transverse magnetic polarization TM. These two notations are defined following a diopter (a plane surface separating two media with different refractive indices). For TE polarization, the non-null component of the electric field \vec{E} is considered parallel to the diopter. On the other hand, for TM polarization, the non-null component of

the magnetic field \vec{H} is parallel to the diopter (Fig.2.2). Moreover, these two polarization states can also be named as s-polarization for TE, and p-polarization for TM.

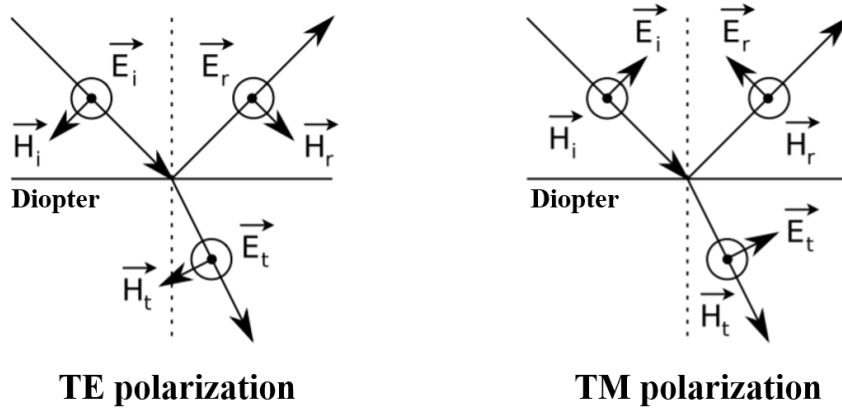


Fig. 2.2 Representation of the TE and TM polarization

2.4.2 Polarization of the field exciting the diffraction grating

We take into consideration the 1D grating depicted in Fig.2.1. The structure is illuminated with a monochromatic and polarized plane wave with a wavelength λ in the free space and an amplitude equal to unity. The angle of incidence of the plane wave is defined as θ_{inc} . In addition, the incident plan corresponds to (oxz) , the periodization axis is following x , and the propagation axis is along z , while along the axis y the structure is considered invariant. This invariance along y leads to the nullity of the derivative of the electric field and the magnetic field along y . Therefore, the system of Eq.(2.13) can be reduced as,

$$\left\{ \begin{array}{l} -\frac{\partial E_y}{\partial z} = j\omega\mu_0 H_x \end{array} \right. \quad (2.14a)$$

$$\left\{ \begin{array}{l} \frac{\partial E_x}{\partial z} - \frac{\partial E_z}{\partial x} = j\omega\mu_0 H_y \end{array} \right. \quad (2.14b)$$

$$\left\{ \begin{array}{l} \frac{\partial E_y}{\partial x} = j\omega\mu_0 H_z \end{array} \right. \quad (2.14c)$$

$$\left\{ \begin{array}{l} -\frac{\partial H_y}{\partial z} = -j\omega\varepsilon E_x \end{array} \right. \quad (2.14d)$$

$$\left\{ \begin{array}{l} \frac{\partial H_x}{\partial z} - \frac{\partial H_z}{\partial x} = -j\omega\varepsilon E_y \end{array} \right. \quad (2.14e)$$

$$\left\{ \begin{array}{l} \frac{\partial H_y}{\partial x} = -j\omega\varepsilon E_z \end{array} \right. \quad (2.14f)$$

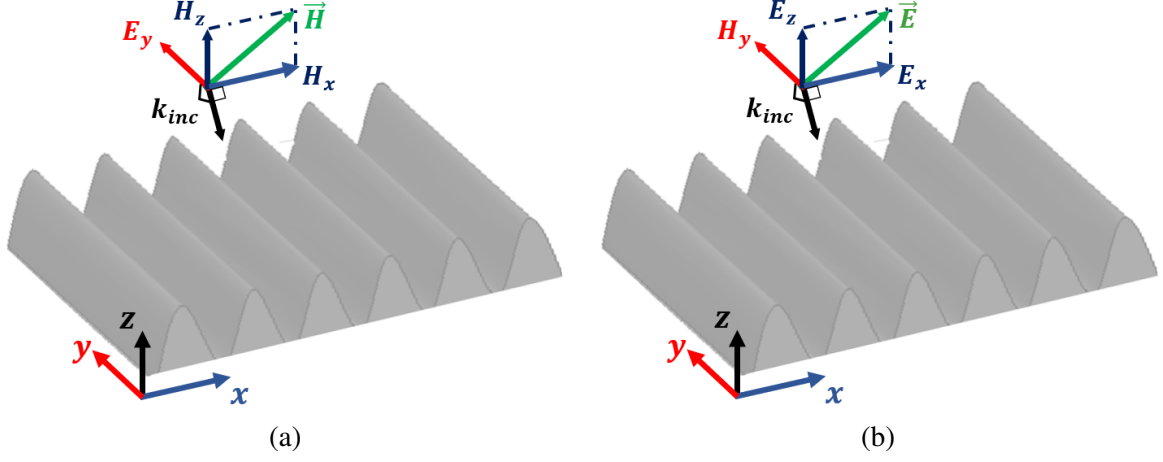


Fig. 2.3 Sinusoidal modulated zone illuminated with a monochromatic and linear polarized plane wave and the electromagnetic field components respectively for \vec{E} and \vec{H} in a cartesian space for (a) TE polarization (b) TM polarization.

Due to this invariance, the previous system can be separated into two independent groups. The first one corresponds to the transverse electric (**TE**) or **s** polarization where the electric field is parallel to oy (Fig.2.3a), and that depends on E_y , H_x and H_z :

$$\left\{ \begin{array}{l} -\frac{\partial E_y}{\partial z} = j\omega\mu_0 H_x \\ \frac{\partial E_y}{\partial x} = j\omega\mu_0 H_z \\ \frac{\partial H_x}{\partial z} - \frac{\partial H_z}{\partial x} = -j\omega\varepsilon E_y \end{array} \right. \quad \begin{array}{l} (2.15a) \\ (2.15b) \\ (2.15c) \end{array}$$

The other group introduces the transverse magnetic (**TM**) or **p** polarization, where the magnetic field is parallel to oy and transverse to the incidence plan (Fig.2.3b). In that case, the propagation of electromagnetic fields depends on H_y , E_x and E_z :

$$\left\{ \begin{array}{l} \frac{\partial E_x}{\partial z} - \frac{\partial E_z}{\partial x} = j\omega\mu_0 H_y \\ -\frac{\partial H_y}{\partial z} = -j\omega\varepsilon E_x \\ \frac{\partial H_y}{\partial x} = -j\omega\varepsilon E_z \end{array} \right. \quad \begin{array}{l} (2.16a) \\ (2.16b) \\ (2.16c) \end{array}$$

2.5 Fourier expansion of the field

Basically, the DM-FFF and the RCWA belong to the family of Fourier space methods. They are all characterized by expanding the electromagnetic field \vec{E} and \vec{H} and the medium

permittivity ϵ_r into Fourier series. For an arbitrary diffraction grating of period Λ and periodized following x , the spatial wavenumber can be expressed as $\sigma_n = n \frac{2\pi}{\Lambda}$ with $n \in \mathbf{N}$. Consequently, a periodic function $f(x)$ can be described by an infinite number of harmonics. And the harmonic amplitude F_n linked to a specific wave number n is issued from the following integral:

$$F_n = \frac{1}{\Lambda} \int_0^\Lambda f(x) e^{-j\sigma_n x} dx \quad (2.17)$$

2.5.1 The general form of the field outside the modulated zone in TE polarization

In case of homogeneous zone, the wave vector $k = \frac{2\pi}{\lambda} \cdot n_{inc} = \frac{2\pi}{\lambda} \cdot \sqrt{\epsilon_{inc}}$ is always constant with n_{inc} the refractive index of the incident homogeneous zone. Therefore, in these regions, only the phase of the electromagnetic field of the plane wave varies while its norm stays identical. In that case, the propagation system can be reduced into the Helmholtz's equation of homogeneous zones. In TE polarization, the transverse electric and magnetic field components (E_y and H_x) can be linked to their derivative following the propagation axis z to form a differential coupled equation system. By incorporating Eq.(2.15b) in Eq.(2.15c), the obtained system is the following one:

$$\begin{cases} -\frac{\partial E_y}{\partial z} = j\omega\mu_0 H_x & (2.18a) \\ \frac{\partial H_x}{\partial z} = -j\omega\epsilon E_y + \frac{1}{j\omega\mu_0} \frac{\partial^2 E_y}{\partial x^2} & (2.18b) \end{cases}$$

The substitution of Eq.(2.18a) in Eq.(2.18b) leads to the simplified propagation equation of Helmholtz:

$$\Delta E_y(x, z) + k^2 E_y(x, z) = 0 \quad (2.19)$$

Meanwhile, the invariance along y and the periodicity following x that induces the equality $\frac{\partial}{\partial x} = -j\sigma_n$ allow to write the Helmholtz's Equation of one harmonic n as,

$$\frac{\partial^2 E_n}{\partial z^2} + (k^2 - \sigma_n^2) E_n = 0 \quad (2.20)$$

Where E_n represents the Fourier coefficient in the x direction of the electric field E_y at the harmonic n . Such type of differential equation of second order can be easily solved in terms of complex exponential solutions. Therefore, one harmonic of the Fourier transformation of

the electric field component along z can be expressed in terms of its forward and backward components as,

$$\begin{aligned} E_n &= A_n^+ \exp(j\beta_n z) + A_n^- \exp(-j\beta_n z) \\ &= E_n^+ + E_n^- \end{aligned} \quad (2.21)$$

With A_n^+ and A_n^- are the amplitude of the forward and backward components of the field and $\beta_n = \sqrt{k^2 - \sigma_n^2}$ the propagation constant along z of the harmonic n .

Indeed, to reconstitute the electric field $E_y(x, z)$ in the cartesian space, an inverse Fourier transformation can be simply applied,

$$f(x) = \sum_n F_n e^{j\sigma_n x} \quad (2.22)$$

Practically, the periodicity along x imposes the discretization into the Fourier space following σ_n and its complex amplitude F_n . For any incident plane wave, the Fourier space should be centralized to its spatial frequency $\sigma_0 = k \sin(\theta_{inc}) = \frac{2\pi n_{inc}}{\lambda} \sin(\theta_{inc})$ to ensure the phase matching. Thus, σ_n can be expressed as,

$$\sigma_n = \sigma_0 + n \frac{2\pi}{\Lambda} \quad (2.23)$$

Finally, $E_y(x, z)$ can be expressed as,

$$E_y(x, z) = \sum_{n=-\infty}^{+\infty} \left(A_n^+ e^{j\beta_n z + \sigma_n x} + A_n^- e^{-j\beta_n z + \sigma_n x} \right) \quad (2.24)$$

Where A_n^+ and A_n^- are the forward and backward eigen modes field amplitudes. In that case, the eigen modes are the plane waves of spatial frequency σ_n following x and $\beta_n = \sqrt{k^2 - \sigma_n^2}$.

2.5.2 TM polarization

In a similar way, the magnetic field outside the modulated zone in case TM polarization verifies the Helmholtz's equation of the magnetic field H ,

$$\Delta H_y(x, z) + k^2 H_y(x, z) = 0 \quad (2.25)$$

After the same discretization following σ , $H(x, z)$ can be expressed as,

$$H(x, z) = \sum_{n=-\infty}^{+\infty} \left(B_n^+ e^{j\beta_n z + \sigma_n x} + B_n^- e^{-j\beta_n z + \sigma_n x} \right) \quad (2.26)$$

Outside the modulated zone, the eigen modes of the field for \vec{E} and \vec{H} represent the plane waves in these regions. On the other hand, inside the modulated zone, the Maxwell's equations are projected on their Fourier series. Therefore, the Fourier decomposition enables the use of electromagnetic numerical methods to handle the propagation of fields inside the modulated area. These numerical tools transform generally the system into a set of ordinary differential equations in order to tackle the problem easily.

Chapter 3

Principles of the Differential Method associated with Fast Fourier Factorization

This chapter is devoted to describe the equation used by the DM-FFF for the modeling of 1D diffraction gratings. It allows to study the diffraction of a plane wave by a multi-layered structure. Besides, it gives access to obtain the intensities of different diffracted orders when an oblique incident plane wave excites the periodic structure. Noting that the propagation axis is z , the grating is periodized following x . And finally, the grating and the waves are invariant along y .

3.1 The differential Theory in TM polarization

3.1.1 The classical Differential method: the transient equations of the electric and the magnetic fields inside the modulated zone

As the magnetic field component H_y , parallel to the invariant axis y , is always continuous at each boundary, the electromagnetic propagation equations, that rule the TM polarization, depend only on H_y , E_x and E_z . By combining Eq.(2.14b) and Eq.(2.14c), and by assuming that $H_y' = \omega\mu_0 H_y$, the classical system of differential equations of propagation in TM polarization can be expressed as,

$$\begin{cases} \frac{\partial E_x}{\partial z} = jH'_y + j \frac{\partial}{\partial x} \left(\frac{1}{k^2} \frac{\partial H'_y}{\partial x} \right) \\ \frac{\partial H'_y}{\partial z} = jk^2 E_x \end{cases} \quad (3.1a)$$

$$\begin{cases} \frac{\partial E_x}{\partial z} = jH'_y + j \frac{\partial}{\partial x} \left(\frac{1}{k^2} \frac{\partial H'_y}{\partial x} \right) \\ \frac{\partial H'_y}{\partial z} = jk^2 E_x \end{cases} \quad (3.1b)$$

We suppose that a monochromatic plane wave (wavelength λ in the free space and an amplitude equal to unity) is incident under an angle θ_{inc} coming from the superstrate. As a result, the forward propagating wave can be expressed following $\exp(j\beta z)$.

3.1.2 The harmonic Fields equations inside the modulated zone

Inside the modulated zone, the bloch-Floquet theorem describes the fields as a generalized Fourier series following the periodicity axis x . However, by discretizing the Fourier space following σ_n as mentioned in section (2.5). Eq.(2.22) turns into an infinite system of coupled differential equations with $n \in]-\infty, +\infty[$. Accordingly, after neglecting the terms of the fields where the spatial frequency σ_n is greater than a particular threshold σ_N , the system of differential equations can be truncated into $2N + 1$ coupled equations following $n \in [-N, +N]$, where N represents the truncation order. Thus, by performing a Fourier transformation following x , the differential system (3.1) can be expressed in the Fourier regime as a set of equations where the only variable is following z .

Accordingly, the Floquet-Bloch theorem of periodic structures allows to describe the electromagnetic field E_x , and H'_y in form of generalized Fourier series as,

$$\begin{aligned} E_x(x, z) &= \sum_{n=-N}^{+N} E_n e^{(j\sigma_n x)} e^{j\beta_n z} \\ H'_y(x, z) &= \sum_{n=-N}^{+N} H'_n e^{(j\sigma_n x)} e^{j\beta_n z} \end{aligned} \quad (3.2)$$

With $\sigma_n = \sigma_0 + n \frac{2\pi}{\Lambda} = \frac{2\pi}{\lambda} n_{inc} \sin(\theta_{inc}) + n \frac{2\pi}{\Lambda}$ and $\beta_n = \sqrt{k^2 - \sigma_n^2}$ is the propagation constant following the propagation axis z . E_n and H'_n are the Fourier coefficients of the stationary fields E_x and H'_y respectively of the spatial frequency σ_n . The harmonic vector notation can be used to describe the $(2N + 1)$ Fourier coefficients $[E_x]$ and $[H'_y]$ with $[E_x] = [E_{-N}, \dots, E_0, \dots, E_{+N}]$, and $[H'_y] = [H'_{-N}, \dots, H'_0, \dots, H'_{+N}]$. On the other hand, the periodicity following the x-axis induces also a decomposition of the evolution of the permittivity ϵ_r

along x into a Fourier series which can be written as,

$$\varepsilon_r(x, z) = \sum_{n=-N}^{+N} \varepsilon_n(z) e^{(j\sigma_n x)} \quad (3.3)$$

With ε_n is the Fourier coefficient at the spatial frequency σ_n of the relative permittivity of ε_r . The harmonic vector of ε_r is defined as $[\varepsilon_r] = [\varepsilon_{-N}, \varepsilon_{-N+1}, \dots, \varepsilon_{N-1}, \varepsilon_N]$. Under these conditions, the use of Fourier series can be tricky while incorporating the Fourier vectors into the differential equations system of propagation. Here, there is a multiplication of two functions where each one of them is described by its unique Fourier series. For example, this type of multiplications appears when we need to express the displacement field D which is given by the multiplication of the relative permittivity ε_r and the electric field components E_x or E_z . Thus, the multiplication may be considered as problematic when the two multiplied functions are discontinuous at the same position x . This discontinuity can be mainly found in TM polarization.

Ideally, if we are dealing with infinite series there is no problem. But, as the Fourier transformation is truncated, the following multiplication $k^2 E_x$ and $\left(\frac{1}{k^2} \cdot \frac{\partial H'_y}{\partial x}\right)$ must be developed. As mentioned before, this multiplication may be discontinuous at some positions along x inducing the slow convergence of the method. Indeed, many previous researches have been conducted to tackle this problem. Lalanne et al. demonstrated that this slow convergence is due to an inadequate formulation of the conventional eigenproblem [51]. Moreover, Granet et al. proposed to use a second-order differential operator associated with the scattering matrix formalism to speed up the convergence of the FMM in TM polarization [27]. In view thereof, Li proposed a new formulation that respects the continuity of the fields when the two multiplied functions are discontinuous at the same position or when one of them is considered discontinuous. This reformulation allows a faster convergence because it uniformly satisfies the boundary conditions in the grating region [55]. In other words, Li has introduced three new mathematical theorems related to the Fourier development of the product of two periodic functions known as Li's Factorization rules. The Fourier space representation of the propagation equations in TM polarization which doesn't respect the Li's rules can be expressed as,

$$\left\{ \begin{array}{l} \frac{\partial [E_x]}{\partial z} = j[H'_y] - jK \left[\left[\frac{1}{k^2} \right] K[H'_y] \right] \end{array} \right. \quad (3.4a)$$

$$\left\{ \begin{array}{l} \frac{\partial [H'_y]}{\partial z} = j[k^2][E_x] \end{array} \right. \quad (3.4b)$$

With $[A]$ is the $(2N + 1)$ harmonic vector of the truncated Fourier components between $-N$ and N . $\llbracket A \rrbracket$ is the Toeplitz matrix, (see appendix A), of the element $\llbracket A \rrbracket_{n,m}$ representing the Fourier component of the spatial frequency σ_{n-m} of the vector A , and K is the $(2N + 1) \times (2N + 1)$ diagonal matrix issued from the spatial frequency σ_n with the ij element being $K_{ij} = [\sigma_0 + (-N + i)\frac{2\pi}{\lambda}] \delta_{ij}$ and $\sigma_0 = \frac{2\pi}{\lambda} \sqrt{\epsilon_{sup}} \sin(\theta_{inc})$.

Li's Factorization Rules

In case of the non-truncated Fourier series, the Fourier component h_n of the product $h(x)$ of two periodic functions $f(x)$ and $g(x)$ can be given by using the Laurent's series as

$$h_n = \sum_{m=-\infty}^{+\infty} f_{n-m} g_m$$

This formulation is considered valid as long as $n \in]-\infty, +\infty[$. Nevertheless, if the Fourier space is truncated ($n \in [-N, +N]$) and in case that $f(x)$ and $g(x)$ are two discontinuous functions, their Fourier product induces numerical instabilities leading to the slow convergence of the multiplication. Consequently, a high number of truncation order N is needed to converge correctly and to ensure the stability of the product.

For that, Li proposed a set of factorization rules that tackles the slow convergence of the truncated Fourier series product in TM polarization. Indeed, Li's rules take advantage with the Fourier space methods (particularly for the RCWA and the Differential Method). Hence, the three factorization rules are stated as follows,

- The first rule of Li states that the Fourier component h_n of the product function $h(x)$ of two periodic and bounded functions $f(x)$ and $g(x)$ can be ruled by the Laurent's rule as long as the two functions don't suffer from simultaneous discontinuities at the same point along the periodization axis (x -axis) and can be expressed in term of the truncated Laurent's series as,

$$h_n = \sum_{m=-N}^{+N} f_{n-m} g_m \quad (3.5)$$

We define $\llbracket f \rrbracket$ the $(2N + 1 \times 2N + 1)$ Toeplitz matrix of $f(x)$ defined by $\llbracket f \rrbracket_{n,m} = f_{n-m}$ (see Appendix.A), and the $2N + 1$ column vector $[h]$ and $[g]$ of the respective Fourier elements h_n and g_m . Therefore, the Fourier matrix representation of Eq.(3.5) can be expressed as,

$$[h] = [f \cdot g] = \llbracket f \rrbracket [g] \quad (3.6)$$

- The second important rule of Li mentions that the Fourier component h_n of the product of two periodic and bounded functions $f(x)$ and $g(x)$ having simultaneous jump discontinuities at the same point along x and their product $h(x) = f(x)g(x)$ is continuous at this point, can be factorized by the inverse rule,

$$h_n = [fg]_n = \sum_{m=-N}^{+N} \left(\left[\frac{1}{f} \right]^{-1} \right)_{n,m} g_m \quad (3.7)$$

In matrix notation, Eq.(3.7) can be expressed as,

$$[h] = [f \cdot g] = \left[\left[\frac{1}{f} \right] \right]^{-1} [g] \quad (3.8)$$

- The third rule given by Li states that the Fourier product of two truncated functions $f(x)$ and $g(x)$ having two simultaneous jumps discontinuous at the same point along x , and their product $h = f(x)g(x)$ is also discontinuous can be factorized neither by Laurent's rule nor by the inverse rule.

Now, we will show the impact of applying the Li's factorization rule on the system of Eq.(3.4). In this equation, the second rule is not respected.

To elaborate more, we consider two functions $f(x) = \varepsilon(x)$ and $g(x) = 1/\varepsilon(x)$, with $\varepsilon(x)$ is a step function (Fig.3.1). Fig.3.1.(b) presents the multiplication of $f(x)$ and $g(x)$ in the Fourier space. As we can see, the two functions are discontinuous at two positions following x . Due to that, if the Li's factorization rules are not respected, parasitic oscillations will appear in the Fourier space. This oscillations induces the slow convergence of the method and some numerical fluctuations (darkred curve). In contrast, if the inverse rule of Li is respected, the oscillation disappears and the multiplication of the two Fourier series is well represented (green curve).

3.1.3 Harmonic propagation equations

The formalism of the differential system by respecting the Li's rule

The multiplication of $k^2 E_x$ appearing in the transient propagation equations (3.1), gives rise to the jump discontinuities conditions explained by Li in the harmonic regime. Therefore, the harmonic equations of propagation in TM polarization must be reformulated to respect the Li's conditions. By respecting the first law of Li, the harmonic multiplication arise the use of the Toeplitz matrix following the truncated Laurent's series as depicted in Eq.(3.4). Although, the second condition of Li must be applied to Eq.(3.4b), where $\left[[k^2] \right]$ must sustain

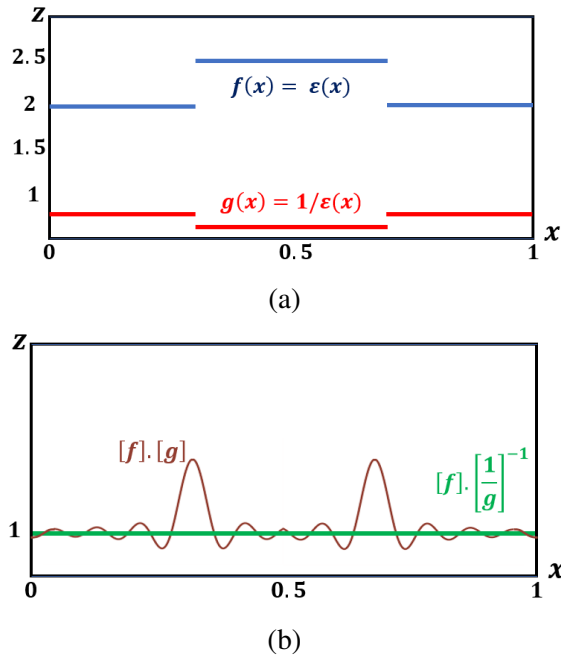


Fig. 3.1 (a) Distribution of the two functions $f(x)$ and $g(x)$ (b) The multiplication of their Fourier series with and without respecting the Li's rules.

the inverse rule. In this case, the Toeplitz matrix of the inverse of the reciprocal wavenumber $\left[\left[\frac{1}{k^2} \right] \right]^{-1}$ takes the place of the Toeplitz matrix of the wavenumber $\left[[k^2] \right]$ when it is multiplied by the Fourier vector $[E_x]$. A much better formulation of the propagation equations in TM polarization that respect Li's rules can be rewritten as,

$$\left\{ \begin{array}{l} \frac{\partial [E_x]}{\partial z} = j[H'_y] - jK \left[\left[\frac{1}{k^2} \right] \right] K[H'_y] \end{array} \right. \quad (3.9a)$$

$$\left\{ \begin{array}{l} \frac{\partial [H'_y]}{\partial z} = j \left[\left[\frac{1}{k^2} \right] \right]^{-1} [E_x] \end{array} \right. \quad (3.9b)$$

This set of equations describes the propagation of the electromagnetic fields in the modulated zone with TM polarized incident plane wave. Indeed, in the case of Lamellar gratings (Fig.3.2), the components of the electric field E_x and E_z , are always parallel to x and z respectively, as well the tangent of the surface \vec{T} and its normal \vec{N} respectively.

Therefore, E_x and E_z are either parallel or perpendicular to the surface. On the other hand, when a non-Lamellar structure is considered (Fig.3.3.(a)), the two components of the electric field becomes discontinuous at the interface of the gratings in TM polarization. At this stage, Popov reformulated the classical method to take into consideration this evolution where the components of the electric field can be expressed in terms of their projected vectors on the

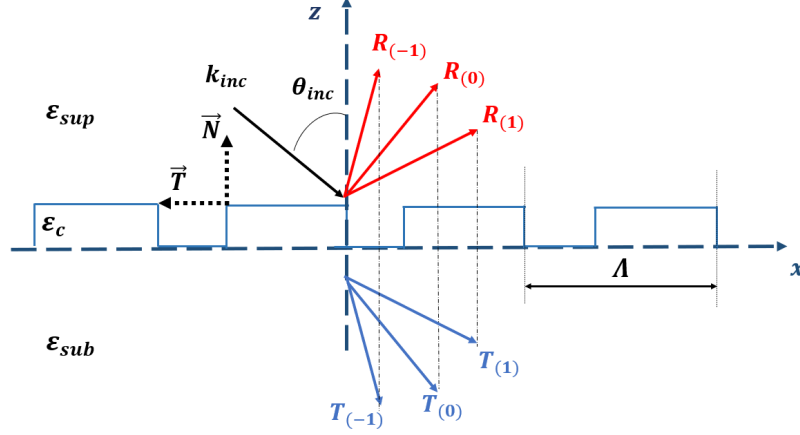


Fig. 3.2 Grating geometry and notations of a lamellar grating illuminated with a TM polarized plane wave.

profile of the surface [94]. This reformulation so-called Fast Fourier Factorization (FFF) associated to the differential theory will now be called as DM-FFF.

3.1.4 FFF associated to the differential theory in TM polarization

We aim to derive the equations describing the propagation of electromagnetic fields in an arbitrary modulated diffraction grating that respects the evolution of the profile in TM polarization. We define the function $f(x) = \frac{A}{2} \left(1 + \sin \frac{2\pi x}{\Lambda} \right)$ depicted in Fig.3.3.(a). $f(x)$ represents here the modulated zone of a sinusoidal periodic structure of period Λ with the peak to peak amplitude A . The Fast Fourier Factorization (FFF) is based on the reformulation of the classical differential theory (Eq.3.9), by proposing a suitable continuation of the incident field in the truncated Fourier space. Under this polarization, E_x and E_z are two discontinuous functions at the boundary of the grating. Therefore, the FFF imposes to express the two components of the electric field in terms of their tangential and normal component along the surface (\vec{E}_t and \vec{E}_n respectively). For that, let us introduce the unit vector $\vec{N} = N_x \vec{u}_x + N_z \vec{u}_z$ the grating's profile normal at a given point, with N_x and N_z are considered as algebraic values. For example, in Fig.3.3.(b) which corresponds to a zoomed part of the sinusoidal function of the grating, $N_x < 0$ and $N_z > 0$. Consequently, by using those components, we can define the unit vector of the grating's profile tangent \vec{T} . This vector is a unit vector perpendicular to the normal of the profile \vec{N} . Thus, $\vec{N} \cdot \vec{T} = 0$ and $\vec{N} \times \vec{T} = \pm \vec{1}$ must be verified. Under these conditions, two possibilities may appear. In our case, we chose $\vec{T} = N_z \vec{u}_x - N_x \vec{u}_z$. Indeed, the orthogonality between the two vectors may be verified by ensuring that the scalar product is equal to nullity.

In case of a sinusoidal profile, the normal vectors on x and z known as N_x and N_z respectively are equal to,

$$N_x = -\sin \theta_n ; N_z = \cos \theta_n$$

Referring to Fig.3.3.(b), θ_n is the cross section angle between the z -axis and \vec{N} . At this chosen point of the grating, the sinusoidal function is increasing along x . Thus, θ_n is positive and can be defined as,

$$\tan(\theta_n) = \frac{\partial f}{\partial x}$$

Consequently, N_x and N_z can be expressed in term of the equation of $f(x)$ as,

$$N_x = -\frac{\tan \theta_n}{\sqrt{1 + \tan^2 \theta_n}} = -\sqrt{\frac{1}{1 + (\partial f / \partial x)^2}} \frac{\partial f}{\partial x} \quad (3.10a)$$

$$N_z = \frac{1}{\sqrt{1 + \tan^2 \theta_n}} = \sqrt{\frac{1}{1 + (\partial f / \partial x)^2}} \quad (3.10b)$$

The scalar product of the incident electric field \vec{E} with \vec{N} and \vec{T} allows us to present the normal and tangential component of the field E_{norm} and E_{tang} as follows,

$$\vec{E} \cdot \vec{N} = E_{norm} = N_x E_x + N_z E_z \quad (3.11a)$$

$$\vec{E} \cdot \vec{T} = E_{tang} = N_z E_x - N_x E_z \quad (3.11b)$$

Therefore, the electric field components E_x and E_z can be expressed in term of E_{norm} and E_{tang} as follows,

$$E_x = N_x E_{norm} + N_z E_{tang} \quad (3.12a)$$

$$E_z = N_z E_{norm} - N_x E_{tang} \quad (3.12b)$$

Moreover, by referring to Eq.(2.8), we define the harmonic vectors of the $[D_x]$ and $[D_z]$ which represent the $(2N + 1)$ Fourier components of the electric displacements D_x and D_z respectively. Moreover, $[D_x]$ and $[D_z]$ are proportional to $[k^2 E_x]$ and $[k^2 E_z]$ respectively since the evolution of the relative permittivity of the profile ϵ_r is represented in $k = \frac{2\pi}{\lambda} \sqrt{\epsilon_r}$. Thus, by combining the displacement harmonic vectors with the previous equations (3.11), and by keeping in mind that $N_x^2 + N_z^2 = 1$, we can write,

$$[k^2 E_x] = \llbracket k^2 \rrbracket [N_x E_{norm}] + \llbracket k^2 \rrbracket [N_z E_{tang}] \quad (3.13a)$$

$$[k^2 E_z] = \llbracket k^2 \rrbracket [N_z E_{norm}] - \llbracket k^2 \rrbracket [N_x E_{tang}] \quad (3.13b)$$

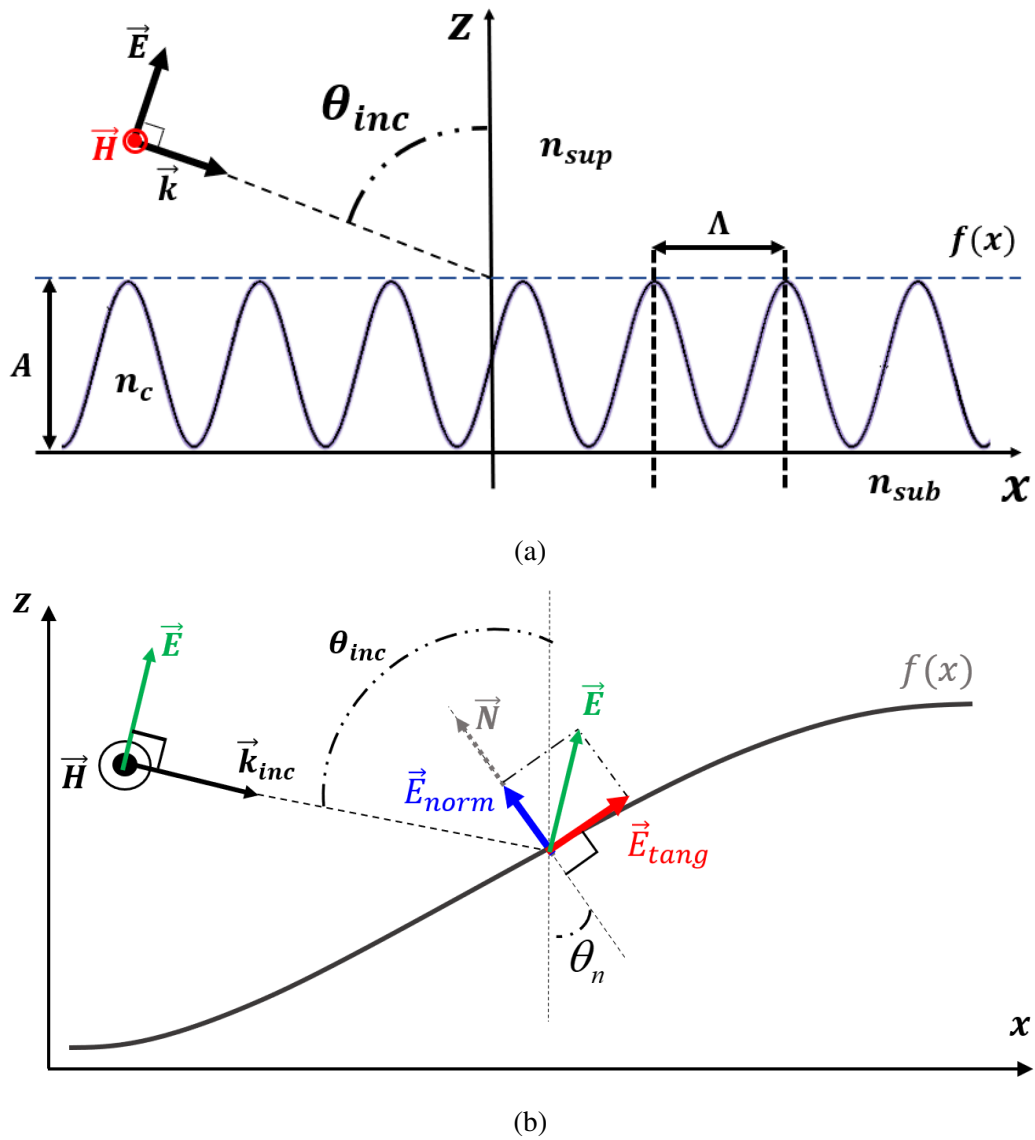


Fig. 3.3 (a) Geometry and notations of a sinusoidal grating (b) Zoomed part of the sinusoidal grating with the decomposition of the electric field E into its normal and tangential component with respect to the surface at a given point of the grating.

Here, the use of a toeplitz matrix for k^2 is due to the multiplication of its Fourier series with the Fourier series of the term $[N_i E_j]$. Nevertheless, we can notice that Eq.(3.13) doesn't respect the inverse rule of Li. Thus, this situation imposes the study of the continuity of the field for each term of the two equations. The first right-handed part of Eq.(3.13a) contains the product of the discontinuous profile permittivity ϵ_r and the transverse component of the electric field E_x . As E_x may be discontinuous at some points of the surface, the jump discontinuities may appear in that case and the product must sustain the inverse rule of Li. On the other hand, the multiplication of the permittivity evolution in the left-handed part of this equation requires the use of Laurent's rule (first condition of Li) as the tangential component of the field is always continuous. Following the same analysis, the first product of the right-handed part of Eq.(3.13b) follows the inverse rule of Li, while the left-handed part requires Laurent's factorization to correctly handle the multiplication. As a result, the set of electric displacement equations that respect Li's conditions are expressed as,

$$[k^2 E_x] = \left[\left[\frac{1}{k^2} \right] \right]^{-1} [N_x E_{norm}] + \llbracket k^2 \rrbracket [N_z E_{tang}] \quad (3.14a)$$

$$[k^2 E_z] = \left[\left[\frac{1}{k^2} \right] \right]^{-1} [N_z E_{norm}] - \llbracket k^2 \rrbracket [N_x E_{tang}] \quad (3.14b)$$

By substituting, E_{norm} and E_{tang} of Eq.(3.11a) and Eq.(3.11b) in the system (3.14), we obtain:

$$[k^2 E_x] = \left[\left[\frac{1}{k^2} \right] \right]^{-1} [N_x^2 E_x + N_x N_z E_z] + \llbracket k^2 \rrbracket [N_z^2 E_x - N_z N_x E_z] \quad (3.15a)$$

$$[k^2 E_z] = \left[\left[\frac{1}{k^2} \right] \right]^{-1} [N_z N_x E_x + N_z^2 E_z] - \llbracket k^2 \rrbracket [N_z N_x E_x - N_x^2 E_z] \quad (3.15b)$$

N_x and N_z are chosen to be always continuous at the discontinuities of the profile evolution (Fig.3.4). Actually, this is the unique constraint of this method to respect the rigorous boundary condition. Nevertheless, it is also possible to choose a discontinuous function for the normal. In this case, the position of the discontinuity must not be common with the position of the discontinuity of the permittivity tensor. Thus, Laurent's rule can be applied while multiplying the normal vectors with k^2 , and the developed form of system (3.15) can be expressed as,

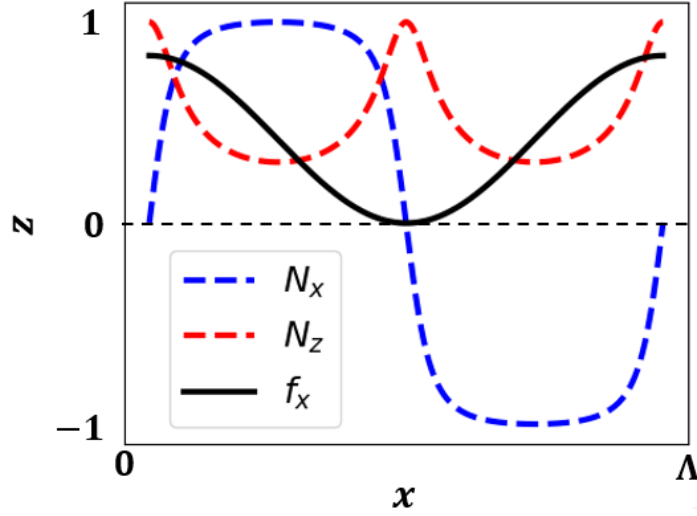


Fig. 3.4 Unit cell of sinusoidal grating profile. $f(x)$ is the function of the profile and N_x , N_z represent the normal distribution of the profile with respect to the x -axis and the z -axis respectively.

$$[k^2 E_x] = \left(\left[\frac{1}{k^2} \right]^{-1} \llbracket N_x^2 \rrbracket + \llbracket k^2 \rrbracket \llbracket N_z^2 \rrbracket \right) [E_x] + \left(\left[\frac{1}{k^2} \right]^{-1} - \llbracket k^2 \rrbracket \right) \llbracket N_x N_z \rrbracket [E_z] \quad (3.16a)$$

$$[k^2 E_z] = \left(\left[\frac{1}{k^2} \right]^{-1} - \llbracket k^2 \rrbracket \right) \llbracket N_x N_z \rrbracket [E_x] + \left(\left[\frac{1}{k^2} \right]^{-1} \llbracket N_z^2 \rrbracket + \llbracket k^2 \rrbracket \llbracket N_x^2 \rrbracket \right) [E_z] \quad (3.16b)$$

Subsequently, we define the matrix Q that allows the transition from the harmonic vectors $[E_x]$ and $[E_z]$ into the vectors that incorporate the evolution of the grating's profile i.e $\llbracket k^2 E_x \rrbracket$ and $\llbracket k^2 E_z \rrbracket$.

$$\begin{bmatrix} k^2 E_x \\ k^2 E_z \end{bmatrix} = Q \begin{bmatrix} E_x \\ E_z \end{bmatrix} = \begin{pmatrix} Q_{xx} & Q_{xz} \\ Q_{zx} & Q_{zz} \end{pmatrix} \begin{bmatrix} E_x \\ E_z \end{bmatrix} \quad (3.17)$$

With,

$$\begin{aligned} Q_{xx} &= \left[\frac{1}{k^2} \right]^{-1} \llbracket N_x^2 \rrbracket + \llbracket k^2 \rrbracket \llbracket N_z^2 \rrbracket \\ Q_{xz} &= Q_{zx} = \left(\left[\frac{1}{k^2} \right]^{-1} - \llbracket k^2 \rrbracket \right) \llbracket N_x N_z \rrbracket \\ Q_{zz} &= \left[\frac{1}{k^2} \right]^{-1} \llbracket N_z^2 \rrbracket + \llbracket k^2 \rrbracket \llbracket N_x^2 \rrbracket \end{aligned}$$

Now, $[[k^2 E_x]]$ and $[[k^2 E_z]]$ can be incorporated into the Maxwell's equation of propagation Eq.(2.14). We have to mention that $k^2 = \omega^2 \mu_0 \epsilon$, $\epsilon = \epsilon_0 \epsilon_r$ and $[H'_y] = \omega \mu_0 H_y$. Thus, the harmonic form of Maxwell's equations in TM polarization can be written as,

$$\begin{cases} \frac{\partial [E_x]}{\partial z} - \frac{\partial [E_z]}{\partial x} = j[H'_y] & (3.18a) \\ -\frac{\partial [H'_y]}{\partial z} = -\omega \mu_0 j[k^2 E_x] 1/(\omega \mu_0) = -j[k^2 E_x] & (3.18b) \\ \frac{\partial [H'_y]}{\partial x} = -\omega \mu_0 j[k^2 E_z] 1/(\omega \mu_0) = -j[k^2 E_z] & (3.18c) \end{cases}$$

The combination of Eq.(3.18c) and Eq.(3.16b) allows to reformulate the system of differential equation in terms of the transverse components. Hence, $[E_z]$ can be written as,

$$[E_z] = Q_{zz}^{-1} \left(j \frac{\partial [H'_y]}{\partial x} - Q_{zx}[E_x] \right) \quad (3.19)$$

Moreover, by substituting $[E_z]$ of Eq.(3.19) in Eq.(3.18a), the differential system of the transverse component can be written as,

$$\begin{cases} \frac{\partial [E_x]}{\partial z} = j[H'_y] + \frac{\partial}{\partial x} \left\{ Q_{zz}^{-1} \left(j \frac{\partial [H'_y]}{\partial x} - Q_{zx}[E_x] \right) \right\} & (3.20a) \\ \frac{\partial [H'_y]}{\partial z} = j[k^2 E_x] & (3.20b) \end{cases}$$

By replacing $[k^2 E_x]$ with its developed form, and by noticing that in the Fourier regime $\frac{\partial}{\partial x} = jK$, with K is the $(4N + 2 \times 4N + 2)$ diagonal matrix of σ where the ii component is equal to $\sigma_0 + (-N + i) \frac{2\pi}{\Lambda}$ the system can be rewritten as,

$$\begin{cases} \frac{\partial [E_x]}{\partial z} = j[H'_y] + jK \left\{ Q_{zz}^{-1} (-K[H'_y] - Q_{zx}[E_x]) \right\} & (3.21a) \\ \frac{\partial [H'_y]}{\partial z} = jQ_{xx}[E_x] + jQ_{xz}[E_z] & (3.21b) \\ = jQ_{xx} + jQ_{xz}Q_{zz}^{-1} (-K[H'_y] - Q_{zx}[E_x]) \end{cases}$$

Therefore, the system of differential equations that takes into account the evolution of the profile and describing the propagation of electromagnetic field in TM polarization can be

expressed as,

$$\begin{cases} \frac{\partial [E_x]}{\partial z} = -jKQ_{zz}^{-1}Q_{zx}[E_x] + j(I_d - KQ_{zz}^{-1}K)[H'_y] \\ \frac{\partial [H'_y]}{\partial z} = (jQ_{xx} - jQ_{xz}Q_{zz}^{-1}Q_{xz})[E_x] - jQ_{xz}Q_{zz}^{-1}K[H'_y] \end{cases} \quad (3.22a)$$

$$\quad (3.22b)$$

The differential system can be re-written in a compact manor as,

$$\frac{\partial}{\partial z} \begin{bmatrix} [E_x] \\ [H'_y] \end{bmatrix} = M(z) \begin{bmatrix} [E_x] \\ [H'_y] \end{bmatrix} \quad (3.23)$$

The Fourier component $[E_x]$ and $[H'_y]$ are composed of $2N + 1$ harmonics for each vector following following σ_n with n between $-N$ and $N \Rightarrow \sigma_{-N}$ to σ_N , where each harmonic represents the amplitude of the involved component. we introduce the matrix $[F]$ which represents the juxtaposition of the two vectors $[E_x]$ and $[H'_y]$, the differential system can be re-written as,

$$\frac{\partial [F]}{\partial z} = M(z)[F] \quad (3.24)$$

On the other hand, $M(z)$ is defined as the propagation matrix of the electromagnetic wave inside the modulated zone that takes the evolution of the profile into consideration so-called FFF,

$$M(z) = j \begin{bmatrix} M_{11} & M_{12} \\ M_{21} & M_{22} \end{bmatrix} \quad (3.25)$$

With,

$$M_{11} = -KQ_{zz}^{-1}Q_{zx}$$

$$M_{12} = I_d - KQ_{zz}^{-1}K$$

$$M_{21} = Q_{xx} - Q_{xz}Q_{zz}^{-1}Q_{xz}$$

$$M_{22} = Q_{xz}Q_{zz}^{-1}K$$

Therefore, the propagating fields, in TM polarization, inside the modulated zone are described by a system of $(4N + 2)$ coupled differential equations, depending on the Fourier components of $[E_x]$ and $[H'_y]$.

3.1.5 Fields outside the modulated zone

In the homogeneous zones, the plane waves are described by the eigenvectors of these regions. Thus, by referring to Eq.(2.24), the transient magnetic field outside the modulated zone (in

the superstrate and the substrate) can be expressed as follows,

$$H'_y(x, z) = \sum_{n=-N}^{+N} \left(B_n^+ e^{j(\sigma_n x + \beta_n z)} + B_n^- e^{j(\sigma_n x - \beta_n z)} \right) \quad (3.26)$$

As a result, the $(2N + 1)$ Fourier space components of $[H'_y]$ can be written as,

$$[H'_y] = [B^+ e^{j\beta z}] + [B^- e^{-j\beta z}] \quad (3.27)$$

$$= [H'_y]^+ + [H'_y]^- \quad (3.28)$$

Where $[H'_y]^+$ and $[H'_y]^-$ belong to the $(2N + 1)$ forward and backward Fourier components of the magnetic field respectively. Moreover, the electric field E_x can be expressed in terms of H'_y as,

$$E_x(x, z) = -\frac{j\omega\mu_0}{k^2} \frac{\partial H_y}{\partial z} = -\frac{j}{k^2} \frac{\partial H'_y}{\partial z}$$

From this equation, the $(2N + 1)$ harmonic vector $[E_x]$ can be expressed as,

$$[E_x] = \frac{\beta}{k^2} [B^+ e^{j\beta z}] - \frac{\beta}{k^2} [B^- e^{-j\beta z}] \quad (3.29)$$

$$= \frac{\beta}{k^2} [H'_y]^+ - \frac{\beta}{k^2} [H'_y]^- \quad (3.30)$$

Introducing $[V]$ which represents the juxtaposition of H'_y^- and H'_y^+ ,

$$[V] = \begin{bmatrix} [H'_y]^- \\ [H'_y]^+ \end{bmatrix} \quad (3.31)$$

As a result, the combination of Eq.(3.29) and Eq.(3.31) allows the transition from the representation of the stationary wave $[F]$ into the backward and forward components of the field $[V]$,

$$\begin{bmatrix} [E_x] \\ [H'_y] \end{bmatrix} = \Psi \begin{bmatrix} [H'_y]^- \\ [H'_y]^+ \end{bmatrix} \quad (3.32)$$

Finally, Eq.3.32 can be written as,

$$[F] = \begin{bmatrix} \Psi_{11} & \Psi_{12} \\ I_d & I_d \end{bmatrix} [V] \quad (3.33)$$

With I_d : Identity matrix of $(2N + 1 \times 2N + 1)$ components, and Ψ_{11}, Ψ_{12} are two $(2N + 1 \times 2N + 1)$ diagonal matrices expressed as,

$$\Psi_{11} = \begin{bmatrix} \ddots & & 0 \\ & -\frac{\beta_n}{k^2} & \\ 0 & & \ddots \end{bmatrix}, \text{ and } \Psi_{12} = \begin{bmatrix} \ddots & & 0 \\ & \frac{\beta_n}{k^2} & \\ 0 & & \ddots \end{bmatrix} \quad (3.34)$$

This set of $(4N + 2)$ harmonic equations describes the field in the homogeneous media. Finally, the existence of a linear link between the homogeneous zones and the modulated zone allows the use of the shooting method via the Ψ matrix introduced above and the transmission matrix of the Eq.(3.23) [10].

3.2 Formulation of the differential theory in TE polarization

3.2.1 Fields inside the modulated zone

In TE polarization, both the the electric and magnetic fields (non magnetic medium), and its normal derivative are all continuous. Therefore, there is neither discontinuous jump nor fields discontinuities at the interface that implies the use of FFF. Based on the transient form of Maxwell's equations in TE polarization, the system of the differential equations to be solved can be summarized in the transverse component H_x and E_y as,

$$\left\{ \begin{array}{l} -\frac{\partial E_y}{\partial z} = j\omega\mu_0 H_x = jH'_x \end{array} \right. \quad (3.35a)$$

$$\left\{ \begin{array}{l} \frac{\partial E_y}{\partial x} = j\omega\mu_0 H_z = jH'_z \end{array} \right. \quad (3.35b)$$

$$\left\{ \begin{array}{l} \frac{\partial H'_x}{\partial z} - \frac{\partial H'_z}{\partial x} = -jk^2 E_y \end{array} \right. \quad (3.35c)$$

With $H'_x = \omega\mu_0 H_x$ and $H'_z = \omega\mu_0 H_z$ and $k^2 = \omega^2\mu_0\epsilon$.

By substituting Eq.(3.35b) in Eq.(3.35c), the system will be only represented by the transverse components of the electromagnetic field with respect to the propagation axis z ,

$$\left\{ \begin{array}{l} \frac{\partial E_y}{\partial z} = -jH'_x \end{array} \right. \quad (3.36a)$$

$$\left\{ \begin{array}{l} \frac{\partial H'_x}{\partial z} = -jk^2 E_y - j\frac{\partial^2}{\partial x^2} E_y \end{array} \right. \quad (3.36b)$$

The Floquet-Bloch theorem allows to describe the electromagnetic fields, E_y and H'_x as a generalized Fourier series,

$$\begin{aligned} E_y(x, z) &= \sum_{n=-N}^{+N} E_n e^{j\sigma_n x} e^{j\beta_n z} \\ H'_x(x, z) &= \sum_{n=-N}^{+N} H'_n e^{j\sigma_n x} e^{j\beta_n z} \end{aligned} \quad (3.37)$$

With, E_n and H'_n are to the Fourier coefficients of the n^{th} harmonic of the electric field E_y and the magnetic field H'_x respectively. Moreover, the harmonic vector notation can be used to describe $(2N + 1)$ Fourier coefficients $[E_y]$ and $[H'_x]$ can be represented as $[E_y] = [E_{-N}, \dots, E_0, \dots, E_{+N}]$ and $[H'_x] = [H'_{-N}, \dots, H'_0, \dots, H'_{+N}]$.

By performing a Fourier transformation, the system of Eq.(3.36) can be expressed in the harmonic regime following a truncated Fourier series of $2N + 1$ components for each field. Therefore, the term $\partial/\partial x$ will be substituted by jK (K is a diagonal matrix where the ii component is equal to $\sigma_0 + (-N + i)\frac{2\pi}{\Lambda}$) and the harmonic differential equations can be written as,

$$\begin{cases} \frac{\partial [E_y]}{\partial z} = -j[H'_x] & (3.38a) \\ \frac{\partial [H'_x]}{\partial z} = j(K^2 - \llbracket k^2 \rrbracket) [E_y] & (3.38b) \end{cases}$$

The system of Eq.(3.38) can be written as a system of $4N + 2$ coupled differential equations representing the electromagnetic fields propagating in TE polarization inside the modulated zone of the grating,

$$\frac{\partial}{\partial z} \begin{bmatrix} [E_y] \\ [H'_x] \end{bmatrix} = M(z) \begin{bmatrix} [E_y] \\ [H'_x] \end{bmatrix} \quad (3.39)$$

Where $M(z)$ is a matrix of $4N + 2 \times 4N + 2$ components with n varying from $-N$ to N , and composed of four blocs with $(2N + 1) \times (2N + 1)$ components for each one,

$$M(z) = j \begin{bmatrix} 0 & -I_d \\ M_{21} & 0 \end{bmatrix} \quad (3.40)$$

with I_d is a Identity matrix of $2N + 1 \times 2N + 1$ components and $M_{21} = (K^2 - \llbracket k^2 \rrbracket)$ being a diagonal matrix of $2N + 1 \times 2N + 1$ components where the ii element is equal to

$[\sigma_0 + (-N + i)\frac{2\pi}{\lambda}] - [\frac{2\pi}{\lambda}\epsilon_n]$. Finally, Eq.(3.39) can be simplified as,

$$\frac{\partial[F]}{\partial z} = M(z)[F] \quad (3.41)$$

3.2.2 Field outside the modulated zone

As the wave vector and the refractive index are always constant in the superstrate and the substrate regions, the field decomposition in Fourier space can follow the Rayleigh expansion as the solution of Helmholtz's equation, in that case, rests on the exponential decomposition of the field into propagating and evanescent plane waves.

By taking into consideration the truncation of the field from $-N$ to $+N$, Eq.(2.22) can be reformulated as,

$$\begin{aligned} E_y(x, z) &= \sum_{n=-N}^{+N} \left(A_n^+ e^{j(\sigma_n x + \beta_n z)} + A_n^- e^{j(\sigma_n x - \beta_n z)} \right) \\ &= \sum_{n=-N}^{+N} \left(A_n^+ e^{j\beta_n z} + A_n^- e^{-j\beta_n z} \right) e^{j\sigma_n x} \\ &= \sum_{n=-N}^{+N} \left(E_n^+ + E_n^- \right) e^{j\sigma_n x} \end{aligned} \quad (3.42)$$

Where E_n^+ and E_n^- , the n^{th} Fourier element of the $2N + 1$ transverse electric field vector in the Fourier space $[E_y]$. Thus, we can write,

$$\begin{aligned} [E_y] &= [A^+ e^{j\beta z}] + [A^- e^{-j\beta z}] \\ &= [E_y^+] + [E_y^-] \end{aligned} \quad (3.43)$$

Where $[E_y^+]$ and $[E_y^-]$ represents the $(2N + 1)$ forward (traveling following $+z$) and backward (following $-z$) Fourier components of the field. The combination of Eq.(3.35a) and Eq.(3.43) allows us to write the harmonic vector $[H'_x]$ of the magnetic field H'_x as,

$$\begin{aligned} [H'_x] &= j \frac{\partial[E_y]}{\partial z} = -[\beta A^+ e^{j\beta z}] + [\beta A^- e^{-j\beta z}] \\ &= -\beta[E_y^+] + \beta[E_y^-] \end{aligned} \quad (3.44)$$

Hence, through the combination of Eq.(3.43) and Eq.(3.44), the matrix that allows the transition from the backward and forward form of the field into the stationary waves can be

expressed as,

$$\begin{aligned} \begin{bmatrix} [H'_x] \\ [E_y] \end{bmatrix} &= \Psi \begin{bmatrix} [E_y^-] \\ [E_y^+] \end{bmatrix} \\ [F] &= \Psi[V] \end{aligned} \quad (3.45)$$

With,

$$\Psi = \begin{bmatrix} I_d & I_d \\ \Psi_{21} & \Psi_{22} \end{bmatrix} \quad (3.46)$$

With I_d : Identity matrix of $2N + 1 \times 2N + 1$ components, and Ψ_{21}, Ψ_{22} are two $2N + 1 \times 2N + 1$ diagonal matrix expressed as,

$$\Psi_{21} = \begin{bmatrix} \ddots & & 0 \\ & \beta_n & \\ 0 & & \ddots \end{bmatrix}, \text{ and } \Psi_{22} = \begin{bmatrix} \ddots & & 0 \\ & -\beta_n & \\ 0 & & \ddots \end{bmatrix} \quad (3.47)$$

Practically, we are concerned with the $[V]$ representation of the field since it provides the components of the incident field, the diffracted fields in the reflection zone, and the diffracted components in the transmission area. However, the $[F]$ representation which takes place in Eq.(3.4) describes the stationary fields in this zone. In contrast, the transition matrix Ψ allows the change-over from the stationary wave representation in Fourier space into the forward and backward Fourier components of the diffracted plane waves in the homogeneous zones.

3.3 Numerical integration of the matrix differential system

The differential systems of Eq.(3.41) and Eq.(3.24), for TE and TM polarization respectively, are considered as a set of first-order coupled differential equations. To solve this kind of system, an integration method should be used. Basically, the differential method discretizes the modulated region into several layers L_s where $z_0 < L_s < z_h$, following a constant integration step D_z (Fig.3.5). The propagation in each layer is described by the differential matrix $M(z)$ via the differential systems mentioned before. Although, $M(z)$ depends on the position of the layer following the propagation axis z . For that, the boundary conditions should be respected between the different discretized sections.

However, to integrate the differential matrix $M(z)$ of each layer, the differential method uses a combination of the Runge-Kutta integration and the shooting method. Indeed, the shooting

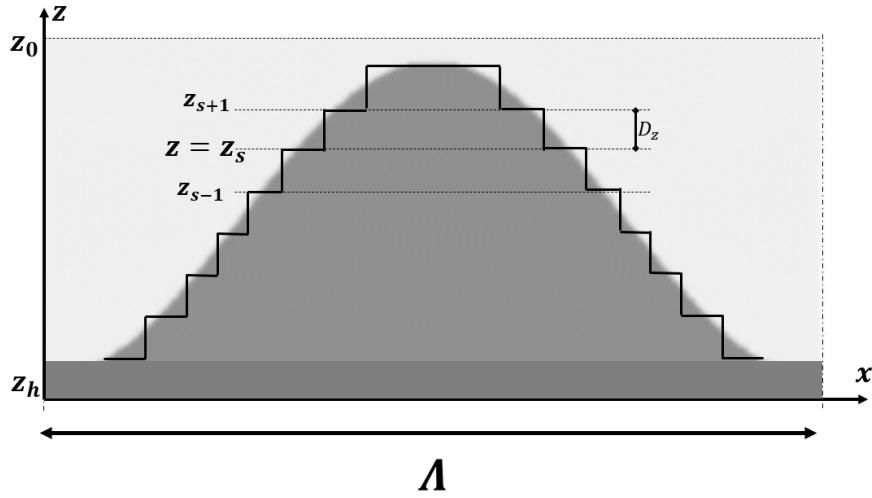


Fig. 3.5 The modulated zone of a unit cell of a sinusoidal grating. The discretization step is D_z where each discretized layer is represented by its T-Matrix.

method is used to calculate the transfer matrix (T-matrix) of propagation in a given layer L_s via the Runge-Kutta integration. For that, initial conditions are necessary to perform the integration. Thus, the use of the shooting method which define the harmonic matrix one harmonic after another consequently. Indeed, this calculation can be simplified by initializing the system as an eye identity matrix.

3.3.1 The Runge-Kutta integration algorithm

Taking into consideration the differential equation depicted below,

$$\frac{\partial F(z)}{\partial z} = M(z)F(z) \quad (3.48)$$

This equation describes exactly our differential problem. Furthermore, the Runge-Kutta algorithm of order 4 is adapted to solve such type of differential equations. In this case, the function $F(z)$ iterates the 4 consecutive layers step by step, starting from a point where the initial conditions are defined (M_1) to the next layer (M_2) and finally till the 4th layer (M_4). The iteration is done using the relationship below,

$$F(z + D_z) = F(z) + \frac{1}{6}M_1 + \frac{1}{6}M_2 + \frac{1}{3}M_3 + \frac{1}{6}M_4 \quad (3.49)$$

With,

$$\begin{aligned}
 M_1 &= D_z M(z, F(z)) \\
 M_2 &= D_z M\left(z + \frac{D_z}{2}, F(z) + \frac{M_1}{2}\right) \\
 M_3 &= D_z M\left(z + \frac{D_z}{2}, F(z) + \frac{M_2}{2}\right) \\
 M_4 &= D_z M(z + D_z, F(z) + M_3)
 \end{aligned} \tag{3.50}$$

Nevertheless, a sufficiently small iteration step must be chosen to ensure the rigorous development of the integration without any divergence problem.

3.3.2 Runge-Kutta algorithm applied to the Differential theory in Fourier space

In the case of the differential theory of grating, the matrix form of differential system that describes the propagation in the layer L_s is described as follows,

$$\frac{\partial[F(z)]}{\partial z} = M(z)[F(z)] \tag{3.51}$$

We aim to integrate this differential system to get the matrix $P(z)$ that links the fields at the position z and $z + D_z$,

$$[F(z + D_z)] = P(z)[F(z)] \tag{3.52}$$

By considering that the integration step is sufficiently thin to ensure the stability of the integration, Eq.(3.49) and Eq.(3.54) allow us to integrate the Fourier space differential system and to write $P(z)$ as,

$$P(z) = I_d + \frac{D_z}{6}M_1(z) + \frac{D_z}{6}M_2(z) + \frac{D_z}{3}M_3(z) + \frac{D_z}{6}M_4(z) \tag{3.53}$$

With,

$$\begin{aligned}
 M_1(z) &= M(z) \\
 M_2(z) &= M\left(z + \frac{D_z}{2}\right) \left(I_d + \frac{1}{2}M_1(z)\right) \\
 M_3(z) &= M\left(z + \frac{D_z}{2}\right) \left(I_d + \frac{1}{2}M_2(z)\right) \\
 M_4(z) &= M(z + D_z) (I_d + M_3(z))
 \end{aligned} \tag{3.54}$$

Nevertheless, the propagation in the overall system can be performed by the consecutive cascade of the propagation matrix $P(z)$ of each discretized layer (layer by layer) by using the transfer matrix mentioned in the next section. Furthermore, we can gather different

propagation matrix P in one scattering matrix. Hence, the propagation matrix of the n_s layers can be cascaded gathering $n_s \in \mathbb{N}$ P-matrices in one propagation matrix.

Each layer possesses its own propagation matrix $P_{z+D_{n_s}}$. We define $P_1(z), P_2(z) \dots P_{n_s}(z)$ as the matrices of the first, second and n_s layers. With,

$$P_1(z) = P(z + D_z)$$

$$P_2(z) = P(z + 2D_z)$$

$$P_{n_s}(z) = P(z + n_s D_z)$$

Therefore, to perform the propagation matrix $P(z)$ of gathering n_s layers, it is sufficient to cascade the sub-matrices as follows,

$$P(z) = P_{n_s}(z) \cdots P_2(z) \cdot P_1(z) \cdot I_d \quad (3.55)$$

Further, the Runge-Kutta integration is considered more adapted with the continuity of the profile. Also, it is examined as more accurate than the eigen resolution of the differential system applied with the FMM [3]. This integration allows us to define the propagation in a modulated zone where the field is not straightforwardly calculated.

3.4 The linear relation that links the modulated region with the homogeneous zones

For both TE and TM polarizations, the last step to perform the propagation, in the entire structure, is to link the calculated field in the modulated zone via the matrix $P(z)$ from one side, with the fields calculated outside the modulated zones (superstrate and substrate) from the other side. We defined before D_z as the constant integration step following the propagation axis z . By discretizing the grating profile by D_z , a given number of layers or sections N_s that depends on D_z and A the depth of the grating can be defined,

$$N_s = \frac{A}{D_z}$$

Accordingly, the recursion relation between the superstrate, the grating sections, and the substrate can be reduced into a linear relation that links the fields of the incident region (for example the superstrate) into the fields of the transmission region (for example the substrate). In other words, the combination of the different zones gives access to the propagation vector in the overall structure, and consequently, we can calculate the transmission and reflection coefficients of the diffracted orders. Thus, by iterating continuously the different modulated sections, discretized by D_z , and the last section L_h at the position $z = h$ (substrate

homogeneous region), we can define the overall propagation matrix P that describes the propagation in the entire periodic structure. In this manner, P links the Fourier coefficients of the stationary fields of the superstrate $[E_x^0]$ and $[H_y^0]$ at $z = 0$ with the stationary field of the substrate layer $[E_x^h]$ and $[H_y^h]$ at $z = h$ as,

$$[F(h)] = P[F(0)] \quad (3.56)$$

With P is the cascade of the propagation matrices of the different sections defined as,

$$P = P^h \dots P^{s-1} \cdot P^s \cdot P^{s+1} \dots P^0$$

Unfortunately, P deals with the Fourier components of the stationary fields $[E_x]$ and $[H_y]$. Under this situation, the access to the eigenvectors of the forward and backward fields at the superstrate and the substrate is not provided. To get access to the different diffracted intensities, a transition from the representation of the stationary field into the forward and backward field ($[E^+]$ and $[E^-]$ for TE polarization, and $[H'^+]$ and $[H'^-]$ for TM polarization) should be done. This transition is executed by combining the Runge-Kutta integration that gives the propagation matrix P and a special algorithm of the shooting method that transforms P into the scattering Transfer matrix T -matrix. As a result, the T-Matrix links the forward and backward fields of a given structure of a given layer at the position z_{s-1} with the forward and backward fields of the next layer at the position z_s . On the other hand, the initial conditions to initialize the calculation are not found. Here, the other role of the shooting method appears by defining with a special algorithm the initial conditions that allow the initialization of the problem and therefore, the application of the Runge-Kutta algorithm.

3.5 Use of the Shooting Method

3.5.1 Defining the initial conditions

The use of Eq.(3.43) and Eq.(3.27) gives rise of the stationary fields, for TE and TM polarization respectively, outside the modulated zones and at their boundaries. Nevertheless, the Fourier coefficients of the backward and forward fields in the homogeneous regions are considered unknown. Consequently, the initial conditions are also considered as unknown values. Indeed, the Shooting Method is based on the existence of the linear relation (Eq.3.56) between $[F(0)]$ and $[F(h)]$ to circumvent the non-existence problem of the initial conditions. To elaborate more, the algorithm of the method rests on the use of arbitrary initial conditions. For example, for the $[F(0)]$ matrix of $2(2N + 1)$ column, we define a harmonic column

$[F_n(0)]$ of $2N + 1$ components where the n^{th} element is equal to unity and all the other components are null. Therefore, the resolution of the diffraction problem consists of turning the boundary value problem into an initial value problem.

Under these conditions, as we integrate the system from $z = 0$ to $z = h$, the resulting vector $[F(h)]$ will depend only on the n^{th} column of P . Consequently, at the 0^{th} slice (the superstrate), we take the $2(2N + 1)$ independent initial column vectors of $[F(0)]$ noted as $F^p(0)$ with $F^p(0)_i = \delta_{pi}$ with $i \in [1, 2(2N + 1)]$.

Consequently, to fill all the columns of the $(2N + 1 \times 2N + 1)$ matrix, each vector of $[F^p(0)]$ is iterated. Finally, the propagation vector P can be completely constituted following the linear relation of Eq.(3.56).

3.5.2 The transition from the stationary fields into the forward and backward representation of the fields

The second role of the shooting method is to allow the transition from the harmonic representation of the stationary field $[E_x]$ and $[H'_y]$ into the intensities of the backward and forward plane waves of the magnetic field for TM polarization, and the electric field for TE polarization. This transition can be done by introducing an infinitely thin homogeneous layer with a given permittivity between each slice. As the eigenmodes are the plane waves in the homogeneous layers, the main aim of these infinitely thin layers is to change over from a description of the total field into the description of the forward and backward fields of each layer. As a result, we can easily determine the reflection and the transmission coefficients of each diffracted plane wave.

To elaborate more, let us consider the unit cell of a sinusoidal grating of Fig.3.6. Here, the modulated zone is bounded between the positions z_0 and z_h . The forward and backward waves of the superstrate at z_0 are $[c_0^+]$ and $[c_0^-]$ which respectively represent $[H_y'^+]$ and $[H_y'^-]$ in TM polarization, and $[E_y^+]$ and $[E_y^-]$ in TE polarization at the position $z = z_0$. Consequently, the forward and backward waves at the substrate ($z = z_h$) are $[c_h^+]$ and $[c_h^-]$ respectively.

We proved before that in the homogeneous layers, a transition matrix Ψ can be applied to ensure the change over from the total field representation into the forward and backward waves vectors (eigen vectors) for TE and TM polarization.

We know that,

$$\begin{aligned} [F(0)] &= \Psi_{sup}[V(0)], \\ [F(h)] &= P[F(0)], \\ [V(h)] &= \Psi_{sub}^{-1}[F(h)] \end{aligned}$$

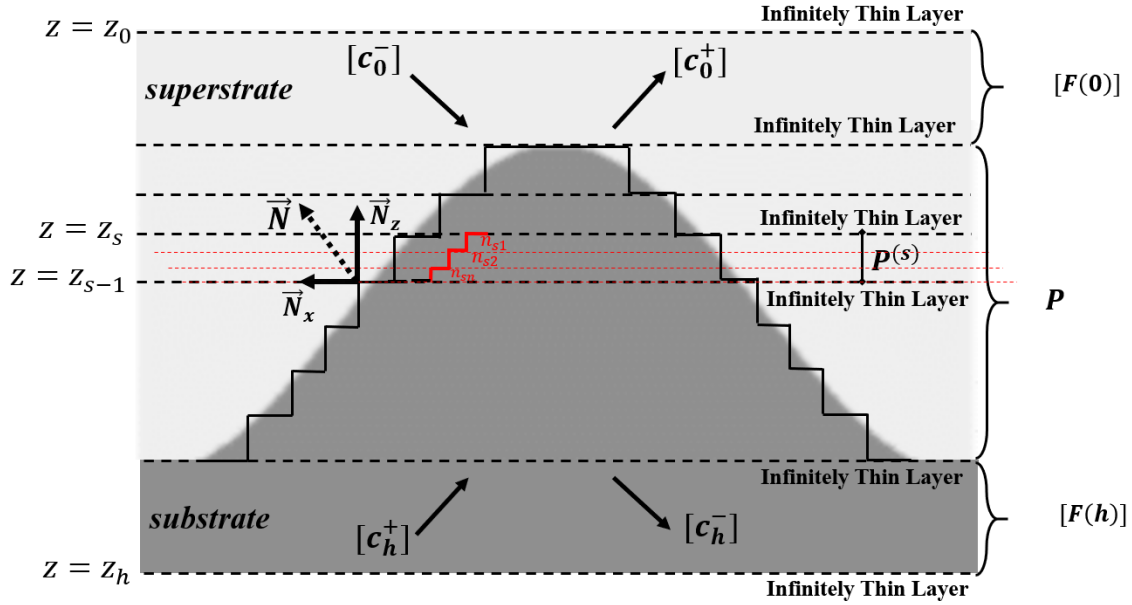


Fig. 3.6 A unit cell of periodic sinusoidal grating. The propagation in the homogeneous layers are calculated via the Ψ matrix and in the modulated zone, the propagation matrix P is a result of the recursion of the Runge-Kutta integration of the different sections.

Thus, by combining the three previous equations, we can write,

$$[V(h)] = \Psi_{sub}^{-1} P \Psi_{sup} [V(0)] \quad (3.57)$$

With,

$$[V(h)] = \begin{bmatrix} [c_h^-] \\ [c_h^+] \end{bmatrix} \text{ and } [V(0)] = \begin{bmatrix} [c_0^-] \\ [c_0^+] \end{bmatrix} \quad (3.58)$$

Finally, we can write the relation of the transmission matrix T that links the incoming and the outgoing fields of the superstrate at z_0 and the substrate at z_h as,

$$[V(h)] = T[V(0)] \quad (3.59)$$

The entire transfer matrix T is a result of the recursion of all the discretized layers of the modulated zone with a thickness of D_z for each one. In other words, each P^s matrix of a given slice z_s is transformed into a T^s matrix as,

$$T^s = \Psi_{sub}^{-1} P^s \Psi_{sup}$$

Consequently, the T^s matrix gives the relation between the field at the z_{s-1}^{th} and the z_s^{th} layers. Indeed, the recursion of the successive T^s matrices gives the total transfer matrix T

as,

$$T = T^h \dots T^{s-1} \cdot T^s \cdot T^{s+1} \dots T^0 \dots \quad (3.60)$$

3.5.3 T-matrix of a given section

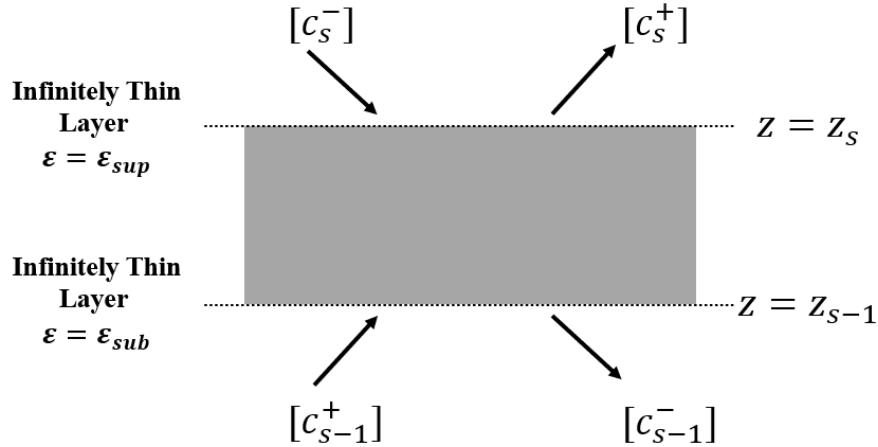


Fig. 3.7 Definition of T-matrix of a given section. This algorithm links the amplitude of the wave of the s^{th} layer with the amplitude of the fields of the $s - 1^{\text{th}}$ layer.

We take into consideration the layer s bounded between the position z_{s-1} and z_s , as depicted in Fig.3.7. The infinitely thin layer at each boundary serves the passing from $[E_x^s]$ and $[H_y^s]$ into $[c_s^-]$ and $[c_s^+]$, the backward (following $-z$) and forward (following $+z$) Fourier coefficients at the position z_s respectively. In general, T^s is the matrix that links the forward and backward field of the layer at z_s with the forward and backward field of z_{s-1} can be expressed as,

$$\begin{bmatrix} [c_s^-] \\ [c_s^+] \end{bmatrix} = T^s \begin{bmatrix} [c_{s-1}^-] \\ [c_{s-1}^+] \end{bmatrix} \quad (3.61)$$

However, T^s can be decomposed into four sub-matrices as,

$$T^s = \begin{bmatrix} T_{11}^s & T_{12}^s \\ T_{21}^s & T_{22}^s \end{bmatrix} \quad (3.62)$$

When the system is truncated between $n \in [-N, +N]$, each sub-matrix represents a $(2N + 1 \times 2N + 1)$ matrix. With,

- T_{11}^s is the reflection matrix at the position z_{s-1} .

- T_{12}^s is the transmission matrix from position z_s to the z_{s-1} position.
- T_{21}^s is the transmission matrix from position $s - 1$ to s .
- T_{21}^s is the reflection matrix of the z_s position.

Nevertheless, it is well known that the T-matrix presents numerical instabilities in the calculation due to the growing exponential of the evanescent modes in the integration step when the dimensions of the matrix are large [54]. Thus, several solutions have been proposed to tackle this instability. The scattering matrix applied by Li on the Fourier space methods has shown its effectiveness with this issue turning the Fourier space methods into stable and efficient tools for the modeling of arbitrarily shaped grating with any groove depth and permittivity.

3.6 Scattering Matrix algorithm (S-Matrix)

3.6.1 Introduction

To ensure the stability of any electromagnetic numerical method, the conservation of energy in any diffraction grating must be respected. In other words, the sum of the diffracted and absorbed energy over the incident energy must always be equal to one. Nevertheless, in some cases, this ratio shows some numerical instabilities by reaching a level higher than one. This divergence has mainly appeared in two cases: 1) when modeling deep groove grating (peak to peak amplitude $> \lambda/10$) 2) multi-coated or multi-layered surfaces. The main origin of this divergence is the exponential term $\exp(-j\beta z)$ of the evanescent modes in the T_{11} sub-matrix of the transfer matrix T at a given layer. The imaginary part of β presented with the evanescent modes grows exponentially with z [84]. At this stage, the T_{11} matrix contains growing values that give rise to a weak numerical precision when inverting or cascading the T-matrices of the layers.

As mentioned before, T is the recursion of the different discretized sections following z . For example when multiplying the two matrices T^s and T^{s-1} of Eq.(3.60). The result of the T bloc of the two matrices will be $T^s \cdot T^{s-1}$. Therefore, when the imaginary part of the exponential term is greater than zero, this multiplication will induce the loss of precision and the numerical instability.

To tackle this problem, different propagation algorithms have been proposed. The first starting point was with the Bremmer series in order to improve the T-matrix algorithm [11]. This method is based on the modal analysis of the Fourier expansion and it has been applied for arbitrarily shaped gratings in TE polarization. Besides, multiple types of Reflection series

have been presented to replace the T-Matrix in multi-layered coated gratings. Indeed, this algorithm has been applied by Li to the RCWA method by using structures with arbitrarily shaped profile, depth, and permittivity.[83, 89]. The first application of the R-matrix with the differential method was performed by Nevière et al. for TM polarization [82]. As a result, this algorithm has eliminated the numerical instabilities problem faced with the DM for more than twenty years. Finally, Li has shown that the scattering matrix (S-Matrix) used for the electromagnetic study of the photonic bandgap can be applied with Fourier space methods under certain conditions [54]. The relevance of this matrix, to the other mentioned algorithms, is that it fragments the sections into sufficient small sections to prevent the numerical instabilities while cascading the scattering matrices from a section to the other, so that the exponentially growing functions disappear from the algorithm.

3.6.2 Definition of the S-Matrix

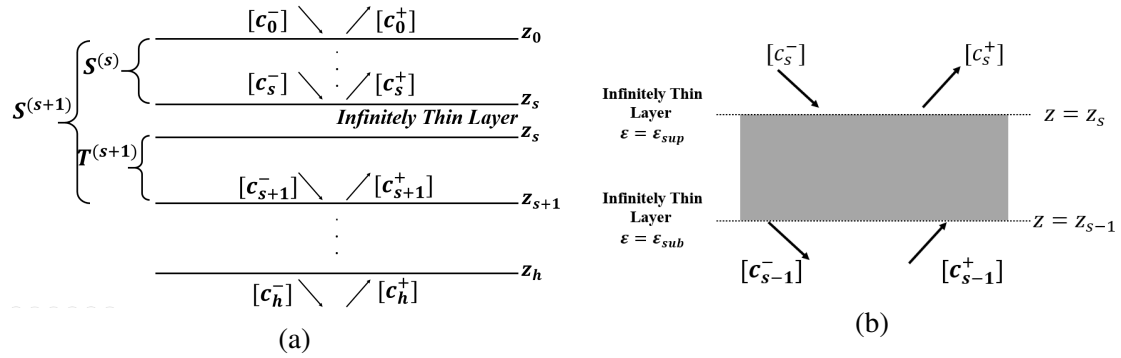


Fig. 3.8 (a) Discretized grating structure, where the horizontal lines represent actual material interfaces. The fields in each layer can be represented as a superposition of upward- and downward-propagating. (b) Definition of the S-matrix of a given s section. This algorithm links the amplitude of the incoming fields towards a given layer with the amplitude of the outgoing fields from this given layer.

As the differential method decomposes the structure into thin horizontal slices to perform the integration of the differential equations, thus it creates numerical layer interfaces. Between two consecutive interfaces (z_s and z_{s+1}), there is a layer with a thickness D_z related to a specific Fourier series that describes the profile evolution of the grating in this layer. The fields in each layer are defined following a specific Fourier series. On the other hand, the interface gives access to the amplitudes of the forward and backward modes (plane waves for scattering study here or eigen modes of a waveguide structure in the transition matrix proposed in the Chapter.7). For that, a series of parallel straight lines has been taken into consideration. In Fig.3.8.(a), the upward and downward arrows schematically represent the forward and

the backward waves respectively. $[c_s^+]$ and $[c_s^-]$ denote the column vectors whose the $2N + 1$ elements are the wave amplitudes. Once the forward and backward modes are determined in each section, the grating problem can be reduced to a problem of determining the amplitude of each mode.

For any $0 \leq s \leq h$, it seeks a stack of S-matrices. Indeed, the S^s -matrix of a stack of s slices (not to be confused with the S-matrix of the s^{th} slice) that links the amplitudes of the forward waves with the backward amplitudes in z_s and medium z_0 can be expressed as,

$$\begin{bmatrix} [c_s^+] \\ [c_s^-] \end{bmatrix} = S^s \begin{bmatrix} [c_0^+] \\ [c_0^-] \end{bmatrix} \quad (3.63)$$

And, S^s is decomposed into four sub-matrices,

$$S^s = \begin{bmatrix} S_{11}^s & S_{12}^s \\ S_{21}^s & S_{22}^s \end{bmatrix}$$

In order to perform the T-matrix to S-matrix transformation of the interface (s), that links the waves of the two adjacent layers at the positions $z = s$ and $z = s + 1$, the sub-matrices of Eq.(3.62) have to be used. Referring to Ref.[54], the T-to-S transformation for a given interface (s) can be performed using the following equations,

$$\begin{aligned} S_{11}^{(s)} &= T_{11}^{(s)} - \left[\left(T_{12}^{(s)} (T_{22}^{(s)})^{-1} \right) T_{21}^{(s)} \right] \\ S_{12}^{(s)} &= T_{12}^{(s)} (T_{22}^{(s)})^{-1} \\ S_{21}^{(s)} &= - (T_{22}^{(s)})^{-1} T_{21}^{(s)} \\ S_{22}^{(s)} &= (T_{22}^{(s)})^{-1} \end{aligned} \quad (3.64)$$

As a result, the growing exponential of the block T_{11}^s are attenuated. So, the numerical fluctuations are suppressed and in that case the numerical errors disappear. Therefore, with the recursive integration from a layer to another, the matrix S^s ($s \in [1, h - 1]$) stays stable.

3.6.3 The total S-matrix of the entire structure

In most of cases, the structure is illuminated from the superstrate at the position $z = z_0$. The initial conditions of the integration are always generated with the calculation of the T-matrix of each layer s (Identity matrix used in the Runge-Kutta integration (Eq.3.55)). Thanks to the T to S-matrix transformation, the S^0 matrix of the zeroth layer can be obtained

from $T^0 = \Psi_{sub}^{-1} P(0) \Psi_{sup}$ by applying the transformation of Eq.(3.64). At the end of the integration of all the layers, the recursion of the S^S -matrices allows obtaining the S-matrix of the whole scattering matrix S^{tot} . This last matrix depends only on the profile of the grating and the optical parameters of the different media. The cascade of the different S-matrices is performed by the recursion of the consecutive S-matrices using the Redheffer-Star product [102].

For example, the cascade of a scattering matrix $S^{(A)}$ with a scattering matrix $S^{(B)}$ can be calculated using the Redheffer-Star product $S^{(AB)} = S^{(A)} \circledast S^{(B)}$ as follows,

$$S^{(AB)} = \begin{bmatrix} S_{11}^{(AB)} & S_{12}^{(AB)} \\ S_{21}^{(AB)} & S_{22}^{(AB)} \end{bmatrix} \quad (3.65)$$

With,

$$\begin{aligned} S_{11}^{(AB)} &= S_{11}^{(A)} + S_{12}^{(A)} \left[I - S_{11}^{(B)} S_{22}^{(A)} \right]^{-1} \\ S_{12}^{(AB)} &= S_{12}^{(A)} \left[I - S_{11}^{(B)} S_{22}^{(A)} \right]^{-1} S_{12}^{(B)} \\ S_{21}^{(AB)} &= S_{21}^{(B)} \left[I - S_{22}^{(A)} S_{11}^{(B)} \right]^{-1} S_{21}^{(A)} \\ S_{22}^{(AB)} &= S_{22}^{(B)} + S_{21}^{(B)} \left[I - S_{22}^{(A)} S_{11}^{(B)} \right]^{-1} S_{22}^{(A)} S_{12}^{(B)} \end{aligned} \quad (3.66)$$

The global S-matrix of the structure S^{tot} is then calculated by the recursion of the different layers as,

$$S^{tot} = S^{(0)} \circledast \dots S^{(s-1)} \circledast S^{(s)} \circledast S^{(s+1)} \circledast \dots S^{(h)}$$

With, $S^{(0)}$ and $S^{(h)}$ are the scattering matrix of the superstrate and the substrate respectively. This global matrix links the diffracted field of the substrate layer at the position $z = z_h$ and the superstrate layer at the position $z = z_0$ to the incident field at z_0 . Thus, the global matrix S^{tot} can be expressed as,

$$\begin{bmatrix} [c_h^+] \\ [c_0^-] \end{bmatrix} = S^{tot} \begin{bmatrix} [c_{inc}^+] \\ 0 \end{bmatrix} \quad (3.67)$$

Once S^{tot} is calculated, the amplitudes of the transmitted diffraction orders $[c_h^+]$ in the transmission zone, and the amplitude of the reflected diffraction orders $[c_0^-]$ in the reflection zone, the $R_{(n)}$ and $T_{(n)}$ which correspond to the efficiency of the reflected order and the

transmitted order (n) respectively can be straightforwardly calculated from,

$$\begin{cases} [c_h^+] = S_{11}^{tot}[c_{inc}^+] \\ [c_0^-] = S_{21}^{tot}[c_{inc}^+] \end{cases} \quad (3.68)$$

As S_{11}^{tot} and S_{21}^{tot} represent the global sub-matrices of the entire structure, the main advantage of this algorithm added to its stability, is the physical interpretation given to the element of the matrix S^{tot} . We can notice, from Eq.(3.68), that the S_{11}^{tot} represents the reflection coefficient of the system. Whereas, S_{21}^{tot} represents the transmission coefficient of this same system.

3.7 The intensities of the diffracted order

In case of the periodic structure, the diffraction efficiency ED_n of a diffracted order n (reflected or transmitted) can be defined as the flux of the Poynting vector of this order n at a surface parallel on the structure, normalized by the flux of the pointing vector of the incident field at the same position of this surface,

$$ED_n = \frac{\iint_S P_{zn} dS}{\iint_S P_{z0} dS} \quad (3.69)$$

With, P_{zn} is the complex Poynting vector associated to the diffracted order n , projected on the propagation axis z , and expressed as,

$$P_{zn} = \frac{1}{2} \text{Real} (E_n \wedge H_n^*)_z \quad (3.70)$$

In the superstrate and the substrate, the field is expressed in terms of the Rayleigh expansion. Therefore, the total field is described as the sum of plane waves and the relation between E_x and H'_y can be written as,

$$E_x = j \frac{1}{k^2} \frac{\partial H'_y}{\partial z} \quad (3.71)$$

For TM polarization, after the integration steps and the calculation of S-matrix of the overall structure, the Fourier coefficients of the forward magnetic field $[c_0^+]$ and the backward magnetic field $[c_0^-]$ at the superstrate ($z = 0$), and the Fourier elements of the forward magnetic field $[c_h^+]$ and the backward magnetic field $[c_h^-]$ at the substrate ($z = h$) are calculated. These coefficients allow the calculation of the different intensities of the diffracted orders depending

on the diffracted magnetic field H'_y .

For $z = 0$, the Fourier series of the reflected magnetic field can be written as,

$$H'_y{}^0(x) = \sum_{n=-N}^{+N} c_{0,n}^- e^{j(n\frac{2\pi}{\Lambda} + \sigma_0)x}$$

On the other hand, at the substrate level the transmitted magnetic field is written as,

$$H'_y{}^h(x) = \sum_{n=-N}^{+N} c_{h,n}^+ e^{j(n\frac{2\pi}{\Lambda} + \sigma_0)x}$$

and the incident field

$$H'_y{}^{inc}(x) = \sum_{n=-N}^{+N} c_{inc,n}^+ e^{j(n\frac{2\pi}{\Lambda} + \sigma_0)x}$$

In general, $[c_{inc}^+]$ is defined as $c_{inc,n=0}^+ = 1$ and $c_{inc,n \neq 0}^+ = 0$. Therefore, the ratio of diffracted flux over the incident flux can be written as,

$$ED_n = \text{Real} \left(\frac{n_{sup} |c_{q,n}|^2 \beta_n}{n_{sub}^2 \beta_0} \right) \quad (3.72)$$

With $\beta_n = \sqrt{k^2 - (n\frac{2\pi}{\Lambda} + \sigma_0)^2}$, with $k = k_{sup}$ or k_{sub} and $c_{q,n} = c_{0,n}^-$ or $c_{h,n}^+$ depending on the calculation position of the reflection or transmission coefficients respectively. $\beta_0 = \frac{2\pi}{\lambda_{inc}} \cdot n_{sup} \cos(\theta_{inc})$. For TE polarization, if we consider the diffracted electric field as,

$$E_y(x) = \sum_{n=-N}^{+N} c_n e^{j(n\frac{2\pi}{\Lambda} + \sigma_0)x}$$

and the incident electric field

$$E_y^{inc}(x) = \sum_{n=-N}^{+N} c_{inc,n}^+ e^{j(n\frac{2\pi}{\Lambda} + \sigma_0)x}$$

The efficiency of a diffracted order n can be written as,

$$ED_n = \text{Real} \left(\frac{\beta_n |c_n|^2}{\beta_0} \right) \quad (3.73)$$

With $ED_n = R_n$ and $c_n = c_{0,n}^-$ for the reflection coefficient, and $ED_n = T_n$ and $c_n = c_{h,n}^+$ for the transmission coefficient. Nevertheless, we must be also careful about the choice of

harmonics. For example, let's consider the calculation of the transmission coefficient of the order n so-called $T_{(n)}$. As $[c_h^+]$ is a $2N + 1$ vector, thus the transmission coefficient of the 0^{th} order is $T_{(0)}$, for the 1^{st} order is $T_{(1)}$ and for the -1^{st} order is $T_{(-1)}$. T_0 is defined for $n = 0$ derived from the $N + 1$ term of $[c_h^+]$. In that case, we can find the same vector projected of the incidence angle following x , i.e $exp(jk_{sup}n_{sup}sin(\theta_{inc}x)) = exp(jk_{sub}n_{sub}sin(\theta_{trans}x))$ with $\theta_{trans} = \theta_{inc}$ is the transmission angle of the order $T_{(0)}$. On the other hand, to get the harmonic of $T_{(-1)}$, we have to use $n = -1$. Therefore, the projected wave vector following x must sustain the N^{th} harmonic of $[c_h^+]$, which is represented as $exp(jk_{sup}n_{sup}sin(\theta_{inc}x)) \cdot exp(j\frac{\lambda}{\Lambda}x)$. Similarly, the $T_{(1)}$ order will be calculated with the $N + 2$ harmonic, which corresponds to the same previous projection but with the opposite sign in the argument part of the second exponential term.

3.8 RCWA extracted from the differential theory

After introducing the algorithm of the differential method, a special form of the Fourier modal Method (FMM) also known as Rigorous Coupled Wave Analysis (RCWA) can be extracted from this theory. Two differences exist between the DM-FFF and the FMM. The integration technique of the differential systems of Eq.(3.22) and Eq.(3.35), and the profile is described as a stack of lamellar sections known as staircase approximation. Therefore, $N_x = 1$ and $N_z = 0$. Under this last condition, the system that describes the propagation polarization of each staircase discretized layer can be expressed in the TM polarization case as,

$$\begin{cases} \frac{\partial [E_x]}{\partial z} = j (I_d - K[[k^2]]^{-1}K) [H'_y] & (3.74a) \\ \frac{\partial [H'_y]}{\partial z} = j \left[\left[\frac{1}{k^2} \right] \right]^{-1} [E_x] & (3.74b) \end{cases}$$

On the other hand, the TE propagation equations remain invariant and similar to system (3.35) as the fields in TE are always continuous. Following the same steps of sec.3.2, the juxtaposition of $[E_x]$ and $[H'_y]$ gives rise to the matrix M which is independent of z in that case and described in the TM polarization case as,

$$M = j \begin{bmatrix} 0 & I_d - K[[k^2]]^{-1}K \\ \left[\left[\frac{1}{k^2} \right] \right]^{-1} & 0 \end{bmatrix} \quad (3.75)$$

For each layer z_s , the RCWA uses the staircase approximation along z . The simulated profile is slightly different from the ideal surface profile. Then, the Eigenvalues ' λ_e ' and

Eigenvectors W issued from the matrix of Eq.(3.74) are used to define the propagation in this same layer. Practically, λ_e represents the vector of $2N + 1$ effective refractive indices propagating in the layer and a column i of the matrix W corresponds to the eigen vector associated to the eigenvalue $\lambda_{e,i}$.

Furthermore, with the diagonal matrix $\lambda_e = Id * [\lambda_e]$, we introduce $D = \exp(\lambda_e \cdot D_z)$. Thus, the propagation matrix $P(z)$ of the propagation matrix of the discretized layer s of thickness D_z between z_{s-1} and z_s can be written as,

$$P^s = P(z) = WDW^{-1}$$

The recursion of all the propagation solution of each layer allows us to define the overall propagation matrix P as,

$$P = P^h \dots P^{s-1} P^s P^{s+1} \dots P^0$$

Thus, the overall relation that describe the propagation in the entire structure and links the superstate by the substrate can be expressed as,

$$[F(h)] = P[F(0)] \quad (3.76)$$

Consequently, the T-matrix of each layer s is obtained by adding the infinitely thin layer at the border of each structure and the scattering matrix of the layer is calculated similarly as the procedure of the DM-FFF. Moreover, if we take into consideration the system of Eq.(3.22) and by applying the eigen integration algorithm instead of the Runge-Kutta algorithm, the DM-FFF will turn into a modal method associated with FFF. Thus, we will call this method RCWA-FFF in the next sections.

3.9 Conclusion

Here, a detailed formulation of the differential method associated with Fast Fourier Factorization (DM-FFF) has been presented. The main advantage of this method is that it takes into consideration the evolution of the profile with respect to both the propagation axis and the periodic axis. So, the problem of the staircase approximation used by the classical Fourier Modal Method can be eliminated. Moreover, a Runge-Kutta integration algorithm of order 4 is used instead of the eigen values and eigen vectors of the FMM. This algorithm is characterized by its stability and accuracy while dealing with complex profile structures.

Now, the method is ready to be implemented and used to modelize and design complex shaped diffraction gratings. Both TE or TM polarization can be used and different aspects

can be modeled. For that, the next chapters of this part are devoted to validate the DM-FFF, to show its enhanced convergence and accuracy with respect to other electromagnetic computational methods, and to apply this method for the modelization of a diffraction grating for visual security applications.

Chapter 4

DM-FFF: Validation and comparison with other electromagnetic computational methods

This chapter is devoted to validate the implemented code containing the DM-FFF and the RCWA and the RCWA-FFF extracted from the differential theory in terms of the calculated efficiencies and the field maps from one side and to present the effectiveness of the DM-FFF compared to other computational methods from the other side.

The code is implemented by using Python v2.7. This language has been chosen for many reasons. First of all, it is a free and open source software with a huge number of free libraries which can be downloaded easily. Moreover, it is faster than Matlab in term of execution time.

4.1 Validation of the methods

4.1.1 Introduction

After the implementation of the code in Python v2.7, the validation of the implemented code is shown here. This code can easily switch between the DM-FFF, the RCWA-FFF and the RCWA with its form explained in sec.3.8. This code is devoted at this scale for the modelization of 1D diffraction grating excited by TE or TM polarized plane waves and with a given angle of incidence θ_{inc} .

In case of Fourier space methods, the accuracy of the chosen method depends essentially on two principal parameters: the number of harmonics $2N + 1$ used in the Fourier domain along the periodization axis x and the spatial discretization D_z along the propagation axis z . The accuracy of the structure profile simulated is proportional to the increase of N and the

decrease of D_z . Indeed, dielectric structures are firstly studied. The energy conservation, the convergence following N and D_z and the spatial field map are going to be checked. Moreover, metallic core structures with a sinusoidal and trapezoidal profiles are also added to the study.

4.1.2 Numerical validation

Dielectric lamellar structure

Here, the dielectric lamellar structure depicted in Fig.4.1 is taken into consideration. The structure is illuminated with TM or TE polarized plane wave at normal incidence ($\theta_{inc} = 0^\circ$). The reference values are calculated by the Reticolo software based on the Fourier Modal Method (FMM). This method is the most suitable one for the modeling of rectangular gratings. For that we consider the values calculated through it as reference values. Thus, the efficiencies of the DM-FFF, the RCWA extracted from the differential theory (sec.3.10), and the RCWA-FFF have been compared to the reference values for TE and TM polarization.

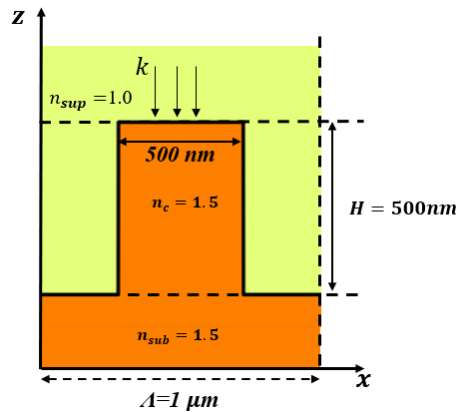


Fig. 4.1 Unit cell of a dielectric rectangular periodic grating of period $\Lambda = 1 \mu m$. The structure is illuminated from the superstrate with a monochromatic and TE or TM polarized plane wave at normal incidence and a wavelength $\lambda = 600 nm$. The refractive indices of the superstrate, the modulated zone and the substrate are $n_{sup} = 1$, $n_c = n_{sub} = 1.5$ respectively. The wave vector is $k = \frac{2\pi}{\lambda} n_{sup}$.

All the values are calculated for a truncated order $N = 30$. For the three methods (DM-FFF, RCWA, and RCWA-FFF), the structure is discretized by a constant step $D_z = 1 nm$ and $N_{FFT} = 2^{13} = 8192$ samples is chosen. This highest value has been considered in order to correctly calculate the harmonic amplitude of the $2N + 1$ truncated Fourier transformation with $N_{FFT} \gg N$. This transformation is used for the DM-FFF, the RCWA and the RCWA-FFF. On the other hand, the classical FMM modelizes the ideal lamellar section by calculating

TM polarization							
Order	FMM	DM-FFF	RCWA	RCWA-FFF	ΔR_1	ΔR_2	ΔR_3
T(-1)	0.34025397	0.34025290	0.34025290	0.34025290	$1 \cdot 10^{-7}$	$1 \cdot 10^{-7}$	$1 \cdot 10^{-7}$
T(0)	0.23283470	0.23283680	0.23283680	0.23283680	$2 \cdot 10^{-6}$	$2 \cdot 10^{-6}$	$2 \cdot 10^{-6}$
TE polarization							
Order	FMM	DM-FFF	RCWA	RCWA-FFF	ΔR_1	ΔR_2	ΔR_3
T(-1)	0.32290883	0.32290449	0.32290449	0.32290449	$4 \cdot 10^{-6}$	$4 \cdot 10^{-6}$	$4 \cdot 10^{-6}$
T(0)	0.18062036	0.18062629	0.18062629	0.18062629	$6 \cdot 10^{-6}$	$6 \cdot 10^{-6}$	$6 \cdot 10^{-6}$

Table 4.1 The transmission coefficient $R(n)$ of the diffracted order -1 , and 0 of the dielectric sinusoidal grating for $N = 30$ with $D_z = 1nm$ and $n_s = 1$ for the S-matrix algorithm. The coefficients are calculated using the DM-FFF, the RCWA extracted from the differential theory, and the RCWA-FFF. The reference values are calculated by the classical FMM using Reticolo. ΔR_1 , ΔR_2 , and ΔR_3 represent the absolute relative error between the values of Reticolo from one side and the values of the DM-FFF, the RCWA, and the RCWA-FFF respectively from the other side

the exact Fourier transformation of a rectangular layer. In that case, $N_x = 1$ and $N_z = 0$. So, the propagation matrix (Eq.(2.65)) falls on the classical matrix without FFF. Table.4.1 shows the values of the transmission coefficients calculated with the different methods. We can notice that, for a lamellar structure, the obtained values of the three methods are almost similar to the values of the classical FMM with an impact on the sixth or seventh digits supposed to come from the FFT. For both polarizations, a relative errors of 10^{-6} and 10^{-7} , between the value of Reticolo from one side and the values of the other methods from the other side, are obtained for both polarizations. Indeed, the values of the DM-FFF, RCWA extracted from the differential theory and the RCWA-FFF are completely similar as the used propagation matrices are similar. The execution time of the FMM stays faster than the methods extracted from the differential theory. Indeed, those methods are based on the discretization into thin layer to perform the integration (Runge-Kutta for the DM-FFF and eigen solution of the RCWA and RCWA-FFF), while the classical FMM calculate the eigenvalues and the eigen vectors of each traversal modulated or homogeneous section without the need of discretization step. Moreover, a reference plane change is associated to the algorithm of the FMM to limit the divergence. This divergence is a consequence of the use of the exponential terms in the propagation matrix while dealing with complex effective indices.

In addition, the field maps obtained by the DM-FFF have been compared to the ones executed by Reticolo. Both are calculated for $N = 30$ and for TE and TM polarization. It is clear that for both polarizations the distribution of the fields is exactly the same between the code of the DM-FFF and Reticolo.

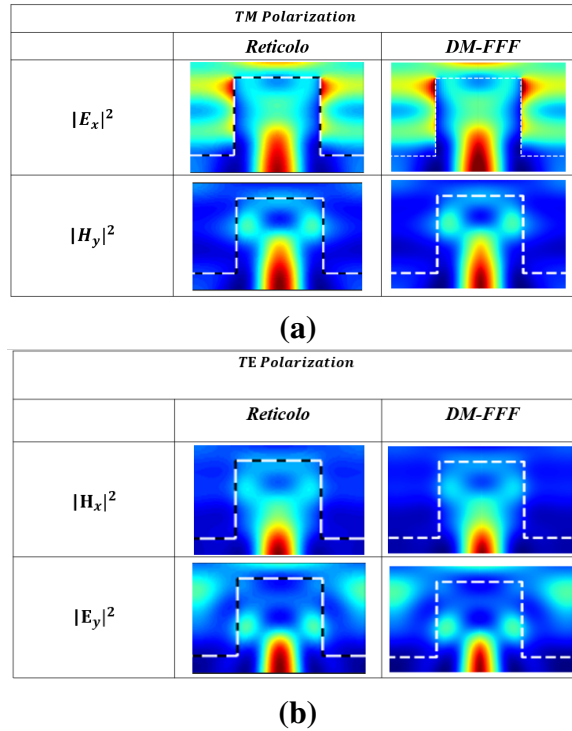


Fig. 4.2 The field maps of the dielectric lamellar structure using the DM-FFF and Reticolo software for (a) TM polarization (b) TE polarization.

As mentioned before, the discretization step D_z is a critical parameter of the DM-FFF. For

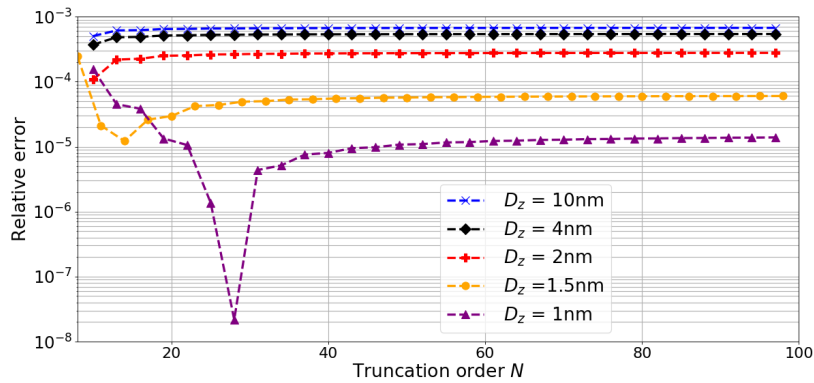


Fig. 4.3 Convergence of the relative error of zeroth order of transmission $|T_{0_{Reticolo}} - T_{0_{DM-FFF}}|$ with $T_{0_{Reticolo}} = 0.23283470$ for different discretization steps.

that, the convergence of the relative error $|T_{0_{Reticolo}} - T_{0_{DM-FFF}}|$ has been studied following the truncation order N for different values of D_z (Fig.4.3). We can clearly notice that the relative error decreases with the decrease of D_z . Indeed, a relative error of 10^{-3} is reached

for $D_z = 10nm$ (blue dashed curve with cross), while a value of 10^{-4} can be obtained for $D_z = 1.5nm$ (orange dashed curve with solid dots). Finally, for better accuracy, D_z can be decreased to reach an error rate of 10^{-5} with $D_z = 1nm$ (purple dashed curve with solid triangles).

Dielectric sinusoidal grating

To upraise the FFF with a continuous structure profile, the dielectric sinusoidal structure (Fig.4.4) has been considered. The power of the diffraction efficiencies of the DM-FFF, the RCWA, and the RCWA-FFF have been compared to those obtained by the Method of fictitious sources (MFS) which is considered as an accurate method for this specific structure [108].

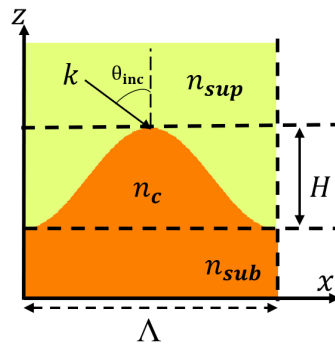


Fig. 4.4 Unit cell of a sinusoidal periodic grating of period Λ . The structure is illuminated from the superstrate by a monochromatic and polarized plane wave k at a wavelength λ . The refractive indices of the superstrate, the modulated zone and the substrate are n_{sup} , n_c and n_{sub} respectively. The wave vector $k = \frac{2\pi}{\lambda} n_{sup}$.

The refractive index of the superstrate is $n_{sup} = 1$, while $n_c = n_{sub} = \sqrt{3}$. The structure is illuminated with a monochromatic plane wave at $\lambda = 1.0\mu m$ from the top. The period of the unit cell is $\Lambda = 3.9\lambda$, the peak to peak amplitude is $H = 0.5\lambda$, while the excitation angle is $\theta_{inc} = 30^\circ$. In addition, $N_{FFT} = 8192$ points and $D_z = 1$ nm have been chosen. Table 4.2 presents the results of the reflection and transmission coefficients calculated by the implemented code of the DM-FFF, the RCWA and the RCWA-FFF extracted both from the differential theory as explained in sec.3.10. We can notice that the three previous methods respect well the law of the conservation of energy where the sum $R + T = 1$.

Moreover, the obtained results of the three methods fit well with the reference values calculated for both TE and TM polarization with a relative error less than $2.3 \cdot 10^{-4}$. For TM polarization, the relative errors of the RCWA are always bigger than the other methods. This

DM-FFF: VALIDATION AND COMPARISON WITH OTHER ELECTROMAGNETIC COMPUTATIONAL METHODS

TE polarization							
Order	MFS	DM-FFF	RCWA	RCWA-FFF	ΔR_1	ΔR_2	ΔR_3
R(-1)	0.01281	0.01277	0.01277	0.01277	$3.6 \cdot 10^{-5}$	$3.4 \cdot 10^{-5}$	$3.4 \cdot 10^{-5}$
R(0)	0.00295	0.00299	0.00298	0.00298	$3.5 \cdot 10^{-5}$	$2.8 \cdot 10^{-5}$	$2.8 \cdot 10^{-5}$
R(+1)	0.05077	0.05076	0.05076	0.05076	$8.2 \cdot 10^{-6}$	$1.3 \cdot 10^{-5}$	$1.3 \cdot 10^{-5}$
R	/	0.09660	0.09659	0.09659	/	/	/
T	/	0.90339	0.9034	0.903400	/	/	/
R+T	/	1.0	1.0	1.0	/	/	/
TM polarization							
Order	MFS	DM-FFF	RCWA	RCWA-FFF	ΔR_1	ΔR_2	ΔR_3
R(1)	0.0087845	0.0087841	0.0087745	0.0087826	$4 \cdot 10^{-7}$	$1 \cdot 10^{-5}$	$2 \cdot 10^{-6}$
R(0)	0.0013163	0.0013180	0.0013082	0.0013182	$1.7 \cdot 10^{-6}$	$8.1 \cdot 10^{-6}$	$1.9 \cdot 10^{-6}$
R(-1)	0.0085778	0.0085769	0.0085984	0.0085743	$9 \cdot 10^{-7}$	$2 \cdot 10^{-5}$	$3.5 \cdot 10^{-6}$
R	/	0.04636	0.04635	0.04636	/	/	/
T	/	0.95363	0.95364	0.95363	/	/	/
R+T	/	1.0	1.0	1.0	/	/	/

Table 4.2 The reflection coefficient $R(n)$ of the diffracted order $-1, 0, +1$ of a dielectric sinusoidal grating for $N = 30$ with $D_z = 1nm$ and $n_S = 4$ for the S-matrix algorithm. The coefficients are calculated using the DM-FFF, the RCWA extracted from the differential theory, and the RCWA-FFF. R and T represent the total reflection and the total transmission of the all reflected orders respectively. $\Delta R_1, \Delta R_2,$ and ΔR_3 represent the absolute relative error with respect to the values of the MFS and the values of the DM-FFF, the RCWA, and the RCWA-FFF respectively.

is a direct effect of the FFF associated with the DM and the RCWA. For the DM-FFF and the RCWA-FFF, all the calculated values are almost similar. But, due to the accuracy of the Runge-Kutta integration, the relative errors of the DM-FFF are always smaller. On the other hand, for TE polarization, all the calculated values give almost the same error as the problem of discontinuity of the fields is not presented with this polarization. Fig.4.5 shows the impact of associating the FFF to the differential method and the RCWA. Indeed, the relative error of the zeroth order of transmission has been calculated with respect to the value obtained by each method at $N = 150$ (301 harmonics). It is clear that the RCWA converge slowly following N , truncation order $N = 100$ is necessary to reach a relative error of 10^{-4} . On the other hand, 21 harmonics ($N = 10$) are sufficient to reach a relative error of 10^{-5} for the DM-FFF and the RCWA-FFF. Moreover, an error of 10^{-7} can be attended for $N > 40$.

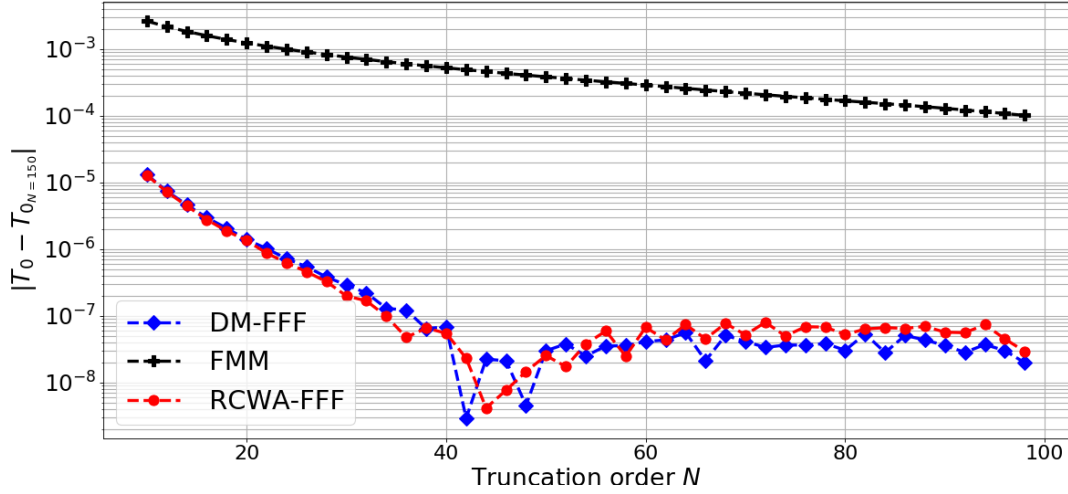


Fig. 4.5 The relative error of the zeroth order of transmission T_0 of the sinusoidal dielectric structure following N with respect to T_0 for $N = 150$ of each method. With $T_{0_{N=150}} = 0.412428713, 0.412673209, 0.412406292$ for the DM-FFF, the FMM and the RCWA-FFF respectively. $D_z = 1nm$ and $N_{FFT} = 8192$ samples.

4.2 The DM-FFF compared to other electromagnetic computational methods

4.2.1 Introduction

As mentioned in Chapter 3, the DM-FFF is an electromagnetic computational method adapted for complex-shaped diffraction gratings. By taking into consideration the evolution of the normal and tangential components of the electric field in the algorithm of the method, the power efficiency of the diffraction orders are now considered more accurate and more rigorous. To ensure that, we will perform a convergence test to the values of the different diffracted orders calculated by the DM-FFF, and we will compare them to the values obtained by the Fourier Modal Method (FMM), the RCWA-FFF and the last one is the Chandezon Method (C-Method) available with the MC-Grating software. Two structures will be considered. The first one is a simple metallic sinusoidal grating, and the second one is a metallic trapezoidal structure. The two profiles have been chosen for several reasons. First of all, in case of metallic structures, high contrast of refractive indices appears between the incident medium and the core of the grating. Moreover, the first one is a continuous profile where its normal varies rapidly following the periodization axis. On the other hand, the trapezoidal profile is a function mixing continuous zone with discontinuous areas. In that case, the normal varies following the inclined side of the structure. Indeed, in both cases, the association of the

FFF will suppress the stack of lamellar layers (staircase approximation) used by the classical FMM or the RCWA extracted from the differential theory. However, as all the mentioned methods belong to the family of the modal method which deal with the problem in the Fourier domain, all the comparisons will be performed following N which represents the truncation order in the Fourier space.

4.2.2 Sinusoidal Metallic Grating

Convergence Test of the structure

In order to appraise the performance of the FFF, the evolution of the normalized intensities of the minus first order of reflection ($R_{(-1)}$) is compared. The C-Method is based on a non conformal coordinate transformation that alter the corrugated zone into a surface plan boundary with a specific permittivity tensor [16]. For the sinusoidal profile, this method needs only one harmonic. All those methods are based on Fourier series development. Thus, a comparison with respect to the number of harmonic $2N + 1$ used in the Fourier space could be realized. We conducted a convergence test for the case of simple Aluminum

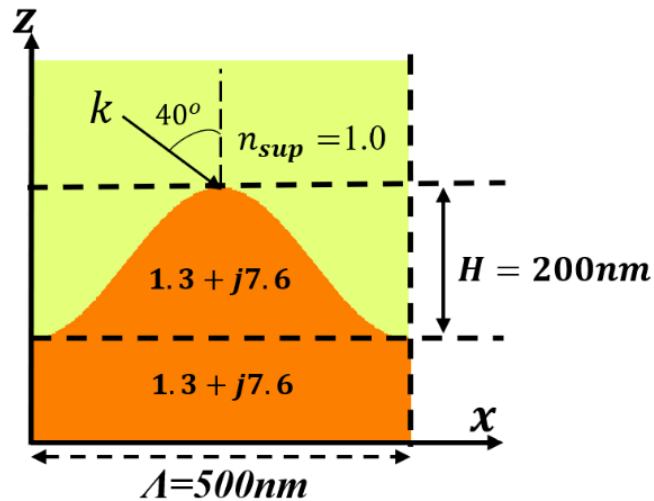


Fig. 4.6 Unit cell of the periodic grating. The structure is illuminated with a TM polarized plane wave at $\lambda = 673.2nm$

sinusoidal grating (Fig.4.6). The structure is illuminated with a TM polarized plane wave at $\lambda = 632.8nm$. The relative error has been studied by taking into account a reference value computed with the integral method with $R_{(-1)_{ref}} = 0.8785309971543$.

For both RCWA-FFF and DM-FFF, $n_S = 4$. Indeed, to correctly execute the comparison with the same number of S-Matrices, we considered $D_z = 0.25nm$ for the DM-FFF, the FMM

and the RCWA-FFF. So that, 200 scattering matrices S_i have been cascaded for the modulated region. Figure 4.7 shows the relative error for the four different methods by taking the result obtained with the integral method as reference [3].

Only one harmonic is sufficient for the C-Method to remain constant with respect to N . Consequently, this method is the most suitable for the modeling of 1D sinusoidal profiles as the relative error stays stable along the evolution of N .

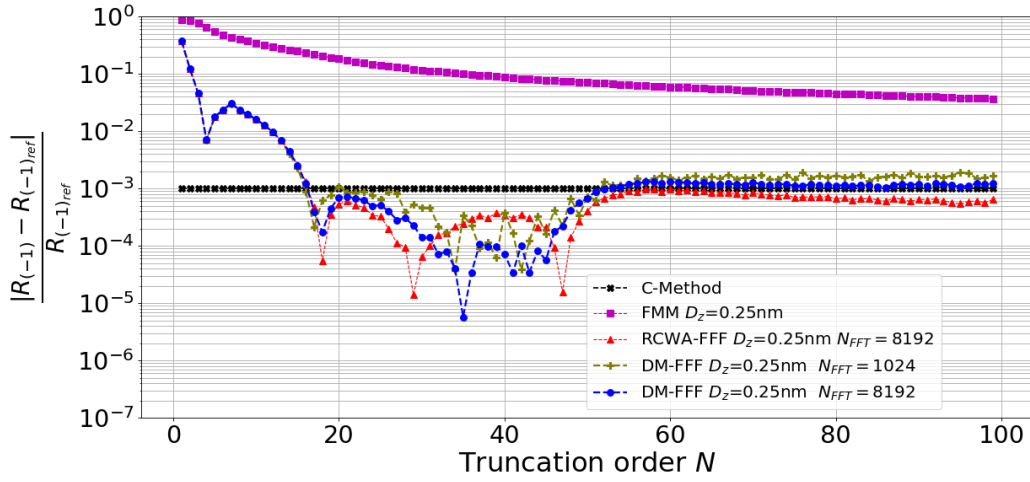


Fig. 4.7 Relative error with respect to the number of harmonics N for the different methods

The 10^{-3} error induced by this method is probably due to the relative error of the integral method with respect to the C-Method. Meanwhile, as the RCWA uses the staircase approximation ($N_x = 1$ and $N_z = 0$), and doesn't take into account the continuity of field at the dielectric-metal interface of the continuous profile, its error evolution converges slowly and the method needs a high number of harmonics in order to reach an acceptable relative error ($< 10^{-2}$). On the other hand, while associating the FFF with RCWA, the convergence is significantly enhanced. It can reach less than 10^{-2} beyond a truncation order $N = 20$. The slope of the surface profile set in each section is sufficient to strengthen the convergence of the method and turn the RCWA into an efficient and rigorous tool in term of accuracy and execution time. Finally, we can notice that the DM-FFF converges rapidly from $N = 18$. After $N = 50$, the solid blue dots curve representing the convergence of the DM-FFF follows closely the C-Method error evolution. The relative error of the DM-FFF oscillates around the error of the C Method. Moreover, the relative error of the DM-FFF with respect to the C-Method remains smaller than 2.5×10^{-4} from $N = 50$ to $N = 200$. This oscillation could be induced by the FFT algorithm. The accuracy increases with the increase of N_{FFT} as shown in Fig.4.7. This convergence emphasizes our hypothesis concerning the C-method.

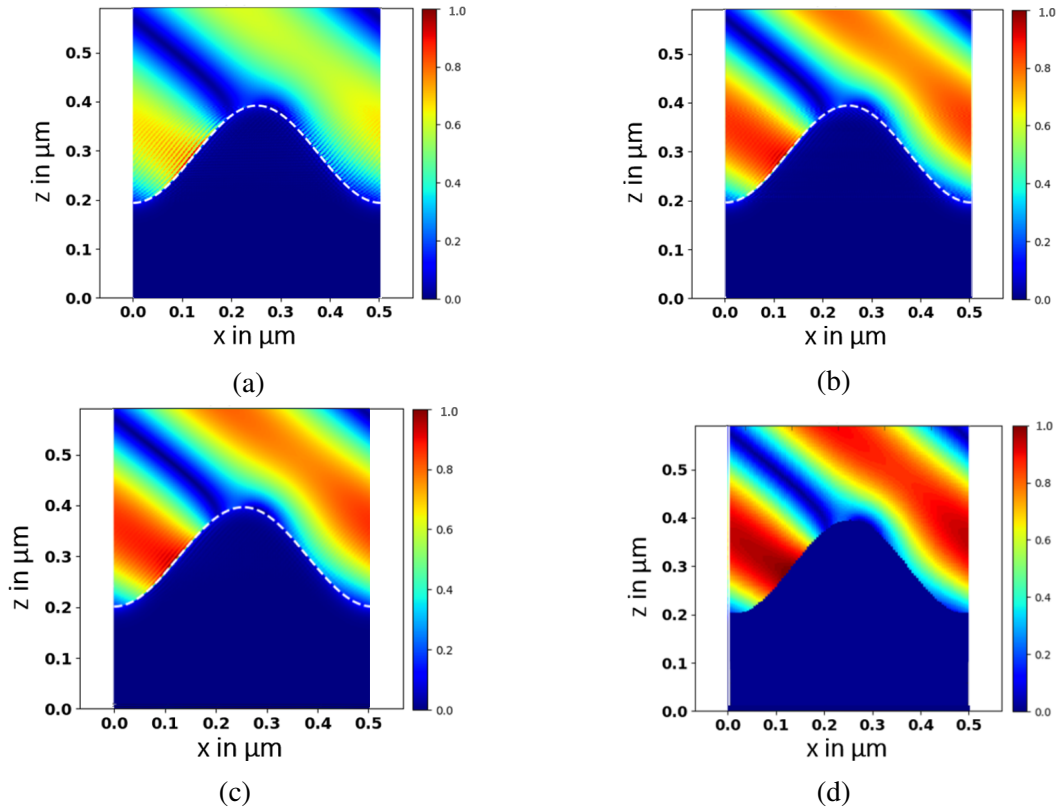


Fig. 4.8 Evolution of $|E_x|$ with (a) FMM, (b) RCWA-FFF, (c) DM-FFF and (d) C-Method

Minus First order of Reflection $R_{(-1)}$				
N	DM-FFF	RCWA-FFF	FMM	C-Method
10	0.892714	0.892685	0.575684	0.877652
30	0.878587	0.878407	0.776522	0.877652
50	0.878178	0.878042	0.816513	0.877652
100	0.877454	0.877960	0.846460	0.877652

Table 4.3 The minus first order of reflection transmission $R_{(-1)}$ for the metallic sinusoidal structure at $N = 10, 30, 50, 100$ using the four modal methods RCWA-FFF, DM-FFF, FMM, and C-Method

Field Maps

To reveal the problem induced by the continuous profiles on the field representation, the evolution of $|E_x|$ is studied for the metallic sinusoidal structure with $N = 50$ truncation (the number of harmonics is $2N + 1$). Due to the staircase approximation, parasitic reflections appear at the dielectric-metal interface with the FMM (Fig.4.8.(a)). When the RCWA is associated with FFF, the problem is alleviated (Fig.4.8.(b)). While in case of DM-FFF

(Fig.4.8.(c)), the problem is mostly treated and the field distribution fits with the representation computed with that of the C-Method (Fig.4.8.(d)).

Comparison of the execution time of the DM-FFF, RCWA-FFF and RCWA

Now, the execution time of the different methods has been compared. With the Intel core i7 and 8GB RAM computational resources, the three Fourier space methods extracted from the same code (DM-FFF, RCWA, and RCWA-FFF) have been compared for the sinusoidal metallic structure with $D_z = 0.25nm$. In that case, 600 S-matrices are cascaded to obtain the overall scattering matrix of the structure.

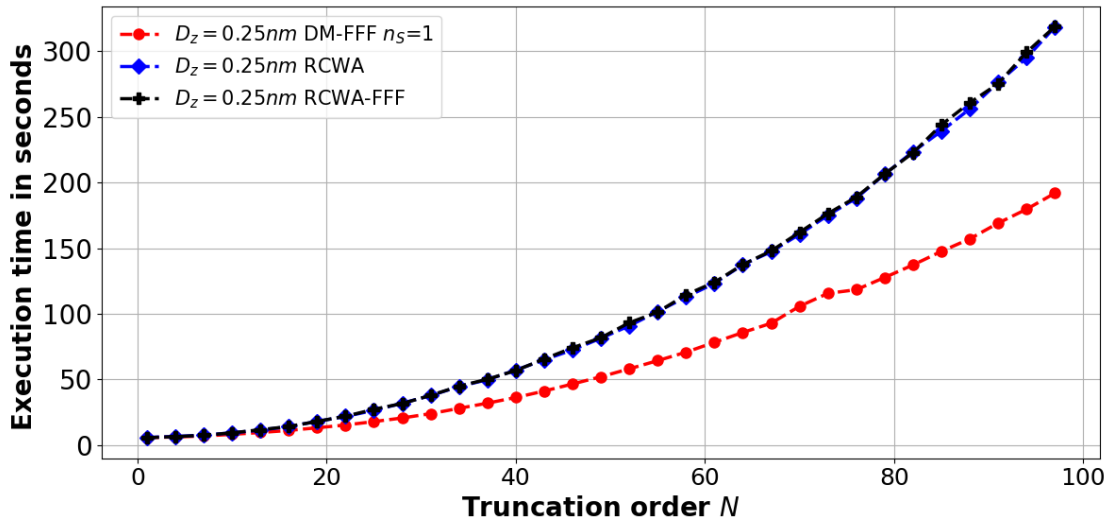


Fig. 4.9 The execution time following the truncation order N for 600 cascaded layers.

Fig.4.9 presents the evolution of the time needed to calculate the efficiency of the diffracted orders following N . For $N < 20$, the three methods need almost the same time to perform the calculation. On the other hand, for higher truncation orders the DM-FFF (red dashed curve with solid dots) is faster than the RCWA and the RCWA-FFF. Indeed, the time consumption decreases by 40% with the DM-FFF compared to the two other methods. This is due to the Runge-Kutta integration algorithm which is faster than the calculation of eigen values and the eigen vectors used with the RCWA and the RCWA-FFF. For example, for $N = 97$, the DM-FFF takes 47.7s to perform the calculation. In contrast, the RCWA and the RCWA-FFF need 79.4s for the same truncation orders.

In term of accuracy, if we fix a relative error of 1% with respect to the value of the integral method, so that 10^{-2} on the Fig.4.7, $N = 14$ is sufficient for both RCWA-FFF and DM-FFF

to reach this accuracy. As a result, the DM-FFF needs 2.5s and the RCWA-FFF takes 3s to finish the calculation. On the other hand and by performing a polynomial fit having the form of $0.008N^2 - 0.08N + 2.7$ to the time evolution and the form of $2.2N^{-0.87}$ to the error evolution of the RCWA, the classical RCWA needs $N > 150$ to reach the same limit of accuracy. So that, a calculation time $> 190s$ is required in that case. In term of speed, a factor of 76 can be achieved if we use the DM-FFF instead of the RCWA.

Now, if the relative error threshold is fixed for 0.1% (10^{-3}), $N = 18$ is sufficient for the methods associated with the FFF. The calculation is performed in 3.33s by the DM-FFF, and 4.57s by the RCWA-FFF. By using the same previous fitting, we found that this threshold is reached for $N > 1000$ with the RCWA, so that this method needs 8732s to finish the execution procedures. At this scale, a factor of 2622 in term of speed is reached if we use the DM-FFF compared to the RCWA. Finally, it is clear that the DM-FFF is irremediably faster than the RCWA in terms of accuracy and execution time. Indeed, after fixing a given error threshold so that a given N , the use of the DM-FFF saves a huge calculation time in case of complex shaped diffraction gratings. Indeed, if a considerable homogeneous layer must be taken into consideration, the DM-FFF needs to discretize this layer following D_z . On the other hand, the RCWA simulates this zone as one layer. As a result, the DM becomes slower. The ideal case is to hybridize the two methods in order to get an optimal trade-off.

The effect of the multi layers n_S on the convergence and the speed of the DM-FFF

As mentioned in Section 3.4, the Runge-Kutta algorithm can be also performed by gathering the P-matrices of n_S layers. This combination allows to gather different P matrices into one propagation matrix. So that, the number of the cascaded S-matrices will be reduced by the factor n_S . In this way, and as the same number of the propagation matrices P is calculated, the accuracy of the DM-FFF doesn't change. Using this method, we can only reduce the execution time of the DM-FFF due to the decrease of the number of cascaded S-matrices. To elaborate more, if the modulated section with $H = 200nm$ is discretized following $D_z = 0.25nm$, we will have 600 propagation matrices P in this zone. If $n_S = 1$, each P-matrix will produce one S-matrix. Now, if $n_S = 4$, we will calculate 600 propagation matrices but each 4 P-matrix are finally gathered in one S-matrix. So that, we will have 150 S-matrices to be cascaded. At this scale, the execution time can be reduced as the number of cascaded S-matrices decreases.

In Fig.4.10.(b), the execution time of the DM-FFF for different n_S layers has been studied. A decrease in term of the consumed time of 11% can be reached if we use $n_S = 4$ for $N > 40$ (blue dashed curve with solid diamonds) instead of $n_S = 1$ (red dashed curve with solid dots).

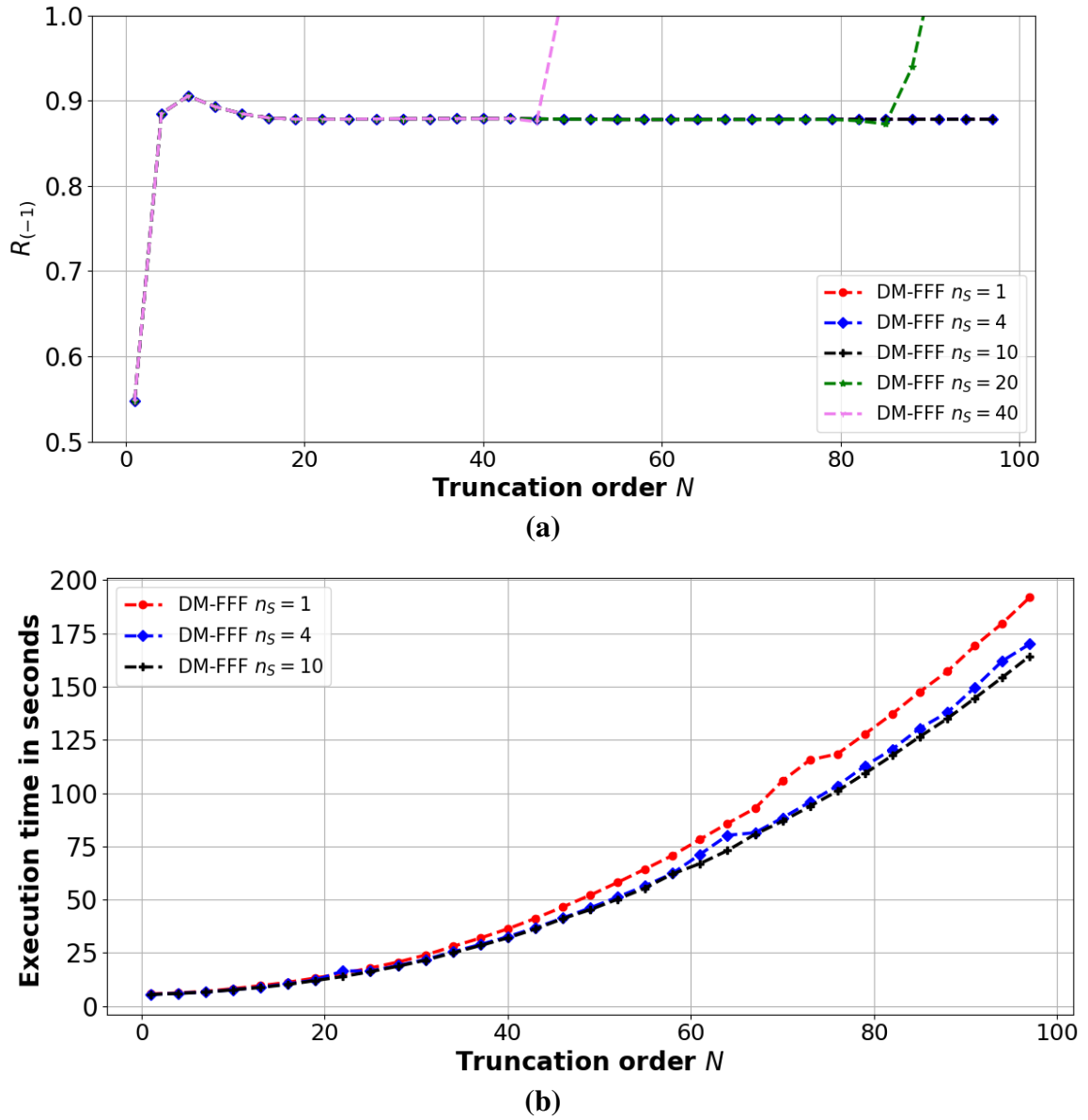


Fig. 4.10 (a) The evolution of the minus first order of reflection following N for different sub-layers n_S (b) The execution time following the truncation order N of the DM-FFF with $D_z = 0.25nm$ and n_S layers.

It is clear that the curve of $n_S = 10$ is very close to the one of $n_S = 4$. At this scale, and for this structure, 30 S-matrices are cascaded instead of 150. So, we can deduce that the calculation of the propagation matrix has the highest impact on the execution time. From Fig.4.10.(a), we can notice that for $n_S > 10$ and for high truncation orders ($N > 40$), the DM-FFF can numerically diverge. This is due to the python algorithm where numerical errors can appear if we use high values in a range $> 10^{15}$ [88].

4.2.3 Discontinuous structure: A Trapezoidal metallic grating as an example

Here, a trapezoidal structure mixing continuous part with discontinuous profile is chosen. Indeed, the exact normal to the profile is inclined along the internal interface of the structure and depends on the taper angle α and the angle between the inclined surface and the transverse one $\beta = \frac{\pi-\alpha}{2}$. Thus, $N_x = \mp \sin(\beta)$ and $N_z = \cos(\beta)$.

As mentioned before, the DM-FFF and the RCWA-FFF take into consideration the projection of the normal \vec{N} on the propagation axis z and the periodic axis x in each discretized section. On the other hand, while using the classical FMM, the trapezoidal sections are considered as a cascade of rectangular layers. Therefore, the staircase approximation risks to do not respect the continuation of the field from one side and to do not represent the ideal desired structure from the other side since $N_x = 1$ and $N_z = 0$. Besides, the C-Method transforms the corrugated zone of the trapezoidal into a plane surface with changed permittivity tensor $n_c(x', z')$. We can notice that, sharped angle can't be implemented with the C-Method. For that, all the corners of the trapezoid are rounded by a curvilinear continuation. To elaborate more, the C-Method describes the periodic structure as a Fourier series following a given number of harmonic. Thus, it needs a continuous structure in order to implement correctly the desired structure. The trapezoidal metallic grating depicted in Fig.4.11 has been considered.

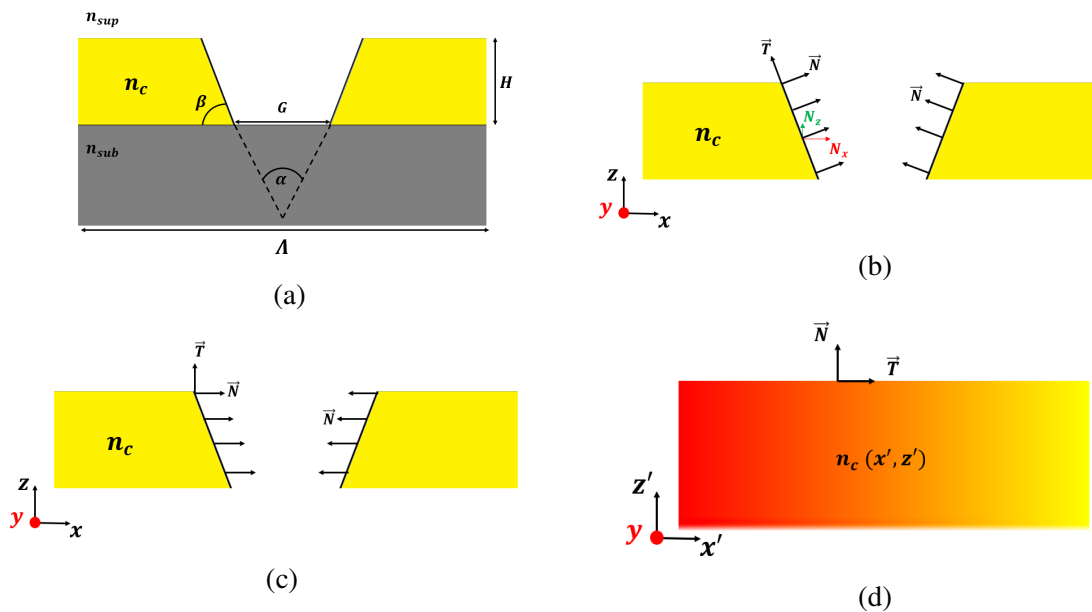


Fig. 4.11 (a) Schematic representation of a trapezoidal unit cell. The normal and the tangent to the trapezoidal region using the (b) DM-FFF, (c) FMM, (d) C-Method

To illustrate that, the evolution of the zero order of transmission $T_{(0)}$ has been studied following the truncation order N . The structure is illuminated with a TM polarized plane wave at $\lambda = 645nm$ under normal incidence ($\theta_{inc} = 0^\circ$). The geometrical parameters of the structure are the following: $H = 180nm$, $G = 65nm$, $\alpha = 10^\circ$ and $\Lambda = 500nm$, while $n_{sup} = n_{sub} = 1.0$ and $n_c = 1.46 + j7.78$. The Fourier series transformation of the DM-FFF and the RCWA-FFF are calculated via the FFT with $N_{FFT} = 8192$ samples and the structure is discretized by a step $D_z = 1nm$.

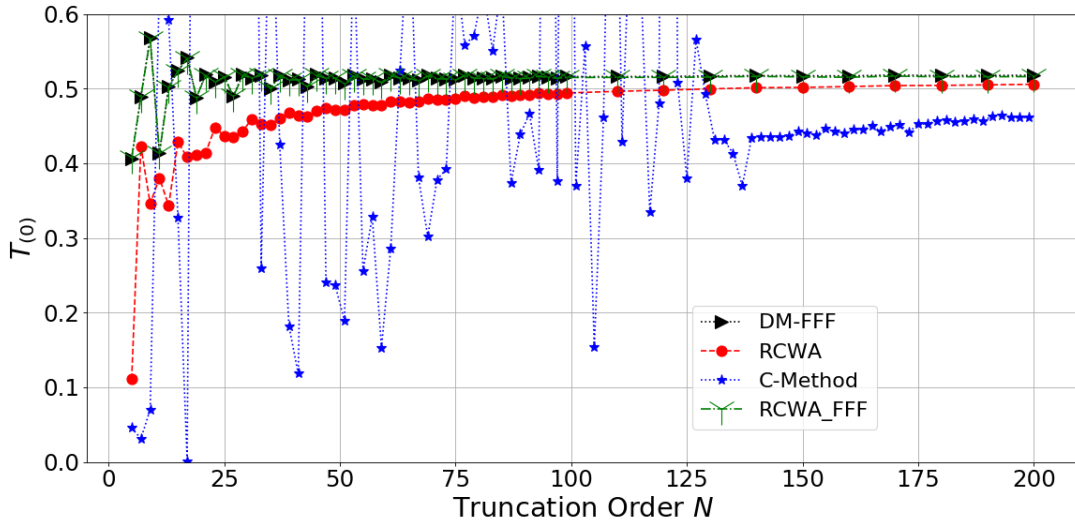


Fig. 4.12 Relative error with respect to the number of harmonics N for the different methods

Zero order Transmission $T_{(0)}$				
N	DM-FFF	RCWA-FFF	FMM	C-Method
10	0.413436	0.413112	0.380388	0.646747
30	0.518331	0.513915	0.459392	1.565636
50	0.517835	0.513608	0.471392	0.189199
100	0.515982	0.514791	0.494124	0.369410
150	0.517107	0.515647	0.501570	0.440184
200	0.517714	0.516010	0.505738	0.461345

Table 4.4 The zero order of transmission $T_{(0)}$ for the metallic trapezoidal structure at $N = 10, 30, 50, 100, 150,$ and 200 using the four modal methods RCWA-FFF, DM-FFF, FMM, and C-Method

Fig.4.12 illustrates the evolution of $T_{(0)}$ with respect to N for the four different methods. Indeed, the DM-FFF needs $N > 40$ to correctly converge to the right value and to stabilize along N (black dotted curve with solid triangles). Nevertheless, the FMM converges slowly in a monotonic manner (red dashed curve with solid dots). Besides, this method needs

more than $N = 150$ to reach the value of the DM-FFF. This slow convergence is a direct consequence of the staircase approximation and the non-respect of the continuity of the electric field in TM polarization.

On the other side, when associating the FFF to the RCWA, (the method extracted from the differential theory), the convergence rate is incredibly enhanced (green dashed curve with triangle-like markers). A faster and more accurate results are now obtained where the $T_{(0)}$ stabilizes for $N > 50$. Meanwhile, it is clear that the values calculated with the RCWA-FFF and the DM-FFF are indistinguishable and both methods converge very closely with each other to the same value following N (see Table 4.4). Undoubtedly, this result shows the effectiveness of associating the FFF with the modal methods turning them into more rigorous and accurate methods for the modeling of different shaped diffraction grating. Finally, we can notice that the C-Method (blue dotted curve with solid asterisk) fails to convergence. Indeed, a truncation order $N > 140$ is needed to suppress the numerical fluctuations. After this harmonic the C-method starts to slowly converge in an asymptotic way without reaching the values of the other methods. Here, we can note that the C-Method completely fails to converge in case of Lamellar structure (α is close to 0°).

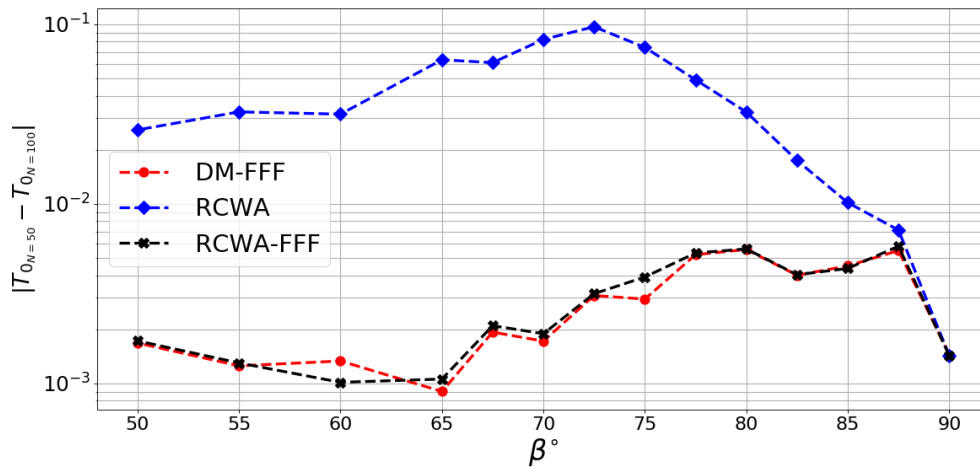


Fig. 4.13 Relative error with respect to the angle β for the different methods

Finally, the evolution of the relative error of the zeroth order of transmission $T_{(0)}$ has been evaluated following to β (Fig.4.13). $T_{(0)}$ of each method has been calculated for $N = 50$ and the relative error has been calculated with respect to the value of the transmission for $N = 100$. Indeed, it is clear that when β increases the relative error of the classical RCWA decreases (blue dashed curve with solid squares). To elaborate more, when $\beta = 90^\circ$ (lamellar structure),

Method \ Profile	Sinusoidal	Discontinuous	Lamellar	Continuous
DM-FFF	R	HR	NR	HR
RCWA-FFF	R	HR	NR	R
C-Method	HR	NR	NR	R
FMM	NR	NR	HR	NR

Table 4.5 The recommended modeling method with respect to the grating profile in TM polarization with dielectric-metal interface. With HR: Highly recommended, R: recommended, NR: Not Recommended

the error rate of 1.4×10^{-3} is equal to the one of the RCWA-FFF and the DM-FFF. On the other hand, when $\beta = 70^\circ$, this error increases to reach a value of 9.9×10^{-2} . Nevertheless, the error evolutions of the DM-FFF and the RCWA-FFF are almost stable along the evolution of β . However, it increases from 1.6×10^{-3} to 4.6×10^{-3} for β between 50° and 87.5° . These results shows the impact of the FFF on the calculation of efficiency as the staircase approximation is suppressed with the FFF.

4.3 Conclusion

In this chapter, the power efficiency using the FFF has been compared with different electromagnetic computational methods belonging to the Fourier space family. Therefore, the evolution of the diffraction efficiencies and the error rate can be evaluated following the harmonic truncation order N .

Different profiles have been evaluated. For that, Table 4.5 summarizes how to choose the numerical method with respect to the grating profile. In case of lamellar grating, the most useful and fast method will be the FMM. Although, for sinusoidal profiles, the C-Method is definitely recommended due to its fast convergence and efficiency. While in case of the profiles mixing continuous shape with discontinuous geometry (triangular, trapezoidal, sinusoidal associated with discontinuities, curvilinear structures for examples...) either RCWA-FFF or DM-FFF are considered powerful methods for the modeling of 1D gratings. Finally, we had to notice that the C-Method can't simulate the ideal lamellar profiles.

Indeed, in this chapter, the metals used are considered lossy ($Re(n_c) \gg 0$). Nevertheless, when a metallic core with lossless index is considered, the FMM, DM-FFF and RCWA-FFF suffer from divergence and instabilities due to the rapid change of the permittivity at the dielectric metal interface from a real positive value to a real negative one. Until now, there is no existing solutions deployed with the differential theory to tackle this problem. For that,

the next chapter is devoted to explain a straightforward and easy solution for this problem which doesn't extremely affect the calculated values and the accuracy of the methods.

Chapter 5

The differential theory and the lossless permittivity metals: Problem and solution

5.1 Definition of the problem

In the previous chapters, we demonstrated that the DM-FFF showed a more powerful and more accurate performance while modeling the different profiles of diffraction gratings. Nevertheless, for metallic core structures, the refractive index is composed of real and imaginary parts $n_c = \sqrt{\epsilon_c} = n_{re} + jn_{im}$.

At a specific wavelength, near the plasmon resonance, the involved metal can have a real part n_{re} almost close to zero. The use of the well known modal methods as the FMM and the analytic modal method (AMM) [9] with metallic core showed that when real part of the metal is considered quasi-null ($n_{re} \approx 0$), some numerical instabilities and field singularities appear with the Fourier space method [59]. To elaborate more, when $n_{re} \approx 0$, then, the permittivity is considered purely negative real value (near the plasmonic resonance of the metal). In that case, the risk of the nonconvergence of the method increases. This nonconvergence depends only on the refractive index of the core, the surrounding material and the shape of the grating. On the other hand, it is independent from all the other opto-geometrical parameters of the structure, i.e. $\frac{\lambda}{\Lambda}$ ratio, groove depth, etc..

Although, to tackle this problem, many solutions have been proposed by the researchers involved with the modal methods [31, 32]. Firstly, Li et al. have shown that the physical origin of this nonconvergence comes from the singularities of the electromagnetic field at the metal-dielectric interface [57]. In other words, when a structure is illuminated by a TM

polarized electromagnetic wave, both the transverse component of the electric field E_x and the longitudinal component E_z may be singular at the edge of the dielectric-metal interface due to the singular Toeplitz matrix of the permittivity distribution of the profile. Meanwhile, if a rapid change of permittivity from positive real value ($\epsilon_{dielectric}$) to purely negative value (ϵ_{metal}) appears at the boundary of the modulated region, the Li's factorization rules may not be respected, and may induce numerical fluctuation and divergence of the method. Thus, it is complicated to simulate the diffractive structure with such refractive index using the modal methods.

A solution has been proposed by Li and Granet by defining a threshold value Δ to predict if a given structure can numerically diverge or not depending of the refractive index of the metal n_c and the surrounding medium n_{sup} and n_{sub} [59]. Therefore, if $\Delta < 0$ the modal methods do not converge. On the other hand, if $\Delta > 0$ or complex, the modal methods correctly converges without any numerical fluctuations.

Nevertheless, Popov suggested to replace the highly conducting metallic layer at the interface by a not-so-highly conducting metal with a thickness equal to the skin depth of the studied metal (typically $20nm - 30nm$) [93]. He applied this algorithm to the differential theory on a lamellar grating. Therefore, he demonstrated that the non-respect of the Li's rule by quickly passing from a real positive permittivity to a pure negative value induces the singularity of the Toeplitz matrix of ϵ . As a result, the fast transition of the permittivity from positive values to a real negative value can be alleviated and the singularity of the Toeplitz matrix can be solved. Therefore, the numerical instabilities disappear. Indeed, as the thickness of the artificial layer is not considered negligible, this proposition suffers from the lacks of accuracy especially when a thin plasmonic surface is used.

Another solution has been demonstrated by Watanabe [116]. He suggested to discretize the core of the modulated zone into several small layers to mitigate the growing exponential functions. Another approaches have been investigated with the FMM, Lyndin et al. used the filtering principle to suppress the spurious high spatial frequencies modes created by the plasmon-like Fourier modes [63]. Other solutions based on the use of Adaptive Spatial Resolution (ASR) and the addition of graded index layers at the metal-dielectric interface have been recently proposed for the FMM method and C-Method [30, 71, 111, 126]. Indeed, the ASR works very well if the real non linear coordinate transformation is the same for all the layers of the profile (lamellar sections).

As far as we know, no previous research investigated this problem with the RCWA-FFF or the DM-FFF when dealing with non-lamellar structure. Thus, an approach inspired by Ref.[71] has been applied to the algorithm of the DM-FFF by adding a nanometric Graded index layer (GIL) at the discontinuous dielectric-metal interface of the structure. For example,

some metallic diffractive structures with purely real and negative permittivity are needed to be simulated for optical security or biomedical applications. Our aim is to compromise between the non-convergence of the method and the accuracy of the obtained results in order to predict the optical response of the structure by numerically modifying the used computational method. This numerical modification solves the problem of divergence and allows to calculate with the minimum loss of accuracy the right response of the structure. Thus, this improvement showed that just few nanometers (0.2 to 2nm depending on the thickness of the metal) of linearly varying graded index layer is sufficient to ensure the stability of the method without the lack of accuracy found in other techniques.

5.2 Implementation of Graded Index Layer (GIL) at the metal-dielectric interface with pure negative and real permittivity metallic gratings

The idea of the GIL rests on the implementation of linearly varying refractive index nanometric layers at the discontinuous dielectric-metal interfaces. In other words, the GIL works as intermediate region between the metal core and the dielectric medium. So, the layer at the discontinuous interface will be replaced by a medium with gradually varying index. As a result, the irregular field singularities will be removed.

In Fig.5.1.(a), a real negative permittivity metallic core is considered for a trapezoidal structure. The field singularity may appear at the internal edges of the structures. Thus, the shadowed regions of the modulated zone of width δ contain the metal-dielectric interface having the transition of the permittivity. Therefore, the GIL layer must be implemented within δ in a manner that within the left and right regions, the real and the imaginary parts of the complex refractive index n_{GIL} are set to change linearly between the refractive index of the metal n_c and the refractive index of the dielectric region n_d .

Indeed, as the structure is discretized into cascaded layers by a constant discretization step D_z , the linear algorithm is applied on each layer of the core by varying w depending on the position of the layer following z . Within δ , the real part of n_{GIL} varies linearly from $\text{real}(n_c)$ to $\text{real}(n_d)$ (Fig.5.1.(b)). On the other hand, the imaginary part of the added layer decreases linearly from $\text{Im}(n_c)$ to $\text{Im}(n_d)$ equal to 0 (Fig.5.1.(c)). Although, for a unit cell between $0 < x < \Lambda$, the equations describing the evolution of the real part of the refractive index of the GIL in each layer can be expressed as,

On the other hand, the imaginary part evolution of the refractive index of the *GIL* can be written as,

$$Im(n_{GIL}) = \frac{Im(n_c) - Im(n_d)}{\delta} \cdot x + Im(n_c) - \frac{Im(n_c) - Im(n_d)}{\delta} \cdot \frac{\Lambda - w - \delta}{2},$$

for $\frac{\Lambda - w - \delta}{2} < x < \frac{\Lambda - w + \delta}{2}$

$$Im(n_{GIL}) = \frac{Im(n_d) - Im(n_c)}{\delta} \cdot x + Im(n_c) - \frac{Im(n_d) - Im(n_c)}{\delta} \cdot \frac{\Lambda + w + \delta}{2},$$

for $\frac{\Lambda - w - \delta}{2} < x < \frac{\Lambda - w + \delta}{2}$

5.3 Application of the GIL on a triangular metallic grating with quasi-real negative permittivity

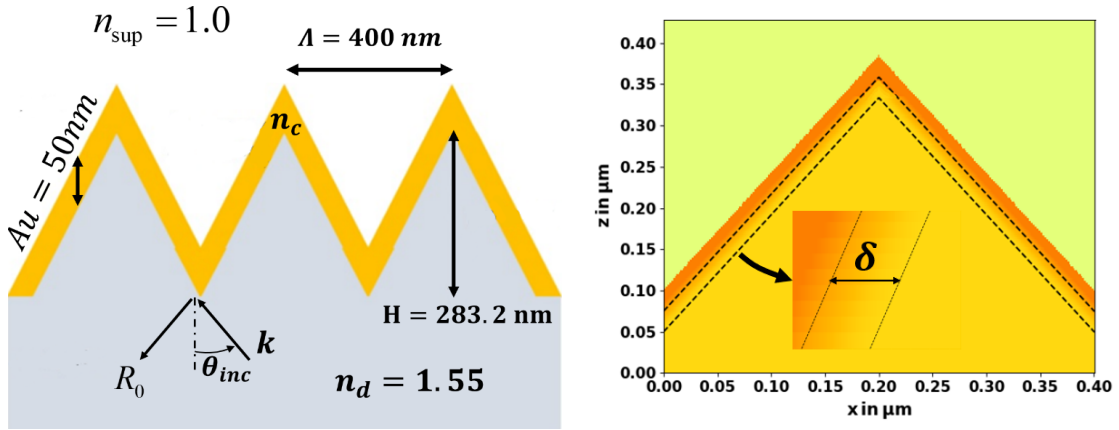


Fig. 5.2 (a) Geometry of the triangular grating: gold core of thickness of 50nm, $\Lambda = 400$ nm. The structure is excited from the substrate with $n_{sub} = 1.55$. (b) Unit cell of the grating with GIL of thickness δ added at the dielectric-metal interface.

To highlight the problem, triangular grating with lossless Au core has been considered. This structure is a special case of the trapezoidal structure considered in the previous section ($w = 0$ and $G = \Lambda$) with $\Lambda = 400$ nm. This geometry induces specific plasmonic resonances that produce high concentration of the electric field at the profile's apices. It is thus highly recommended to simulate it accurately. However, in this case, two difficulties arise: firstly a profile mixing continuous zones and a discontinuous shape and secondly a metal with a low real part of its complex refractive index. Throughout our numerical simulations, the structure was illuminated from the substrate with a TM polarized plane wave at $\lambda = 810$ nm

and $\theta_{inc} = 15^\circ$. At this wavelength $n_c = 0.16 + j5.26$. As the real part of n_c is close to zero, GIL must be added at the glass-Au interface to avoid the field singularity and therefore the numerical divergence of the method.

The zero order of reflection $R_{(0)}$ has been evaluated following the number of harmonics $2N + 1$. The Fourier series of the profile used in the DM-FFF is calculated via a FFT with $N_{FFT} = 8192$ samples. Firstly, the Watanabe solution based on the discretization of the structure with thin discretization steps D_z has been studied without implementing the GIL [116]. Fig.5.3 shows that even the use of thin discretized layer doesn't prevent the non-convergence of the method but shifts the problem into higher truncation order N . Indeed, for $D_z = 1nm$ and without the implementation of the Graded Index Layer, the divergence appears for $N = 44$ (81 harmonics). Moreover, if we decrease D_z from 1.0 to 0.25nm, the numerical instability is red shifted for $N = 50$ for $D_z = 0.5nm$ and $N = 65$ for $D_z = 0.25 nm$. Therefore, to neutralize the numerical fluctuations, teeny discretization steps are needed, which implies a very high execution time and a lack of memory.

Nevertheless, if the GIL is implemented with higher discretization steps, the execution time

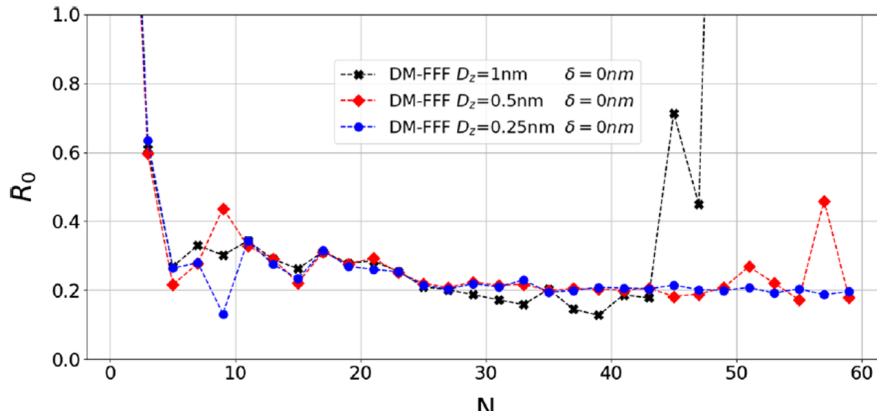


Fig. 5.3 The evolution of the zeroth order of reflection $R_{(0)}$ following N of the triangular Au grating for different discretization step D_z

and the involved memory space stay reasonable. However, the accuracy of the calculated efficiency decreases with the increase of δ . Fig.5.4 shows the same results but with implemented GIL at the internal dielectric metal interface of the triangular grating. The zeroth order efficiency has been studied by varying δ from 1nm to 10nm. However, we can see that without the GIL (black dashed curve with solid X), the DM-FFF risks to diverge for $N = 45$. On the other hand, for $\delta = 1nm$ the method converges quickly from $N > 14$ and stabilizes along the evolution of the truncation order N , ensuring the efficiency of the method and suppressing the numerical instabilities due to the field singularities. In contrast, if δ increases the accuracy of the method decreases. For example an absolute error of 5.2×10^{-2}

is obtained between the value with $\delta = 1nm$ and $\delta = 5nm$ (red dashed curve with solid square). Besides, this error increases to 1.2×10^{-1} if $\delta = 10nm$ (purple dashed curve with solid plus).

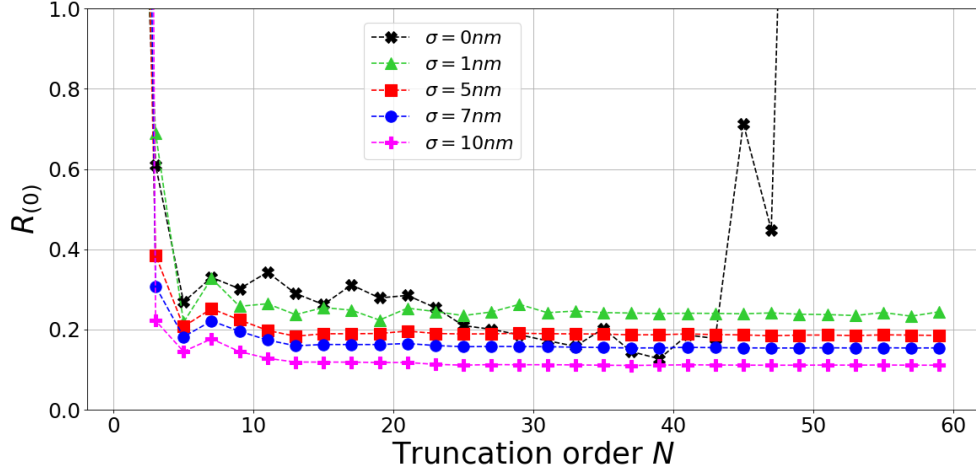


Fig. 5.4 The evolution of the zeroth order of reflection $R_{(0)}$ following N of the triangular Au grating modeled via the DM-FFF for $D_z = 1nm$ and different thicknesses δ of the graded index layer (GIL)

After checking the functionality of the implemented technique, we aim to study the stability and the accuracy of the DM-FFF with GIL compared to the other numerical modal methods. For this reason, few comparisons with the RCWA-FFF, the FMM and the C-Method have been done. We considered the same geometrical parameters of Fig.5.2.(a). Firstly, the structure is now illuminated with a TM polarized plane wave at $\lambda = 810nm$ and $\theta_{inc} = 15^\circ$. The evolution of the zeroth order of reflection $R_{(0)}$ has been evaluated following N . At this wavelength, the refractive index of the metal is $n_c = 0.19 + j4.78$ and as the real part is close to zero the DM-FFF, the RCWA-FFF and the FMM risk to diverge at higher harmonics.

Fig.5.5 presents the evolution of $R_{(0)}$ using the four different methods. If the DM-FFF is used without the add of GIL, the method converges rapidly beyond $N = 15$. But, it also suffers from discrete divergence for $N = 95$ (black dashed curve with solid X). The same case appears with the FMM and the RCWA-FFF. To overcome this problem a graded index layer of thickness $\delta = 1nm$ has been added at the discontinuous interfaces of the triangle for the three mentioned methods. Thus, by just setting this layer thickness at $\delta = 1nm$, the stability is achieved along N for both the DM-FFF, the RCWA-FFF (dashed red curve with solid square and dashed green curve with solid triangle respectively). The zoomed part shows that GIL causes a small degradation of the obtained value. Moreover, it shows the tiny difference between the value of the RCWA-FFF and the DM-FFF. Nevertheless, the

FMM fails to converge and stays unstable with respect to N due to the sharpened apex of the structure. On the other side, the result obtained with the C-Method (blue curve with solid dots) shows that a minimum of $N = 40$ (81 harmonics) is needed to begin the convergence and after $N = 95$, this method diverges again due to the complexity of the structure. Indeed, this result re-affirms the conclusion of the previous section telling us that the DM-FFF is a powerful method for the modeling of complex shaped diffraction gratings.

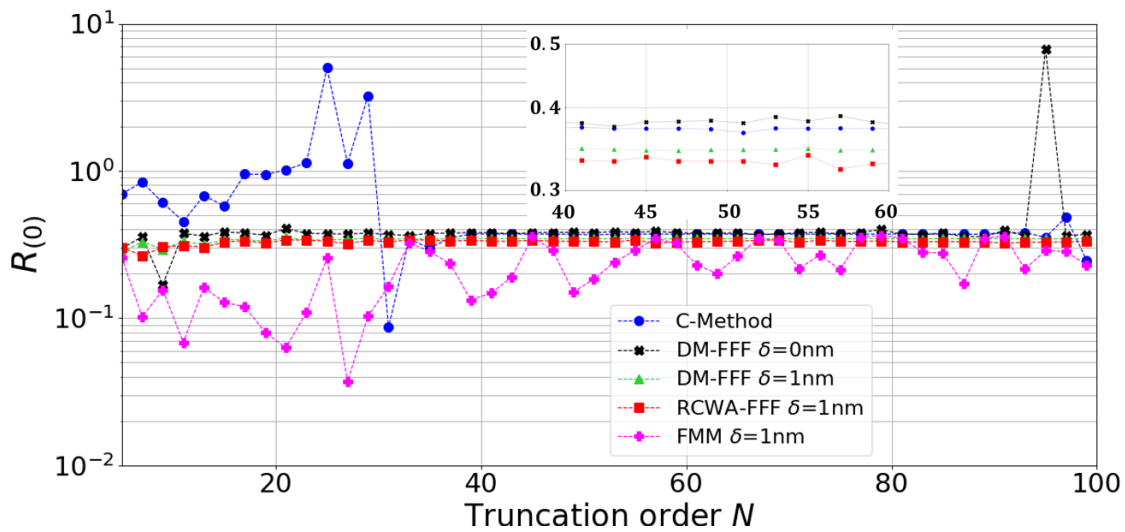


Fig. 5.5 Comparison of the evolution of the zeroth order of reflection $R_{(0)}$ following N of the triangular Au grating between the four different types of modal methods: DM-FFF, RCWA-FFF, FMM, and C-Method

Another interesting example that illustrates the divergence problem is given in Fig.5.6. In this figure, the spectrum of the zeroth order of transmission $T_{(0)}$ has been studied at the same excitation angle and with the same geometrical parameters. A truncation order $N = 50$ (101 harmonics) is used with all methods. If the DM-FFF is applied with $\delta = 0nm$ (blue dashed curve), some numerical instabilities appear at different positions of the spectrum. However, a layer of $\delta = 1.0nm$ is considered sufficient and solves this problem by making the spectrum efficient and stable along λ (red dashed curve with solid asterisk). The small difference between the C-Method and the DM-FFF can be explained by the addition of the GIL added at the dielectric-metal interface and the non-accuracy of the C-Method with such type of discontinuous structure.

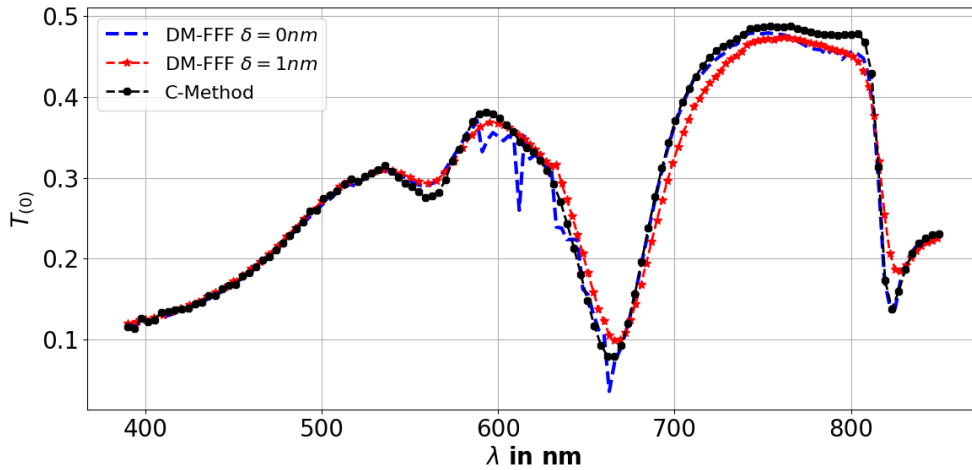


Fig. 5.6 Spectrum of the zeroth order of transmission $T_{(0)}$ for the DM-FFF (with and without GIL) and the C-Method. The values of both methods are calculated for $N = 45$ and $D_z = 1nm$ is used with the DM-FFF

5.4 Conclusion

When a metallic core grating with lossless refractive index is used some numerical instabilities appear inducing the divergence of the method. Indeed, the rapid change in the permittivity doesn't respect the Li's rule. For that, graded refractive index layers (GIL) must be added at the dielectric metal interface to alleviate this change and ensuring the stability of the differential method. Moreover, the thickness of these layers are in the scale of $1nm$. With the Fourier Modal Method, adaptive spatial resolution could be added to decrease the thickness of these layers. But, as the DM-FFF and the RCWA almost deal with non-lamellar structure, the ASR can't be easily applied here due to the need of variable function of the ASR from layer to another. Finally, after solving this problem, the DM-FFF is now ready to be applied to modelize rigorously and accurately any type of 1D metallic or dielectric diffraction gratings under TM or TE polarization.

The work presented in Chap.4 and Chap.5 has been published in 1 scientific journal (A2 of Appendix.D: Springer, Journal of Optical and Quantum Electronics, A.2020, 52(2), p.127.) and presented in one french national conference (C2 of Appendix.D: JNOG 2018, Toulouse, France) and one international conference (B3 of Appendix.D: OWTNM 2019, May 2019, Malaga, Spain).

Chapter 6

DM-FFF applied to visual security structures: A full study

6.1 Introduction

One of the most important applications of the diffraction gratings is the color filters. This type of filters is commonly used for display devices, visual security structures, image sensors and many other applications. However, the theory of producing colors using diffraction gratings is explained in details in Ref.[47] and [20]. Moreover, the grating can be constituted of semiconductors [44, 125], metal [52, 86], polymer [43] or even all dielectric materials [26, 65, 114]. Practically, both transmittance and reflectance color filters may used.

Nowadays and based on the well-known laws of optical waves (interference and diffraction), different families of visual security structures have been appeared. Among all of them the diffractive optically variable devices (DOVIDs) composed of diffraction gratings, commercially known as security holograms, are playing a predominant role in the market of authentication and document security.

Basically, the main role of diffraction gratings is to diffract and split the incident light into several beams propagating in several directions. Moreover, the grating structure can be composed of all-dielectric material or a metal-dielectric combinations. So, the appeared dips or peaks depend on many parameters as the polarization of the incident light, the incident angle, the period of the grating and the involved materials.

Indeed, the physical origins of the reflected or transmitted colors from the hologram belong to multi-types of resonances that appear depending on the material and the opto-geometrical dimensions of the diffraction grating consisting those devices (Rayleigh's anomalies [90, 98, 99, 118, 119], Guided Mode Resonance (GMR) [109, 114, 115], or

the excitation of Surface Plasmon Polariton (SPP) [21, 24, 38, 39, 79, 110]). These resonances induce peaks and dips in the reflection or transmission spectrum of the visible domain ($380nm \leq \lambda \leq 780nm$). As a result, a reflected or transmitted color can be seen by the human eye. In this chapter, the implemented DM-FFF will be used in order to modelize a dielectric visual security device. Only TM polarization will be studied to upraise the FFF.

6.2 Spectrum to color transformation

The color spaces are like all mathematical representation of physical phenomena which can be represented in different ways. Some of them are designed to help human to select color and other are developed to ease data processing of colors in machine. Historically, many color spaces exist. However, the main goal of any space is to minimize the number of variables which describe the space and to maximize the range of coverage of colors.

Indeed, three variables in almost all the color space are considered sufficient to describe the color. For example, in the RGB color space [105], the color is described as an addition of the three colors Red, Green, and Blue. On the other hand, the $L^*a^*b^*$ color space is a space defined by the International commission of illumination (CIE) which describes the color following three values: 1) L^* for the lightness from black (0) to white (100). 2) a^* from green to red 3) b^* from blue to yellow [106]. The XYZ is a color space based on how the human eye perceives the light. It includes all color that are visible to a human-being with an average vision. However, the XYZ letters of this space are analogous to the actual response of the cone cell in the human eye. In 1931, the CIE established a set of three color matching related to the red, green and blue cone cells of the eye [104].

Fig.6.1 illustrates the color matching functions of the eye cone cells. Indeed, the tristimulus values X , Y , and Z can be described through the following equations as,

$$\begin{aligned} X &= \frac{1}{K} \int_{\lambda} S(\lambda)D(\lambda)\bar{x}(\lambda)d\lambda \\ Y &= \frac{1}{K} \int_{\lambda} S(\lambda)D(\lambda)\bar{y}(\lambda)d\lambda \\ Z &= \frac{1}{K} \int_{\lambda} S(\lambda)D(\lambda)\bar{z}(\lambda)d\lambda \end{aligned} \quad (6.1)$$

Where, $K = \int_{\lambda} D(\lambda)\bar{y}(\lambda)d\lambda$ is a normalization factor, $S(\lambda)$ represents either the transmittance or the reflectance spectrum. $D(\lambda)$ is the standard illuminant defined by the CIE which represents the D65 standard that matches with the normal daylight. \bar{x} , \bar{y} , and \bar{z} are the 2° CIE color matching which describes the cone cells of the human eye.

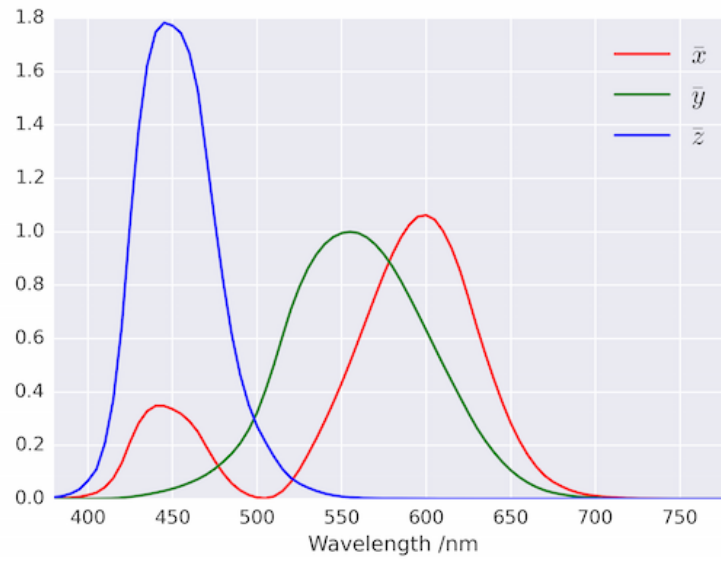


Fig. 6.1 CIE 1931 color matching functions

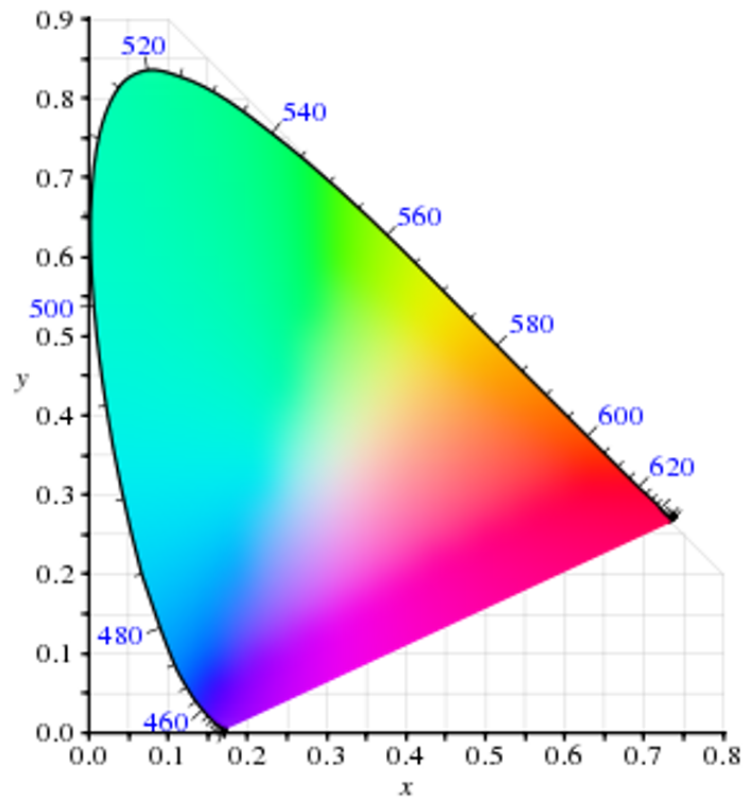


Fig. 6.2 CIE 1931 color space chromaticity diagram known as xy space. The outer numerated boundary is the spectral locus with wavelengths in *nm*.

Moreover, the XYZ parameters can be normalized to form the xy space as,

$$\begin{aligned} x &= \frac{X}{X+Y+Z} \\ y &= \frac{Y}{X+Y+Z} \\ z &= \frac{Z}{X+Y+Z} = 1 - x - y \end{aligned} \quad (6.2)$$

In this form, only two parameters (x and y) are needed to describe the resulting color from the transmittance or reflectance spectrum which are represented on the CIE chromaticity diagram depicted in Fig.6.2.

Further, the conversion of the xy space to the other spaces (RGB, $L^*a^*b^*$, etc..) requires a transformation by an appropriate chromaticity matrix.

6.3 All dielectric structures as a reflection visual security device

6.3.1 Geometry of the structure

The geometry considered throughout this section is depicted in Fig.6.3. It is an all-dielectric diffractive sinusoidal structure associated to a buffer layer with controlled chromatic response and compatible with mass production. The profile of the structure is then defined as $f(x) = \left[\frac{A}{2} + \frac{A}{2} \cos\left(\frac{2\pi x}{\Lambda}\right) \right] + T$ (Fig.6.3.(b)). A is the peak to peak amplitude of the sinusoidal profile and T is the thickness of the buffer layer. The incident medium is assumed to be the air with $n_{sup} = 1$, and the substrate belongs to a homogeneous lossless dielectric layer of SiO_2 with a refractive index $n_{sub} = 1.45$. The grating region is filled with silicon nitride (Si_3N_4) of refractive index n_c , where its dispersion depends on the incident wavelength. Then, the structure is illuminated from the top with TM or TE polarized monochromatic plane wave with an incident angle θ_{inc} . All the chromatic response are calculated following the recommendation of the CIE in the $x - y$ color space. The DM-FFF with $N = 25$, $D_z = 1nm$ and $N_{FFT} = 8192$ samples are used in all the following calculations. Two major factors will be studied, firstly the chromaticity of the color and their gamut while changing a desired opto-geometrical parameter.

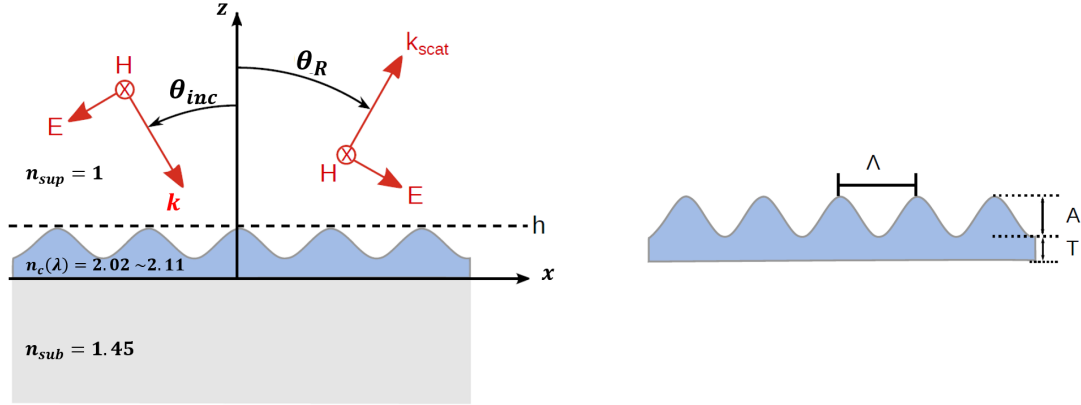


Fig. 6.3 Geometry of the studied structure

6.3.2 The impact of the buffer layer on the chromatic response of the structure

Spectral response

A structure with a fixed period of $\Lambda = 320 \text{ nm}$ is considered. The structure is illuminated with TM polarized plane wave under normal incidence ($\theta_{inc} = 0^\circ$). Due to the periodicity of the structure and the presence of an effective refractive index, such structures support two types of resonances: the rayleigh anomaly and the guided mode resonance (GMR).

In any types of periodic structures, the Rayleigh anomaly occurs at a well-known wavelength when a pass-off of a spectrum of higher order ($order > 0$) appears. Indeed, this resonance depends on the grating period, the incident wavelength and the incident angle. For a p^{th} order this pass-off wavelength can be calculated depending on the following equation,

$$\lambda_p = \frac{n_{inc}\Lambda}{p} (\pm 1 + \sin(\theta_{inc})) \quad (6.3)$$

With, n_{inc} is the refractive index of the incident medium, Λ the period of the grating, and θ_{inc} is the incidence angle of the excited plane wave.

On the other hand the GMR effect is based on the diffraction and interference of the electromagnetic waves inside the sub-wavelengths structures [100]. In other word, the evanescent modes of a diffracted order (reflected or transmitted) can excite one or more guided mode inside the buffer layer. This effect is a result of the reradiated leaky mode of the waveguide when a constructive or destructive zero interference occurs with a transmitted or reflected order. Indeed, a phase matching between the leaky mode of the waveguide $\beta_{x,p}$ and the

diffracted order must be fulfilled in order to excite the guided mode in the buffer layer,

$$\beta_{x,p} = k_{inc} \left(n_{sup} \sin(\theta_{inc}) - p \frac{\lambda}{\Lambda} \right) \quad (6.4)$$

With $\beta_{x,p} = \frac{2\pi}{\lambda} n_{eff}$ is the propagation constant of the guided mode coupled with the evanescent order p , and n_{eff} is the effective refractive index of the guided mode. The condition to excite the guided mode is to have $n_c > n_{eff} > n_{sub} > n_{sup}$.

With such geometry, the modulated region play the role of a waveguide layer even if $T = 0$. Actually, as long as the condition of refractive indices is respected, the modulated region can be seen as a Bragg grating with a given effective index n_{eff} . Thus, this layer can induce a filtering effect due to the phase matching condition of the guided mode resonance. To see the impact of varying the effective refractive index of the grating and the buffer layer, the thickness of the buffer layer has been evaluated for different values. For that, A is considered always constant with $A = 200nm$. And, the thickness T varies between 0 to $200nm$.

Let's start with a brief study of the structure with $T = 0nm$. Ideally, Eq.6.3 tells us that the

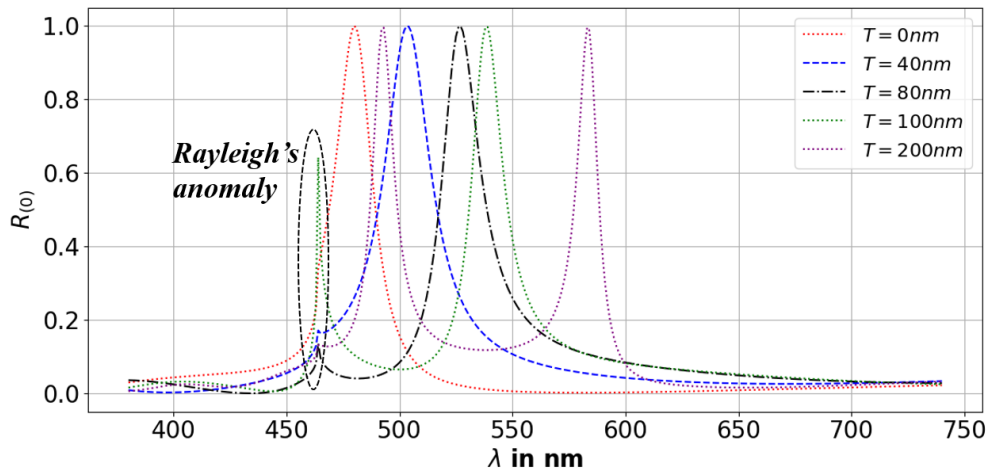


Fig. 6.4 Spectral calculation as a function of the wavelength for the grating of $\Lambda = 320nm$, $A = 200nm$ and variable T . The DM-FFF has been used for the calculation with $N = 25$ and $D_z = 1nm$.

pass-over of the first order ($p = 1$) of the transmission occurs for $\lambda = 464nm$ with normal incidence. Indeed, the reflectance spectrum of $T = 0nm$ (red pointed curve of Fig.6.4) shows that the structure supports two types of resonance : 1) The weak jump relies to the famous Rayleigh's resonance that occur at $\lambda = 464nm$. 2) the wide-band resonance belongs to

the excitation of the guided mode inside the modulated zone. Under proper illumination conditions, this guided mode is coupled and out-coupled along the diffraction grating. The reflectance spectrum presents a maximum at the wavelength that coincides with the guided mode (phase matching condition of Eq.(6.4) is fulfilled). We can mention that, at normal incidence just the propagating guided mode can be excited.

Subsequently, when T increases from 0 to $100nm$, the effective refractive index increases. This growth induces a red shift of the peak of resonance due to the phase matching condition. For example, the peak of resonance of $T = 40nm$ occurs for $\lambda = 503nm$ (blue dashed curve). On the other hand, when $T = 100nm$, this peak appears for $\lambda = 538.5nm$. As long as, the effective thickness of the grating zone supports one mode (monomode), only the fundamental guided mode can be excited inducing one peak in the reflectance spectrum. In contrast, when the mean thickness $H_{mean} = \frac{A}{2} + \frac{T}{2} > 200nm$, the modulated region can support two or more guided modes. Consequently, for $T = 200nm$ (purple dashed curve), and in addition to the Raleigh's peak, two resonances appear which belong to the fundamental TM_0 mode and the TM_1 guided mode ($\lambda = 583.5nm$ and $\lambda = 492.5nm$ respectively).

Chromatic response

T	0nm	40nm	80nm	100nm	120nm	160nm	200nm
R_0	Blue	Green	Green	Green	Green	Green	Light Green
T_0	Yellow	Pink	Pink	Pink	Pink	Pink	Yellow

Fig. 6.5 Color palette obtained from the numerical simulation of $R_{(0)}$ and $T_{(0)}$ at normal incidence with $\Lambda = 320nm$, $A = 200nm$ and variable T .

With reference to Fig.6.5, we can find that the colorfulness of $T_{(0)}$ is low and the color gamut is narrower. This happens because the transmission needs multi-resonances or broader resonances to display high colorfulness colors [22]. In contrast, the numerical evidence shows that when the thickness of the buffer layer varies from 0 to $200nm$, the reflectance spectrum presents a high colorfulness color especially for $T = 0nm$ and $T = 80nm$ (black dashed curve). Nevertheless, when the total amplitude of the grating increases, a pale of the colorfulness appears. This colorless is a result of either the excitation of multi guided modes ($T = 200nm$) or the high reflection of the Rayleigh's anomaly that disturbs the evident reflected color of the guided mode resonance ($T = 40nm$ and $T = 100nm$). From here, we can conclude that the thickness of the buffer layer affect the chromaticity of the reflected color and not the color gamut as all the reflected colors are between blue and green.

6.3.3 Impact of the period on the chromatic response of the structure

Practically, two facts matter in an optical security device: 1) the originality of the structural reflected or transmitted colors. 2) the visible changes of the colors when an opto-geometrical parameter is changed. Indeed, the period of the grating is considered as the major factor to produce a desired structural color. This periodicity determines the wavelength of pass-over of different orders, the phase matching of the guided mode resonance, and the wavelength of the excitation of the surface plasmon polariton if a metallic core grating is considered. For that, studying the impact of varying Λ is a major factor on the reflection spectrum. Moreover, referring to Fig.6.5, the structure with $A = 200nm$ and $T = 80nm$ have been chosen because it is monomode with visible wavelengths, and due to its original structural color response in the reflection region.

Spectral response

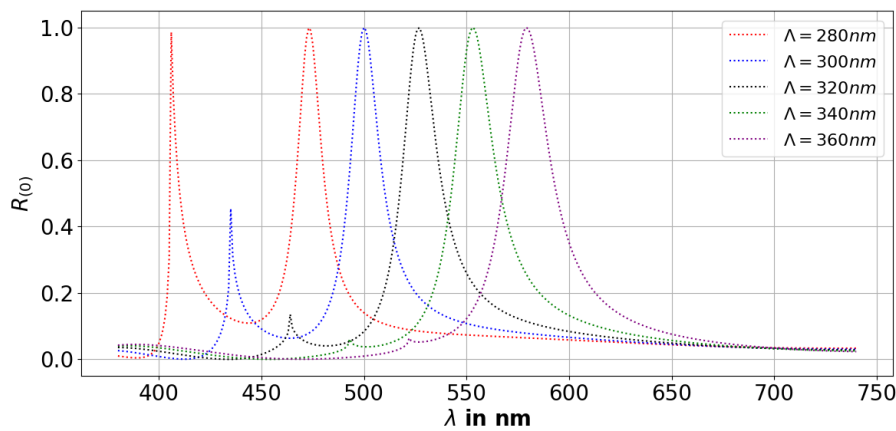


Fig. 6.6 Spectral calculation of $R_{(0)}$ as a function of the wavelength for $A = 200nm$, $T = 80nm$ for different periods Λ .

Always with a TM polarized plane wave excited at normal incidence, Fig.6.6 shows the spectral response of the dielectric grating for different values of Λ . However, as the periodicity increases, the structure supports mainly one resonance. To elaborate more, when Λ increases, the guided modes of the waveguide-like layer are excited and simultaneously decoupled through the grating. With this situation, the guided mode carries the highest part of the energy while the reflected energy of the Rayleigh's anomaly loses its efficiency. Moreover, when Λ increases, the spectrum and the position of resonances are red shifted. The wavelengths of resonance can thus be easily calculated by referring to Eq.(6.3) and Eq.(6.4).

Chromatic response

Λ	280nm	300nm	320nm	340nm	360nm
R_0					
T_0					

Fig. 6.7 Color palette obtained from the numerical simulation of $R_{(0)}$ and $T_{(0)}$ at normal incidence for different values of the period Λ .

Referring to Fig.6.7, the numerical simulations show that the reflected colors cover a large spectral range that goes from blue to red. Moreover, the generated structural colors presents a high colorfulness. Indeed, varying the period gives a wide gamut of reflected colors. So, depending on the prescribed color of the security device or the application, a precised structural color can be selected by varying Λ . We also choose the structure of $\Lambda = 320nm$, $A = 200nm$ and $T = 80nm$ due to its original and non typical chromatic response (olive green).

6.3.4 Impact of varying the amplitude of the grating A

Spectral response

In this section, $T = 80nm$ and $\Lambda = 320nm$ are always considered, while the amplitude A of the sinusoidal region is variable. Under normal incidence and TM polarized plane wave, Fig.6.8 shows the spectral response of the structure when varying A from $40nm$ to $300nm$. Consequently, the variation of A can affect two parameters: 1) the wavelength of excitation of the guided mode resonance. 2) The full width half maximum (FWHM) of the resonance. Those two changes are linked to one physical origin. For example, for $A = 40nm$ (red dashed curve pf Fig.6.8), a single guided mode is excited at $\lambda = 483nm$ with a $FWHM = 3.7nm$. In contrast when, $A = 80nm$ (black dashed curve), the phase matching occurs at $\lambda = 496.5nm$ with $FWHM = 12.7nm$. Moreover, the GMR peaks are red shifted and the FWHM increases with the increase of A . This shift can be explained by referring on the grating law and the GMR law where the phase matching occurs since its proportional to the effective refractive index of the structure. Moreover, when A increases, the diffraction effects increase. Therefore, the loss of the leaky mode increases which induces a larger resonance. Finally, when a large A is chosen, another guided mode can be excited at lower wavelengths. This happens, for example, with $A = 300nm$ (purple dashed curve). In that case, the modulated zone becomes multimode and can support two or more guided modes. To interpret this variation, the effective refractive index of the entire zones has been evaluated for the different values of

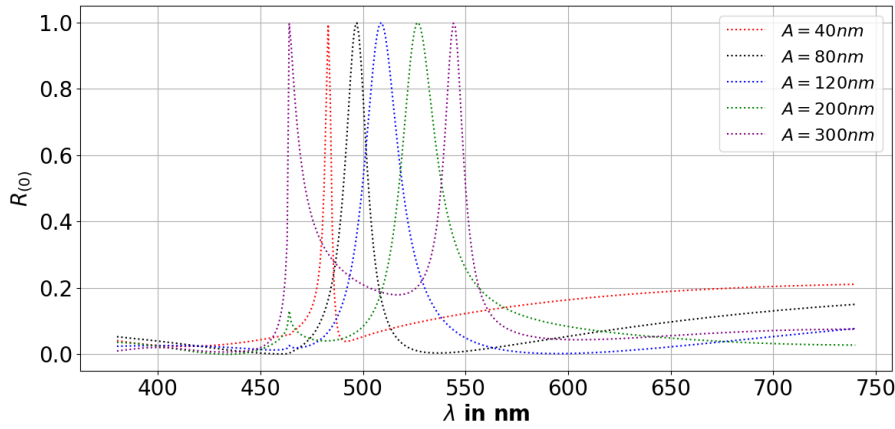


Fig. 6.8 Spectral calculation of $R_{(0)}$ as a function of the wavelength for $\Lambda = 320nm$, $T = 80nm$ for different values of A .

A (Fig.6.9). For that, the entire structure can be replaced by a non-corrugated waveguide of Si_3N_4 sandwiched between the air and a substrate of $n_{sub} = 1.45$. Therefore, an effective width of $\frac{A}{2} + T$ is considered. Using the a-FMM, the evolution of the effective refractive index is then studied following the wavelength λ . Accordingly, this figure shows that when

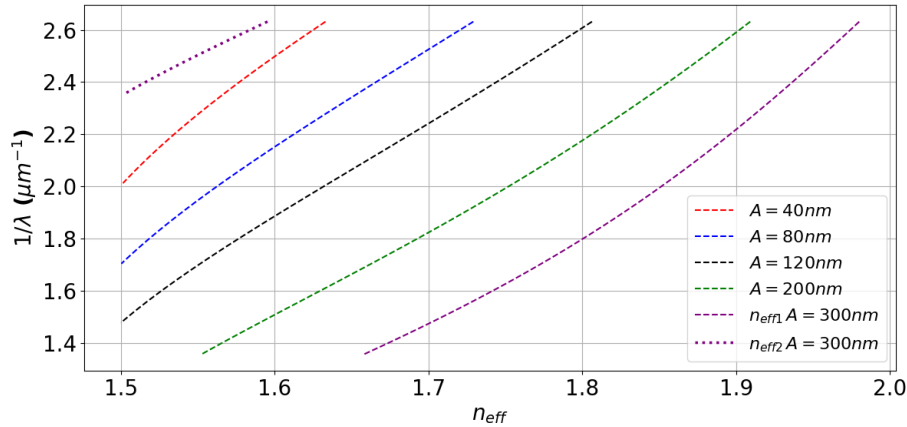


Fig. 6.9 The evolution of the effective refractive index following $1/\lambda$ with $T = 80nm$ and different values of A .

A increases the value of the effective refractive index increases. Indeed, in guided structure, when n_{eff} approaches to the refractive index of the core, the guided mode is more confined and the FWHM is smaller. On the other hand, n_{eff} is directly proportional to $\beta_{x,p}$ of the phase matching equation (Eq.(6.4), thus when n_{eff} increases the wavelength of resonance is shifted to the red wavelengths to keep $\beta_{x,p}$ constant. As mentioned before, when $A = 300nm$,

two effective indices appear which refer to the TM_0 and TM_1 guided modes (purple dashed curve and purple pointed curve respectively).

Chromatic response

A	40	60	80	100	120	140	160	180	200	220	240	300
R_0												

Fig. 6.10 Color palette obtained from the numerical simulation of $R_{(0)}$ at normal incidence for $T = 80nm$, $\Lambda = 320nm$ and different values of A in nm .

Finally, the chromatic response of the reflectance $R_{(0)}$ has been evaluated for different values of A . As depicted in Fig.6.10, for small values of A , almost there is no reflected color due to the high reflection all over the spectrum. In contrast, when $A \geq 80nm$, colors between turquoise and white green appear. The amplitude of the grating affects thus the chromaticity of the color more than the gamut of the reflected color. A high chromaticity and colorfulness of the green is obtained for $140nm \leq A \leq 220nm$. Moreover, the amplitude that reflects the more chromatic green is $A = 180nm$. For that, we will choose this value in order to finally study the most important parameter in an optical security device which is the incident angle θ_{inc} .

6.3.5 Impact of the incident angle θ_{inc}

The most important parameter in the performance of an optical security device is the incident angle. Indeed, the originality of a visual security structure is distinguished by its ability to produce original structural colors under different angles of incidence. Practically, the periodic structures must diffract (transmit or reflect), two original colors between $\theta = 0^\circ$ and 30° to be considered as good visual security structure. With such structures, when $\theta_{inc} \neq 0$, the GMR is characterized carrying two modes: 1) the propagating guided mode (following $+x$) and the anti-propagating guided mode (following $-x$). Those two modes are a result of the propagating effective refractive index $+n_{eff}$ and the anti-propagating effective refractive index $-n_{eff}$. The equations that describe the wavelengths of excitation of the two modes via the phase matching with the leaky mode of a given order p are the following,

$$\frac{\Lambda}{\lambda_{propa}} \cdot \sin(\theta_{inc}) + p = \frac{\Lambda}{\lambda_{propa}} \cdot (+n_{eff})$$

$$\frac{\Lambda}{\lambda_{antipropa}} \cdot \sin(\theta_{inc}) + p = \frac{\Lambda}{\lambda_{antipropa}} \cdot (-n_{eff})$$

To illustrate that, Fig.6.11 shows the spectrum of the zeroth order of reflection $R_{(0)}$. For normal incidence (red dashed curve), $\lambda_{(T0)} = 464nm$ represents the Rayleigh's resonance of the evanescent first order of transmission. Moreover, $\lambda_{g0} = 523nm$ belongs to the excitation of the fundamental propagating guided mode in the modulated region. On the other hand, for $\theta_{inc} = 10^\circ$ (blue dashed curve), Eq.6.3 tell us that the pass-over of the evanescent minus first order of the transmission occurs for $\lambda_{T(-1)} = 408nm$, $\lambda_{T(1)} = 544nm$ for the first order of transmission. On the other hand, Referring to Fig.6.9, assuming that the average effective refractive index $n_{eff} = 1.65$ for $A = 180nm$. Thus, the resonance wavelength of the propagating guided mode appears for $\lambda_{g1} = \frac{\Lambda}{p}(n_{eff} - \sin(\theta_{inc})) = 472nm$ with $p = 1$. Moreover, the resonance wavelength of the anti-propagating guided mode appears for $\lambda_{g2} = -\frac{\Lambda}{p} \cdot (n_{eff} + \sin(\theta_{inc})) = 554nm$ with $p = -1$. Following the same ideology, the position of the resonances can be predicted for the other values of the incident angles. While analyzing

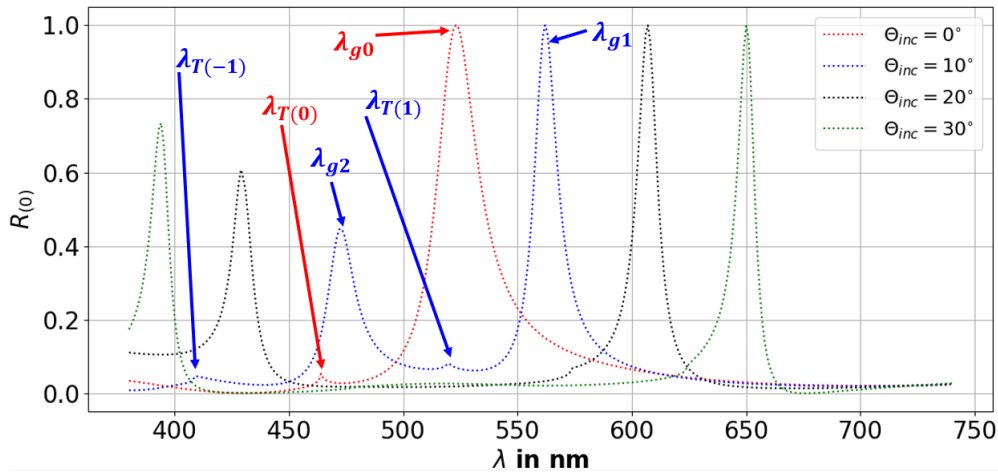


Fig. 6.11 Spectral response of the dielectric structure with $T = 80nm$, $A = 180nm$, $\Lambda = 320nm$ for different incident angles θ_{inc} .

a periodic structure with propagating modes, it is important to present the modal dispersion of modes in function of the wavelengths for example. For that, what's called the band diagram can describe the evolution of the modes, its absorption, reflection or transmission coefficients with respect to the wavelengths and k_z (the projection of the wavevector on the propagation axis z). Thus, to validate our analysis, the band diagram of the chosen structure has been presented in Fig.6.12. Three regions can be distinguished in the band diagram: 1) above the light cone of the superstrate ($k_z = \frac{2\pi}{\lambda}n_{sup}$) where the propagating modes can be excited via plane waves (Region of our interest in this chapter), 2) Under the light cone of the substrate ($k_z = \frac{2\pi}{\lambda}n_{sub}$) where only the guided modes can be excited, 3) between the two cones where the propagating modes can be excited via evanescent coupling. Indeed, for

$\theta = 0^\circ$, the replication of the first order and the minus first order of transmission produces a band gap, which can excite the Rayleigh's anomaly at $1/\lambda = 2.15\mu m^{-1}$. On the other hand, the dispersion of the guided mode excited via the plane wave constitute another band gap for $1/\lambda = 1.92\mu m^{-1}$ producing the famous guided mode resonance. Moreover, all the resonances of the different incident angles can be demonstrated by following the same ideology.

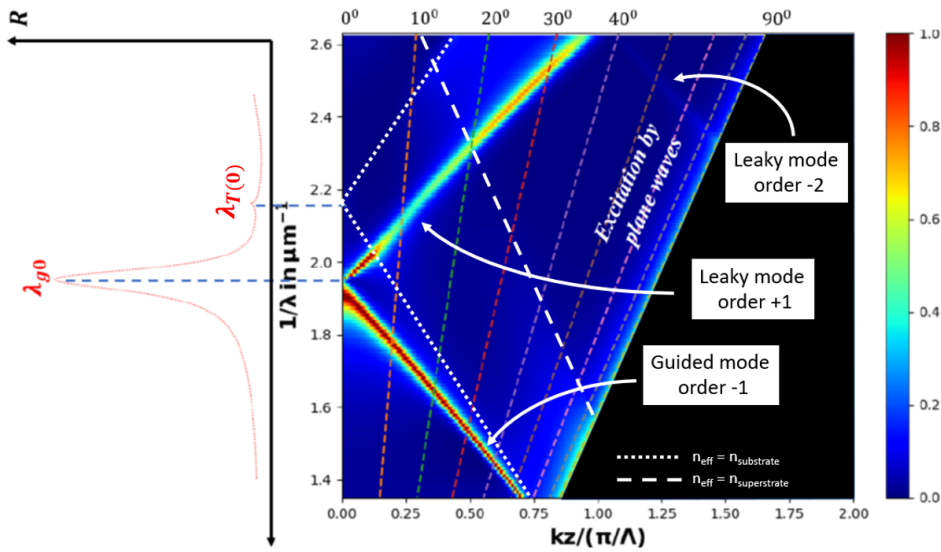


Fig. 6.12 Band diagram of the sinusoidal GMR structure with $T = 80nm$, $A = 180nm$ and $\Lambda = 320nm$. The colored straight line represents the different incident angles θ_{inc} . The left sided spectrum belongs to the reflection spectrum of the chosen structure with $\theta_{inc} = 0^\circ$.

Chromatic response

θ°	0	10	20	30
R_0				

Fig. 6.13 Chromatic response of the final chosen structure for different incident angles θ_{inc} .

The chromatic response of the dielectric GMR structure is depicted in Fig.6.13. Always, the spectrum to color conversion of section.7.2. is used to illustrate the color in the xy space. Indeed, a wide gamut can be covered by this structure in the practical incident angles of a visual security device (between 0° and 30°). Now, when the structure is illuminated with a white light source (bulb, sunlight,...), the front end user will perceive a green olive color for normal incidence. Moreover, when the structure is pulled down to 10° , a less colorfulness

green will be seen. The interesting effect happens, when θ_{inc} increases to 20° . At this stage, a rose purple color will be reflected and seen by the human eye. Moreover, this color stays in the range of pink red for $\theta_{inc} = 30^\circ$. The transition from olive green to the red color respects well the prerequisite condition of the slow transition of color with a wide gamut of color change. Thus, we believe that this structure could represent an interesting reflection visual security device due to its original reflected colors, the facility of fabrication, and the complexity of the physical origins of the formed structural colors.

6.4 Use of the DM-FFF for the inverse tailoring of structural color

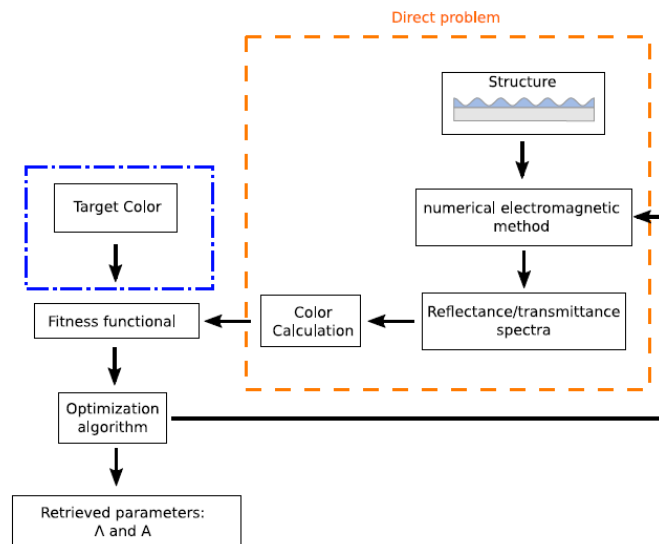


Fig. 6.14 Stages of the inversion scheme proposed to retrieve the geometrical parameters of a desired chromatic response

With a joint work between us and our colleagues in the laboratory of Light, nanomaterials and nanotechnologies (L2N) in Troyes-France, an all-dielectric structure almost similar to the previous one has been investigated to tailor the chromatic response of the all-dielectric grating using inverse problem [26]. This work has been inspired from Ref.[64]. Moreover, the same grating of Fig.6.3 has been considered. Furthermore, the algorithm of the inversion scheme is depicted in Fig.6.14.

The first step is the direct problem (dashed red box). Here, the reflectance and transmittance spectrums of randomly generated opto-geometrical parameters are calculated via the DM-FFF. After that, the respective tristimulus value of the XYZ space are calculated via Eq.(6.2). The

next stage is based on the comparison of the calculated color with the one to be reproduced (blue point-dashed box). Finally, this process is repeated until the minimum/ maximum difference between the target and the iteratively generated colors has been found. Indeed, to tailor a desired reproduced color, the color difference ΔE must be calculated. This parameter belongs to the difference between two colors defined in CIE $L^*a^*b^*$ space. For that, a transformation from XYZ space to the $L^*a^*b^*$ color space must be performed. It is important to mention that a $\Delta E < 2.3$ is indistinguishable for the human eye [66]. Thus ΔE is given by,

$$\Delta E = \sqrt{(\Delta L)^2 + (\Delta a)^2 + (\Delta b)^2} \quad (6.5)$$

With $\Delta L = L^{target} - L^{calc}$, $\Delta a = a^{target} - a^{calc}$, $\Delta b = b^{target} - b^{calc}$ of the calculated transmission or reflection spectrum by the DM-FFF. Finally, by using a neural network and the swarm optimization method (PSO) [46], the prediction of the opto-geometrical parameters of the structure that reproduces a desired structural color can be automatically done.

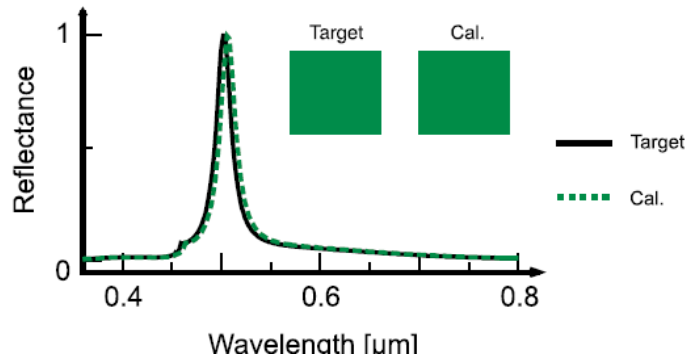


Fig. 6.15 Stages of the inversion scheme proposed to retrieve the geometrical parameters of a desired chromatic response

To illustrate that, the tropical rain forest color depicted in Fig.6.15 has been taken as an example. In the $L^*a^*b^*$, this selected color has $L = 51$, $a = -47.9$ and $b = 26.4$. After searching the optimal solution, the parameters retrieved in Table.6.1 are almost similar to the ideal ones. Moreover, $\Delta E = 1.3$ has been found which is less than the distinguishable criterion $\Delta E < 2.3$.

Parameters	Λ (nm)	A (nm)
Target	320	300
Retrieved	319.4 ± 6.6	293 ± 12

Table 6.1 Target and Retrieved Geometrical Parameters Related to the Tropical Rain Forest Depicted in Fig.6.15

6.5 Conclusion

In this chapter, a detailed study of a reflection visual security device has been done. The structure corresponds to an all dielectric structure which gives interesting visual effect. The mixing of two physical effects gives a wide range of freedom to manipulate the diffracted color. Due to all interpretations, we found that the most important parameter to have a wide gamut under normal incidence is the period Λ . The other parameters (A , T) can affect the colorfulness of the reflected color. Moreover, the GMR resonance can be optimized by changing the thickness of the waveguide layer (buffer layer) by the coupling of one or more guided modes.

Consequently, more complex diffraction grating may be studied, from metallic gratings inducing plasmonic effects into the continuous, discontinuous or/and structures mixing continuous part with discontinuous geometries. However, our industrial collaborator, SURYS, uses the roll to roll technology for mass production of visual security devices. With this technique, the change of the thickness of the structure is considered difficult of the same wafer. Nevertheless, different gratings with different periods Λ can be realized on the same wafer which can be realized with their platforms.

Due to the code developed in Python and the spectrum to color conversion. I contributed as a co-author in the work published in one international journal (A3 of Appendix.D: . Applied optics, 57(14), pp.3959-3967.) and presented in one international European conference (B4 of Appendix.D: EOSAM2018, Oct 2018, Delft, Netherlands.).

Part II

Electromagnetic Numerical Tools for the propagation of light in guided structures

Chapter 7

DM-FFF applied to optical guided structures: Theoretical interpretation

In this chapter, a reformulation of the differential theory associated with Fast Fourier Factorization used for periodic diffractive structures is presented. This reformulation allows the rigorous modeling of non-lamellar guided structures by preventing the problem of the staircase approximation of the aperiodic Fourier Modal Method (a-FMM).

7.1 Introduction

The rapid growth in the domain of integrated optics has compelled researchers and engineers to step up their efforts in the development of more rigorous and accurate electromagnetic numerical methods dedicated to the modeling of optical guided structures (microresonators, optical filters, plasmonic structures,...). A photonic guided structure is often an open structure, composed of guided layers sandwiched between two semi-infinite half space and homogeneous zones so-called the superstrate and the substrate. At this scale, the outgoing wave conditions in the homogeneous zone must be respected by absorbing the outgoing waves and preventing their reflections. Indeed, to fulfill these conditions, Perfect matching layer has been introduced firstly by J-P Berenger [4]. The concept of PML is based on the implementation of absorbing layer around the guided structure. The role of these layers is to achieve a highly absorbing boundary conditions at the edge of the structure by absorbing the electromagnetic waves without any reflection. Thus, PML are considered as artificial absorbing layers for wave equations. It is a commonly used technique to respect the boundary conditions in guided structures for different electromagnetic numerical methods as the Finite Element Method (FEM) [28], and the FDTD [78], to modelize problems with open boundary.

In 2001, this concept has been proposed to the Fourier Modal Method (FMM) allowing the modelization of an open photonic structure using the grating theory [103]. This concept is based on the association of complex coordinate transformation playing the role of PML to the propagation equations of the FMM turning the method into an aperiodic method so-called aperiodic Fourier Modal Method (a-FMM) [36]. This theory features improvements of the existing methods in terms of convergence speed and accuracy. But, the a-FMM is considered accurate as long as lamellar structures are considered (structures with rectangular sections). For that, the evolution of the core waveguide profile along the propagation axis z is characterized by cascaded rectangular layers describing the overall structure. Indeed, each layer is defined by a specific refractive index profile of the waveguide following the transverse axis and the propagation axis. Unfortunately, a photonic device is normally composed of continuous refractive index evolution. In that case, the a-FMM will discretize the structure with the lamellar condition which doesn't rigorously belong to the guided structure. Indeed, the boundary conditions risk not to be respected specifically in TM polarization case. This problem is well known in the grating theory for the modelization of continuous refractive index grating profile [96]. Consequently, under this polarisation the aperiodic FMM can suffer from slow convergence and lack of accuracy especially for high refractive index contrast structure (dielectric or metallic). By now, the only way to tackle this problem is to use hybrid method as Finite Element Method (FEM) for continuous section and aperiodic FMM for lamellar sections[35, 50]. The DM-FFF takes the evolution of the grating profile. Moreover, this method also prevents the problem of staircase approximation. It demonstrated a faster convergence and a better accuracy by respecting the boundary condition of each discretized layers (Chapter 3 and 4). However, by now this method is essentially applied to diffraction grating problems. So, the input and output layers are composed of homogeneous zones and driven by plane waves.

The use of the methods based on the harmonic decomposition of respectively the fields and the permittivity evolution brings many advantages to modelize the integrated optics structures. Indeed, those methods are bidirectional. Moreover, all modes can be taken into consideration (guided, evanescent and diffracted). And, a wide range of material can be chosen by introducing a complex permittivity or permeability (anisotropic medium, magnetic material, lossy,...). For that, as the DM-FFF is a Fourier based method that prevents the staircase approximation of the FMM, the idea was to reformulate the differential theory of grating to be adapted with the modelization of integrated optic devices. This reformulation is based on two facts: firstly, a complex coordinate transformation of type Hugonin-Lalanne playing the role of PML must be associated to the propagation equations of the DM-FFF in order to neglect the incoming and outgoing waves of the neighboring cell [36]. Secondly, a

in TM polarization, the transient system of Maxwell's equations has been already described in the equations (3.1a) and (3.1b). The materials used are always considered isotropic and non magnetic in this chapter.

Our aim is to solve the previous mentioned equations of propagation while satisfying the outgoing wave conditions of an open structure in Region I and Region II using the differential method used in grating theory. To fulfill the outgoing conditions, an analytical continuation of the fields E_x and H'_y will be defined in a suitable complex plane so that the incoming wave in Region I and Region II are strongly attenuated. This fact will be performed by associating a simple complex coordinate transform to the propagation equations (3.1a) and (3.1b) that allow one to map this infinite complex plane into a bounded segment of a new real space. Thus, the complex coordinate transformation play the role of perfectly matched layers (PML) by suppressing the incoming and outgoing waves of the neighboring cell.

7.2.2 Perfectly Matched Layer as non-linear complex coordinate transformation

Introduction

Generally, PML are described as graded constant to minimize the material contrast reflection [18, 68]. In their paper [37], Hugonin et al. have demonstrated that by fulfilling the outgoing wave conditions of the propagation equations in the boundary zone (Region I and Region II), an infinite complex space can be mapped through a finite plane by applying a complex coordinate transformation playing the role of PML. In other words, a new complex space X composed of two semi-infinite complex domains X_I and X_{II} and a real space $X_{III} = x$, mainly in the substrate and superstrate zones, will be introduced. Consequently, instead of dealing with Eq.(3.1).(a) and Eq.(3.1).(b) in $x \in]-\infty, +\infty[$, the propagating fields will be calculated in the new complex coordinate system $X \in]-\infty - j\infty, +\infty + j\infty[$. Thus, the integration of the differential equations will be conducted in X , which is mapped in a new finite and bounded space (x') of period Λ , where $-\frac{\Lambda}{2} \leq x' \leq \frac{\Lambda}{2}$. It is thus represented by the unit cell of periodic grating in the artificial periodized space x' .

Cartesian function of the coordinate transformation

To be associated to the differential theory, this transition can be performed by integrating a non-linear complex coordinate transformation $X = F(x')$, to the system of the periodic structure, by artificially periodizing the guided structure as depicted in Fig.7.2. The aim of

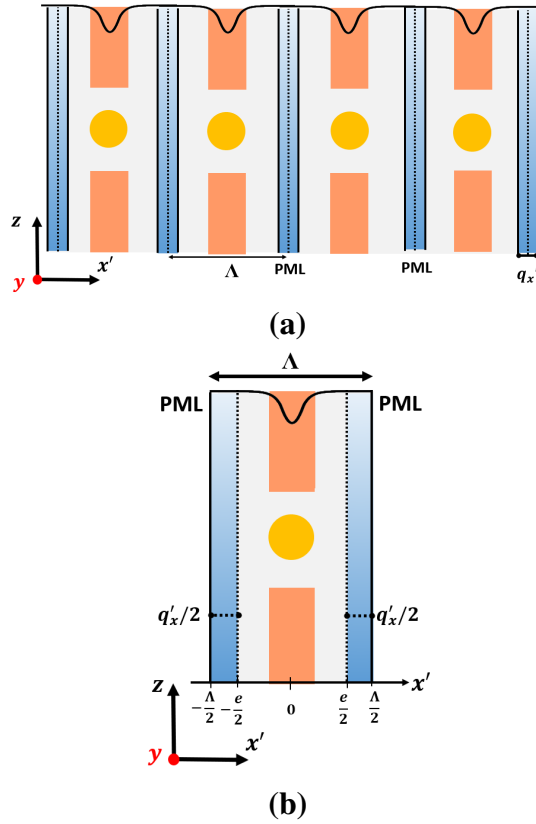


Fig. 7.2 Non linear transform for modeling a 2D infinite structure in a bounded finite space (a) Artificial periodized structure with period Λ bounded in imaginary space ($X \in [-\infty - j\infty, +\infty + j\infty]$.) after applying a complex coordinate transformation. (b) Unit cell of the artificially periodized structure bounded in ($x' \in [-\frac{\Lambda}{2}, +\frac{\Lambda}{2}]$). q_x' represents the total thickness of the PML. $e = \Lambda - q_x'$ is the thickness not affected by the PML. The structure is excited with a guided mode. The input and output waveguide core refractive index is n_g . The cylindrical reflector refractive index is n_d . The superstrate and the substrate are two homogeneous zones of refractive index n_{ext} .

the stretching of the bounded space is to strongly suppress the electromagnetic fields near the boundaries of the unit cell turning it into an isolated cell instead of periodic cell. An analogy can be done here between the PML and the anechoic chamber used for the study of antenna radiations where the boundaries absorb the incident fields without inducing a new reflection on its surface.

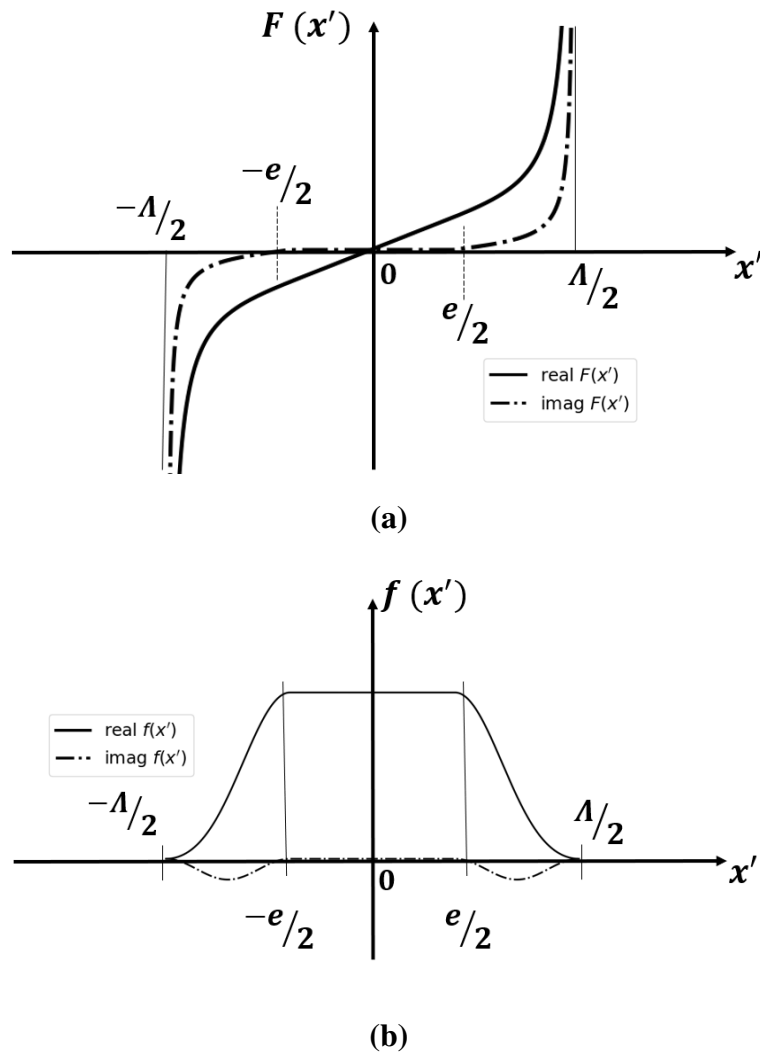


Fig. 7.3 Non-Linear coordinate transformation (a) the complex coordinate transformation $X = F(x')$ for $\gamma = \frac{1}{1-j}$ (b) its derivative $f(x')$ with respect to x' .

Generally, for an open boundary problem illuminated by a polarized guided mode, the outgoing wave condition implies that $H_y(x, z)$ and $E_x(x, z)$ must tend to zero far away from the guided zone of the structure. Under this condition, the open problem of Fig.8.1 can be replaced by an artificially periodized guided structure (Fig.7.2.(a)) where the stationary fields $E_{x'}(x', z)$ and $H_y(x', z)$ are strongly suppressed at the boundaries of each cell due to the complex coordinate transformation.

Indeed, several coordinate transform can be investigated. The same coordinate transformation $F(x')$ proposed in Ref.[37] is used. Other coordinate transformations are available but the previous one is efficiently enough in terms of accuracy and convergence speed. Moreover, it is motivated by its easy implementation in Fourier space and has been inspired by a

previous work that calculates the bounded modes of rectangular core waveguide [33]. Thus, to implement the coordinate transformation in the propagation equation, the derivative of the coordinate transformation functions $f(x') = \partial X / \partial x'$ must be defined.

Consequently, it is presented in Fig.7.3 the coordinate transformation $F(x')$ and its derivative $f(x')$ along one period Λ of the new coordinate system x' . Indeed, at the boundary of the unit cell $x' = \pm \frac{\Lambda}{2}$, the real and imaginary part of the coordinate transformation $F(x')$ tends to $\pm\infty + j\pm\infty$. As a result, the fields at the boundary of each cell are strongly attenuated due to the stretching following the periodicity axis x' . Nevertheless, the equation describing the complex coordinate transformation is expressed as follows,

$$F(x') = x' \text{ for } |x'| < e/2$$

$$F(x') = \frac{x'}{|x'|} \left(\frac{e}{2} + \frac{q_{x'}}{\pi(1-\gamma)} \left[\left(\pi \frac{|x'| - e/2}{q_{x'}} \right) - \frac{\gamma}{\sqrt{1-\gamma}} \tan \left(\pi \frac{|x'| - e/2}{q_{x'}} \right) \right] \right), \quad (7.1)$$

$$\text{for } e/2 < |x'| < \Lambda/2$$

Where, $e = \Lambda - q_{x'}$, $q_{x'}$ is the total thickness of the PML ($q_{x'}/2$ from each side) and $\gamma = \frac{1}{1-j}$. Thus, referring to Eq.7.1, the new coordinate system $X = F(x')$ can be simply describes as,

$$F(x') \text{ is real for } |x'| < e/2$$

$$F(x') \rightarrow +\infty + j\infty \text{ for } x' = +\Lambda/2$$

$$F(x') \rightarrow -\infty - j\infty \text{ for } x' = -\Lambda/2$$
(7.2)

Under the above conditions, the open problem can be replaced by an artificially periodized structure where the stationary fields $H'_y(x', z) \rightarrow 0$ and $E_{x'}(x', z) \rightarrow 0$ at the boundaries of each cell. In contrast, far away from the edges of the unit cell, the electromagnetic fields correspond to their real representations, and exactly follow the desired propagation of an open boundary structure.

As mentioned before, to express Eq.(7.3) in the new coordinate space, only the derivative $dx'/dX = f(x') = dF/dx'$ is needed. So, this function is given by,

$$f(x') = 1, \text{ for } |x'| < e/2$$

$$f(x') = \left[1 - \gamma \sin^2 \left(\pi \frac{|x'| - e/2}{q_{x'}} \right) \right] \cos^2 \left(\pi \frac{|x'| - e/2}{q_{x'}} \right),$$

$$\text{for } e/2 < |x'| < \Lambda/2$$

Thus, in order to express Eq.(3.1a and 3.1b) in the new coordinate system, each $\partial/\partial x$ in Eq.(3.1a and 3.1b) has to be replaced by $f(x') \partial/\partial x'$. Hence, the new propagation differential system that sustains the complex coordinate transformation can be expressed as,

$$\begin{cases} \frac{\partial E_{x'}}{\partial z} = jH'_y + jf(x') \frac{\partial}{\partial x'} \left(\frac{1}{k^2} f(x') \frac{\partial H'_y}{\partial x'} \right) \\ \frac{\partial H'_y}{\partial z} = jk^2 E_{x'} \end{cases} \quad (7.3)$$

Actually, this approach has been implemented to the Fourier Modal Method by Hugonin et al. [36]. Nevertheless, the aperiodic FMM (a-FMM) suffers from staircase approximation while modeling profiles with continuous evolution along the propagation axis, (trapezoidal tapers, micro-disks, ...) [2, 13]. For that, only lamellar profiles are requested to reach accurate results with the a-FMM. Thus, the idea was to reformulate the differential theory associated with Fast Fourier Factorization of Chapter 3, in order to modelize and simulate more rigorously the non-lamellar photonic waveguide structures, instead of diffractive gratings, which we call the aperiodic DM-FFF (a-DM-FFF). Furthermore, as long as there is no growing exponential, the outgoing wave conditions are fulfilled, and electromagnetic fields very close to zero are expected at the boundaries of each cell when using a sufficient truncation order N .

7.3 Formulation of the aperiodic DM-FFF (a-DM-FFF)

7.3.1 Propagation equation in TM polarization

The aim of this section is to establish a set of equations suitable for the electromagnetic numerical resolution of 2D arbitrary shaped guided structure. The DM-FFF is a well known modeling method used in grating theory. But, turning this method into the simulation of guided structures is not treated before.

As mentioned in Chapter 3, the differential theory belongs to the Fourier base family. This family is characterized by expanding the electromagnetic fields and the permittivity distribution into a truncated Fourier series, in the new mapped space x' , following the truncation order N [10, 73]. However, in the new coordinate system x' , the generalized Fourier series of the electromagnetic fields $E_{x'}$, H'_y , and the permittivity distribution ε_r

following the artificial periodization axis x' can be expressed as,

$$\begin{aligned} E_{x'}(x', z) &= \sum_{n=-N}^{n=+N} E_n(z) e^{jnKx'} \\ H'_y(x', z) &= \sum_{n=-N}^{n=+N} H'_n(z) e^{jnKx'} \\ \epsilon_r(x', z) &= \sum_{n=-N}^{n=+N} \epsilon_n(z) e^{jnKx'} \end{aligned} \quad (7.4)$$

With $K = \frac{2\pi}{\Lambda}$, and E_n, H'_n, ϵ_n are the Fourier coefficient of the harmonic n , of the electric fields $E_{x'}$, the magnetic field H'_y , and the medium permittivity ϵ_r respectively. The harmonic vector notation can be used to describe the $(2N + 1)$ Fourier coefficients $[E_{x'}], [H'_y], [E_z]$, and $[\epsilon]$ with $[E_{x'}] = [E_{-N}, \dots, E_0, \dots, E_N]$, $[H'_y] = [H'_{-N}, \dots, H'_0, \dots, H'_{+N}]$ and $[\epsilon_r] = [\epsilon_{-N}, \dots, \epsilon_0, \dots, \epsilon_{+N}]$. Referring to Eq.(7.3), the Fourier space system of the $4N + 2$ coupled differential equations of the a-DM-FFF can be extracted from Eq.3.22. Indeed, this system takes into account the evolution of the profile, and describes the propagation of electromagnetic field in open boundary structure in TM polarization,

$$\begin{cases} \frac{\partial [E_x]}{\partial z} = -j[[f]]KQ_{zz}^{-1}Q_{zx}[E_x] + j(I_d - [[f]]KQ_{zz}^{-1}[[f]]K)[H'_y] & (7.5a) \\ \frac{\partial [H'_y]}{\partial z} = (jQ_{xx} - jQ_{xz}Q_{zz}^{-1}Q_{xz})[E_x] - jQ_{xz}Q_{zz}^{-1}[[f]]K[H'_y] & (7.5b) \end{cases}$$

With, K is a diagonal matrix where $K_{ij} = (-N + i)\frac{2\pi}{\Lambda}\delta_{ij}$ with δ_{ij} is 0 for $i \neq j$ and 1 for $i = j$. $[[f]]$ the Toeplitz matrix of the complex coordinate transformation $f(x')$ where its Fourier transformation f_n is defined in Appendix.B. The other parameters of the system are defined in the Eq.(3.22) of Chapter 3. As a result, this last equation can be simplified into a set of $4N + 2$ first-order differential equations written in two block matrices form:

$$\frac{\partial}{\partial z} \begin{bmatrix} [E_{x'}] \\ [H'_y] \end{bmatrix} = jM(z) \begin{bmatrix} [E_{x'}] \\ [H'_y] \end{bmatrix} \quad (7.6)$$

7.3.2 Propagation equation in TE polarization

Following the same methodology of TM polarization, the complex coordinate transformation can be applied to the propagation equation of each discretized layer s . Thus, each $\partial/\partial x$ will be replaced by $f(x')\partial/\partial x'$. Therefore, in the Fourier space, the system of equations that

describes the propagation of the transverse electromagnetic fields can be expressed as,

$$\begin{cases} \frac{\partial [E_y]}{\partial z} = -j[H'_x] & (7.7a) \\ \frac{\partial [H'_x]}{\partial z} = j([\mathbb{f}][K][\mathbb{f}][K] - [k^2]) [E_y] & (7.7b) \end{cases}$$

The system of Eq.(7.7) can be written as a system of $2(2N + 1)$ coupled differential equations representing the electromagnetic fields propagating in TE polarization of the guided photonic structure,

$$\frac{\partial}{\partial z} \begin{bmatrix} [E_y] \\ [H'_x] \end{bmatrix} = M(z) \begin{bmatrix} [E_y] \\ [H'_x] \end{bmatrix} \quad (7.8)$$

Following the same methodology of the grating theory, the aperiodic DM-FFF discretizes the artificially periodized structure into s layers by a constant discretization step D_z . As long as we stay in the medium that sustains this transformation, the cascade of S matrices follows the same rules as Chapter 3.

Although, in the differential theory of grating, the matrix Ψ of section 3.1.5 allows the transition from the stationary field to the forward and backward representations of the field in the different layers from one side (by introducing the infinitely thin layers between the sections), and describes the propagating fields in the input and output homogeneous layers (the superstrate and the substrate) from the other side. From this transition matrix, the propagation matrix $P^s = \Psi_{sup} T^s \Psi_{sub}^{-1}$ of the layer s can be determined. Nevertheless, in case of a guided photonic structure, the input and output layers are no longer homogeneous, and the excited mode is not a plane wave but a guided mode. Therefore, the i/o layers are now represented by a given evolution of permittivity following z (input/output waveguides). In that case, and if the classical Ψ matrices are used two problems arise:

1. The i/o waveguides come out on homogeneous medium. Thus, the guided mode will suffer from diffraction and reflection at the input and the output of the waveguide. For example, if silicon waveguides are considered as the input and output waveguides of Fig.8.1, and the Ψ matrix describes the propagating fields in the air, Fabry-Perot effects will appear inducing dips and peaks of the transmission or reflection coefficients. This case is close to the practical real case. But, the access guides are generally longer which reduces strongly the free spectral interval.
2. The eigen modes of the homogeneous medium surrounded by PMLs are no longer the plane waves. Indeed, the eigenvectors are slightly different. If we absolutely want to

use the the plane waves issued from a cell without PML, a coordinate change should be performed at the input and output interfaces. This transition generally requires a calculation with an FFT which induces errors.

To tackle this problem, two solutions can be implemented. Thus, we will begin with the first solution based on the representation of the Ψ matrix in a form where the eigen field of the guided mode is represented in terms of the eigen distribution of the effective refractive index of the i/o layers.

7.3.3 Input/Output Ψ as an equivalent guided zone

Formulation of the Ψ matrix in TM polarization

This situation resembles to the one used by the a-FMM except that this latest one gives directly the access to the Eigen modes of the guided structure in transmission and reflection. For simplicity reason, two identical waveguides are considered for the input and output zones. Moreover, the fundamental guided mode is chosen to excite the monomode input waveguide. Indeed, this eigen mode can be described by a Fourier series, where the harmonic vectors belong to the guided electric field E_g and the guided magnetic field H'_g associated to the eigen value $\beta_{eff} = \frac{2\pi}{\lambda}n_{eff}$. In that case, the relation between the forward and backward electric field and the magnetic field of the harmonic n can be written as,

$$\begin{aligned} E_{g,n}^+ &= \frac{\beta_{eff}}{k^2} H_{g,n}'^+ \\ E_{g,n}^- &= -\frac{\beta_{eff}}{k^2} H_{g,n}'^- \end{aligned}$$

E_x and H'_y are always the transverse fields. At this stage, a new transition matrix Ψ_g is proposed to be used which represents the eigen mode of the waveguide. As the structure is reciprocal, $\Psi_0 = \Psi_h = \Psi_g$. Moreover, in TM polarization, a multiplication of the Toeplitz matrix of the permittivity and the vector that represents the electric field is required. So, the Li's factorization rules must also be sustained in the representation of the transition matrix Ψ_g . Indeed, the matrices Ψ_{11} and Ψ_{12} of setion 3.1.5 become $\Psi_{g,11}$ and $\Psi_{g,12}$ respectively. Thus, the Ψ_g matrix can be expressed as,

$$\Psi_g = \begin{bmatrix} \llbracket \Psi_{g,11} \rrbracket & \llbracket \Psi_{g,12} \rrbracket \\ I_d & I_d \end{bmatrix} = \begin{bmatrix} -\frac{\beta_{eff}}{k_0^2} \llbracket \epsilon_r \rrbracket^{-1} & \frac{\beta_{eff}}{k_0^2} \llbracket \epsilon_r \rrbracket^{-1} \\ I_d & I_d \end{bmatrix} \quad (7.9)$$

with k_0 , the propagation constant in the empty space and ϵ_r the relative permittivity harmonic vector of the i/o waveguides (Fig.8.1). Here, the previous propagation coefficient β_n is replaced by the eigenvalue of the eigen mode so that $\beta_{eff} = \frac{2\pi}{\lambda} n_{eff}$. Moreover, $1/k^2$ has been replaced by $\frac{1}{k_0^2} \llbracket \epsilon_r \rrbracket^{-1}$.

Consequently, the problem of the diffraction and Fabry-Perot effect at the i/o layers has been solved. Nevertheless, the choice of this matrix imposes that the input and output structures must tend to a single mode propagation corresponding to the eigen mode chosen in the matrix. It can be the case if the spatial filtering is enough efficient. In other words, the input and output waveguides must have a minimum length to reach a specific transmission or reflection accuracy.

Guided mode excitation

When the coordinate transformation is applied, the eigen modes of the homogeneous layer are not anymore the plane waves. Thus, to perform the guided mode excitation, the eigen mode of the input waveguide must be calculated using the eigen vector and eigen values solution of the differential system $M(z)$ of Eq.(7.6). After selecting the effective refractive index of the desired guided mode, the $2(2N + 1)$ eigen vector $[W_g]$ that corresponds to this n_{eff} is obtained. Moreover, the first $2N + 1$ components of $[W_g]$ correspond to the transverse electric field E_g of the guided mode. On the other hand, the last $2N + 1$ components describe the transverse magnetic field H'_g . Therefore, the forward propagating magnetic field H'_g belongs to the excitation vector and can be defined at the position $z = z_0$ as,

$$\begin{bmatrix} [H'_g{}^-(0)] \\ [H'_g{}^+(0)] \end{bmatrix} = \Psi_g^{-1} \cdot [W_g] = \Psi_g^{-1} \begin{bmatrix} [E_g(0)] \\ [H'_g(0)] \end{bmatrix} \quad (7.10)$$

The use of this Ψ_g matrix imposes to have only the guided mode at each end of the waveguide. To elaborate more, if the right representation of the eigen mode is used only the $2N + 1$ components of $H'_g{}^+(0)$ will exist before propagation, while all the other components are null. After performing the propagation of the excited guided mode, and by calculating the T-matrices of the different sections as $T^s = \Psi_{g,h}^{-1} P \Psi_{g,0}$, the same T-matrix to S-matrix transformation of chapter 3 is performed. Thus, the overall cascaded S-matrix gives access to the transmitted wave of the input waveguides via the $2N + 1$ vector $[H'_h{}^+]$ and the reflected waves of the input waveguides via $[H'_0{}^-]$. For each case, the decomposition of the harmonic vector of the magnetic field is proportional either to the amplitude of the transmitted guided mode or the amplitude of the reflected mode. At this scale, t_g donates to the transmission

coefficient and r_g to the reflection coefficient. Thus, we can write:

$$\begin{aligned} [H_g^{\prime+}(h)] &= t_g [H_g^{\prime+}(0)] \\ [H_g^{\prime-}(0)] &= r_g [H_g^{\prime+}(0)] \end{aligned}$$

The Fourier series form of r_g and t_g can be written as,

$$\begin{aligned} \sum_{n=-N}^{n=N} a_{hn}^+ e^{jKnx} &= t_g \sum_{n=-N}^{n=N} a_{0n}^+ e^{jKnx} \\ \sum_{n=-N}^{n=N} a_{hn}^- e^{jKnx} &= r_g \sum_{n=-N}^{n=N} a_{0n}^+ e^{jKnx} \end{aligned} \quad (7.11)$$

With a_{hn}^+ , a_{hn}^- and a_{0n}^+ are the amplitude of the harmonic n of the upward vector $[H_g^{\prime+}(h)]$, the forward vector $[H_g^{\prime-}(0)]$ and the excitation vector $[H_g^{\prime+}(0)]$ respectively. However, to obtain the intensity of the transmitted or reflected wave, a projection of the upward and forward harmonic vectors on the incident harmonic vector must be performed. Using the orthogonal propriety of the exponential term, the transmission and the reflection can be calculated as follows:

$$\begin{aligned} \frac{1}{\Lambda} \int_{\Lambda} \sum_{n=-N}^{n=N} a_{hn}^+ e^{(jKnx)} \sum_{n=-N}^{n=N} a_{0n}^{*+} e^{(-jKnx)} dx &= \\ \frac{1}{\Lambda} \int_{\Lambda} t_g \sum_{n=-N}^{n=N} a_{0n}^+ e^{(jKnx)} \sum_{n=-N}^{n=N} a_{0n}^{*+} e^{(-jKnx)} dx & \\ \Leftrightarrow \sum_{n=-N}^{n=N} a_{hn}^+ a_{0n}^{*+} = t_g \sum_{n=-N}^{n=N} a_{0n}^+ a_{0n}^{*+} & \\ \Leftrightarrow t_g = \frac{\sum_{n=-N}^{n=N} a_{hn}^+ a_{0n}^{*+}}{\sum_{n=-N}^{n=N} a_{0n}^+ a_{0n}^{*+}} & \end{aligned}$$

Thus, the transmission power T_g of the guided mode can be written as,

$$T_g = |t_g|^2 = \left| \frac{\sum_{n=-N}^{n=N} a_{hn}^+ a_{0n}^{*+}}{\sum_{n=-N}^{n=N} a_{0n}^+ a_{0n}^{*+}} \right|^2$$

Consequently, the reflection coefficient can be derived as,

$$\begin{aligned}
 & \frac{1}{\Lambda} \int_{\Lambda} \sum_{n=-N}^{n=N} a_{0n}^- \exp(jKn x) \sum_{n=-N}^{n=N} a_{0n}^{*+} \exp(-jKn x) dx = \\
 & \frac{1}{\Lambda} \int_{\Lambda} r_g \sum_{n=-N}^{n=N} a_{0n}^+ \exp(jKn x) \sum_{n=-N}^{n=N} a_{0n}^{*+} \exp(-jKn x) dx \\
 & \Leftrightarrow \sum_{n=-N}^{n=N} a_{0n}^- a_{0n}^{*+} = r_g \sum_{n=-N}^{n=N} a_{0n}^+ a_{0n}^{*+}
 \end{aligned}$$

The reflection efficiency R_g can be then written as,

$$R_g = |r_g|^2 = \left| \frac{\sum_{n=-N}^{n=N} a_{0n}^- a_{0n}^{*+}}{\sum_{n=-N}^{n=N} a_{0n}^+ a_{0n}^{*+}} \right|^2$$

With this technique the reflection and transmission powers of the excited guided mode could be easily determined. But, there is no information concerning the other modes. Actually, this solution suffers from two drawbacks: 1) A part of the transmitted power in the propagation direction is lost. Therefore, the resulting field maps obtained through Ψ_g are not exactly correct. Indeed, the projection is done on an incomplete basis. Thus, to obtain exact field maps, the projection should be performed on all the eigen modes of the input waveguides. For that, for each mode i , the transition matrix Ψ_i associated with each β_i should be calculated. 2) Due to the special form of mode excitation (excitation by a sum of plane waves), a spatial filtering must be performed of all modes different from the guided mode which is realized with a sufficient length of the straight waveguides at the input and output of the structure. This instability is originated from the use of Ψ_g .

To highlight this problem, the 2D guided structure of Ref.[103] has been considered. It consists of an InGaAsP core waveguide, with $n_c = 3.5$, placed on an InP substrate, $n_{sub} = 2.9$, and an air superstrate. The input waveguide is $0.3\mu m$ deep, and the distance between all the all the waveguides parts is fixed to $0.15\mu m$ (Fig.7.4).

In Fig.7.5.(a), the evolution of the reflection coefficient R_g calculated with the a-DM-FFF by

N	R_g (a-FMM)	R_g (a-DM-FFF)
20	0.356186	0.355641
50	0.355619	0.355210
150	0.355494	0.355258

Table 7.1 R_g $N = 20, 50$ and 150 using the a-FMM and the a-DM-FFF of the reference structure.

varying the input waveguide length H is reported with $N = 30$. Indeed, a minimum length of $H = 11\mu m$ is needed to ensure the filtering and the stability of R_g nearby the third digit with respect to the reference value calculated in Ref.[103] (Black horizontal dashed line). Thus,

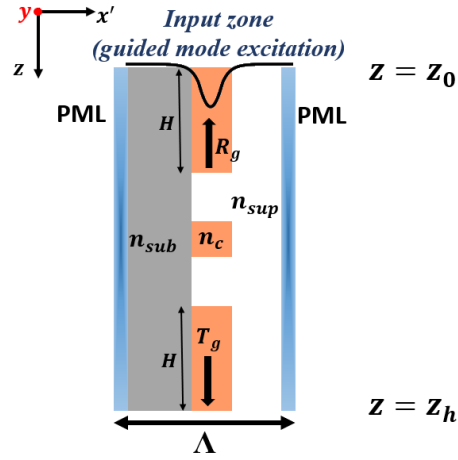


Fig. 7.4 Unit cell of the lamellar artificially periodized guided structure. The structure is excited by its fundamental TM polarized guided mode at $\lambda = 0.975\mu m$ with a period $\Lambda = 1.1\mu m$ and a total thickness of PML $q_{x'} = \lambda/2$ and $\gamma = \frac{1}{1+j}$. x' is the periodization axis, z is the propagation axis and y is considered invariant.

an input waveguide of length $H = 12\mu m$ has been chosen for the rest of the calculations. Moreover, Table.7.1 presents the reflection coefficient R_g of the lamellar dielectric guided

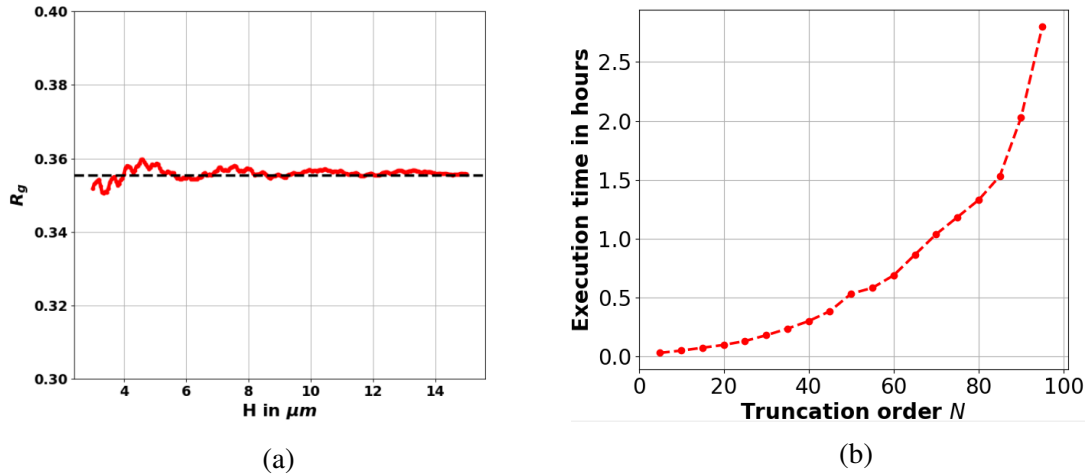


Fig. 7.5 (a) The evolution of R_g with respect to the length of input waveguide H . The black dashed line represents the reference value calculated in Ref.[103] with $R_{ref} = 0.3554787$ (b) The execution time of the a-DM-FFF of the reference structure with $H = 12\mu m$, $D_z = 5nm$ and $N_{FFT} = 8192$ samples following the truncation order N .

structure calculated by the a-FMM and our a-DM-FFF for different truncation orders N . Indeed, for $N = 20$, a relative error of 5.45×10^{-4} with respect to the value of a-FMM can be obtained by the new method (a-DM-FFF). This error reaches a value of 4×10^{-4} for $N = 80$

and decreases to 2.36×10^{-4} with $N = 150$.

Notwithstanding that this formulation gives a relative error in the range of 10^{-4} . But, it is also considered as time consuming and memory exhausting technique. For example, with $D_z = 5nm$ and $H = 12\mu m$, approximately 3 hours are needed to calculate the reflection and transmission coefficients for $N = 100$ with a system of *corei7@2.7GHz* and *8GB* physical memory (Fig.7.5.(b)).

Here, the center of our attention was devoted on the eigen guided mode of the structure. The Ψ_g matrix was used to perform the transition from the stationary fields representation into the harmonic forward and backward vectors of the field. Due to the disregard of the effect of the other modes, a spatial filtering is needed to obtain accurate results. Meanwhile, another solution can be implemented which consider and uses all the eigen mode of the structure. The next section will be devoted to arise the formulation of this transition technique which brings many advantages and assets.

7.3.4 The use of a transition matrix that directly links the amplitude of the eigen modes with the stationary harmonic vectors

Formulation of the transition matrix W

As mentioned before, the algorithm of the differential theory uses a transition matrix that crossover from the stationary harmonic vector representation into the forward and backward harmonic vector of the magnetic field in TM polarization and the electric field in TE polarization. In case of guided structure, and if the input waveguide is a straight waveguide (rectangular distribution of the permitivity), a symmetric distribution of the eigen values can be obtained which represents the forward and backward refractive indices of the modes ($2N + 1$ positive real part eigenvalues for the forward modes, and $2N + 1$ opposite (negative) real part eigen values for the backward modes). Indeed, this symmetry can be exploited in order to directly have access to the amplitude of each eigen mode at each interface (input or output).

As a result, the amplitudes of the transmitted and reflected guided mode become directly accessible. To demonstrate that, the matrices W_I (input waveguide) and W_O (output waveguide) have been defined. For simplicity reason, a symmetric structure has been chosen. Thus, $W_I = W_O$.

The truncated differential equations system (7.3) can be solved as an Eigen problem producing the $4N + 2$ vector D and $(4N + 2) \times (4N + 2)$ matrix W . In this situation, D is a vector containing the $4N + 2$ effective refractive indices of the discretized layer s . Under this

situation, the positive real values of D represent the effective refractive indices of the forward modes and the negative ones refer to the backward modes. Those modes are symmetric in case of rectangular structure, mainly the input and output waveguides, with $2N + 1$ forward modes and $2N + 1$ backward modes. On the other hand, a column i of W describes the harmonic representation of the eigen modes for one effective refractive index D_i .

Therefore, the matrix W and the vector D are rearranged to associate the first half column of W to the backward modes and the second part to the forward modes. The excited fundamental mode is associated to one of this column.

The a-DM-FFF deals with the stationary Fourier components of the fields $[E_{x'}]$ and $[H'_y]$ to solve the propagation system. Thus, a transition matrix is needed to pass into the guided mode representation $[c^-]$ and $[c^+]$ of the backward and forward Fourier amplitude of the field. Hence, by applying the eigen solutions to the propagation $T^{(s)}$ matrix of the first slice of the structure. We define W_I representing the eigen mode of the input waveguide. The same thing happens for the last slice, where W_O represents the eigen modes of the output waveguide.

Here, we will elaborate the algorithm of the transition from the stationary wave components of the fields into the eigen forward and backward modes through the transition matrix W_I of the input waveguide. Using the same analogy, the transition matrix of the output waveguide can be calculated. It is important to mention that the same algorithm of eigenvectors arrangement can be applied for both TE and TM polarizations.

The transient form of $E_{x'}$ and H'_y can be represented in terms of the eigenvector W of the input waveguide, and K as follows,

$$\begin{aligned} E_{x'}(x', z = 0) &= \sum_q \left(c_{0,q}^- \sum_p W_{E_{qp}}^- e^{jK_{qq}x} + c_{0,q}^+ \sum_p W_{E_{qp}}^+ e^{jK_{qq}x} \right) \\ H'_y(x, z = 0) &= \sum_q \left(c_{0,q}^- \sum_p W_{H'_{qp}}^- e^{jK_{qq}x} + c_{0,q}^+ \sum_p W_{H'_{qp}}^+ e^{jK_{qq}x} \right) \end{aligned}$$

Where, $c_{0,q}^+$ and $c_{0,q}^-$ are the Fourier coefficient of the forward and backward eigenmodes q respectively. $W_{E_{qp}}$ is the harmonic coefficient p of the eigenvector q of the electric field vector $[E_z]$, and K_{qq} is the harmonic coefficient q of the eigenvector q from the matrix K . Therefore, in the Fourier space, the transition matrix W_I of the input layer can be expressed as,

$$\begin{bmatrix} [E_{x'}] \\ [H'_y] \end{bmatrix} = W_I \begin{bmatrix} [c_0^-] \\ [c_0^+] \end{bmatrix}$$

with:

$$W_I = \begin{bmatrix} W_E^- & W_E^+ \\ W_{H'}^- & W_{H'}^+ \end{bmatrix}$$

Therefore, W_I is obtained by organizing the $(4N + 2) \times (4N + 2)$ Eigen-vector matrix of the first layer in a manner where the first $2N + 1$ columns represent the backward modes (propagating following $-z$) and the last $2N + 1$ belong to the forward modes (propagating following $+z$). The multiplication of W_I and W_O^{-1} with the solution of Eq.(7.6), P , gives access to the amplitudes of the forward waves and backward waves. Moreover, the same matrix is used to convert the stationary field harmonic vectors $[E_x]$ and $[H'_y]$ vectors into the harmonic amplitudes of the forward and backward vectors $[c^-]$ and $[c^+]$ for each s layer at the position of the infinitely thin layer.

The excitation and the propagation of the guided mode

After calculating the transition matrices W_I and W_O , the matrix I_d is used to initialize the Runge-Kutta integration by an initial-value problem. Consequently, the $T^{(s)}$ matrix that links the fields at the position z_s and the fields at the position z_{s+1} can be expressed as,

$$T^{(s)} = W_I P^{(s)} W_O^{-1} \quad (7.12)$$

The matrix W_O^{-1} is inverted to give the inverse transition (from the vector $[c^+]$ and $[c^-]$ to the harmonic vector of the fields). Indeed, the same algorithm of cascade of S-matrices of the grating theory is used here to link the incoming waves with the outgoing ones. The only difference is that the amplitude of the eigen mode of the i/o waveguides are now considered instead of the eigen vectors of the plane waves.

The main advantage of this formulation with respect to the previous one (Ψ_g) is that all the eigen modes of the i/o waveguides are now represented. Therefore, all the information of these modes are accessible. Consequently, in term of calculation, there is no need for spatial filtering and small input and output waveguides are sufficient to ensure the accuracy and stability of the method. Indeed, Fig.7.6.(a) shows that the reflection coefficient of the lamellar reference structure (Fig.7.4) stays stable following the evolution of the input/output length H . Moreover, the execution time and the memory space are incredibly reduced by a factor of 32 (Fig.7.6.(b)). For example, with the previous transition matrix Ψ_g , the calculation of the R_g/T_g coefficients needs approximately 32 minutes for $N = 50$. On the other hand, 1 minute is sufficient to get the exact values of R_g and T_g with the new W matrix. Nevertheless, the representation of each Ψ of each β_{eff} is also not mandatory, and the field maps are now rigorously represented without any approximation.

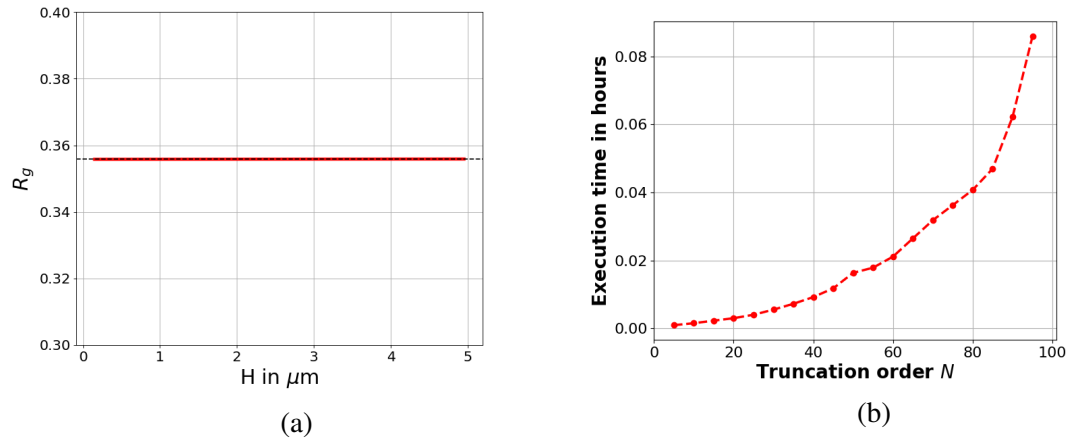


Fig. 7.6 (a) Reflection coefficient R_g following the length of the i/o waveguides H (b) the calculation time using the new transition matrix W

7.4 Validation of the method

All the results of the a-DM-FFF will be validated and calculated in the next parts by using the new transition matrix W due to its many advantages. For that, the lamellar structure of Fig.7.4 has been considered as the reference structure. The convergence, following the truncation order N , has been evaluated with respect to the values of R_g calculated by the a-FMM and depicted in Ref.[37]. The structure has been excited by its fundamental, TE or TM polarized, guided mode, with $\lambda = 975\text{nm}$. The period of the artificial periodized structure is $\Lambda = 1.1\mu\text{m}$ and the thickness of the PML form each side is $q_{x'} = \frac{\lambda}{4}$. Moreover, the structure is discretized with $D_z = 5\text{nm}$ while using the a-DM-FFF. This lamellar structure has been chosen since the a-FMM gives accurate and rigorous results with the structures composed of rectangular sections. All the Fourier transformation, of the a-DM-FFF, are performed through a Fast Fourier Transform (FFT) by using $N_{FFT} = 8192$ samples. The $2N + 1$ harmonics needed for the modelization are issued from this vector.

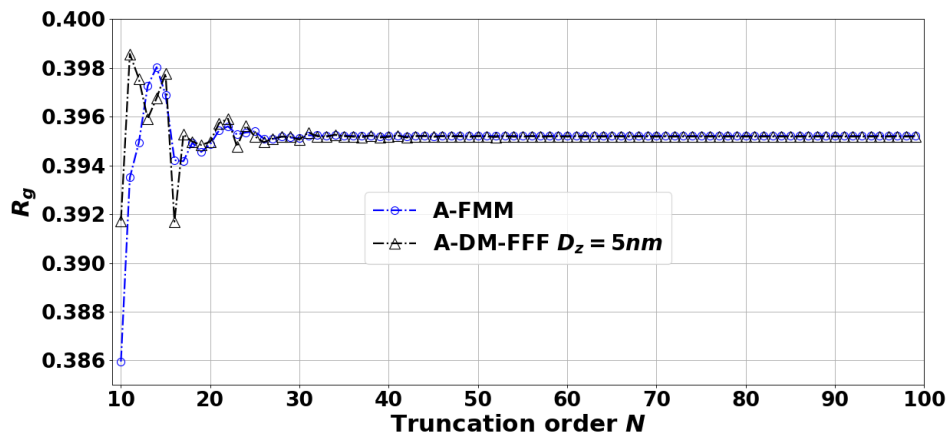
7.4.1 TE polarization

Now, the lamellar structure is excited by its fundamental TE polarized guided wave. In case of non-magnetic materials, the electric field \vec{E} and the magnetic field \vec{H} are always continuous in TE polarization. Thus, the inverse rule of Li and the FFF reformulation are useless with this polarization.

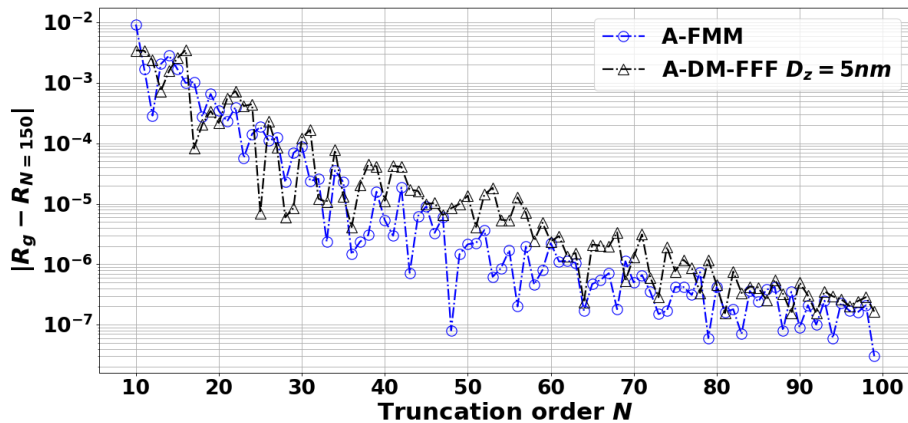
The convergence rate of R_g following N for TE polarization is depicted in Fig.7.7.(a). It is clear that the results obtained with the new a-DM-FFF (black dashed curve with open triangles) collides very well with the values of the a-FMM (blue dashed curve with open

dots). Moreover, to study the convergence rate, the relative error $|R - R_{N=150}|$ has been evaluated with respect to N for the two previous methods polarization respectively, where $R_{N=150}$ represents the value of the reflection coefficient calculated for each method at $N = 150$ (see Table.7.2).

However, only $N = 15$ is sufficient to reach a relative error of 10^{-3} . This error decreases



(a)



(b)

Fig. 7.7 Performance of the a-DM-FFF compared to the a-FMM for a lamellar structure as a reference in TE polarization. (a) Convergence of R_g following N (b) Relative Error $|R_g - R_{N=150}|$ following N

with the increase of the truncation order N . For $N = 100$, a relative error of $1.5 \cdot 10^{-7}$ can be reached. The very tiny difference between the two methods can be explained by two facts: 1) the use of FFT instead of the ideal Fouries series of the lamellar sections used by the a-FMM. In that case, N_{FFT} may not be considered big enough to reach the same exact value of the

N	R_g (a-FMM)	R_g (a-DM-FFF)
10	0.385952	0.391732
20	0.395141	0.395176
30	0.395141	0.395176
50	0.395212	0.395190
60	0.395212	0.395190
80	0.395211	0.395186
100	0.395211	0.395185
150	0.395211	0.395185

Table 7.2 R_g using the a-FMM and the a-DM-FFF of the reference Lamellar structure in TE polarization.

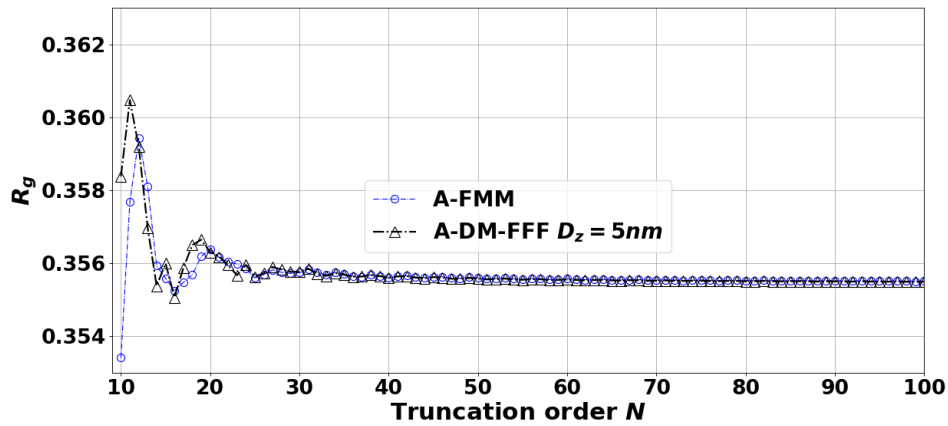
a-FMM. 2) A small error induced by the Range-Kutta algorithm where a smaller integration step D_z or higher number of sub-sections n_S are needed in the integration process.

7.4.2 TM polarization

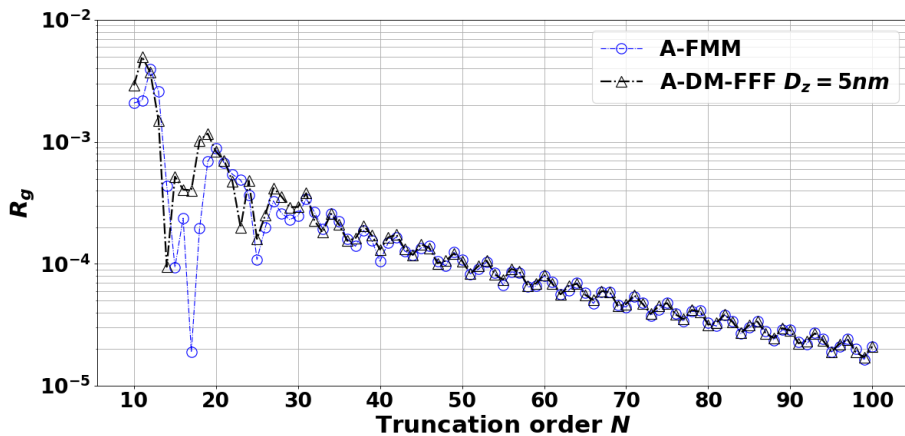
In this section, the reference structure is illuminated with the same opto-geometrical parameters with its fundamental TM polarized guided wave. However, in case of Lamellar structures, the FFF is useless ($N_x = 0$ and $N_z = 1$). Therefore, the only main difference between the a-FMM and the a-DM-FFF is the integration algorithm. Fig.7.8.(a) illustrates the convergence and the accuracy performance of R_g for the reference structure in TM polarization. The blue open dots are always obtained using the a-FMM, and the black open triangles refer to the a-DM-FFF depicted in Eq.7.6.

As same as the TE polarization results, the reflection coefficients calculated by the a-DM-FFF fits very well with the ones of the a-FMM (Fig.7.8.(a)). The convergence rate of both methods depicted in Fig.7.8.(b) shows that $N = 20$ to reach a relative error with respect to the value calculated for $N = 150$ (see Table.7.3). Moreover, the errors decrease in a monotonic way to reach a value of $2 \cdot 10^{-5}$ with $N = 100$.

As a result, our formulations are now validated for both polarizations. Thus, the a-DM-FFF is now ready to be applied for more complicated structures where the a-FMM suffers from the staircase approximation. As the electromagnetic fields in TE polarization are always continuous, the FFF has no impact on the convergence rate. On the other hand, the impact of the FFF appears for TM polarization only. Therefore, in the next sections all the structures will be excited by their fundamental TM_0 guided mode.



(a)



(b)

Fig. 7.8 Performance of the a-DM-FFF compared to the a-FMM for a lamellar structure as a reference in TM polarization. (a) Convergence of R_g following N (b) Relative Error $|R_g - R_{N=150}|$ following N

7.5 Conclusion

In this chapter a new reformulation of the differential theory used with periodic structure has been presented. Indeed, the association of a complex coordinate transformation to the algorithm of the differential method can turn the DM-FFF into an aperiodic method so-called a-DM-FFF. However, as the DM-FFF takes into consideration the evolution of the profile with respect to the transverse axis. This method can be used to modelize complex shaped guided structure by eliminating the staircase approximation of the a-FMM. Our method has been implemented numerically and validated with respect to a lamellar reference structure. The obtained results with the a-DM-FFF for both TE and TM polarizations show a large degree

N	R_g (a-FMM)	R_g (a-DM-FFF)
10	0.353410	0.358382
20	0.356186	0.356649
30	0.355725	0.355768
50	0.355619	0.355598
60	0.355560	0.355545
80	0.355536	0.355517
100	0.355525	0.355502
150	0.355494	0.355476

Table 7.3 R_g using the a-FMM and the a-DM-FFF of the reference Lamellar structure in TM polarization.

of concordance with those calculated with the a-FMM. Indeed, to upraise the performance of the FFF, non-lamellar structure must be taken into consideration. In that case, the a-FMM must suffers from slow convergence and inaccuracy especially with high contrast guided structures (dielectric or metallic).

Chapter 8

A-DM-FFF compared to the a-FMM: Application on complex shaped photonic guided structures

The effect of the staircase approximation of the a-FMM appears with high contrast guided structures (metallic or dielectric). In this chapter, non lamellar guided structures are considered. Our aim is to prove the effectiveness of the a-DM-FFF compared to the classical a-FMM while dealing with complex shaped photonic structures.

8.1 Application of the a-DM-FFF on curvilinear guided reflector

8.1.1 Geometry of the structure

To appraise the performance of the FFF, a 2D cylindrical rod is placed at the center of the structure (Fig.8.1). This case elaborates a complicated geometry for the a-FMM. During the integration process, the normal components vary rapidly from horizontal to vertical position. Due to this rapid change, the cylindrical rods are considered the most difficult case to be computed [94]. Indeed, the FFF handles the situation.

For simplicity reasons, the structure is considered symmetrical. Thus, $n_{ext} = n_{sup} = n_{sub}$. The structure is excited from the top ($z = z_0$) with the fundamental TM_0 guided mode at $\lambda = 1.5\mu m$. The refractive index of the input and output waveguides is $n_g = 3.5$. Moreover, the input/output waveguides are $0.3\mu m$ wide (along x), and the length of the waveguides and the gap (G) (along z) is fixed to $0.15\mu m$. The refractive index of the cylindrical reflector

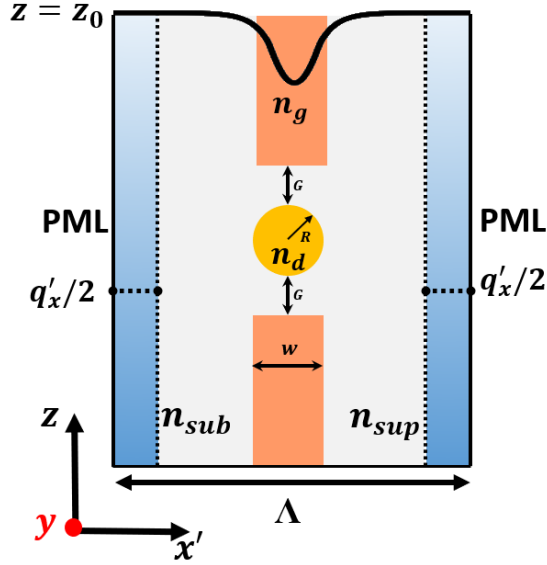


Fig. 8.1 Unit cell of the artificially periodized guided reflector

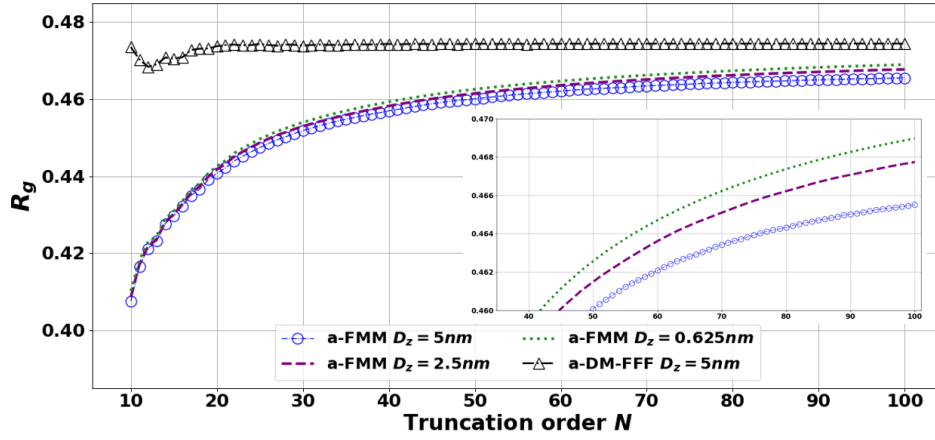
placed at the center of the structure is n_d and its radius is $R = 150nm$. Furthermore, the period of the unit cell is $1.1\mu m$, and the thickness of the PML is $q_{x'} = 0.4875\mu m$.

For both, the a-DM-FFF and the a-FMM, the structure is discretized with a constant discretization step $D_z = 5nm$, and $n_s = 4$ sub-layers are used in the Runge–Kutta algorithm of the a-DM-FFF. So that, 60 S-matrices are cascaded in the cylindrical region. All the Fourier transformations of the a-DM-FFF are performed through a fast Fourier transform (FFT) by using $N_{FFT} = 8192$ samples. The $2N + 1$ harmonics needed for the modelization are issued from this vector. The formulas of the normal to the profile, $N_{x'}$ and N_z , of the 2D cylindrical pillar are depicted in Appendix.3.

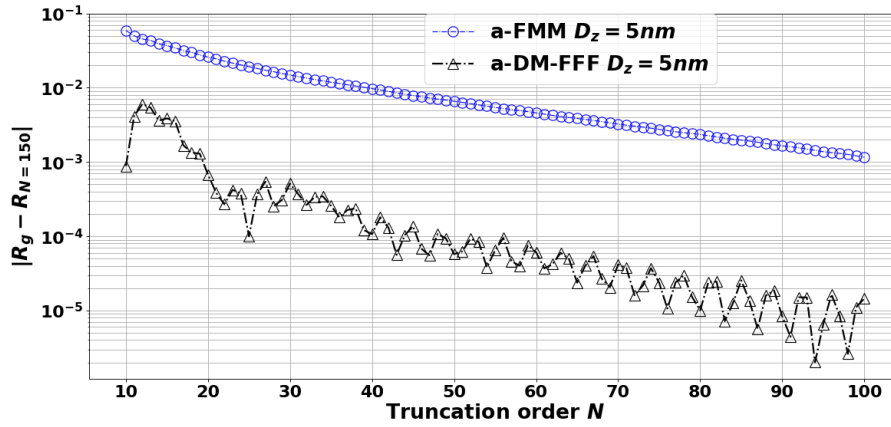
8.1.2 TM polarization: Dielectric high contrast index structure

Now, a dielectric 2D cylinder is considered. To achieve the high refractive index contrast condition, the guided zone is surrounded by air with $n_{ext} = n_{sup} = n_{sub} = 1$. Moreover, the dielectric cylinder of refractive index $n_d = 3.5$ has been chosen (so that $\Delta n = |n_d - n_{ext}| = 2.5$). The evolution of the reflection coefficient of the guided structure has been evaluated following N using the a-DM-FFF and the a-FMM (Fig.8.2.(a)).

As expected, and despite the small discretization step, $D_z = 5nm$, the a-FMM converges slowly following N (blue curve with open circles). This is a direct consequence of the staircase approximation that induces the unadapted continuity of the field at the interface of the cylinder, and the parasitic points effect that appears with the high refractive index



(a)



(b)

Fig. 8.2 Convergence of the high refractive index contrast case with a dielectric cylinder rod reflector of the a-DM-FFF and the a-FMM (a) R_g following N (b) The relative error $|R - R_{N=150}|$ following N .

contrast structures.

Moreover, the zoomed part in this figure shows that decreasing D_z of the a-FMM from $5nm$ to $0.625nm$, (so that the cascade of 60 S-matrices to 480 S-matrices), does not enhance the convergence speed of the method. The same monochromatic evolution is reached, but it brings out slowly the result at $N = 100$ to the value of the a-DM-FFF. In contrast, with $D_z = 5nm$, the a-DM-FFF (open black triangles) converges rapidly. $N = 20$ is largely sufficient to ensure the stability and the convergence of the reflection coefficient following N . In addition, Fig.8.2.(b) presents the evolution of the error rate of R_g calculated for each method with respect to the values obtained for $N = 150$ (see Table.8.1). It is clear that with the a-DM-FFF, an error rate less than 10^{-3} can be achieved beyond $N = 20$. This error

decreases in a mono-tonic manner with the increases of N to reach a value of 1.29×10^{-5} for $N = 100$. On the other hand, with the same discretization step (same number of cascaded S-matrix), the a-FMM converges very slowly with the evolution of N . Errors of 1.45×10^{-2} , 9×10^{-3} and 7.7×10^{-3} are achieved for $N = 50, 100$, and 150 respectively with respect to the value of the a-DM-FFF at $N = 150$ (see Table.8.1). It is not guaranteed to reach the same value of the a-DM-FFF while increasing N of the a-FMM. But, the stability of the new formulation (a-DM-FFF) can be emphasized and taken into account in order to believe that the value calculated with the a-DM-FFF for $N = 150$ could be considered as the new exact reference.

N	R_g (a-FMM)	R_g (a-DM-FFF)
20	0.439008	0.473137
50	0.459852	0.474339
100	0.465512	0.474418
150	0.466671	0.4744329

Table 8.1 R_g at $N = 20, 50, 100$ and 150 of the a-FMM and the a-DM-FFF for the structure with high refractive index contrast dielectric pillar.

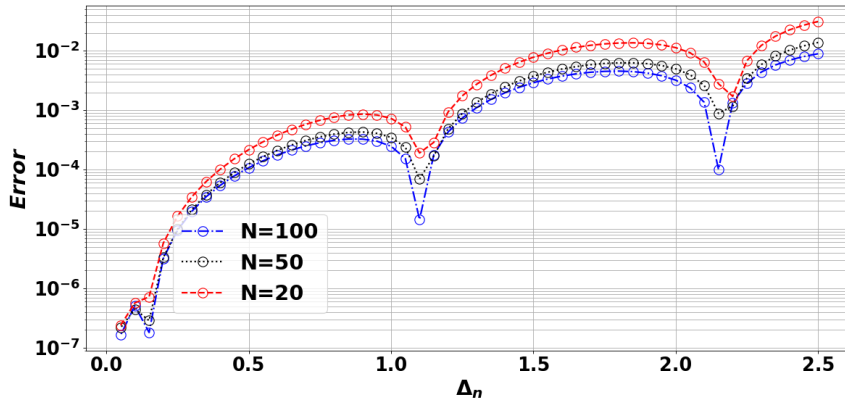


Fig. 8.3 Evolution of the reflection coefficient error $|R_{ga-DM-FFF} - R_{ga-FMM}|$ following Δn . All R_g are calculated for $N = 100, 50$ and 20 with $D_z = 5 \text{ nm}$ for both methods.

To ensure this hypothesis, the error of the difference between R_g of the a-DM-FFF and R_g of the a-FMM ($|R_{a-DM-FFF} - R_{a-FMM}|$) has been studied with respect to $\Delta n = n_d - n_{ext}$, by varying n_{ext} from 1 to 3.4 (Fig.8.3). For $N = 100$ (blue dashed curve with open dots), we can notice that the error's envelop increases with the increase of Δn . An error of 1.6×10^{-7} is achieved between the values of the two methods when $\Delta n = 0.1$ ($n_{ext} = 3.4$ and $n_d = 3.5$).

However, the error acts of the third digit ($< 10^{-3}$) for $\Delta n < 1.2$. For bigger values of Δn , the error increases by acting of the second digit and inducing the inaccuracy of the a-FMM. However, when N decreases to 50 and 20 (black and red dashed curves with open dots respectively), the error difference slightly increases due to the famous staircase approximation of the a-FMM. As a result, this figure ensure our hypothesis telling that the value of the a-DM-FFF can be considered as a reference value. Moreover, the results given by the a-DM-FFF are interesting for such a difficult problem faced by the a-FMM. This new method leads to higher accuracy with fewer harmonics and bigger D_z . It induces fewer S-matrices used to perform the propagation, so that fewer memory and time consumption.

8.1.3 TM polarization: Metallic 2D pillar

The second situation where the a-FMM fails to rapidly converge occurs when this method deals with metallic structure with non-lamellar profile, despite the refractive index of the surrounding medium. For that, the same opto-geometrical parameters of the previous sections have been considered with a 2D metallic pillar of refractive index $n_d = 1 + j7$ and $n_{ext} = 2.9$.

In Fig.8.4.(a), the computed evolution of the reflection coefficient R_g shows that the a-FMM converges slowly in a quasi-monotonic manner as the truncation order N increases. In contrast, the a-DM-FFF needs $N > 30$ to converge and stabilize following N . Moreover, we can notice that at higher harmonics ($N = 100$), the zoomed part of Fig.8.4.(a) shows that the a-FMM converges to the value of the a-DM-FFF (see Table. 8.2). In that case, the Δn difference modulus is smaller than the dielectric pillar case of the all-dielectric structure case. The resonance effect due to the metal losses is perhaps weaker, decreasing the field interaction on the pillar periphery.

Moreover, the evolution of error with respect to the value of R_g calculated for $N = 150$ has been presented in Fig.8.4.(b). It is clear that a 10^{-3} relative error is reached with $N > 40$ ($2N + 1 = 81$ spectral orders) with the a-DM-FFF and this error decreases to attain a value of 1.6×10^{-4} for $N = 100$. On the other hand, the convergence of the a-FMM with the metallic pillar is much more slower than the dielectric case. It needs more than 100 harmonics ($2N + 1 = 201$ spectral orders) to reach an error $< 10^{-3}$ threshold, where an error of 3×10^{-3} is reached with the a-FMM with the same N .

As a result, the dominance of the new method (a-DM-FFF) over the a-FMM is noticeable. The obtained results demonstrate the potential of the FFF while dealing with guided non-lamellar structures. The continuity of fields taken into consideration in Eq. (7.6), at the dielectric–metal or the high refractive index contrast dielectric–dielectric interface, solves the problem of staircase approximation of the a-FMM especially for TM polarization. Therefore,

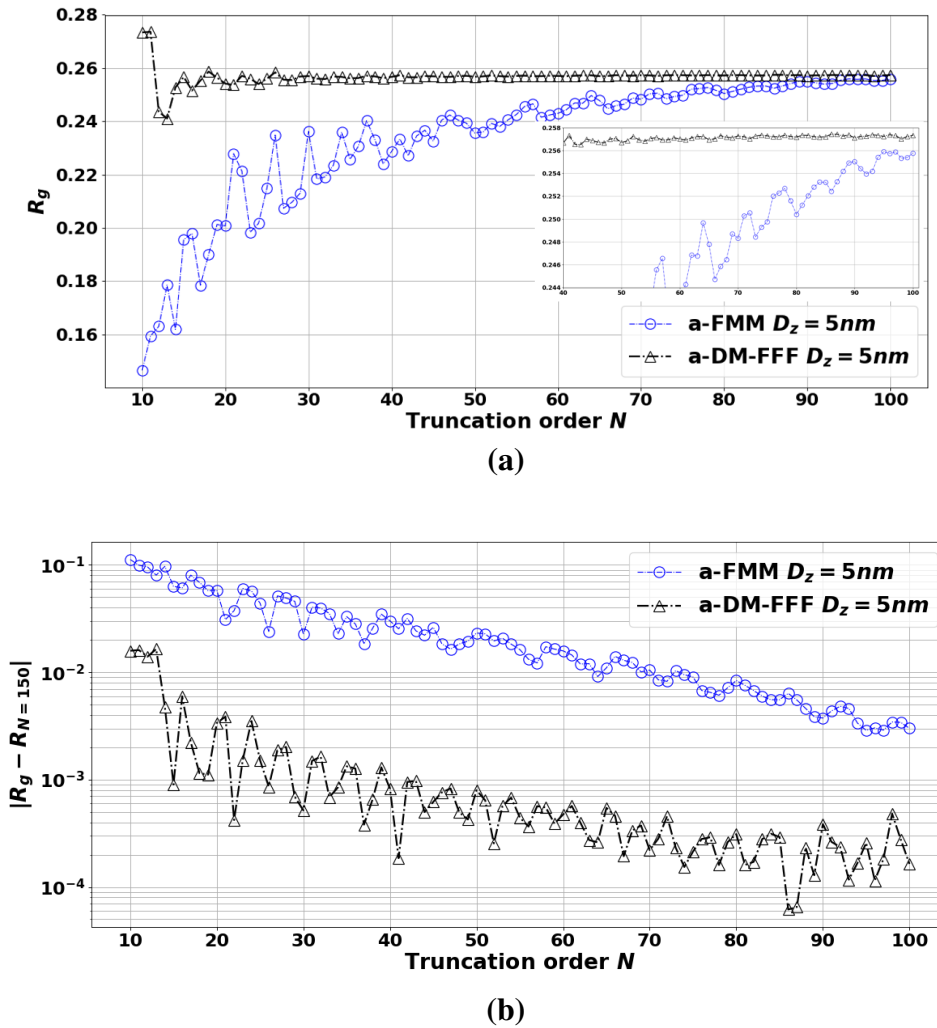


Fig. 8.4 Convergence of the guided structure with metallic pillar reflector (a) R_g following N (b) The relative error $|R - R_{N=150}|$ following N .

the convergence is extremely enhanced, and the coefficient accuracy is boosted. Moreover, to show the impact of the parasitic point effect induced by the staircase approximation of the a-FMM, the field map of the transverse electric field E_x has been plotted for $N = 50$ for both methods (Fig.8.5). Firstly, resonant effects appear with the a-FMM at each corner of stairs inducing interference outside the cylinder. This phenomenon is strongly reduced with the a-DM-FFF. Secondly, the discontinuity of the field is better defined in the straight waveguide with the a-DM-FFF. Indeed, the electrical field is directly obtained from the matrix containing the Q-matrix taking in account the normal evolution. With the a-FMM, the electrical field is reconstituted from the magnetic field calculation. And a division of the permittivity is used in the space domain to ensure an optimized repartition as proposed by

N	R_g (a-FMM)	R_g (a-DM-FFF)
20	0.201265	0.256375
50	0.239316	0.257063
100	0.255773	0.257324
150	0.258777	0.257292

Table 8.2 R_g at $N = 20, 50, 100$ and 150 of the a-FMM and the a-DM-FFF for the structure with metallic pillar.

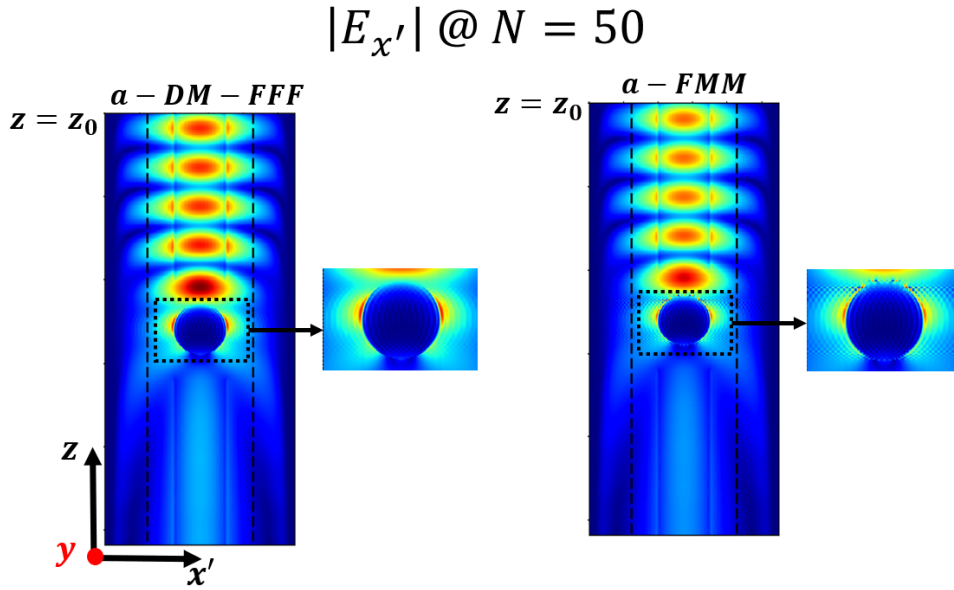


Fig. 8.5 Evolution of $|E_{x'}|$ with TM polarization of the a-DM-FFF and the a-FMM for $N = 50$.

Jurek et al. So, the matrix of a-DM-FFF is two times the matrix of a-FMM but the repartition is better and easier to obtain.. Moreover, we can notice that at the border of the unit cell the field is totally suppressed due to the absorption of PML.

8.1.4 TE polarization

As mentioned many times before, the electromagnetic fields in TE polarization are always continuous. Thus, there is no impact of the FFF on the convergence rate, and the a-FMM is considered sufficient and rigorous with such structures. But, to ensure the functionality and the stability of the new a-DM-FFF, the convergence of both metallic and dielectric structures has been evaluated while exciting the structure with its TE₀ fundamental guided mode (Fig.8.6).

For both structures, we can notice that the reflection coefficients R_g of both the a-DM-FFF and the a-FMM are exactly identical following the truncation order N . Moreover, the convergence

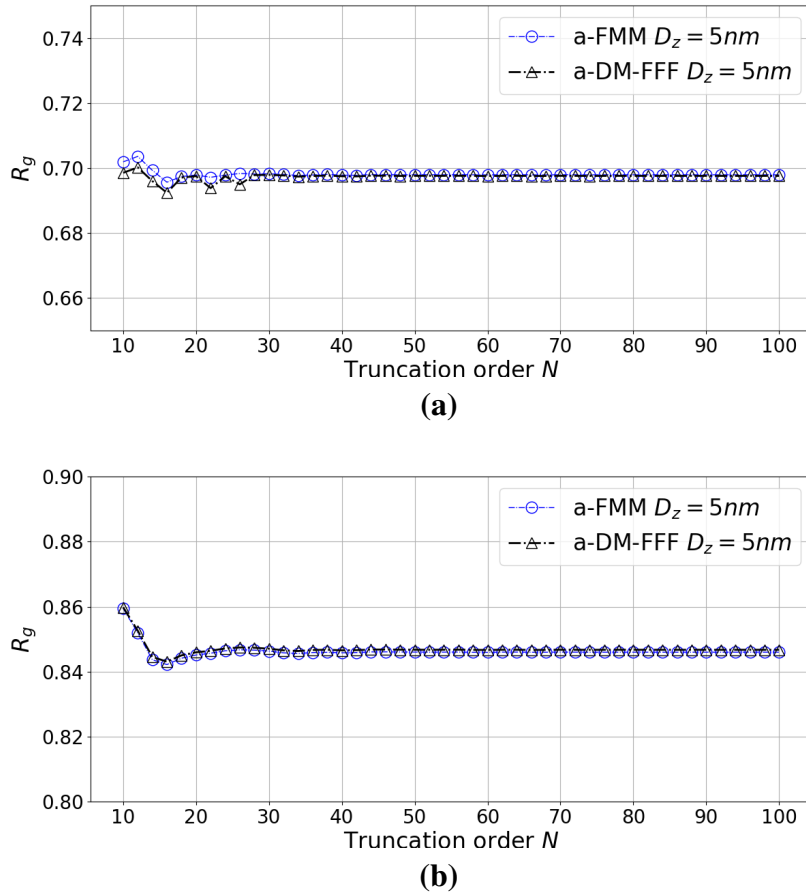


Fig. 8.6 Convergence of the guided structure excited by the fundamental TE_0 guided mode (a) dielectric structure of sec.8.1.3 with $n_d = 3.5$ and $n_{ext} = 1$ (b) metallic structure of sec.8.1.4 with $n_d = 1 + j7$ and $n_{ext} = 2.9$.

rate is similar for both methods. Thus, the association of the FFF has no impact and useless in case of TE polarized guided mode. Physically, it is interested to note that the staircase approximation has a first order role in this case. This discretization can slightly change the mean radius of the cylinder which can explain the small difference between the two methods on the reflection value calculated.

8.1.5 Conclusion

The convergence tests conducted on different structures have proved that the a-DM-FFF can incredibly enhance the convergence compared to the a-FMM in the case of high refractive index contrast and continuous structures (metallic and dielectric) especially when the structure is illuminated with TM polarized guided wave. For that, this method will open the way to

modelize complex-shape guided structures. The W matrix definition is also an interesting way to reach a hybrid method. This formulation opens the way to cascade a-FMM zones with a-DM-FFF zones. Indeed, the numerical integration can be focused on continuous evolution in order to optimize the calculation speed.

8.2 Application of the a-DM-FFF on resonant cavities: Microdisk resonators as examples

8.2.1 Introduction

In the last two decades, huge technological leaps have been performed in the domain of microphotronics, basically to realize photonic structures using the silicon on insulator (SOI) technology [7]. Indeed, the mastering of this technology allows now the fabrication and the realization of novel integrated photonics structures which are considered as the basis elements of passive photonic structures used in the optical routing [1, 60, 87], in the non-linear optics for signal modulation [121], and as active devices for the realization of optical sources [120]. However, the microrings and the microdisks are two main backbones of this new technology. They are considered as structures which respect a cylindrical symmetry. Moreover, their open periphery stimulates the radiation of the optical signal from the internal surface of the disk to the external medium. Thus, the novel algorithm of the a-DM-FFF developed in chap.7 can be now exploited to modelize such types of resonators.

Indeed, the modelization of 2D microdisk rests on the simulation of invariant cylinder following the y -axis as depicted in Fig.8.7. The refractive index difference between the disk (n_d) and the external medium (n_{ext}) can be seen as an optical cavity. Under certain conditions, the resonances inside the disk may appear inducing the filtering effect of cavities. Both TE and TM polarization may considered and only non-magnetic material are used.

8.2.2 Problem of doublet resonances

Mainly two methods are used to predict the resonances in this type of cavities:

- The forced oscillation regime: it corresponds to a real measurement. It can be an external source coming from outside sent into the disk and the reflected/transmitted signals are observed. To ensure the excitation of the resonant mode, the excitation must be preferentially adapted to the resonant mode. A sweep of different real wavelengths is

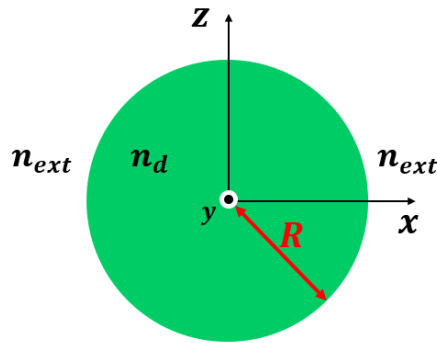


Fig. 8.7 Schematic representation of a microdisk cavity of radius R .

necessary to detect the resonance in the spectral domain. Using a fit with an appropriate mathematical function, the quality factor and the resonant wavelength can be obtained.

- The free oscillation regime: this is an ideal case. There is no source used. In this configuration, infinite energy has been radiated by the resonator at an infinite time in the past. The resonant wavelength in this case is characterized by a complex wavelength. From its real and imaginary parts, the quality factor and the resonant wavelength can be obtained.

To elaborate more, both regimes use the S -matrix algorithm that links the ongoing waves (c_s^- and c_{s-1}^+) with the outgoing waves (c_s^+ and c_{s-1}^-) to describe the propagation in the structure (Fig.3.8.(a)). In the forced oscillation regime, the input signals are fixed to given values (for example $c_s^- = 0$ and $c_{s-1}^+ = 1$). Therefore, the i/o ratios are compared by varying the real optical wavelength of the source. In contrast, in the free regime, both input signals are null which imposes that the multiplication of the output signals with the inverse of the S -matrix (S^{-1}) is equal to zero. This condition is satisfied only if the determinant of S^{-1} is equal to nullity. Therefore, the eigen modes that describe the oscillation can be obtained under the form of complex wavelengths.

In this dissertation, only the first regime will be studied. Mainly, all these structures are based on the propagation of the Whispering Gallery Mode (WGM) along the periphery of the disk. Thus, the high contrast of refractive index between the disk and the external medium can lead to high total quality factor $Q = \frac{\lambda_{res}}{\Delta\lambda}$ (Fig.8.8) within few micrometers of radius. Indeed, if the conditions of phase-matching and coupling are fulfilled between the disk and the input wave, power variation can be achieved at the structure output and the

resonant wavelengths are filtered.

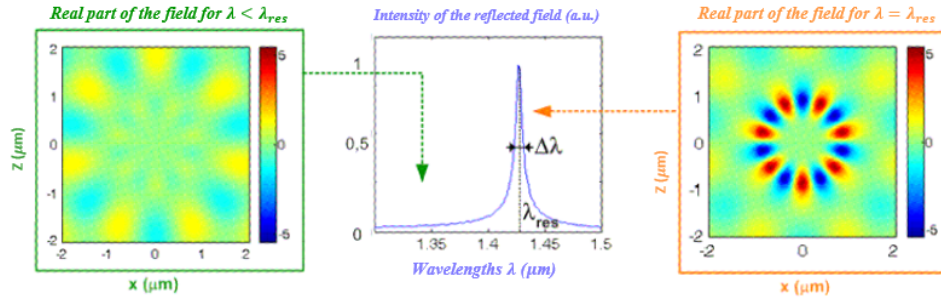


Fig. 8.8 Spectral response of the forced oscillation regime. In this case, the excitation is a besel function which corresponds to the wave radiated by the microdisk. The phase matching in amplitude and phase is ensured [40].

However, when the surface roughness exists another factor may affect the total quality factor Q . This last one can thus be defined as,

$$\frac{1}{Q} = \frac{1}{Q_i} + \frac{1}{Q_s} \quad (8.1)$$

With, Q_i is the quality factor of the ideal disk, and Q_s is the factor of the roughness. We can notice that, when Q_s increases, the total quality factor approaches to the ideal quality factor of the disk. Thus, a higher Q_s refers to a disk with less surface roughness.

Consequently, in this forced regime, the propagation of light inside the disk is supposed to be described by the sum of the clockwise and counter clockwise WGM forming a stationary resonant mode. As the ideal microdisk follows a revolution symmetry, the stationary mode solutions (even and odd with respect to the vertical symmetry axis passing by the center of the disk for example) are degenerated, and only one resonance is expected to a given azimuthal and radial order too. In contrast, experimental investigations on high Q-factor microdisks have reported the observation of doublet of resonances for a given azimuthal order [61, 117]. This doublet has been explained by the effect of surface roughness coming from the realization steps (photolithography and etching process)..

The same type of doublet can be also predicted by numerical simulations by exciting the even and odd stationary waves. Indeed, numerical simulations use in general a spatial mapping which discretize the structure in small squares or basic elements. This feature is defined by the staircase phenomena explained in the previous parts. So, an artificial roughness can appear with curvilinear or non-rectangular structure and the field projection is also not respected.

For Fourier methods, the spectral truncation of the series induces a small modification of the boundary profile. Moreover, the use of lamellar discretization can affect the normal vector evolution from the ideal case. As mentioned before the DM-FFF is sensitive to the spectral truncation whereas the both ones modify the response of the FMM. In this case, the symmetry evolution is not anymore respected. A plane symmetry can be defined. And the even and odd mode resonant wavelengths are not anymore in this case degenerated. This phenomena must more be observed with the a-FMM than the a-DM-FFF. It can be interesting to use the a-DM-FFF in order to see the gain in accuracy for the wavelength resonance calculation of the CW and anti-CW modes. Actually, the staircase approximation of the a-FMM creates an added artificial degeneracy of the symmetry especially with high contrast index resonators which induce a reduction in the analytically calculated Q-factor and the spacing between the CW and anti-CW modes. Indeed, it can be shown that at a first order the reflection brought by the roughness is proportional to $\Delta n^2 = n_d^2 - n_{ext}^2$ [61].

8.2.3 Microdisk cavities excited by plane waves

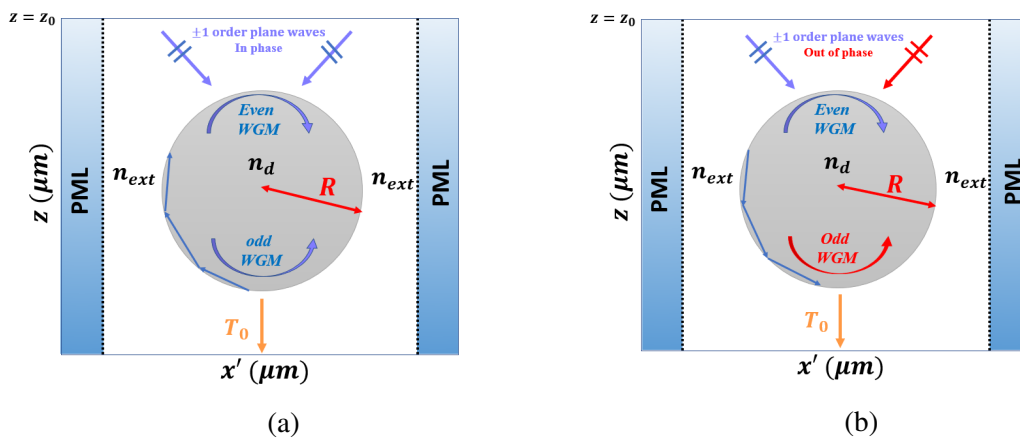


Fig. 8.9 Schematic top view of microdisk resonator (a) Excitation by two in phase plane waves, at the resonant wavelength clockwise WGM is coupled to the disk (b) Excitation by two out of phase plane waves, at the resonant wavelength anti-clockwise WGM is coupled to the disk.

To upraise the performance of the a-DM-FFF, the microdisk of Fig.8.9 has been taken into consideration. The equation of normal vectors used in the propagation Eq.(7.6) are detailed in Appendix.B. To simulate the disk as an isolated structure, a total PML of thickness $q_x = 1\mu\text{m}$ is considered at the boundary of the unit cell ($0.5\mu\text{m}$ from each side). Meanwhile, to differentiate the resonant wavelengths of the even mode (sum of the CW and anti-CW traveling modes) and the odd mode (difference of the CW and anti-CW traveling

modes) two situations are considered. Indeed, the odd mode can be excited by illuminating the structure by two symmetrical plane waves with respect to the central vertical axis of the disk. They are characterized by having the same amplitude and the same phase (in phase) as the depicted in Fig.8.9.(a). On the other hand, the even mode can be excited by two symmetrical plane waves with the same amplitude and opposite phase (out of phase) as depicted in in Fig.8.9.(b). We have to mention that the excitation with plane waves is not the optimal case with microresonators. But, for simplicity reasons, a general idea of the problem can be extracted by using it. To numerically present the difference, the resonant wavelengths of both modes (odd and even) have been numerically computed with the zeroth order transmission spectrum using both the a-FMM and the a-DM-FFF for isolated microdisks with different radii from one side and different refractive index from the other side. Moreover, a truncation order $N = 60$ has been considered for both methods, $D_z = 10nm$ and $N_{FFT} = 8192$ samples have been used.

The optimized wave to excite the microdisk must be a Hankel function [23, 101, 113]. But due to the method algorithm, it is firstly easier to use plane waves excitation. So, the phase and amplitude matching is far to be ideal but a small part of the signal emitted is coupled to the cavity mode. As the optical leaking is radial, a decrease of the transmission order 0 is expected. To optimize the coupling, the incident angle of the plane wave is changed following the azimuthal order of the WGM. And finally, the effect of the PML is considered negligible on the transmission analysis.

Microdisk resonator with $n_{ext} = 1$ and $n_d = 2.2$

Here, the external medium is air with $n_{ext} = 1$ and the refractive index of the disk is $n_d = 2.2$. As $\Delta n = n_d - n_{ext} = 1.2$, the high Q-factor can be obtained using disk with R in the range of few microns. In Table.8.3, the analytically calculated values of the resonant wavelength and the quality factor are given for different radii. Indeed, the ideal structure can be studied analytically (cylinder without roughness [76]). Disk radii from $1\mu m$ to $4\mu m$ with $0.5\mu m$ step have been chosen for this study.

Fig.8.10.(a) presents the transmission spectrum while exciting the odd and the even mode of $R = 4\mu m$. As the interface evolution of the microdisk is taken into consideration with the a-DM-FFF, the resonant wavelengths of both the in phase and out of phase excited plane waves are almost at the same position. Indeed, $\lambda_{odd} = 1.54398256\mu m$ and $\lambda_{even} = 1.54398825\mu m$. Thus, a doublet splitting $|\lambda_{odd} - \lambda_{even}| = 5pm$ is then obtained. This difference can be a result of the truncation of the Fourier series of the a-DM-FFF which creates a very small surface roughness. On the other hand, and due to the staircase approximation, a higher

A-DM-FFF COMPARED TO THE A-FMM: APPLICATION ON COMPLEX SHAPED PHOTONIC GUIDED STRUCTURES

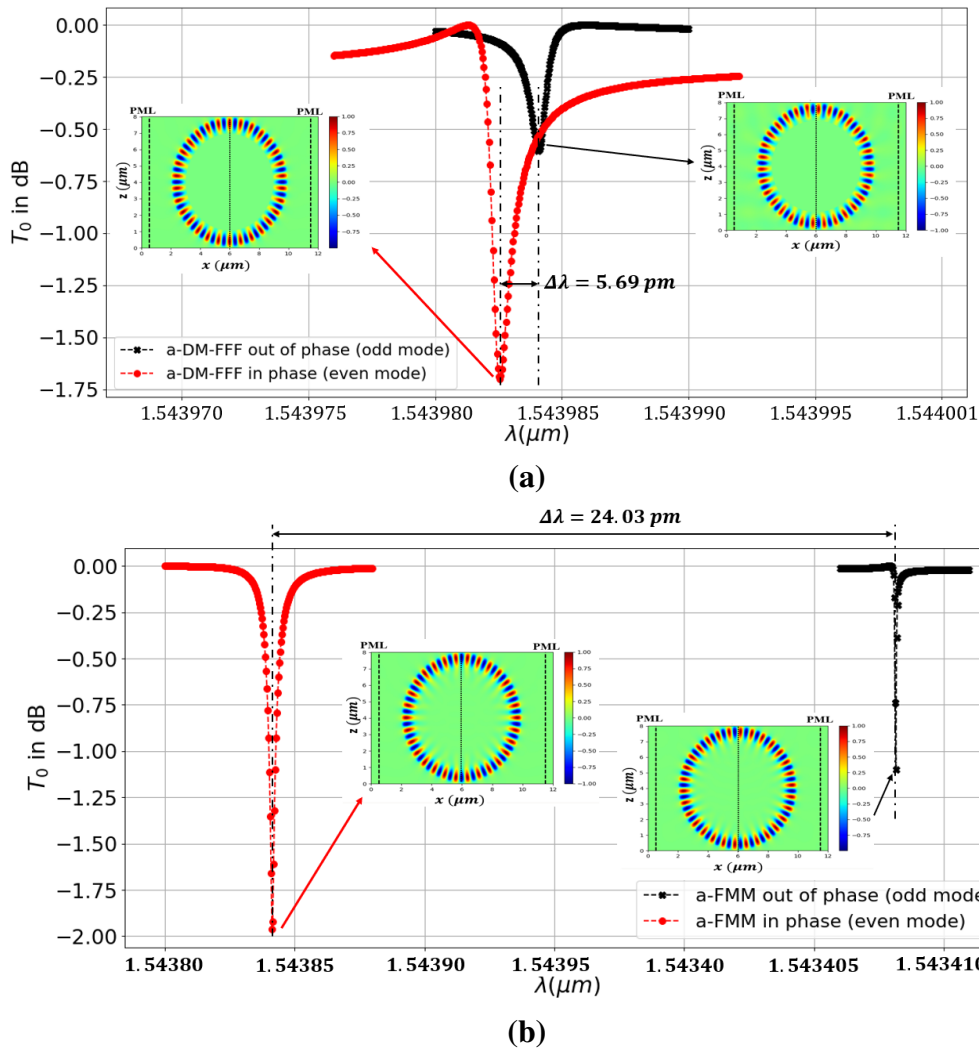


Fig. 8.10 The zeroth order of transmission response of the excited in phase and out of phase plane waves of the microdisk with $R = 4\mu m$ (a) Using the a-DM-FFF (b) Using the a-FMM. The small subfigures represent the field map of the magnetic field $Real(H_y)$ at the resonant wavelengths with $m = 30$ (azimuthal order). The central axis belongs to the radial axis of symmetry where the in phase or out of phase excitation can be distinguished (optimum in case of the in phase excitation and zeroth in the out of phase case).

artificial degeneracy of the two modes is generated with the a-FMM. The resonances are thus excited at $\lambda_{odd} = 1.54338415\mu m$ and $\lambda_{even} = 1.5436101\mu m$. A doublet splitting of $24\mu m$ can be obtained which correspond to ≈ 5 times more split than the a-DM-FFF result. Three conclusions can be extracted: 1) the staircase approximation increases the appearance of the degeneracy of the odd and even modes. In case of the a-FMM of the staircase approximation and the truncation of the Fourier series are the two factors of the splitting, while in

8.2 APPLICATION OF THE A-DM-FFF ON RESONANT CAVITIES: MICRODISK
RESONATORS AS EXAMPLES

R	λ_a	m_a	Q_a	$\lambda_{a-DM(even)}$	$\lambda_{a-DM(odd)}$	$\lambda_{a-FMM(even)}$	$\lambda_{a-FMM(odd)}$
1.0	1.469998	6	$8.27 \cdot 10^1$	1.466075	1.465075	1.465075	1.464075
1.5	1.60310	9	$1.13 \cdot 10^3$	1.60270	1.60210	1.601950	1.60150
2.0	1.5850384	13	$4.38 \cdot 10^4$	1.5846915	1.5846630	1.5840206	1.5838580
2.5	1.58225721	17	$1.87 \cdot 10^6$	1.58191746	1.5818889	1.58120482	1.58116346
3.0	1.52148747	22	$2.23 \cdot 10^8$	1.52116075	1.52115697	1.52074197	1.52069175
3.5	1.53376472	26	$1.08 \cdot 10^{10}$	1.53344428	1.53343865	1.53285197	1.53281788
4.0	1.54398412	30	$5.41 \cdot 10^{11}$	1.54398256	1.54398825	1.54340816	1.54338413

Table 8.3 The resonant wavelengths with respect to the radius of the disk R for odd and even modes calculated via the a-DM-FFF and the a-FMM. $n_{ext} = 1$, $n_d = 2.2$ and all the values are calculated in μm . λ_a , m_a and Q_a represents the analytically calculated values of the resonant wavelength, the azimuthal order of this wavelength, and the quality factor of the microdisk at this wavelength respectively.

case of the a-DM-FFF, only the truncation of the Fourier series induces the splitting of the wavelengths. 2) the staircase approximation induces a higher relative error of the values of resonant wavelengths with respect to the analytical ones. (Table.8.3). 3) the average values of the both resonant wavelengths of each method are not the same. So, the staircase modifies slightly the disk diameter and induces the red shift of the resonance.

Now, let's define the normalized doublet splitting factor Q_b as:

$$Q_b = \frac{\lambda_0}{\Delta\lambda} \quad (8.2)$$

With $\lambda_0 = \frac{\lambda_{odd} + \lambda_{even}}{2}$ and $\Delta\lambda$ is the wavelength difference between the even and the odd modes. Fig.8.11 illustrates Q_b for each of the measured microdisk radii, where for each microdisk we chose the nearest azimuthal order which resonates near $\lambda = 1.55\mu m$ for the first radial order as with this last one the field interaction with the disk-edge surface is maximized.

Eq.(8.2) tell us that when Q_b increases the doublet splitting decreases. The red dashed curve belonging to the a-FMM shows an evolution of Q_b between 3×10^{-4} and 5×10^4 for R between 2.5 and $4\mu m$. In contrast, the splitting quality factor increases to reach 2×10^5 with the a-DM-FFF for $R = 4\mu m$. It is clear that a saturation effect appears for $R > 3\mu m$, this saturation may refer to the limit of the methods due to the truncation order, the FFT or the other approximations. As a conclusion, a four times less splitting distance can be obtained with the a-DM-FFF than the a-FMM and a thus a four times higher range of accuracy can be reached. Finally, it is important to mention that, the resonant wavelengths of the a-DM-FFF act on the fifth digits compared to the analytical resonant wavelengths whereas the a-FMM

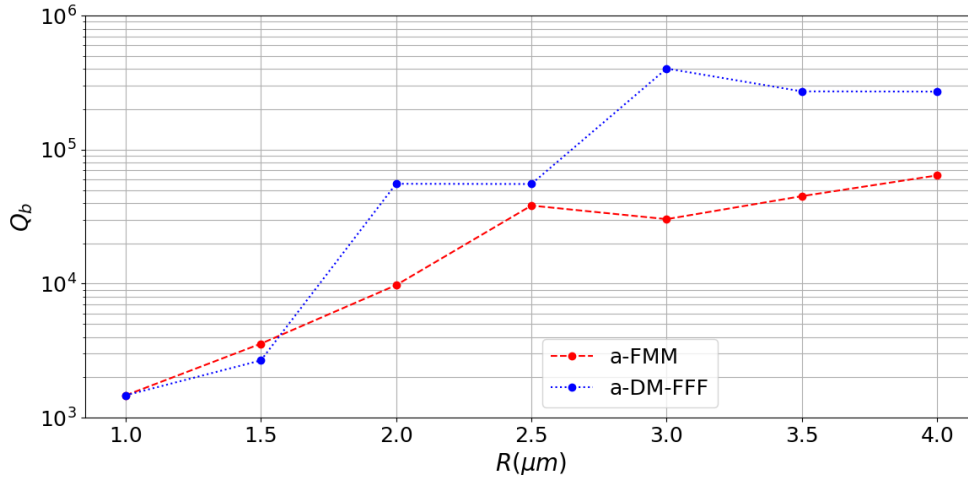


Fig. 8.11 Normalized doublet splitting quality factor (Q_b) versus disk radius for $n_d = 2.2$ and $n_{ext} = 1$.

acts on the fourth ones where a factor of 4 is always brought in terms of accuracy and precision.

Microdisk resonator with $n_{ext} = 1$ and $n_d = 3.5$

R	λ_a	m_a	Q_a	$\lambda_{a-DM(even)}$	$\lambda_{a-DM(odd)}$	$\lambda_{a-FMM(even)}$	$\lambda_{a-FMM(odd)}$
0.5	1.48758096	4	$5.18 \cdot 10^2$	1.48660	1.486350	1.481970	1.48220
0.6	1.53430586	5	$2.81 \cdot 10^3$	1.53353600	1.53361600	1.52776500	1.52725750
0.7	1.57409564	6	$1.55 \cdot 10^4$	1.57353840	1.573310	1.5681470	1.5677150
0.8	1.60818887	7	$8.65 \cdot 10^4$	1.6075660	1.60750	1.60259250	1.60227550
0.9	1.49714659	9	$2.79 \cdot 10^6$	1.49660728	1.49649913	1.49231015	1.492030
1	1.53299473	10	$1.61 \cdot 10^7$	1.53243560	1.53237130	1.5283550	1.52815470
1.1	1.56439931	11	$9.41 \cdot 10^7$	1.56385524	1.56375904	1.55996492	1.55878497
1.3	1.52224909	14	$1.94 \cdot 10^{10}$	1.52167620	1.52166768	1.51834933	1.51820608
1.5	1.57312083	16	$7.02 \cdot 10^{11}$	1.57257480	1.57256526	1.56940881	1.56928430
2	1.54153745	23	$2.46 \cdot 10^{17}$	1.54100288	1.54099328	1.53853509	1.53841403

Table 8.4 The resonant wavelengths with respect to the radius of the disk R for odd (in phase) and even (out of phase) modes calculated via the a-DM-FFF and the a-FMM. $n_{ext} = 1$, $n_d = 3.5$ and all the values are calculated in μm . λ_a , m_a and Q_a represents the analytically calculated values of the resonant wavelength, the azimuthal order of this wavelength, and the quality factor of the microdisk at this wavelength respectively.

As demonstrated in section 8.1.3, the a-FMM suffers from slower convergence, loss of accuracy and higher impact of the staircase approximation with high contrast refractive

index. For that, a cylinder of silicon with $n_d = 3.5$ is now considered. The numerical calculation of the resonant wavelengths reveals that the a-DM-FFF gives more accurate values of resonant wavelengths especially for $R > 0.8\mu m$ where the Q-factor of the disk is higher (see Table.8.4). Moreover, in terms of the splitting degeneracy, the same mechanism is observed. A difference of even and odd resonant wavelengths that varies between 10^{-4} and $10^{-5}\mu m$ can be achieved with the a-DM-FFF between $R = 0.5\mu m$ and $2\mu m$ respectively. On the other hand, the a-FMM reveals a doublet splitting difference for all the values of R in the range of $10^{-4}\mu m$. So that, a predominance splitting reducing factor of 10 can be achieved with the a-DM-FFF (factor of 4 with $n_d = 2.2$). Following the same methodology of the previous study, the normalized doublet splitting factor Q_b will be illustrated following the evolution of R (Fig.8.12). When R increases, so that the intrinsic Q-factor increases Q_b dramatically increases with the a-DM-FFF to reach a value of 1.8×10^5 for $R = 1.3\mu m$ (blue dashed curve). In contrast, Q_b of the a-FMM increases slowly to reach a value of 1.05×10^4 for the same R (red pointed curve). After this R, Q_b of both methods stabilizes following R and indicating the limitation of both methods due to the approximation constraints mentioned before and its evolution following $R^{3/2}$ [8]. Again, this result reaffirms that the artificial roughness brought by the approximations of the methods creates the break of symmetry of the odd and even modes which finally leads to the higher wavelengths splitting of both modes of the microdisk. From our numerical simulations, we can assume that the accuracy factor brought by the a-DM-FFF is directly proportional to the contrast of permittivity $\Delta\epsilon$.

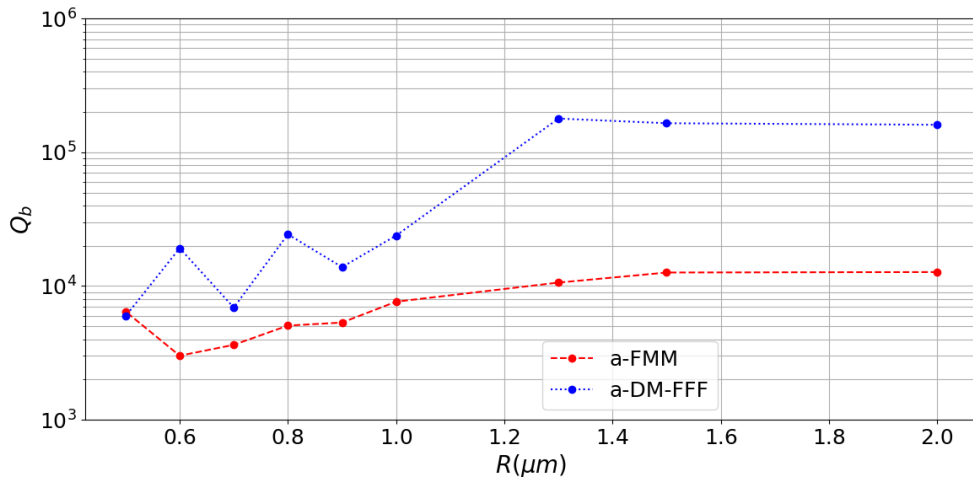


Fig. 8.12 Normalized doublet splitting quality factor (Q_b) versus disk radius for $n_d = 3.5$ and $n_{ext} = 1$.

8.2.4 Microdisk-guide coupling

Introduction

Circular high-index contrast microdisk resonator associated with optical waveguide are able to support highly-confined WGM with high Q-factors. For that, they are widely used as microlaser cavities [53, 77], channel dropping filters [60], WDM demultiplexers [19], and as notch and add-drop filters [29, 97]. Indeed, with high contrast refractive index, high quality factors compact lasers sources can be obtained with few microns of diameters. Nevertheless, such systems requires the association of optical waveguides in order to correctly operate. In other words, the waveguides work as intermediate medium that allow the recovering and the injection of light into the resonator using the evanescent wave coupling [67].

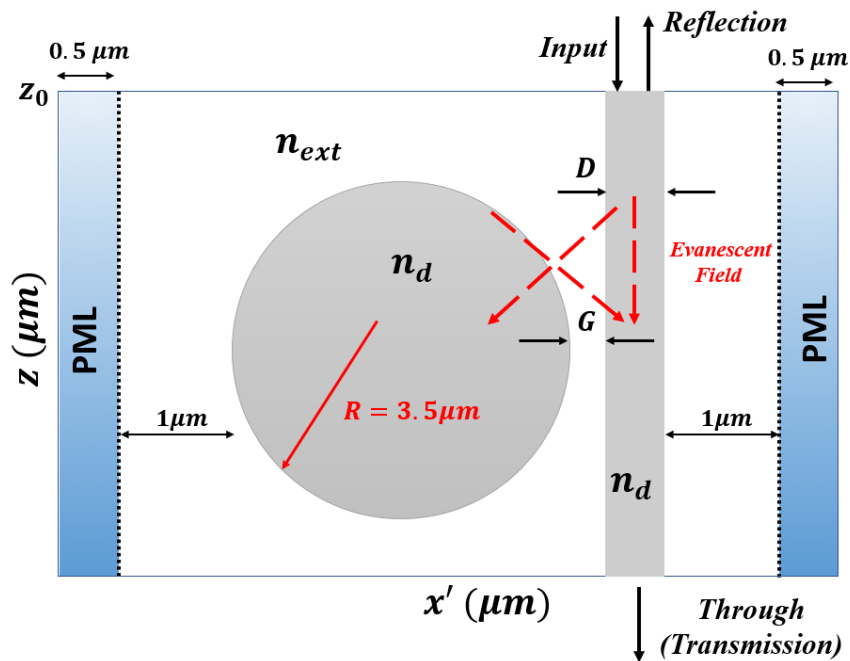


Fig. 8.13 Unit cell of an artificially periodized 2D microdisk resonator associated to a bus waveguide.

Now, as the evanescent coupling through a waveguide is the most common used method to excite the WGM in microdisk resonators, the effect of adding a bus waveguide to the microdisk will be studied using the a-FMM and the a-DM-FFF. Indeed, the association of the waveguide break more and more the symmetry of the structure and lead to an additional asymmetry as the disk to guide transition is not necessarily adiabatic.

To bring forward this impact on such structures, the 2D microdisk resonator depicted in

Fig.8.13 has been taken into account. The opto-geometrical parameters are the following: $n_d = 2.2$ and $n_{ext} = 1$. Moreover, a monomode bus waveguide of width $D = 380nm$ is selected to ensure that only one mode can propagate in the wavelengths spectrum of $1.4\mu m$ to $1.6\mu m$. Always the fundamental TM mode is chosen to illuminate the input waveguide.

Coupling regimes

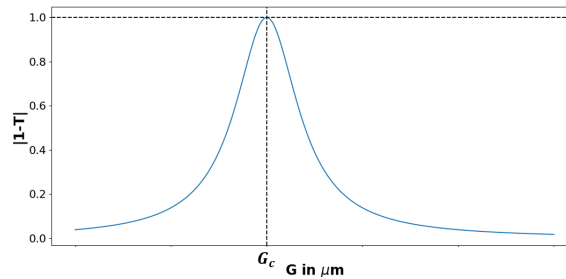


Fig. 8.14 Schematic representation of the proportional of the transmission $|1 - T|$ with respect to the disk to guide gap G .

With the evanescent wave coupling, the gap G plays a major role in the coupling and decoupling efficiency between the guide and the microdisks. In other words, the overlap between the resonant mode of the disk and the evanescent wave of the guide determines the amount of light coupled in the resonator. As a result, three regimes can be identified by manipulating the gap G as depicted in Fig.8.14 and described as:

- **Over-coupled:** It happens when decreasing the gap $G < G_c$ between the resonator and the guide. This effect decreases the amount of light coupled to the disk since the light is scattered by the waveguide.
- **Critical coupling:** It represents the value where $G = G_c$. Here, the transmission is considered perfect $T \approx 0$ so that $|1 - T| \approx 1$. At this point all the light is coupled into the resonator.
- **Under coupling:** It happens for $G > G_c$. In that case, a small amount of the guided mode overlaps with the resonant disk mode.

When the guide is associated to the microdisk, an additional quality factor Q_c which represents the quality factor of the coupling must be added to the equation of the total Q-factor. Thus, Eq.(8.1) can be reformulated as,

$$\frac{1}{Q} = \frac{1}{Q_i} + \frac{1}{Q_s} + \frac{1}{Q_c} \quad (8.3)$$

Indeed, the decreases of the coupling efficiency induces a higher Q_c and thus when Q_c and $Q_s \rightarrow \infty$, Q can reach the quality factor of the ideal resonator.

Analytical fitting equations

In order to facilitate the calculations of the Quality factor Q and the degeneracy difference $\Delta\lambda$ between the odd and even WGM, the resonance in optical resonator is ideally described following a Lorentzian function,

$$F(\omega) = \frac{E_0^2}{4(\omega - \omega_0)^2 + \gamma^2}$$

With $\omega = \frac{2\pi}{\lambda} (rd/\mu m)$ is the angular frequency. E_0 is the efficiency of either the transmitted or the reflected power, and ω_0 is the central angular frequency. In the ideal case, and if $\omega = \omega_0$, $F(\omega_0) = E_0^2/\gamma^2$. The frequencies of the bandwidth obtained when the maximal power is divided by two $\Delta\omega$ are calculated for $F(\omega) = F(\omega_0)/2$. Thus, $\gamma = \frac{1}{Q} = \frac{\Delta\omega}{\omega_0}$. Moreover, with such structures, the transmission spectrum is characterized by a band reject (notch) filtering effect. Therefore, to fit well with the Lorentzian function, we must consider $F(\omega) = |1 - T(\omega)|$.

Practically, the roughness of the periphery of the microdisks arises the presence of reflections. We know that the propagating wave in a given direction is generated by the sum of two stationary waves. Nevertheless, this roughness breaks the symmetry of the odd and even modes of the stationary waves and induces the reflections. In case of ideal resonators, the two stationary modes are degenerated and resonate at the same wavelength. In contrast, with the presence of the roughness, a degeneracy of modes appears by arising the appearance of the doublet. Now, the sum of these two modes results a propagating wave in a given direction. But, it also generates another anti-propagating mode taking the form of reflections. The filtering effect is therefore characterized by the presence of doublet. This doublet can be only identified if the quality factor of the roughness is equivalent to the intrinsic quality factor of the disk Q . Finally, for $G = G_c$ and if the doublet splitting doesn't exist, almost null transmission and reflection coefficients can be obtained at the resonant wavelength (ideal case) [122]. If the doublet exists, both reflection and transmission may not attain zero. The Lorentzian fit of the doublet can be described by a sum of two Lorentzian functions shifted in frequency. Thus, it can be expressed as,

$$F(\omega) = \frac{E_0^2}{4(\omega - \omega_0)^2 + \gamma^2} + \frac{E_0^2}{4(\omega - \omega_0 + \Delta\omega)^2 + \gamma^2}$$

With, $\Delta\omega$ is the difference between the resonant wavelengths of the two peaks. For simplicity reasons, we assumed here that the amplitudes of the peaks are identical which is not necessarily the case. More degree of freedom can be added by adding other constants to the previous fitting equation. Moreover, as the peaks of doublet are equal and it corresponds to a sum of two resonances, the quality factor has been calculated for one peak.

Numerical simulation

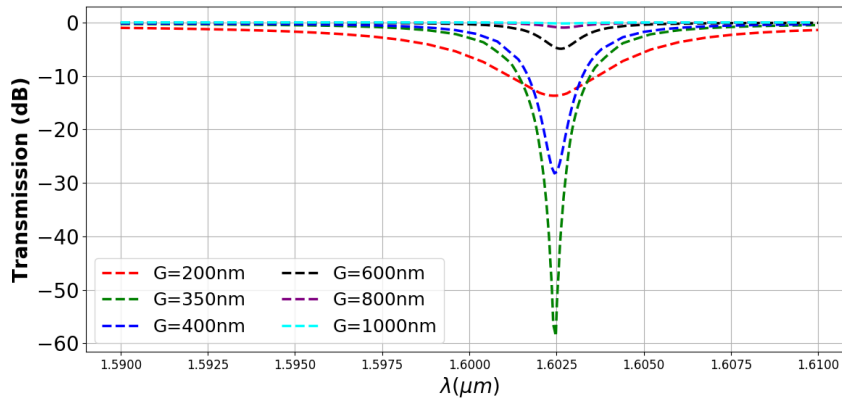
The Lorentzian equations explained in the previous part will be used to fit the numerical results obtained by the a-DM-FFF and the a-FMM with $N = 60$, $D_z = 10nm$ and $N_{FFT} = 8192$ samples. And therefore, predicts the quality factor Q and the modes degeneracy distance $\Delta\lambda$ (μm). For the structure of Fig.8.13, all the parameters are constant, only the gap G will be varied. The PML thickness is $0.5\mu m$ from each side and the distance from the PML to the periphery of the disk from the left side, and to the guide from the right side is always $1\mu m$. The transmission spectrum has been numerically calculated for different values of the gap G .

Numerical results for $R = 1.5\mu m$

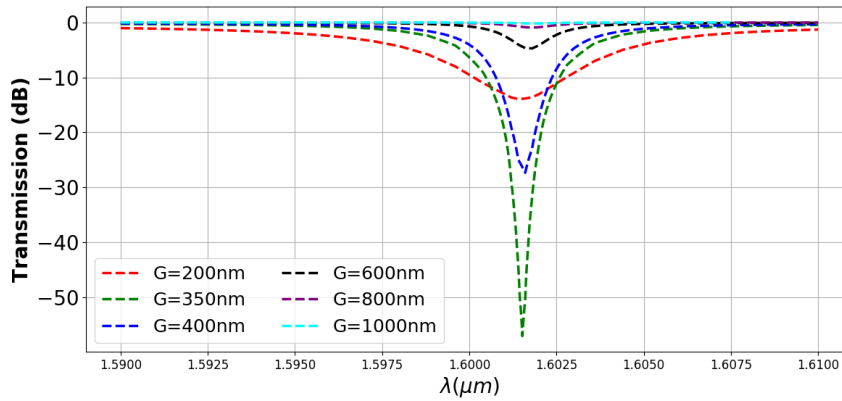
Firstly, the disk with radius $R = 1.5\mu m$ has been chosen. The analytical calculated results of Tab.8.3 tell us that the quality factor of the isolated disk resonator with $R = 1.5\mu m$, $n_{ext} = 1$ and $n_d = 2.2$ is $Q = 1130$. We aim to analyse the azimuthal order $m = 9$. Practically, this structure is not considered as high quality factor resonator. In that case, the effect of the roughness of the surface is considered negligible as the respective quality factor associated to the roughness is higher than the intrinsic quality factor. Therefore, the wavelength splitting must not appear with such resonators.

Fig.8.15 illustrates the calculated transmission spectrum of the microdisk associated to the waveguide for different gaps G using the a-DM-FFF and the a-FMM. The spectral response of both methods is similar with a blue shift of the a-FMM due to the small impact of the discretization. Indeed, the phase should stay constant in every round inside the disk. Moreover, it is proportional to both the effective index of the disk and the optical path effected by each round (i.e $n_{eff} \cdot \text{Round}$). On the other hand, the phase is inversely proportional to the applied wavelength. Thus, if the wavelength decreases, the optical path increases and the real part of the effective refractive index decreases. Hence, the optical mode is more affected by the surrounded medium (air) than the material of the disk.

As it is expected, the doublet splitting doesn't appear here. Only one peak of resonance exists for the different gap and with both methods. The expected critical coupling occurs



(a)



(b)

Fig. 8.15 Spectral calculations as a function of the wavelength for different gap G between the cylinder and the guide calculated by using (a) a-DM-FFF (b) a-FMM.

for $G = 350\text{nm}$ with both methods. So either the a-FMM or the a-DM-FFF can be used to modelize low quality factor structures without any impact of the staircase approximation of the a-FMM on the results.

Furthermore, the evolution of the quality factor has been studied following the gap G with both methods. The coupled mode theory (CMT) explained in Ref.[41] has been used to analytically compare the quality factors calculated using the Lorentzian fit (explained in the previous section)

The respective results are shown in Fig.8.16. The three methods tend toward the value of a single cylinder quality factor over $G = 1000\text{nm}$ where the effect of the waveguide becomes negligible. The analytic method (CMT) follows the evolution of the two method curves.

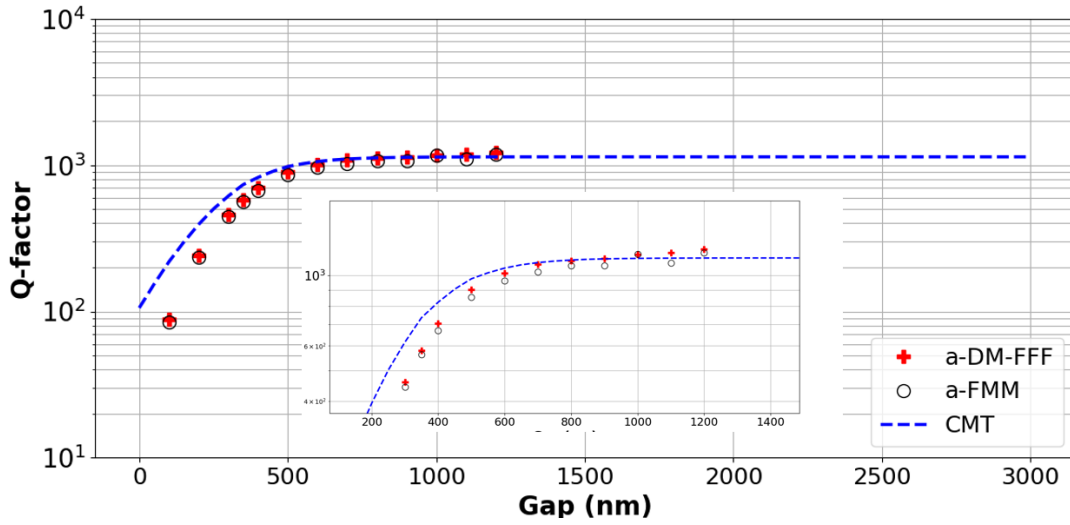


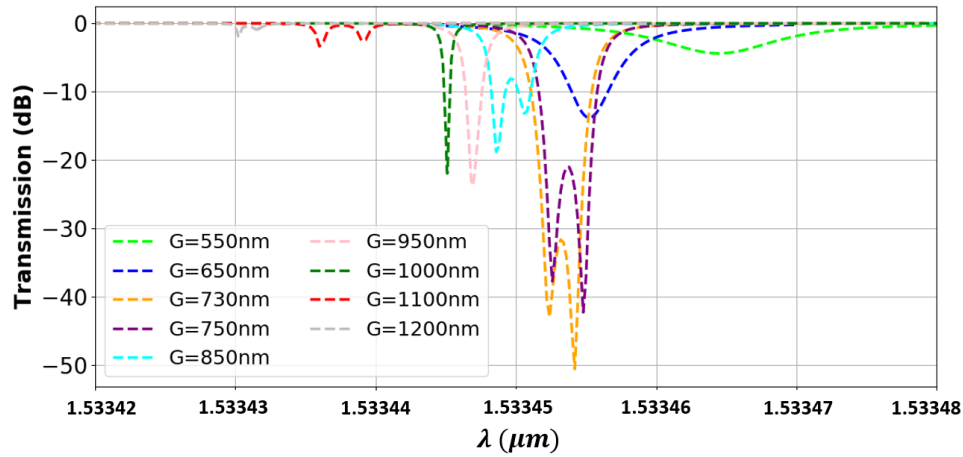
Fig. 8.16 Comparison of the quality factor evolution with the gap between the analytical method (CMT) and the 2D a-DM-FFF and the 2D a-FMM.

Moreover, the quality factors of the a-FMM follows exactly the a-DM-FFF with the increases of G .

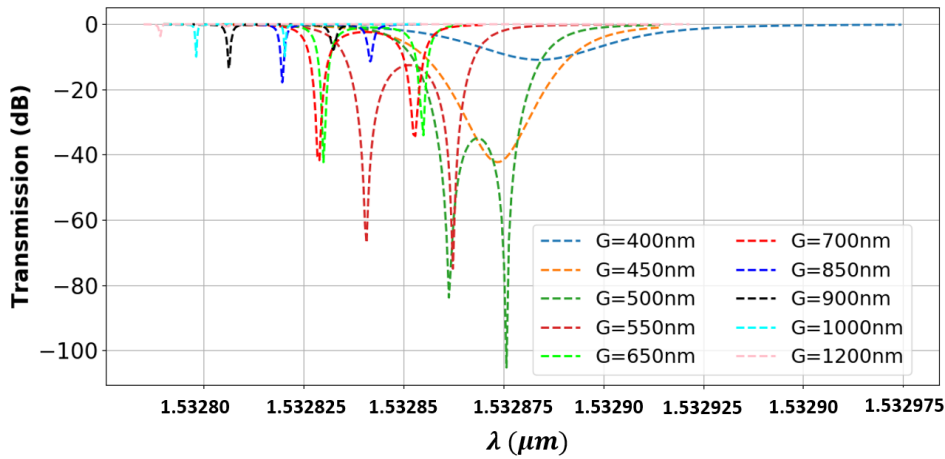
As a result, with low quality factor resonators, either the a-DM-FFF or the a-FMM can be used, a small blue shift in resonant wavelegnths is obtained with the a-FMM due to the staircase approximation. Moreover, the quality factor of the a-DM-FFF is slightly higher than the factor calculated by the a-FMM (zoomed part of Fig.8.16). So, in the next section the a-DM-FFF will be tested with higher quality factor.

Numerical results for $R = 3.5\mu m$

Analytically, the quality factor of the single microsidk with $R = 3.5\mu m$ is $Q = 1.08 \times 10^{10}$. Using the same optogeometrical parameters of the structures with $R = 1.5\mu m$. The reflection / transmission spectrum and the quality factor of the microdisk associated with the bus waveguide will be studied for different gaps G . In Fig.8.17, and for small gaps ($G = 550nm$ to $650nm$ with the a-DM-FFF and $G = 400nm$ to $450nm$ with the a-FMM), large transmissions. In this gap range, the quality factor of the coupling Q_c is prominent from the isolated disk ones Q_i and Q_b induced by the roughness. It is important to mention that with the a-DM-FFF the fifth digits of the wavelengths changes while the fourth is affected with the a-FMM. This large resonance is a direct consequence of the over coupled regime ($G < G_c$). Now, when G increases the coupling between the disk and the bus waveguide decreases (Q_c increases) until an equivalent critical coupling is achieved with the a-DM-FFF for $G_c = 730nm$ and $G_c = 500nm$ with the a-FMM. In this case, the filtering effect is more efficient but the doublet begins to appear. At this stage, the effect of the break of symmetry



(a)



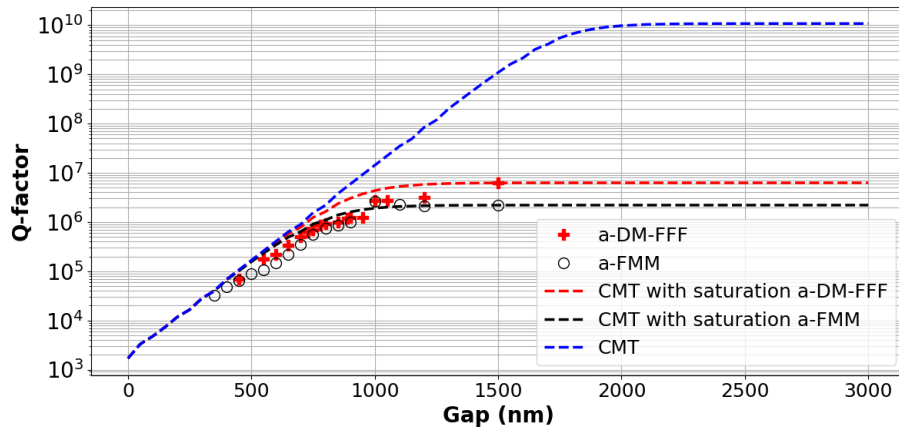
(b)

Fig. 8.17 Spectral calculations as a function of the wavelength for different gap G between the cylinder and the guide calculated by using (a) a-DM-FFF (b) a-FMM.

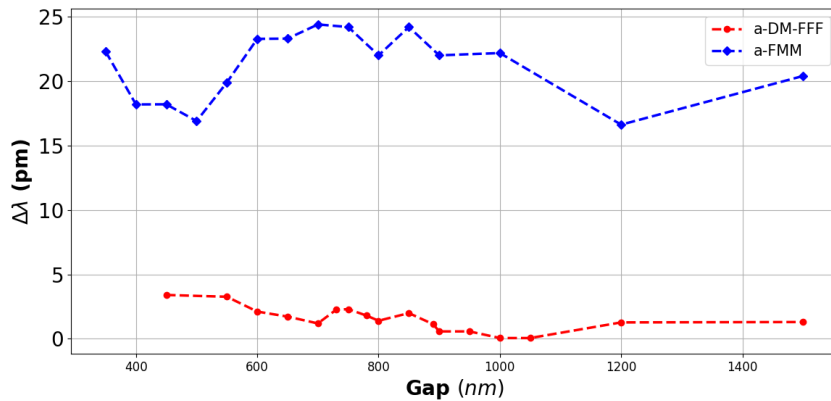
induced by the bus waveguide and the profile truncation begins to arise. Moreover, a smaller wavelength difference between the two peaks is obtained with the a-DM-FFF. This effect can degraded the filtering due to the removing degeneracy. In this domain Q_i , Q_c and Q_s are close. For this last method, the coupling efficiency decreases for higher G and we enter in the regime of under coupling. Thereafter, two curves are interesting in Fig.8.14.(a), mainly for $G = 950nm$ and $G = 1000nm$. Here, it is clear that the doublets are invisible, we think that at this stage, the effect of roughness cancels the asymmetry due to the bus waveguide which only induces one narrow band resonance. For $G > 1000nm$, the doublets show up again. The small effect of the roughness of the cylinder is presented and the structure tends to the isolated disk case. In contrast, with the a-FMM and as the impact of the surface roughness

is stronger than the effect of the bus waveguide, two resonances which correspond to the odd and even modes are always obtained. Q_s seems to be smaller than Q_c without a possible compensation.

The resulting model of the Lorentzian functions is used to fit the data of Fig.8.17 in order to facilitate the calculation of the linewidth parameters, the quality factor Q , the central angular frequency ω_0 and the doublet splitting $\Delta\lambda$.



(a)



(b)

Fig. 8.18 (a) The evolution of the Q-factor calculated by the fitting equation following G for $n_d = 2.2$ and $n_{ext} = 1$. (b) The evolution of the doublet splitting $\Delta\lambda$ following G for the a-FMM and the a-DM-FFF.

Fig.8.18.(a) illustrates the evolution of the total quality factor Q of one peak following G which is predicted by the Lorentzian fitting equations. The blue, black and red dashed curves represent the quality factor analytically calculated by the coupled mode theory. The red and black curve are saturated with respect to the values of the a-DMM-FFF and the a-FMM respectively for $G = 1500nm$ (after this gap, the transmission spectrum vanishes

and the Q-factor can't be calculated). Indeed, the Q-factor of both methods increases in monotonic way following the increases of G and fit very closely to the saturated curves of the CMT. With the a-DM-FFF, $Q = 7 \times 10^4$ is reached for $G = 450nm$ and $Q = 2 \times 10^6$ is obtained for $G = 1000nm$. Nevertheless, for $G \geq 1000nm$, the Q-factor of the a-FMM stops his growing and stabilizes following the evolution of G . This stability is a direct consequence of the calculation limit of the a-FMM due to the staircase approximation, and in this case, Q is different than Q_s . In the other hand, the Q-factor calculated by the a-DM-FFF continues its expansion to reach a value of 6×10^6 for $G = 1500nm$. A gain ratio of 4 is reached between the saturation value of the a-DM-FFF and the value of the a-FMM. The truncation of the Fourier series induces a saturation in the range of 10^6 while the analytical quality factor is in the range of 10^{10} (blue dashed curve). To summarize, the scattering effect at the periphery of the disk is directly visualized in Fig.8.18.(a). This analysis was difficult to see for the isolated disk analysis due to the miss-adapted excitation technique. The gain in Q-factor demonstrates again the performance of our novel method even with not high contrast refractive index structures.

In addition, Fig.8.18.(b) shows the wavelength splitting in picometers (pm) with respect to the evolution of the gap. We can notice that both methods follows at a first order the same evolution. Indeed, this evolution decreases to attain a minimum and then it increases after a given G . With the a-DM-FFF, the opposition of both effects (surface roughness and guide asymmetry) compensate to reach a value of zero (no wavelengths splitting). Moreover, we can notice that, for $G > 1000nm$ (a-DM-FFF) and $G > 1200nm$ (a-FMM), there is a more fluctuating zone delimited by the appearance of the doublet. At this stage, $1/Q_i + 1/Q_s > 1/Q_c$ (effect of guide coupling decreases). Indeed, the wavelength splitting $\Delta\lambda$ is reduced by a factor of 10 while using the a-DM-FFF.

Finally, in order to highlight the effect of wavelength splitting with respect to the ideal case, the minimum of the transmission and the maximum of the reflection for a given gap G have been illustrated in Fig.8.19 for the a-DM-FFF and the a-FMM. Indeed, in the ideal case, the transmission must separates the system into the three resonance regimes described before. At $G = G_c$, the transmission and the reflection must attain zero. Indeed, due to the wavelength splitting, the not expected excitation of the anti-CW WGM induces a non negligible rate of reflections which must attain zero using the temporal perturbation theory which remains an approximation of the real case [8]. With the a-DM-FFF, the equivalent critical coupling is reached with $G = 730nm$ where a first minimum of transmission $T_g = -45dB$ is found. Nevertheless, due to the wavelength splitting, a maximum of the reflection coefficient $R_g = -3.5dB$ is also obtained. When the two break of symmetry effect

8.2 APPLICATION OF THE A-DM-FFF ON RESONANT CAVITIES: MICRODISK RESONATORS AS EXAMPLES

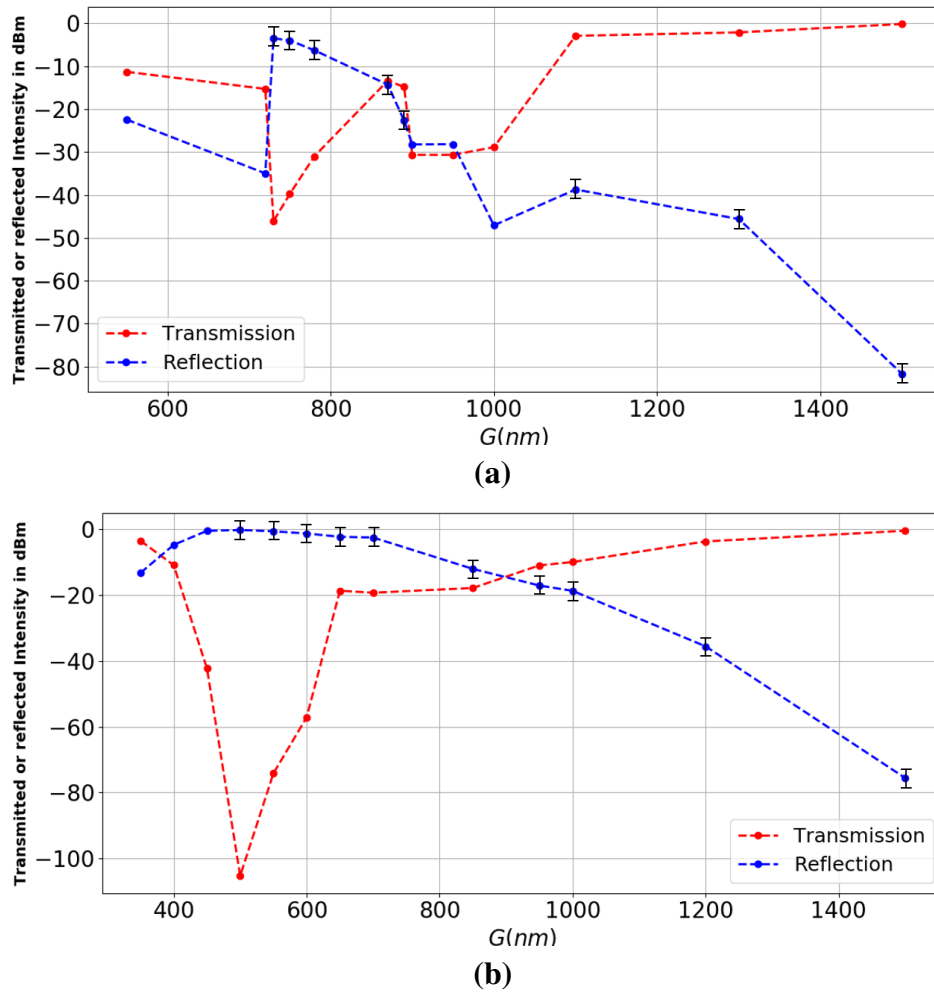


Fig. 8.19 The evolution of the minimum transmission intensity and the maximum reflection intensity following the gap G for the (a) a-DM-FFF (b) a-FMM. The black bars belongs to the gap where the doublet clearly appears in the spectrum.

combines destructively (the effect of the roughness of the disk and the bus waveguide), another minimum of transmission is attained for $G = 1000nm$ where $T_g = -30dB$. But, as the doublet is now weak, the power is quasi transmitted to the CW WGM which strongly reduces the reflection relied to the excitation of the anti-CW WGM. A reflection of $-48dB$ is reached in this case. After this value, we enter in the under-coupling regime. In this domain the interaction between the microdisk and the waveguide becomes more and more smaller. So the transmission tends to $0dB$ and the reflection tends to $-\infty dB$, the asymptotic case of the isolated waveguide.

In contrast, when the critical coupling of the a-FMM is reached ($G = 500nm$), a minimum of transmission is attained. This drop of transmission induces a maximum of reflection of

$-0.2dB$ due to the high effect of the roughness of the surface. Indeed, as the staircase approximation impact is always predominant on the effect of the guide with the a-FMM, there is no compensation of effects in that case, the doublet never reach zero and always the high reflection exists around the critical coupling region.

As a conclusion, in spite of taking the evolution of the profile into consideration with the a-DM-FFF, the surface roughness always exists due to the truncation of the Fourier series. Compared to the analytical values calculated by the perturbation theory, this method can take all the restriction of this last method into consideration especially in TM polarization where the field is discontinuous at the periphery. Moreover, the comparison of the results obtained by the a-DM-FFF are totally different to the ones obtained by the a-FMM. This difference demonstrates the high impact of the artificial roughness of the surface induced by the staircase approximation on the simulation parameters especially with high Q-factor microdisks. In addition, the resonant wavelengths of the a-DM-FFF are considered much closer to the analytical ones than the a-FMM. The only inconvenient of the a-DM-FFF is the small roughness of the surface brought by the truncation of the Fourier series and which induces some reflections in specific region and doesn't allow to clearly specify the effect of the bus waveguide. So, to totally eliminate the effect of the roughness, some studies of the same microdisk could be done as perspectives in TE polarization where the field is always continuous and the effect of the roughness of the surface is much lesser.

8.3 Conclusion

In this chapter, the developed aperiodic DM-FFF has been applied on guided structures with continuous profiles. The convergence tests, conducted on different types of structures, prove that the a-DM-FFF can remarkably enhance the convergence compared to the a-FMM in case of high refractive index contrast and continuous structures (metallic and dielectric). Moreover, with the microdisk excited by plane waves closer results to the analytical calculated values are obtained with the a-DM-FFF compared to the a-FMM. Moreover, when associating a bus waveguide to the microdisk, the design parameters of both methods (a-DM-FFF and a-FMM) are totally different especially when considering high quality factors resonators (microdisks, for example, where the misrepresentation of the disk peripheries can induce error and affect the quality factor of the resonators). The numerical evidence shows the rapid saturation of the a-FMM where limit of calculating higher Q-factors is achieved. Moreover, this last method always suffers from the presence of the wavelength splitting with high difference due to the staircase approximation. In contrast, this difference is much more reduced with the a-DM-FFF but it is also presented due to the truncation of the Fourier series with a given

order N .

This totally novel method allows me to write four scientific contributions. The algorithm of the method, its validation and application on high contrast refractive index and metallic pillar have been published in the Journal of Optical Society of America (A1 of appendix.D). Moreover, I presented this work in two international conferences (B1 and B2 of Appendix.D) and one french national conference (C2 of Appendix.D).

Part III

Experimental results of Bragg grating filters

Chapter 9

Fabrication and Characterization of Bragg Reflection filters associated with ion-exchanged waveguides

9.1 Principles of Bragg grating waveguide used as wavelength filter

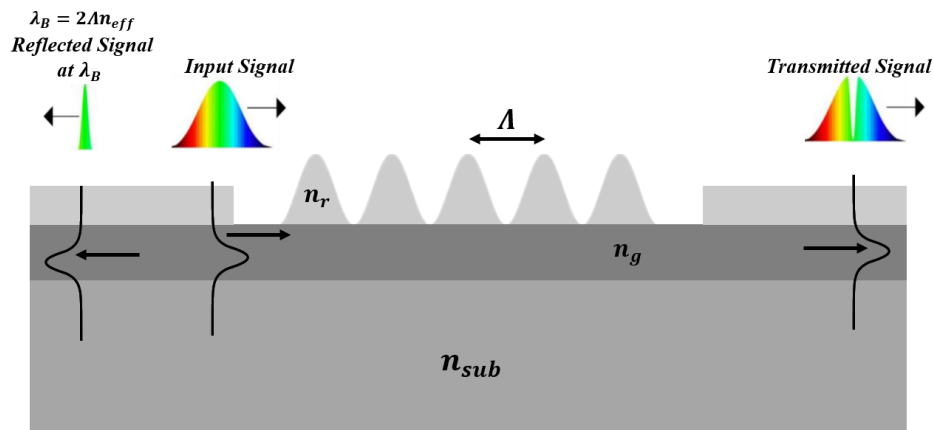


Fig. 9.1 Schematic representation of a Bragg filter. n_{eff} is the effective refractive index of the entire structure.

Bragg Grating Filters (BGF) are fundamental components in the optical domain. They are mainly used in optical communications, in DBR lasers, grating couplers, etc...

If a BGF is associated to a waveguide as the GMR case, a narrowband passband filter can be obtained in the reflection spectrum. On the other hand, a narrow notch filter is reached in the

transmission case. So if a large spectral bandwidth input signal is used, a narrow bandwidth spectrum centered to the Bragg wavelength can be obtained with the reflected signal. This wavelength depends on the effective index (n_{eff}) of the waveguide under the grating, and the period of the grating as shown in the following expression.

$$\lambda_B = 2\Lambda n_{eff} \quad (9.1)$$

The common form of Bragg grating filters is the fiber bragg grating (FBG). Moreover, it can be fabricated using the integrated glass channel waveguides [49]. The technology of glass ion-exchanged waveguides can also be associated with Bragg grating. This concept has already been used to realize glass integrated laser [6]. Nevertheless, the set-up used in our lab can reach a minimum grating period not enough small to filter visible wavelength. In this case, the grating is etched in the surface glass waveguide directly allowing a sufficient interaction between the grating and the waveguide.

Ideally, the equation describing the amplitude of the evanescent field of the guided mode in the superstrate takes the form of $exp(-\alpha_{sup}z)$ with $\alpha_{sup} = k_0\sqrt{n_{eff}^2 - n_{sup}^2}$. If we want to predict the thickness z from which a given percentage (ratio) of the guided mode amplitude can penetrate the superstrate, the following calculation must be applied:

$$\begin{aligned} exp(-\alpha_{sup}z) &= \text{ratio} \\ \Leftrightarrow -\alpha_{sup} \cdot z &= \ln(\text{ratio}) \\ \Leftrightarrow z &= -\frac{\ln(\text{ratio})}{\alpha_{sup}} \end{aligned} \quad (9.2)$$

Meanwhile, IMEP-Lahc is a leading laboratory in the fabrication and characterization of ion exchanged waveguides for different applications [5, 69]. On the other hand, our industrial collaborator SURYS is a leading group in the world of holograms industry. Thus, the aim here is to combine the technology of ion exchanged waveguides with the roll by roll technology of gratings in order to have a hybrid bragg grating filters working in the visible and near infrared wavelengths. Nevertheless, there are some constraints to study: the thickness of the layer used by SURYS to realize the grating, the amplitude of the grating, and the optical properties of the layer compared to the glass waveguide

9.2 Ion Exchanged waveguides principle

9.2.1 Principle of ion exchange

Ion exchanged waveguides have proved to be an efficient, low cost and high performance technology to realized integrated optical structures. Moreover, the used refractive indices can highly reduce the Fresnel reflection at the input of the waveguide, and the shape of the optical waveguide mode can also be similar to the optical fiber mode (similar numerical apertures). This propriety reduces the coupling losses at the input. And finally, the propagation losses are very low in the near infrared spectral domain. This technology is also a low cost technology. Meanwhile, the refractive index of a glass substrate can be locally modified by ion exchange

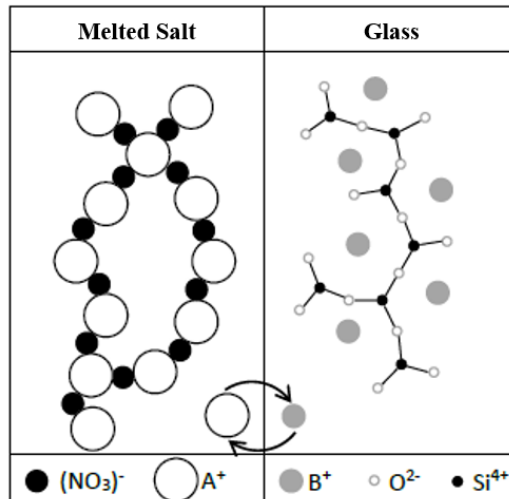


Fig. 9.2 Schematic representation of ion exchange.

process in order to realize optical waveguides [42]. Therefore, the main purpose of the ion exchange is to replace specific ions in the glass with another chosen ions. This principle, described in Fig.9.2, allows a low production cost. In this dissertation, the A^+ ion is the potassium K^+ and the B^+ ion is the sodium Na^+ . During the process, the glass substrate is heated to provide the thermal energy needed to break the ionic bonds and set the new desired ions. By setting in contact the glass with a well-chosen ions source (ionic melted salt KNO_3 for example), the positive ions of the source (K^+) diffuse into the glass while the modifiers of the glass (Na^+) diffuse outside. Thus, the glass properties are modified and therefore the refractive index is locally modified. Here, we seek to realize waveguides with the minimum propagation loss in the visible and NIR wavelengths. Thus, the standard Ag^+/Na^+ ion exchange can't ensure this condition due to the presence of the silver particles

on the surface of the waveguide increasing the losses in the visible wavelengths. In contrast, this can be reachable by the K^+/Na^+ exchange.

9.2.2 Description and Fabrication of optical waveguides

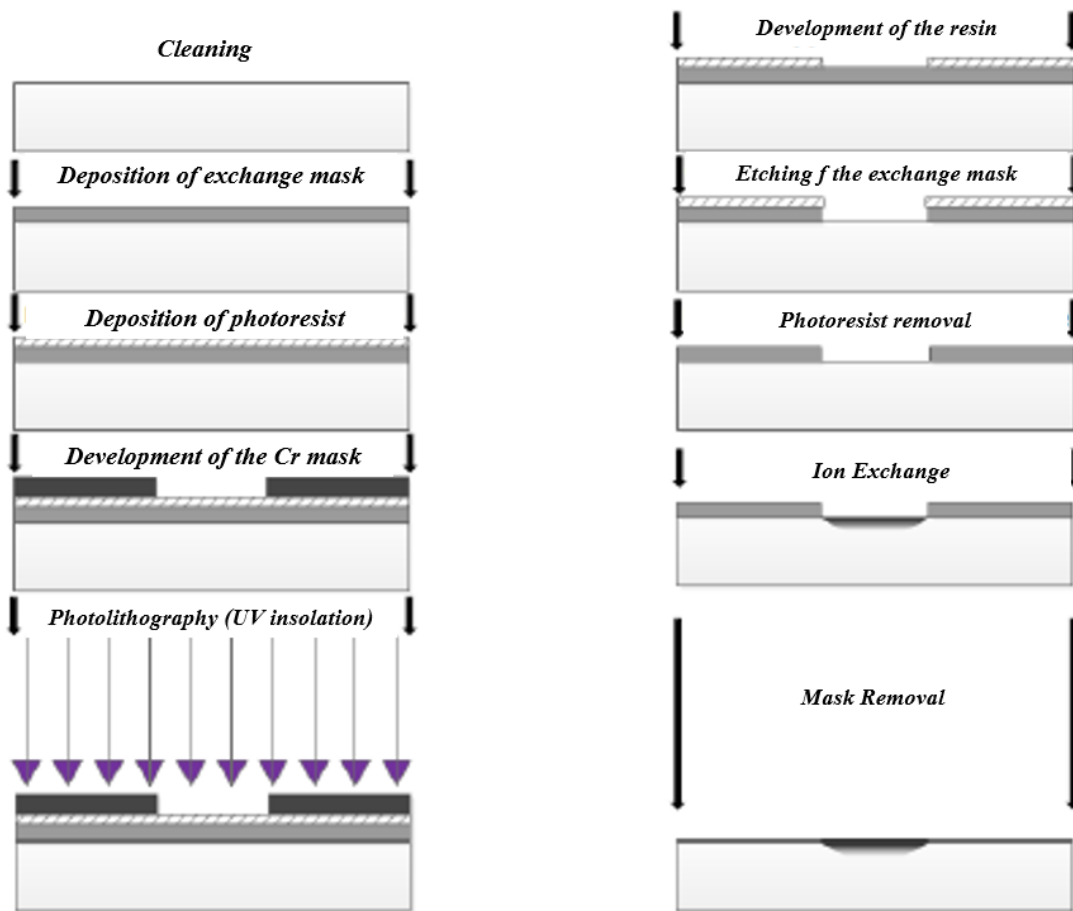


Fig. 9.3 Optical waveguide by ion exchange fabrication process.

In Fig.9.3, the fabrication process of optical waveguide by ion exchange is presented. A GO14 sample of glass developed by Teem PhotonicsTM is used in this process. This type of glass is optimized to reach the minimal propagation loss in the visible and NIR. It is also manufactured to have a specific and controlled composition and the same optical properties from one batch of glasses to another. Moreover, it guarantees to always have the same properties on a 6cm diameter chip where its surface is polished with great precision to $\lambda/10$. After cleaning the substrate, a 200nm thin film of Aluminum, by vapor phase deposition (see Appendix.4), is deposited to create a mask on the sample surface. It is then important to etch

the positions where the waveguides are previewed. This step is known as Photo-lithography. For that, a positive resin S1805 (which becomes brittle after the UV insolution) is placed on the surface by overthrowing this resin on the rotating sample (spin coating). After the spin coating, a chrome mask on quartz substrate is inserted in a Karl Suss MA56 Mask aligner. The chrome mask interface and the resin sample interface are then come into contact (void contact) to ensure an optimized reproduction of the mask reference (Test ECH in Appendix) in the resin layer. Therefore, the aperture of waveguides of width w are defined by a standard photo-lithography followed by the development of the photoresist in a developer bath MF26-A which suppress the vulnerable resin. After this step, the sample is placed in a bath of Al remover which will only etch the exposed Aluminum. For the ion exchange process, the sample is horizontally immersed in a KNO_3 melted salt for a duration of 8 hours at $380^\circ C$. When this process is finished, the sample is immersed for 30 minutes in a Flash bath of $NaNO_3$ at $350^\circ C$ in order to create a thin Na-doped surface layer. It is important to notice that the K^+ ions are considered much bigger than the exchanged Na^+ ions. Due to that several remarks can be listed:

- Strong mechanical stresses can swell the surface of the glass
- The refractive index of the waveguide is strongly dependent on these mechanical constraints
- The mask can be weakened which induces a plane waveguide on the surface which is reduced by the second step of the exchange
- Geometrical roughness may remain on the surface which induces losses, especially if the superstrate is air.

Due to all the above reasons, the flash of $NaNO_3$ is realized. Finally, the remaining aluminum layer is removed by Al remover and the sample that contains the confined waveguides is cleaned. It is important to mention that, the K^+/Na^+ technique creates a maximal refractive index contrast $\Delta n = 8 \times 10^{-2}$ between the core of the confined waveguide and the substrate [12].

9.2.3 Characterization of the guides

Three characterization techniques must be performed in order to ensure that the fabrication process of the waveguides is successfully completed.

1. The profile of the output waveguide mode in order to check the functionality of the guides and to identify if the guide is monomode or multimode. This profile is not directly measured. The diffracted light at the output of the waveguide passing through an objective lens is measured into a camera.
2. The insertion losses induced by the fiber-waveguide coupling losses, the Fresnel reflection, and the propagation losses .
3. Spectral analysis to eventually detect the spectral monomode bandwidth and the evolution of the losses following the wavelength.

Profile of the radiated waveguide output mode

The main purpose of the profile analysis is to see the behavior of the input signal at the output of the waveguide. The test bench is depicted in Fig.9.4. Meanwhile, the sample

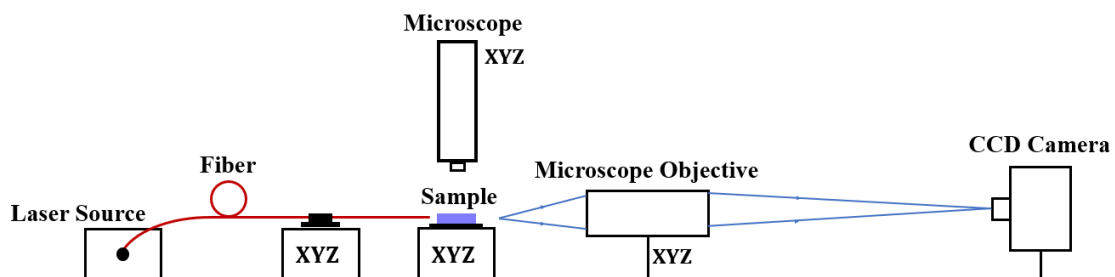


Fig. 9.4 Schematic representation of the test bench of the radiation analysis

contains a set of 4 series, each containing 6 patterns. Each pattern contains 11 waveguides of 0.5, 0.8, 1, 1.5, 2, 2.5, 3, 3.5, 4, 7, 10 μm widths (See appendix.4). In this configuration, the sample is illuminated with a red laser source (centered at $\lambda = 635\text{nm}$), a SM600 Single Mode Optical Fiber 633nm is used between the sample and the source to only ensure the propagation of the fundamental mode. After the sample, a $\times 20$ microscopic objective (Mitutoyo Apo NIR 20 \times) is used to focus and magnify the output light of the waveguide. Finally, this light is directed to an InGaAS GOODRICH SUI camera and visualized via the SUI image analysis software. Therefore, if a fiber is centered at the middle of the waveguide, one maximum will appear on the mode profile (Fig.9.5.(a)). On the other hand, two or more maximum may appear in case of multimode waveguides when input single mode fiber is slightly moved in the horizontal direction (Fig.9.5.(b)).

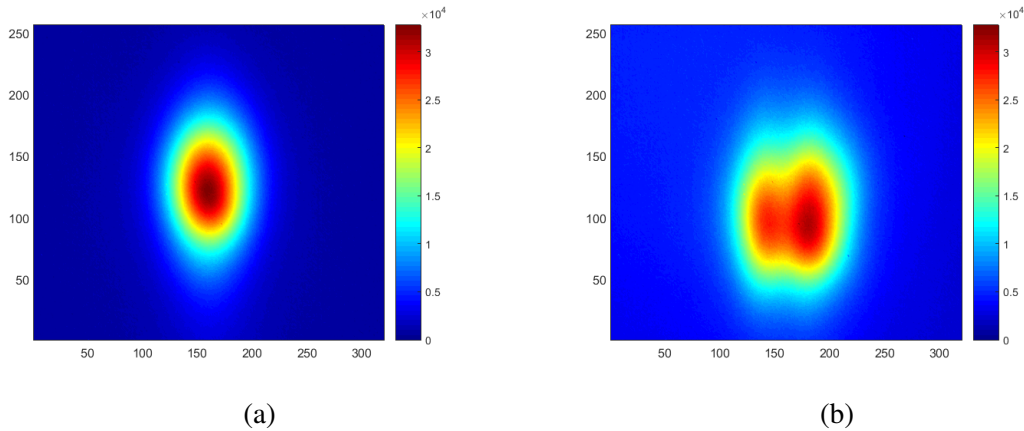


Fig. 9.5 Radiation analysis using the SUI camera (a) Monomode waveguide with $4\mu m$ width (b) Multimode waveguide with $10\mu m$ width. The x and the y axis represent the pixels of the SUI camera.

Propagation loss measurement

The aim of this process is to measure the insertion loss within the propagation of light inside the waveguide. The basic principle is to place the sample between an input fiber at the entrance of the waveguide followed by an output fiber having the same characteristics at the output of the sample. A power-meter is then placed after this fiber which measure the transmitted power directly proportional to the input source power (Fig.9.6).

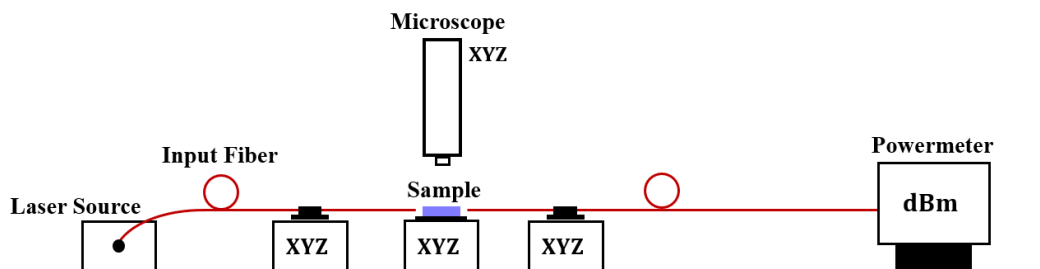


Fig. 9.6 Schematic representation of the test bench of the propagation loss measurement

By measuring the optical power by placing the sample between two fibers and without the sample (Fiber to fiber case), the insertion loss of the waveguide α_{ins} can be straightforwardly deduced. However, for the i/o fibers, the same Thorlabs 633nm single mode fibers of the previous section have been chosen for this manipulation. After performing the loss calculation method. The insertion loss (IL) in the different waveguides with different widths can be summarized in the following table (Table.9.1). We consider $P1$ as the fiber-sample-fiber power in dBm , $P2$ the fiber to fiber power in dBm , $P3$ the fiber-objective lens power in

dBm , and finally P_4 as the fiber-sample-objective lens power in dBm . The Fresnel losses are considered negligible. And, the fiber sample coupling is considered constant. From these measurements, the different loss parameters can be calculated as:

- Insertion losses (IL) in dB : $P_2 - P_1$.
- Coupling losses between the fiber and the sample waveguide (CL) in dB : $P_2 - P_1 - (P_3 - P_4)$
- Attenuation losses (AL) in dB/cm : $(IL - 2CL)/Length$. With Length Sample = 4.1 cm.

Width(μm)	P_1	P_2	P_3	P_4	IL	CL	AL
0.8	8.51	1.07	0.04	4.68	7.44	2.80	0.44
1	8.66	1.07	0.04	5.37	7.59	2.26	0.74
1.5	7.95	1.07	0.04	4.43	6.88	2.49	0.46
2	8.72	1.07	0.04	4.55	7.65	3.14	0.33
2.5	8.66	1.07	0.04	4.2	7.59	3.43	0.18
3	8.41	1.07	0.04	4.43	7.34	2.95	0.35
3.5	8.76	1.07	0.04	5.85	7.69	1.88	0.95
4	8.14	1.07	0.04	4.2	7.07	2.91	0.31

Table 9.1 The attenuation loss in dB/cm of the different monomode waveguides with K^+/Na^+ ion exchange at $380^\circ C$ for $8h$ and with a $NaNO_3$ flash at $350^\circ C$ for 30 mins and red laser source centered at $\lambda = 635nm$.

Spectral analysis

The objective of the spectral analysis is to determine the spectral range for which a waveguide is considered single mode. For that, a white light source is placed at the input of the guide and a spectrum analyzer at the output. In the configuration of Fig.9.7, Multimode fibers in the visible and the NIR domain have been used at the input and the output of the waveguides to ensure the coupling of all modes. At the output, an optical spectrum analyzer HP50970A with spectra range from $900nm$ to $1700nm$ is used with a wavelength resolution of $0.5nm$ and minimum sensibility of $-86dB$.

Fig.9.8 shows the spectral response of $4\mu m$ width waveguide. Indeed, there is a jump of the intensity passing through the guide which appears at a wavelength of $1128nm \pm 1nm$. This jump corresponds to the border between the area where the electromagnetic wave is too wide to be propagated in the guide and the area where it is thin enough to be guided. Indeed, the waveguide isn't isotropic with symmetry revolution. Therefore, the cut-off wavelength

9.3 ROLL TO ROLL GRATING WITH ION EXCHANGED WAVEGUIDE: DIRECT INTERACTION

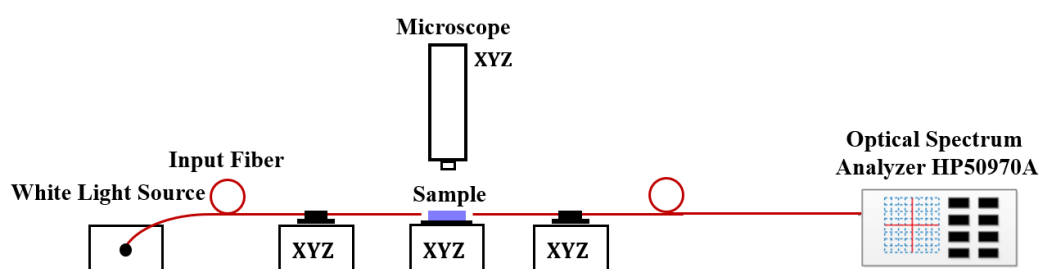


Fig. 9.7 Schematic representation of the test bench of the spectral analysis.

may differ following the TE or TM polarizations. In the monomode zone, the evolution of the power evolves in a linear way. In contrast, when we are close to the cut-off wavelength, the power falls down due the increase of the propagation loss and the coupling loss. Practically, the cut-off wavelength is considered when a decrease of power of 5dB is reached (Fig.9.8). Moreover, the profile of the modes performed in the red zone shows that the guides with widths $\leq 4\mu\text{m}$ are always monomode in this band of wavelengths which ensure the goal of monomodicity in the red and NIR wavelengths.

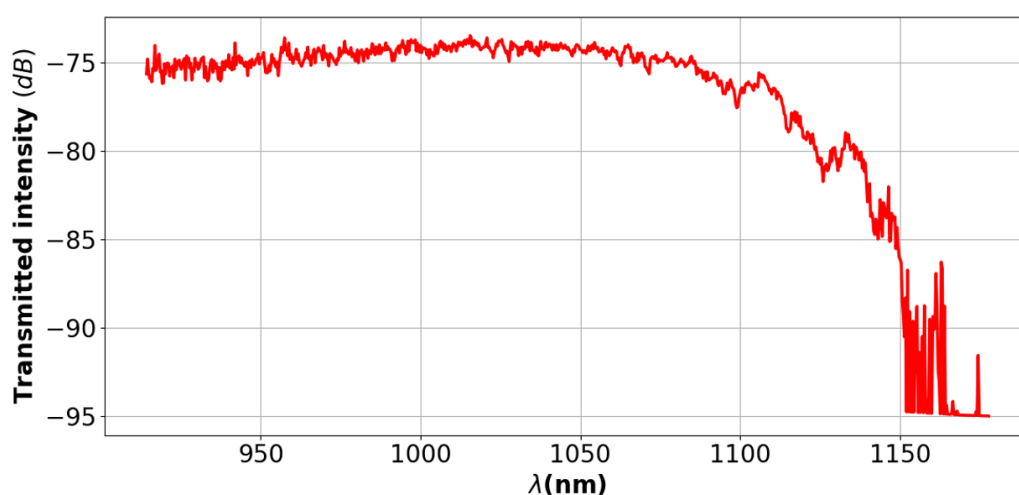


Fig. 9.8 Spectral response of the waveguide of $4\mu\text{m}$ width using the HP 70950A optical spectrum analyzer.

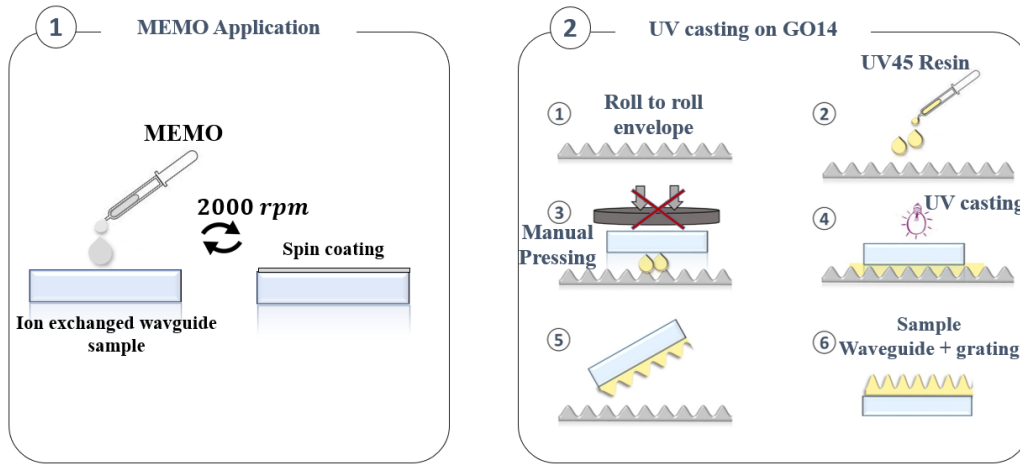


Fig. 9.9 The fabrication procedure of the grating associated to the ion exchanged waveguides sample

9.3 Roll to roll Grating with ion exchanged waveguide: direct interaction

The second important part in any BGF is the surface grating. After checking the functionality of the waveguides. A way to associate bragg gratings to the waveguide sample that work in the visible and NIR domains must be found. In that case the buffer layer is the UV54 of refractive index $n_3 = 1.483$. The peak to peak amplitude of the grating is $65nm$ and the period is $\Lambda = 240nm$. Thus, by applying the calculation of Eq.(9.2), if a field amplitude of the evanescent mode between 10% and 30% is needed (this percentages are issued from the field of the non-corrugated mode with the resin as superstrate), minimum thickness z of the buffer layer between $0.57\mu m$ and $1.06\mu m$ is required to ensure the evanescent coupling between the guided mode and the grating in the visible and NIR wavelengths ($\lambda = 729nm$ is considered in this calculation).

To ensure this last calculation, the 2D a-FMM has been used to simulate the structure depicted in Fig.9.10 which represents the side view of the square profile grating used in the simulation instead of the realized sinusoidal profile. This change can slightly modify the position of the resonant wavelength but the evanescent field dependence can be close. Fig.9.11.(a) illustrates the minimum transmission in dB with respect to the transverse length of the grating L in cm . At the both extremities of the grating, there is a waveguide with non corrugation. Which means that the mismatch at each side is taken in account in the simulation. Two aspects appear here, firstly, the transmission decreases with the increase of the gap thickness. Secondly, the minimum transmission increases with the increase of the

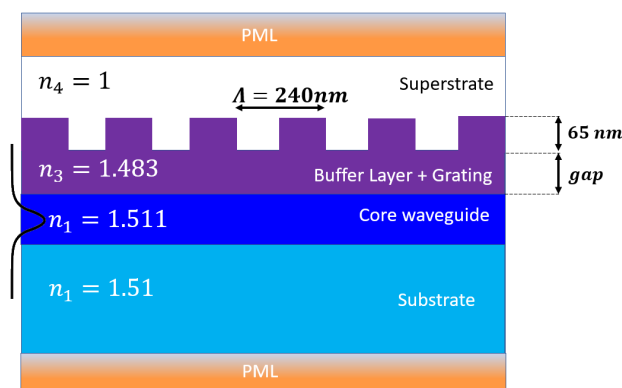


Fig. 9.10 Bragg grating associated to the simulated waveguide. The ion exchanged waveguide has been replaced by an equivalent refractive index step waveguide.

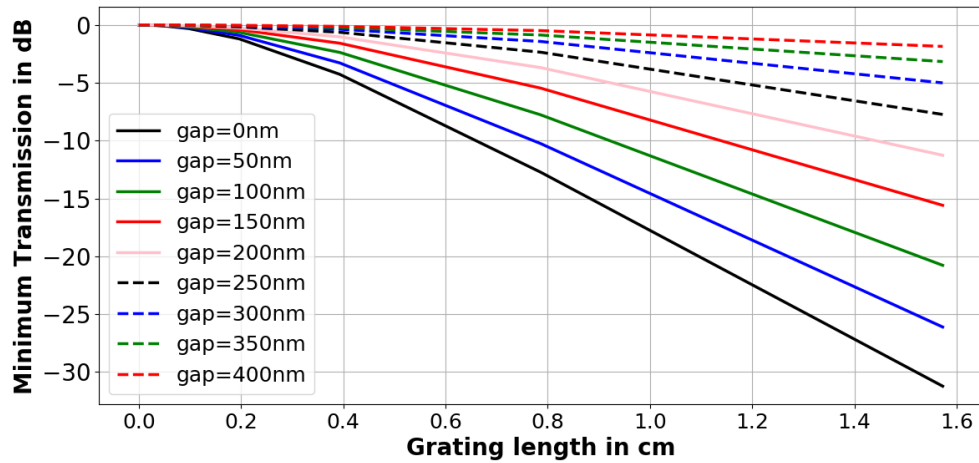
grating length L . A transmission of $-1.5dB$ is obtained for $L \approx 1.5cm$ and a gap = $400nm$. On the other hand, a minimum transmission of $-30dB$ is reached for the same length but with a gap = $0nm$.

In Fig.9.11.(b), the spectral response of the BGF is depicted. The gap thickness representing the buffer layer is tuned between $0nm$ and $400nm$ for a fixed grating length $L = 1.57cm$. It is clear that for $gap \geq 400nm$, the minimum transmission is closer to $0dB$ and the bragg filtering effect vanishes. Thus, the challenge with such structure is to reach a buffer layer thickness less than $400nm$, while the half power beam width $HPBW = 0.07nm$.

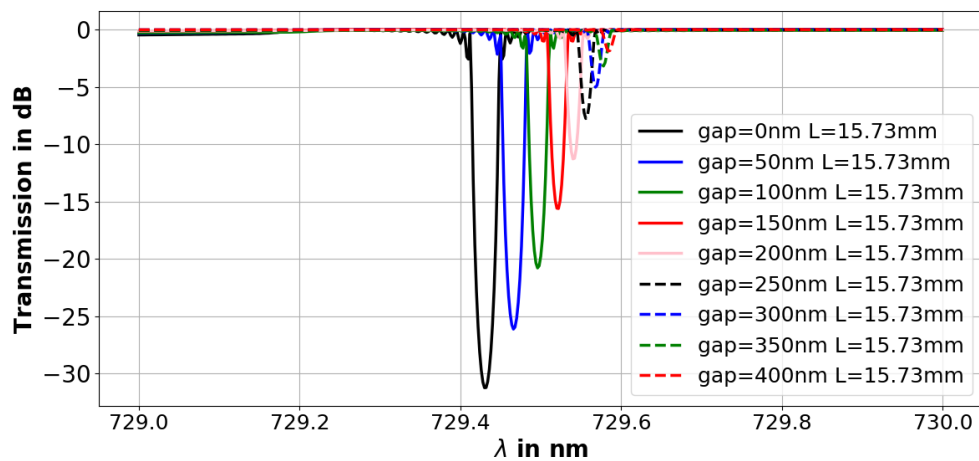
As mentioned before, SURYS uses the roll to roll technology to replicate the gratings on the surface of the samples. Using this technology, many printing techniques have been investigated to reach this goal. Firstly, the samples containing the ion exchanged waveguide have been sent to the gray room of SURYS where the roll to roll printing occur. The first trial depicted in Fig.9.9 has been done by the following steps.

- a special chemical solution called Memo ¹, that works as an adhesive between the the GO14 substrate and the deposited resin layer, has been dropped to the sample containing the ion exchanged waveguides. Indeed, this adhesive creates a molecular surface with molecular thickness (few atoms). For that, its thickness is considered negligible.
- After a spin coating with $2000rpm$ to consistently distribute the MEMO on the surface, 2 drops of special resin fabricated by SURYS and called UV54 and having a small

¹This solution is prepared by mixing $50ml$ of isopropanol ($CH_3CHOHCH_3$), $1.5ml$ of acetic acid (CH_3COOH) of concentration 10%, and $0.15ml$ of 3-(Trimethoxysilyl)propyl methacrylate.



(a)



(b)

Fig. 9.11 (a) The minimum transmission in dB with respect to the transverse length of the grating (b) The transmission spectrum of the BGF with $L = 1.57\text{cm}$ and for different gaps.

viscosity with respect to the commercial resin are dropped to the roll to roll envelope of the grating.

- After many trials with the machine pressing. A manually pressing technique of the envelope has been chosen in order to maximize the pressure on the surface and therefore minimize the deposited layer.
- UV casting is performed to print the inverse envelope on the surface of the sample.

- When the roll to roll envelope is removed, a grating layer composed of the resin UV54 is therefore printed on the surface of the waveguides sample.

We will call this sample sample 'Test1'. Moreover, another sample has been fabricated by using one drop of the UV54 resin instead of 2 in order to thinner the layer. This sample is then called 'Test2'.

After receiving both samples, we checked firstly the thickness of the buffer+grating layer

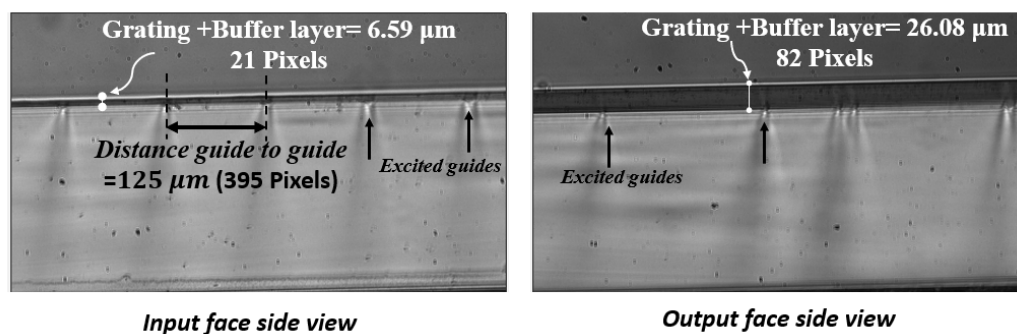


Fig. 9.12 The normalized transmission power of the ion exchanged waveguide of width $3\mu m$ associated to a surface grating of period $\Lambda = 240nm$.

of the input and the output face of the sample with a CCD camera (HD CCD camera from Hamamatsu). Fig.9.12 illustrates the thickness of the resin layer (Buffer+grating) which is manually deposited of the sample Test2. Indeed, a straightforwardly calculation depending on the camera pixels and the distance between 2 consecutive waveguides (distance guide to guide = $125\mu m$) reveals that the thickness of the two faces is much greater than $1\mu m$. An approximate average thickness of $7\mu m \pm 1\mu m$ has been achieved with the input face and an average thickness of $19\mu m \pm 5\mu m$ is obtained for the output waveguide side. So, the thicknesses are much higher than $400nm$. The coupling of the evanescent part of the waveguide mode with the grating surface can't be achieved. In all cases and to ensure this hypothesis, the spectral analysis has been performed for both samples without showing any significant filtering effect. As a result, the Bragg filtering was not achieved. And, this methodology has demonstrated its failure.

9.4 Roll to roll Grating with ion exchanged waveguide: Hybridization by MEMO

9.4.1 Hybridization process

In the previous section, we mentioned that the chemical solution called MEMO creates a molecular interaction with negligible thickness between the deposited layer and the GO14 substrate. The idea was to exploit this specification in order to realize a direct interaction without any buffer layer between the grating and the ion exchanged waveguides. For that, a hybridization method has been proposed in order to reach this goal (Fig.9.13). Using this method, two samples are needed. The first one must only contains the ion exchanged waveguides while the surface of the second one must be occupied by the grating of period $\Lambda = 240nm$. In that case, the buffer layer is the air. Thus, Eq.(9.2) tells us that a thickness $230nm \leq z \leq 460nm$ is needed to couple between 10% and 30% of the evanescent field (these percentages are issued from the field of the non-corrugated mode with the air as superstrate). The first step is to add some drops of MEMO on the surface of the waveguides samples. By

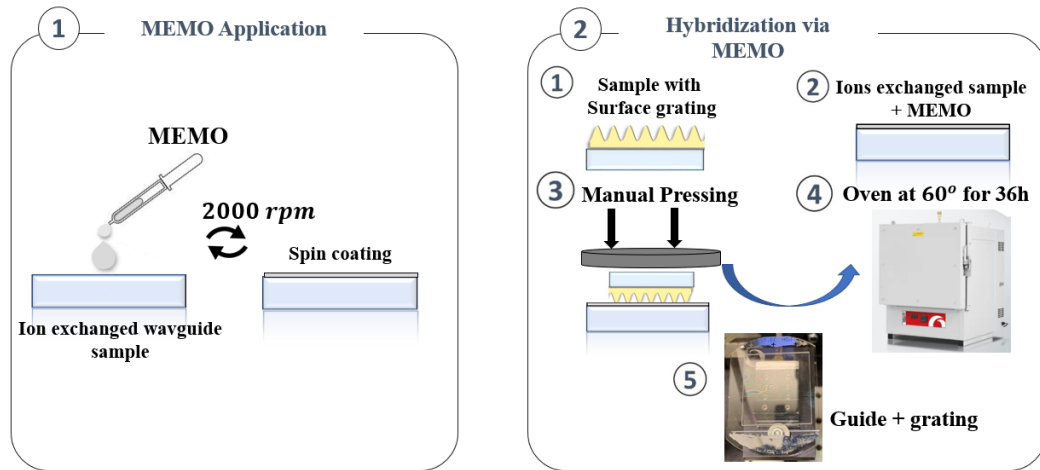


Fig. 9.13 The fabrication procedures of the grating associated to the ion exchanged waveguides sample with the hybridization method

spin coating, the solution will be harmoniously distributed on the sample's surface. After that, the sample of the Bragg grating is directly elaborated, from the side where the grating is found, on the top of the first sample. By manual pressing both samples will be fixed and the air gaps will be almost removed. Finally, in order to ensure the hybridization, the structure is heated inside an oven calibrated at 60° for 36h.

9.4.2 Simulated results

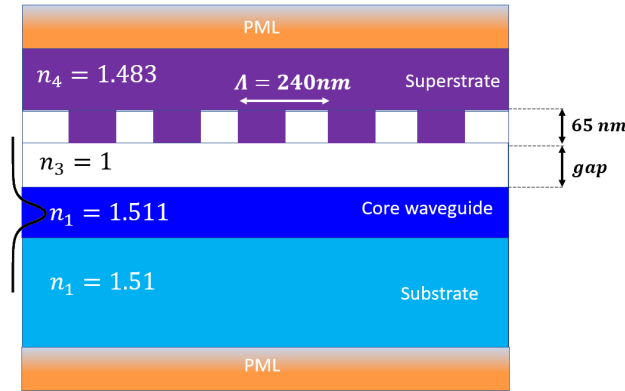


Fig. 9.14 Schematic representation of the hybridized Bragg filter.

Now, the structure depicted in Fig.9.14 represents our hybridized structure. This structure will be simulated by the 2D a-FMM to reveal its optical response. The study of the transmission with respect to the length of the grating (Fig.9.15.(a)) shows that the transmission evolution decreases with the increase of the gap. A minimum transmission of $-1.8dB$ is obtained for $L = 1.57cm$ and a $gap = 120nm$. In that case, a contact air gap less than $120nm$ is needed to ensure the filtering effect where the necessity of the MEMO appears. In Fig.9.15.(b), a grating length of $1.57cm$ has been fixed, the spectrum for different gap is then studied. We can see that for a negligible gap of $0nm$ (black curve) the minimum transmission attains less than $100dB$ with a half power beam width $HPBW = 0.15nm$. With, the increases of the gap, both the minimum transmission and the HPBW decreases. To be close to zero, for gaps higher than $120nm$. We can notice that for small gaps, a decrease of transmission appears between $729nm$ and $729.2nm$. This drop in transmission is linked to the appearance of the leaky waves coupled to a diffraction order in the superstrate and radiated to the exterior of the structure.

9.4.3 Spectral analysis

For the spectral analysis of the hybrid structure, the same test bench of Fig.9.6 has been used. Meanwhile, at the input side a Leukos supercontinuum laser source which works for the visible and NIR wavelengths associated to a Bebop adjustable wavelength and spectral bandwidth filter. A spectral range between $680nm$ and $750nm$ has been chosen. Moreover, a $0.2nm$ resolution of $-84dBm$ sensitivity has been calibrated for the OSA HP50970A. The transmitted power spectrum for different waveguides of width w are shown in Fig.9.16.

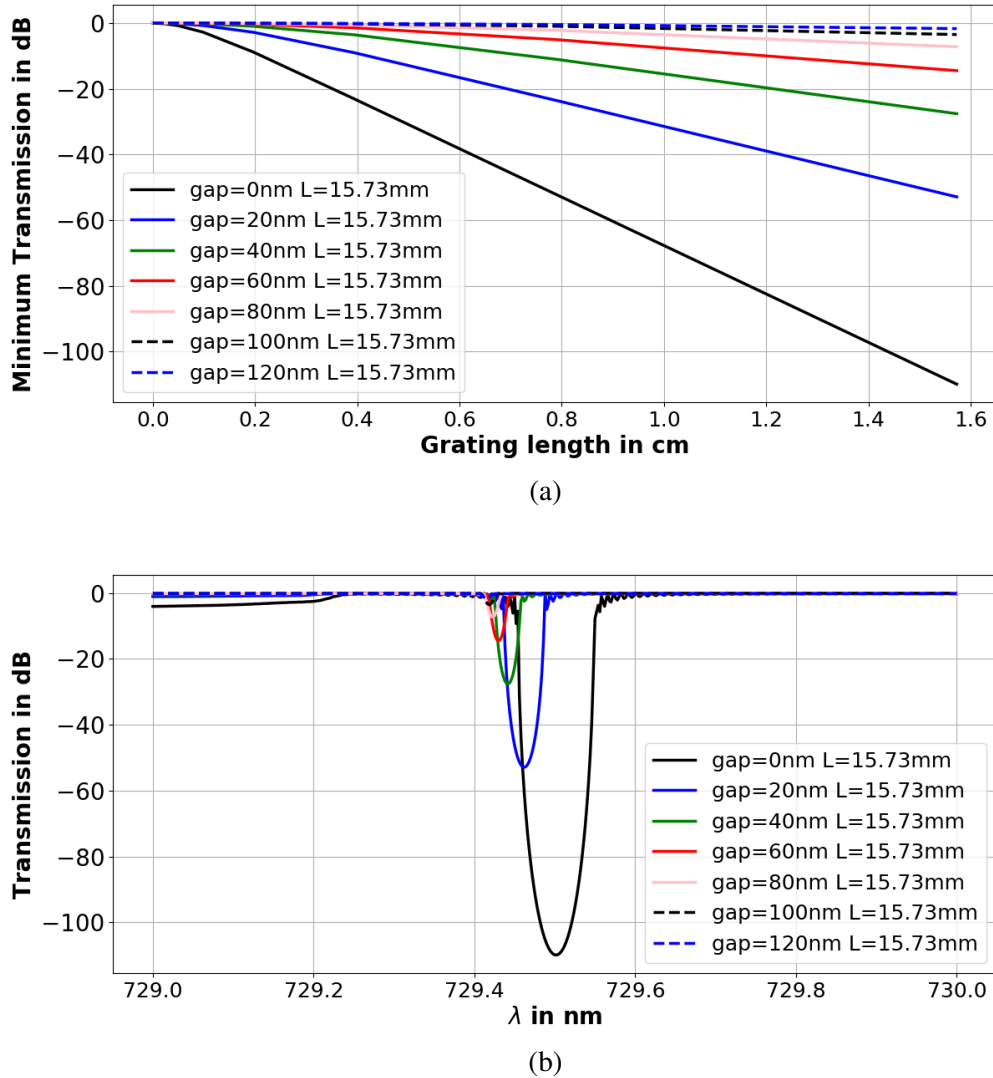


Fig. 9.15 (a) The minimum transmission in dB with respect to the transverse length of the grating (b) The transmission spectrum of the BGF with $L = 1.57 \text{ cm}$ and for different gaps.

Ideally, by referring to Eq.(9.1), and by taking $\Lambda = 240 \text{ nm}$ and $n_{eff} \approx 1.51$, the bragg reflection wavelength is $\lambda_B = 729 \text{ nm}$. Nevertheless, periodically repeated dips appears in the transmission spectrum. Maybe they are a results of an interference between the propagating modes inside the waveguides. Moreover, it can be the effect of Fabry-Pérot cavity between the fiber and the waveguide or the waveguide and the guide+grating. There is no particular resonance which may represent a real filtering effect.

However, after the hybridization process, we found that some zones contain the interference fringes (where the air layer may exists) and other not (Fig.9.17). In the zone of fringes, the

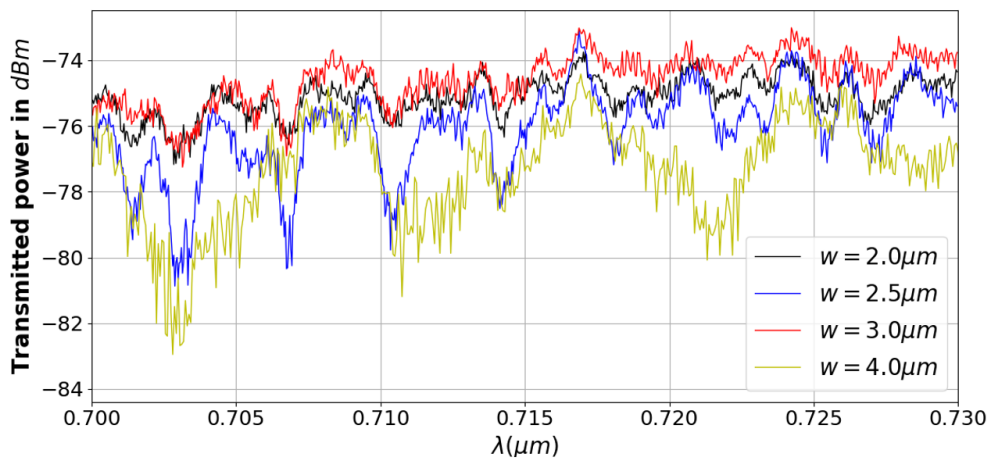


Fig. 9.16 The measured transmission spectrum of the hybrid structure for different width of ion exchanged waveguides.

guide-grating contact is ensured. But, the thickness of the air gap is not known. In the other zones, it is not guaranteed to have a contact between the samples. The waveguides are tested in the zones of the interference fringes. As a conclusion, we may say that the contact is not sufficiently efficient ($z > 120nm$) between the two samples to have the Bragg filtering (none negligible air gaps, excessive quantity of MEMO with big thickness which is not totally evaporated). For that more investigations are needed by either hybridizing other clean and well polished samples, hybridizing smaller samples or controlling the dust rate which is not optimized for the moment (gray room fabrication + transportation effects).

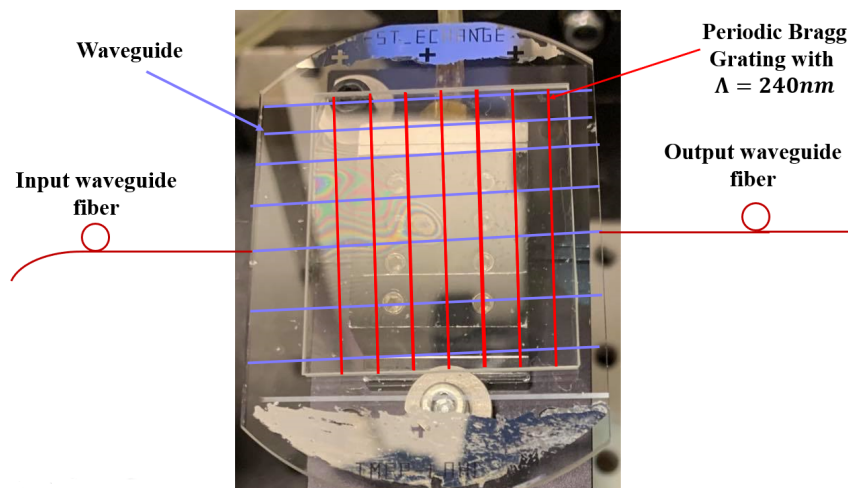


Fig. 9.17 The fabricated hybridized sample. The blue horizontal lines represent the direction of the waveguides and the red vertical lines belong to the periodized grating.

9.5 Conclusion

In this section many fabrication techniques of visible and NIR GBF have been presented. Indeed, the direct deposition of the grating layer on the top of the ion exchanged samples shows that the thickness of the deposited layer is not thin enough to carry the evanescent coupling of the guided mode and result the filtering effect. For that, another technique has been investigated by hybridizing a sample containing the waveguides with another one which contains the Bragg grating. Indeed, to ensure the adhesion of the two surfaces, a chemical adhesive solution known as MEMO has been used. This solution is characterized by creating a molecular adhesive layer with negligible thickness. First promising mechanical results have been obtained with this process. Nevertheless, the optical response expected is not still reached and more investigations and tests are needed.

Chapter 10

Conclusion and Perspectives

10.1 Conclusion

The differential method (DM) is a Fourier space method for the modeling of diffraction optics structures. It is mainly based on the expansion of the electromagnetic fields and the permittivity evolution into Fourier series. Then, it truncates all the series following a given truncation order N . Indeed, associating the Fast Fourier Factorization (FFF) to the algorithm of the method has demonstrated its efficiency and enhancement bringing more accurate results and fastest convergence rates. This algorithm is specialized by taking into consideration the evolution of the profile of the desired structure following the propagation axis and the periodic axis.

In the first part of this dissertation, the algorithm of the DM-FFF has been presented. The coded algorithm is used for the analysis of the diffraction and diffusion of light for different complex-shaped periodic structures. The algorithm has been tested on 1D diffraction gratings which are invariant according to a given dimension with incidence plane waves, in TE and TM polarizations. Nevertheless, the discontinuities of the electric field in TM polarization arises the importance of the FFF compared to other electromagnetic modeling methods as the RCWA which uses the staircase approximation in its algorithm. The C-method can overcome this problem but it is only dedicated to continuous profile. Indeed, the FFF used with the Li's factorization rules, the S-matrix algorithm and the Runge-Kutta integration of order 4 allows to treat the stack of discretized layers and to reach a better accuracy. Moreover, the use of the transition matrix Ψ allows the transition from the stationary fields representation into the forward and backward eigen modes of the structures. This matrix eases thus the access to the amplitude of the reflected and transmitted orders, and therefore, the calculation of the diffraction intensity of each diffracted order.

The DM-FFF has been then applied to different profiles of diffraction gratings. The com-

parison of the convergence rate and accuracy with other Fourier space methods (mainly the RCWA and the C-method) improved the predominance of this method in almost all types of periodic structures if the suitable projection of normal are considered. Moreover, during the simulations, numerical fluctuations of the DM-FFF have been observed mainly while dealing with pure negative and real permittivity profiles near the plasmonic resonance of the metal (Al, Ag, Au,...). Also, these divergences are frequently observed with the FMM. The physical reason of this problem gets back to the rapid change of the permittivity from positive real values to negative and pure real values which do not respect the Li's factorization rule. To tackle this problem, we added Gradually varying refractive Index Layers (GIL) at the dielectric metal interfaces of the structure. These layers alleviate the rapid transition of permittivity where few nanometers are considered largely sufficient to reach stable and accurate results. Moreover, the developed code of the DM-FFF has been used to perform a detailed study of an all-dielectric visual security device. This device is based on the add of buffer layer that acts on the guided mode resonance (GMR) and the other opto-geometrical parameters to produce structural reflected colors. Moreover, the code has been incorporated in a neural network system to easily design diffraction gratings for the visual security applications.

In the second part, a new method so called the aperiodic DM-FFF (a-DM-FFF) dedicated to the modeling of guided optical structures has been presented. This method is based on the association of a complex coordinate transformation inspired from Ref.[37] and playing the role of perfectly matched layers (PML) which suppress the incoming waves from the neighboring cells. Thus, an artificial periodization is found, but the structure is simulated as an isolated problem. Moreover, a transition matrix based on the organization of the eigen vectors has been investigated. This matrix allows the transition from the representation of the EM fields into the amplitude of the forward and backward guided modes. The association of both mechanism (PML and transition matrix) allows the appearance of the a-DM-FFF used for the design and modeling of guided optics problems.

The new method has been firstly validated by taking a rectangular guided structure in TE and TM polarization and the results obtained fits very well with the reference values. Secondly, as the importance of the FFF arises in TM polarization and with continuous and non-lamellar structure. A guided structure with curvilinear evolution has been considered. The comparison of both metallic and dielectric with high contrast index profiles shows the predominance of the a-DM-FFF on the a-FMM in terms of accuracy and convergence rate. Finally, the power of the FFF has been used to study microdisk resonators where more accurate and more rigorous results have been obtained. These results shows the huge impact of the staircase approximation on the simulation parameters where the a-DM-FFF can bring more enhancement and facilities to the design of complex shaped guided optical structures.

The last part of the thesis is devoted to experimentally fabricate integrated optic bragg filters working in the visible and NIR domains by exploiting the association of the ion-exchange waveguide technology of IMEP-Lahc with the roll to roll fabricated diffraction grating technology of SURYS. The first trials with direct deposition reveal big buffer layers at along the ion exchanged samples which prevent the evanescent coupling of the guided mode with the top grating. Another technique based on the deposition on a chemical adherent which creates an atomic thickness layers between the grating and the waveguides has been presented. More investigation are needed to ensure the functionality of this technique.

Finally, all the work presented in this thesis has allowed me to contribute in 9 scientific contributions. In total, I was the first author of 2 scientific articles and one of the co-authors in 1 journal. Moreover, I participated in 6 french national and international conferences (See Appendix.D).

10.2 Perspectives

This work opens the way to several research topics which can be more developed and deepened. The accuracy of the DM-FFF used for diffractive optical elements and with the added graded index layers can be now applied for all types of diffraction gratings for different applications where more rigorous results can be obtained compared to the other classical methods. Moreover, the developed aperiodic version of this method opens the way for researchers and engineers to simulate and model new arbitrary shaped guided structure that was considered as problematic before. Finally, the W matrix definition is also an interested way to reach a hybrid method. This formulation opens the way to cascade a-FMM zones with a-DM-FFF zones. Indeed, the numerical integration can be focused on continuous evolution in order to optimize the calculation speed. At this scale, with the 2D a-DM-FFF or the hybrid method (2D a-FMM with the 2D a-DM-FFF), waveguides coupled nanowire as optical antennas can be more rigorously simulated, especially in TM polarization, since such structures mainly use metallic and non rectangular nanowires. Moreover, the field response of guided structures with tapered zones can be more precisely observed by eliminating the approximations brought by the discretization or the meshing techniques. In addition, artificial roughness can be numerically added with a large band of freedom and accuracy in order to predict the impact of manufacturing and photolithography on the results of guided structures. Last but not least, the physical response of the probes with pointed end or/and metallic walls can be more accurately analyzed for the Scanning Near Field Optical Microscopy (SNOM) applications.

Finally, the 3D version of this method can also be deployed to simulate more rigorously 3D

guided structures. For example, the impact of manufacturing roughness which is closer to the real cases can be added to the algorithm of the method to study the attenuation impact on sub-wavelength grating (SWG) metamaterials for silicon photonics [62], the attenuation of the SOI waveguides [72], on the 3D resonators, photovoltaic structures or plasmonic nanoantennas where the boundary conditions are closer to the real cases. Furthermore, discontinuities or known corrugations can be considered to play on the mode degeneracy and splitting for sensors applications (where the wavelengths splitting is sensitive to the corrugation change) or lasers (impact of an emitter near the resonator for example). Concerning the experimental part, more investigations are needed. Thus, well polished and cleaner sample can be used. Moreover, the effect of the gray room manufacturing of the grating can be also controlled in order to reduce the manufacturing impurities.

Finally, all results may be experimentally confirmed in order to show the improvements brought by either the DM-FFF and the a-DM-FFF on the diffractive optics domain and the guided optics domain.

References

- [1] Absil, P., Hryniewicz, J., Little, B., Wilson, R., Joneckis, L., and Ho, P.-T. (2000). Compact microring notch filters. *IEEE Photonics Technology Letters*, 12(4):398–400.
- [2] Armaroli, A., Morand, A., Benech, P., Bellanca, G., and Trillo, S. (2008). Three-dimensional analysis of cylindrical microresonators based on the aperiodic fourier modal method. *JOSA A*, 25(3):667–675.
- [3] Arnaud, L. (2008). *Diffraction et diffusion de la lumière: modélisation tridimensionnelle et application à la métrologie de la microélectronique et aux techniques d'imagerie sélective en milieu diffusant*. PhD thesis, Aix-Marseille 3.
- [4] Berenger, J.-P. et al. (1994). A perfectly matched layer for the absorption of electromagnetic waves. *Journal of computational physics*, 114(2):185–200.
- [5] Bertoldi, O., Broquin, J.-E., Vitrant, G., Collomb, V., Trouillon, M., and Minier, V. (2004). Use of selectively buried ion-exchange waveguides for the realization of bragg grating filters. In *Integrated Optics and Photonic Integrated Circuits*, volume 5451, pages 182–190. International Society for Optics and Photonics.
- [6] Blaize, S., Bastard, L., Cassagnetes, C., and Broquin, J. (2003). Multiwavelengths dfb waveguide laser arrays in yb-er codoped phosphate glass substrate. *IEEE Photonics Technology Letters*, 15(4):516–518.
- [7] Bogaerts, W., Taillaert, D., Luysaert, B., Dumon, P., Van Campenhout, J., Bienstman, P., Van Thourhout, D., Baets, R., Wiaux, V., and Beckx, S. (2004). Basic structures for photonic integrated circuits in silicon-on-insulator. *Optics Express*, 12(8):1583–1591.
- [8] Borselli, M., Johnson, T. J., and Painter, O. (2005). Beyond the rayleigh scattering limit in high-q silicon microdisks: theory and experiment. *Optics express*, 13(5):1515–1530.
- [9] Botten, I., Craig, M., McPhedran, R., Adams, J., and Andrewartha, J. (1981). The dielectric lamellar diffraction grating. *Optica Acta: International Journal of Optics*, 28(3):413–428.
- [10] Boyer, P., Popov, E., Nevière, M., and Renversez, G. (2006). Diffraction theory: application of the fast fourier factorization to cylindrical devices with arbitrary cross section lighted in conical mounting. *JOSA A*, 23(5):1146–1158.
- [11] Bremmer, H. (1951). The wkb approximation as the first term of a geometric-optical series. *Communications on pure and applied mathematics*, 4(1):105–115.

REFERENCES

- [12] Broquin, J.-E. (2007). Glass integrated optics: state of the art and position toward other technologies. In *Integrated Optics: Devices, Materials, and Technologies XI*, volume 6475, page 647507. International Society for Optics and Photonics.
- [13] Bucci, D., Martin, B., and Morand, A. (2012). Application of the three-dimensional aperiodic fourier modal method using arc elements in curvilinear coordinates. *JOSA A*, 29(3):367–373.
- [14] Burckhardt, C. (1966). Diffraction of a plane wave at a sinusoidally stratified dielectric grating. *JOSA*, 56(11):1502–1508.
- [15] Cerutti-Maori, G., Petit, R., and Cadilhac, M. (1969). Etude numérique du champ diffracté par un réseau. *CR Ac. Sc. Paris*, 268:1060–1063.
- [16] Chandezon, J., Dupuis, M., Cornet, G., and Maystre, D. (1982). Multicoated gratings: a differential formalism applicable in the entire optical region. *JOSA*, 72(7):839–846.
- [17] Chartier, G. (2005). *Introduction to optics*. Springer Science & Business Media.
- [18] Chen, J. and Li, K. (1995). Quartic perfectly matched layers for dielectric waveguides and gratings. *Microwave and Optical Technology Letters*, 10(6):319–323.
- [19] Chu, S. T., Little, B. E., Pan, W., Kaneko, T., Sato, S., and Kokubun, Y. (1999). An eight-channel add-drop filter using vertically coupled microring resonators over a cross grid. *IEEE Photonics Technology Letters*, 11(6):691–693.
- [20] Dammann, H. (1978). Color separation gratings. *Applied Optics*, 17(15):2273–2279.
- [21] Fano, U. (1941). The theory of anomalous diffraction gratings and of quasi-stationary waves on metallic surfaces (sommerfeld's waves). *JOSA*, 31(3):213–222.
- [22] Flauraud, V., Reyes, M., Paniagua-Dominguez, R., Kuznetsov, A. I., and Brugger, J. (2017). Silicon nanostructures for bright field full color prints. *Acs Photonics*, 4(8):1913–1919.
- [23] Frateschi, N. and Levi, A. (1995). Resonant modes and laser spectrum of microdisk lasers. *Applied physics letters*, 66(22):2932–2934.
- [24] Garcia-Vidal, F., Sanchez-Dehesa, J., Dechelette, A., Bustarret, E., Lopez-Rios, T., Fournier, T., and Pannetier, B. (1999). Localized surface plasmons in lamellar metallic gratings. *Journal of Lightwave technology*, 17(11):2191.
- [25] Glisson, A. (1989). Numerical techniques for microwave and millimeter-wave passive structures, edited by tatsuo itoh [book review]. *IEEE Antennas and Propagation Society Newsletter*, 31(5):31–32.
- [26] González-Alcalde, A. K., Salas-Montiel, R., Mohamad, H., Morand, A., Blaize, S., and Macías, D. (2018). Optimization of all-dielectric structures for color generation. *Applied optics*, 57(14):3959–3967.
- [27] Granet, G. and Guizal, B. (1996). Efficient implementation of the coupled-wave method for metallic lamellar gratings in tm polarization. *JOSA A*, 13(5):1019–1023.

-
- [28] Greenwood, A. D. and Jin, J.-M. (1999). A novel efficient algorithm for scattering from a complex bor using mixed finite elements and cylindrical pml. *IEEE transactions on antennas and propagation*, 47(4):620–629.
- [29] Grover, R., Ibrahim, T., Kanakaraju, S., Lucas, L., Calhoun, L., and Ho, P.-T. (2004). A tunable gainasp-inp optical microring notch filter. *IEEE Photonics Technology Letters*, 16(2):467–469.
- [30] Guizal, B., Yala, H., and Felbacq, D. (2009). Reformulation of the eigenvalue problem in the fourier modal method with spatial adaptive resolution. *Optics letters*, 34(18):2790–2792.
- [31] Gundu, K. M. and Mafi, A. (2010a). Constrained least squares fourier modal method for computing scattering from metallic binary gratings. *JOSA A*, 27(11):2375–2380.
- [32] Gundu, K. M. and Mafi, A. (2010b). Reliable computation of scattering from metallic binary gratings using fourier-based modal methods. *JOSA A*, 27(7):1694–1700.
- [33] Hewlett, S. J. and Ladouceur, F. (1995). Fourier decomposition method applied to mapped infinite domains: scalar analysis of dielectric waveguides down to modal cutoff. *Journal of Lightwave Technology*, 13(3):375–383.
- [34] Hooke, R. (1665). *Micrographia, xxxvi. Of Peacocks, Ducks, and other Feathers of changeable colours*. (London).
- [35] Hugonin, J.-P., Besbes, M., and Lalanne, P. (2008). Hybridization of electromagnetic numerical methods through the g-matrix algorithm. *Optics letters*, 33(14):1590–1592.
- [36] Hugonin, J. P. and Lalanne, P. (2005a). Perfectly matched layers as nonlinear coordinate transforms: a generalized formalization. *J. Opt. Soc. Am. A*, 22(9):1844–1849.
- [37] Hugonin, J. P. and Lalanne, P. (2005b). Perfectly matched layers as nonlinear coordinate transforms: a generalized formalization. *JOSA A*, 22(9):1844–1849.
- [38] Hutley, M. (1973a). A detailed experimental study of the anomalies of a sinusoidal diffraction grating. *Opt. Acta.*, 20(10):771–782.
- [39] Hutley, M. (1973b). Experimental study of anomalies of sinusoidal diffraction gratings. *Optica Acta*, 20(8):607–624.
- [40] Huy, K. P. (2005). *Etude de micro-structures utilisant le guidage réfractif à fort confinement de la lumière*. PhD thesis.
- [41] Huy, K. P., Morand, A., Amans, D., and Benech, P. (2005). Analytical study of the whispering-gallery mode in two-dimensional microgear cavity using coupled-mode theory. *JOSA B*, 22(8):1793–1803.
- [42] Izawa, T. and Nakagome, H. (1972). Optical waveguide formed by electrically induced migration of ions in glass plates. *Applied Physics Letters*, 21(12):584–586.
- [43] Kanamori, Y., Katsube, H., Furuta, T., Hasegawa, S., and Hane, K. (2009). Design and fabrication of structural color filters with polymer-based guided-mode resonant gratings by nanoimprint lithography. *Japanese Journal of Applied Physics*, 48(6S):06FH04.

REFERENCES

- [44] Kanamori, Y., Shimono, M., and Hane, K. (2006). Fabrication of transmission color filters using silicon subwavelength gratings on quartz substrates. *IEEE photonics technology letters*, 18(20):2126–2128.
- [45] Kaspar, F. G. (1973). Diffraction by thick, periodically stratified gratings with complex dielectric constant. *JOSA*, 63(1):37–45.
- [46] Kennedy, J. and Eberhart, R. (1995). Particle swarm optimization. In *Proceedings of ICNN'95-International Conference on Neural Networks*, volume 4, pages 1942–1948. IEEE.
- [47] Knop, K. (1978a). Diffraction gratings for color filtering in the zero diffraction order. *Applied optics*, 17(22):3598–3603.
- [48] Knop, K. (1978b). Rigorous diffraction theory for transmission phase gratings with deep rectangular grooves. *JOSA*, 68(9):1206–1210.
- [49] Kohnke, G. E., Henry, C. H., Laskowski, E. J., Cappuzzo, M., Strasser, T. A., and White, A. E. (1996). Silica based mach-zehnder add-drop filter fabricated with uv induced gratings. *Electronics Letters*, 32(17):1579–1580.
- [50] Lalanne, P., Besbes, M., Hugonin, J., Van Haver, S., Janssen, O., Nugrowati, A., Xu, M., Pereira, S., Urbach, H., Van de Nes, A., et al. (2007). Numerical analysis of a slit-groove diffraction problem. *Journal of the European Optical Society-Rapid Publications*, 2.
- [51] Lalanne, P. and Morris, G. M. (1996). Highly improved convergence of the coupled-wave method for tm polarization. *JOSA A*, 13(4):779–784.
- [52] Lee, H.-S., Yoon, Y.-T., Lee, S.-S., Kim, S.-H., and Lee, K.-D. (2007). Color filter based on a subwavelength patterned metal grating. *Optics express*, 15(23):15457–15463.
- [53] Levi, A., Slusher, R., McCall, S., Pearton, S., and Hobson, W. (1993). Room-temperature lasing action in in_{0.51}ga_{0.49}p/in_{0.2}ga_{0.8}as microcylinder laser diodes. *Applied physics letters*, 62(17):2021–2023.
- [54] Li, L. (1996a). Formulation and comparison of two recursive matrix algorithms for modeling layered diffraction gratings. *JOSA A*, 13(5):1024–1035.
- [55] Li, L. (1996b). Use of fourier series in the analysis of discontinuous periodic structures. *JOSA A*, 13(9):1870–1876.
- [56] Li, L. (1999). Oblique-coordinate-system-based chandezon method for modeling one-dimensionally periodic, multilayer, inhomogeneous, anisotropic gratings. *JOSA A*, 16(10):2521–2531.
- [57] Li, L. (2012). Field singularities at lossless metal–dielectric arbitrary-angle edges and their ramifications to the numerical modeling of gratings. *JOSA A*, 29(4):593–604.
- [58] Li, L., Chandezon, J., Granet, G., and Plumey, J.-P. (1999). Rigorous and efficient grating-analysis method made easy for optical engineers. *Applied Optics*, 38(2):304–313.

- [59] Li, L. and Granet, G. (2011). Field singularities at lossless metal-dielectric right-angle edges and their ramifications to the numerical modeling of gratings. *JOSA A*, 28(5):738–746.
- [60] Little, B. E., Chu, S. T., Haus, H. A., Foresi, J., and Laine, J.-P. (1997a). Microring resonator channel dropping filters. *Journal of lightwave technology*, 15(6):998–1005.
- [61] Little, B. E., Laine, J.-P., and Chu, S. T. (1997b). Surface-roughness-induced contradictory coupling in ring and disk resonators. *Optics letters*, 22(1):4–6.
- [62] Luque-González, J. M., Herrero-Bermello, A., Ortega-Moñux, A., Molina-Fernández, Í., Velasco, A. V., Cheben, P., Schmid, J. H., Wang, S., and Halir, R. (2018). Tilted subwavelength gratings: controlling anisotropy in metamaterial nanophotonic waveguides. *Optics letters*, 43(19):4691–4694.
- [63] Lyndin, N. M., Parriaux, O., and Tishchenko, A. V. (2007). Modal analysis and suppression of the fourier modal method instabilities in highly conductive gratings. *JOSA A*, 24(12):3781–3788.
- [64] Macías, D., Luna, A., Skigin, D., Inchaussandague, M., Vial, A., and Schinca, D. (2013). Retrieval of relevant parameters of natural multilayer systems by means of bio-inspired optimization strategies. *Applied optics*, 52(11):2511–2520.
- [65] Magnusson, R. and Shokooh-Saremi, M. (2007). Widely tunable guided-mode resonance nanoelectromechanical rgb pixels. *Optics express*, 15(17):10903–10910.
- [66] Mahy, M., Van Eycken, L., and Oosterlinck, A. (1994). Evaluation of uniform color spaces developed after the adoption of cielab and cieluv. *Color Research & Application*, 19(2):105–121.
- [67] Marcuse, D. (2013). *Theory of dielectric optical waveguides*. Elsevier.
- [68] Margengo, E., Rappaport, C. M., and Miller, E. L. (1999). Optimum pml abc conductivity profile in fdtd. *IEEE Transactions on Magnetics*, 35(3):1506–1509.
- [69] Martin, B., Morand, A., Benech, P., Leblond, G., Blaize, S., Lerondel, G., and Lecoarer, E. (2008). A compact swifts spectrograph with a leaky loop structure. In *Integrated Optics: Devices, Materials, and Technologies XII*, volume 6896, page 689617. International Society for Optics and Photonics.
- [70] Maystre, D. (1980). Integral methods. In *Electromagnetic theory of gratings*, pages 63–100. Springer.
- [71] Mei, Y., Liu, H., and Zhong, Y. (2014). Treatment of nonconvergence of fourier modal method arising from irregular field singularities at lossless metal-dielectric right-angle edges. *JOSA A*, 31(4):900–906.
- [72] Melati, D., Melloni, A., and Morichetti, F. (2014). Real photonic waveguides: guiding light through imperfections. *Advances in Optics and Photonics*, 6(2):156–224.
- [73] Moharam, M. and Gaylord, T. (1981). Rigorous coupled-wave analysis of planar-grating diffraction. *JOSA*, 71(7):811–818.

REFERENCES

- [74] Moharam, M. and Gaylord, T. (1983). Rigorous coupled-wave analysis of grating diffraction—e-mode polarization and losses. *JOSA*, 73(4):451–455.
- [75] Moharam, M. and Gaylord, T. K. (1982). Diffraction analysis of dielectric surface-relief gratings. *JOSA*, 72(10):1385–1392.
- [76] Morand, A., Phan-Huy, K., Desieres, Y., and Benech, P. (2004). Analytical study of the microdisk’s resonant modes coupling with a waveguide based on the perturbation theory. *Journal of lightwave technology*, 22(3):827.
- [77] Nakagawa, A., Ishii, S., and Baba, T. (2005). Photonic molecule laser composed of gainasp microdisks. *Applied Physics Letters*, 86(4):041112.
- [78] Navarro, E., Wu, C., Chung, P., and Litva, J. (1994). Application of pml superabsorbing boundary condition to non-orthogonal fdtd method. *Electronics Letters*, 30(20):1654–1656.
- [79] Neviere, M. (1980). Electromagnetic theory of gratings. *de R. Petit. Berlin: Springer-Verlag*, page 20.
- [80] Neviere, M., Cadilhac, M., and Petit, R. (1973). Applications of conformal mappings to the diffraction of electromagnetic waves by a grating. *IEEE Transactions on Antennas and Propagation*, 21(1):37–46.
- [81] Nevrière, M., Cerutti-Maori, G., and Cadilhac, M. (1971). Sur une nouvelle méthode de résolution du problème de la diffraction d’une onde plane par un réseau infiniment conducteur. *Optics Communications*, 3(1):48–52.
- [82] Nevrière, M. and Montiel, F. (1994). Deep gratings: a combination of the differential theory and the multiple reflection series. *Optics communications*, 108(1-3):1–7.
- [83] Nevrière, M. and Popov, E. (1992). Analysis of dielectric gratings of arbitrary profiles and thicknesses: comment. *JOSA A*, 9(11):2095–2096.
- [84] Nevrière, M. and Popov, E. (2018). *Light propagation in periodic media: differential theory and design*. CRC Press.
- [85] Newton, I. (1704). *Opticks*. (William Innys at the West-End of St. Paul’s, London.
- [86] Nguyen-Huu, N., Lo, Y.-L., and Chen, Y.-B. (2011). Color filters featuring high transmission efficiency and broad bandwidth based on resonant waveguide-metallic grating. *Optics Communications*, 284(10-11):2473–2479.
- [87] Niehusmann, J., Vörckel, A., Bolivar, P. H., Wahlbrink, T., Henschel, W., and Kurz, H. (2004). Ultrahigh-quality-factor silicon-on-insulator microring resonator. *Optics letters*, 29(24):2861–2863.
- [88] Overton, M. L. (2001). *Numerical computing with IEEE floating point arithmetic*. SIAM.
- [89] Pai, D. and Awada, K. (1991). Analysis of dielectric gratings of arbitrary profiles and thicknesses. *JOSA A*, 8(5):755–762.

-
- [90] Palmer, C. H. (1952). Parallel diffraction grating anomalies. *JOSA*, 42(4):269–276.
- [91] Peng, S., Tamir, T., and Bertoni, H. L. (1975). Theory of periodic dielect waveguides. *IEEE transactions on microwave theory and techniques*, 23(1):123–133.
- [92] Petit, R. (1966). Diffraction d’une onde plane par un réseau métallique. *Rev. Opt.*, 45:353–370.
- [93] Popov, E., Chernov, B., Nevière, M., and Bonod, N. (2004). Differential theory: application to highly conducting gratings. *JOSA A*, 21(2):199–206.
- [94] Popov, E. and Nevière, M. (2000). Grating theory: new equations in fourier space leading to fast converging results for tm polarization. *JOSA A*, 17(10):1773–1784.
- [95] Popov, E. and Nevière, M. (2000). Grating theory: new equations in fourier space leading to fast converging results for tm polarization. *J. Opt. Soc. Am. A*, 17(10):1773–1784.
- [96] Popov, E., Nevière, M., Gralak, B., and Tayeb, G. (2002). Staircase approximation validity for arbitrary-shaped gratings. *JOSA A*, 19(1):33–42.
- [97] Prabhu, A. M., Tsay, A., Han, Z., and Van, V. (2009). Ultracompact soi microring add-drop filter with wide bandwidth and wide fsr. *IEEE Photonics Technology Letters*, 21(10):651–653.
- [98] Rayleigh, L. (1907a). Iii. note on the remarkable case of diffraction spectra described by prof. wood. *The London, Edinburgh, and Dublin Philosophical Magazine and Journal of Science*, 14(79):60–65.
- [99] Rayleigh, L. (1907b). On the dynamical theory of gratings. *Proceedings of the Royal Society of London. Series A, Containing Papers of a Mathematical and Physical Character*, 79(532):399–416.
- [100] Rosenblatt, D., Sharon, A., and Friesem, A. A. (1997). Resonant grating waveguide structures. *IEEE Journal of Quantum electronics*, 33(11):2038–2059.
- [101] Rowland, D. and Love, J. (1993). Evanescent wave coupling of whispering gallery modes of a dielectric cylinder. *IEE Proceedings J (Optoelectronics)*, 140(3):177–188.
- [102] Rumpf, R. C. (2011). Improved formulation of scattering matrices for semi-analytical methods that is consistent with convention. *Progress In Electromagnetics Research*, 35:241–261.
- [103] Silberstein, E., Lalanne, P., Hugonin, J.-P., and Cao, Q. (2001). Use of grating theories in integrated optics. *JOSA A*, 18(11):2865–2875.
- [104] Smith, T. and Guild, J. (1931). The cie colorimetric standards and their use. *Transactions of the optical society*, 33(3):73.
- [105] Süssstrunk, S., Buckley, R., and Swen, S. (1999). Standard rgb color spaces. In *Color and Imaging Conference*, volume 1999, pages 127–134. Society for Imaging Science and Technology.

REFERENCES

- [106] Suzuki, S., Kusunoki, T., and Mori, M. (1990). Color characteristic design for color scanners. *Applied Optics*, 29(34):5187–5192.
- [107] Tamir, T., Wang, H., and Oliner, A. A. (1964). Wave propagation in sinusoidally stratified dielectric media. *IEEE Transactions on Microwave Theory and Techniques*, 12(3):323–335.
- [108] Tayeb, G. (1994). The method of fictitious sources applied to diffraction gratings. *Applied Computational Electromagnetics Society Journal*, 9(3):90–100.
- [109] Uddin, M. J. and Magnusson, R. (2012). Efficient guided-mode-resonant tunable color filters. *IEEE Photonics Technology Letters*, 24(17):1552–1554.
- [110] Ulrich, R. and Tacke, M. (1973). Submillimeter waveguiding on periodic metal structure. *Applied Physics Letters*, 22(5):251–253.
- [111] Vallius, T. and Honkanen, M. (2002). Reformulation of the fourier modal method with adaptive spatial resolution: application to multilevel profiles. *Optics Express*, 10(1):24–34.
- [112] Volakis, J. L., Chatterjee, A., and Kempel, L. C. (1998). *Finite element method electromagnetics: antennas, microwave circuits, and scattering applications*, volume 6. John Wiley & Sons.
- [113] Wait, J. R. (1967). Electromagnetic whispering gallery modes in a dielectric rod. *Radio science*, 2(9):1005–1017.
- [114] Wang, Q., Zhang, D., Xu, B., Huang, Y., Tao, C., Wang, C., Li, B., Ni, Z., and Zhuang, S. (2011). Colored image produced with guided-mode resonance filter array. *Optics letters*, 36(23):4698–4700.
- [115] Wang, S. and Magnusson, R. (1993). Theory and applications of guided-mode resonance filters. *Applied optics*, 32(14):2606–2613.
- [116] Watanabe, K. (2006). Study of the differential theory of lamellar gratings made of highly conducting materials. *JOSA A*, 23(1):69–72.
- [117] Weiss, D. S., Sandoghdar, V., Hare, J., Lefevre-Seguin, V., Raimond, J.-M., and Haroche, S. (1995). Splitting of high-q mie modes induced by light backscattering in silica microspheres. *Optics letters*, 20(18):1835–1837.
- [118] Wood, R. (1912). Xxvii. diffraction gratings with controlled groove form and abnormal distribution of intensity. *The London, Edinburgh, and Dublin Philosophical Magazine and Journal of Science*, 23(134):310–317.
- [119] Wood, R. W. (1902). On a remarkable case of uneven distribution of light in a diffraction grating spectrum. *Proceedings of the Physical Society of London*, 18(1):269.
- [120] Xu, Q., Almeida, V. R., and Lipson, M. (2005a). Demonstration of high raman gain in a submicrometer-size silicon-on-insulator waveguide. *Optics letters*, 30(1):35–37.
- [121] Xu, Q., Schmidt, B., Pradhan, S., and Lipson, M. (2005b). Micrometre-scale silicon electro-optic modulator. *nature*, 435(7040):325–327.

- [122] Yariv, A. (2000). Universal relations for coupling of optical power between microresonators and dielectric waveguides. *Electronics letters*, 36(4):321–322.
- [123] Yee, K. (1966). Numerical solution of initial boundary value problems involving maxwell's equations in isotropic media. *IEEE Transactions on antennas and propagation*, 14(3):302–307.
- [124] Yeh, C., Casey, K., and Kaprielian, Z. (1965). Transverse magnetic wave propagation in sinusoidally stratified dielectric media. *IEEE Transactions on Microwave Theory and Techniques*, 13(3):297–302.
- [125] Yoon, Y.-T., Lee, H.-S., Lee, S.-S., Kim, S. H., Park, J.-D., and Lee, K.-D. (2008). Color filter incorporating a subwavelength patterned grating in poly silicon. *Optics express*, 16(4):2374–2380.
- [126] Zhu, J., Liu, H., and Zhong, Y. (2016). Treatment of nonconvergence of the fourier modal method and c method arising from field hypersingularities at lossless metal–dielectric arbitrary-angle edges. *JOSA A*, 33(5):845–853.

Appendix A

The multiplication of two Fourier series: Toeplitz matrix formulation

In the previous studies, we often see the multiplication of two functions described in term of their Fourier series. This multiplication results what's called Toeplitz matrix. In this part, the formulation of the Toeplitz matrix will be presented.

Let's assume that we have two functions $f(x)$ and $g(x)$ which are described following their Fourier series as:

$$f(x) = \sum_{p=-N}^{p=N} f_p \exp(j2\pi\sigma px)$$
$$g(x) = \sum_{n=-N}^{n=N} g_n \exp(j2\pi\sigma nx)$$

With $\sigma = 2\pi/\Lambda$ and Λ is the period of the unit cell of the periodic structure. Now, the product of the two functions is carried out and the result $h(x)$ can be expressed as:

$$h(x) = f(x) \cdot g(x)$$
$$= \sum_{p=-N}^{p=N} \sum_{n=-N}^{n=N} g_n f_p \exp(j2\pi(\sigma p + \sigma n)x)$$

Assuming that, $p = n - m$. Thus, $m = p + n$. Then, we can write:

$$h = \sum_{m-n} \sum_n g_n f_{m-n} \exp(j2\pi\sigma pmx),$$
$$h = \sum_{m-n} h_m \exp(j2\pi\sigma pmx),$$
$$h_m = \sum_n g_n f_{m-n}$$

THE MULTIPLICATION OF TWO FOURIER SERIES: TOEPLITZ MATRIX FORMULATION

As n and m vary from $-N$ to $+N$, the harmonics distribution of h can be thus written as:

$$\begin{aligned} h_{m=-N} &= f_0 g_{-N} + f_{-1} g_{-N+1} + f_{-2} g_{-N+2} + \dots + f_{-2N} g_N \\ h_{m=-N+1} &= f_1 g_{-N} + f_0 g_{-N+1} + f_{-1} g_{-N+2} + \dots + f_{-2N+1} g_N \\ &\dots \\ h_{m=N} &= f_{2N} g_{-N} + f_{2N-1} g_{-N+1} + f_{2N-2} g_{-N+2} + \dots + f_0 g_N \end{aligned}$$

This formulation can be simplified by using the notation of the Toeplitz matrix $[[f]]$ expressed as:

$$[[f]] = \begin{pmatrix} f_0 & f_{-1} & f_{-2} & \dots & \dots & f_{-2N} \\ f_1 & f_0 & f_{-1} & \ddots & \ddots & f_{-2N+1} \\ f_2 & f_1 & f_0 & \ddots & \ddots & \vdots \\ \vdots & \ddots & \ddots & \ddots & f_0 & f_{-1} \\ f_{2N} & \dots & \dots & f_2 & f_1 & f_0 \end{pmatrix}$$

Finally, the multiplication of two FOurier series can be expressed as: $[h] = [[f]][g]$. And, thus the harmonic m of h can be simplified as:

$$h_m = \sum_{n=-N}^{n=+N} f_{m-n} g_n$$

Appendix B

The normal of the surface for the different used geometries.

In this dissertation, different geometries have been used. The simulations performed by the DM-FFF and the a-DM-FFF necessitate the presence of the function that takes the evolution of the profile into account. This function is described by the projection of the normal to the surface on the periodization axis x and the propagation axis z . Those last ones are defined by N_x and N_z respectively.

B.1 Rectangular Profile

For a lamellar (rectangular) profile evolution, the x and y components of the normal of the surface are always equal to $N_z = 0$ and $N_x = 1$.

B.2 Sinusoidal Profile

In case of sinusoidal grating, the evolution of the projected normal on x and z can be written following x as:

$$N_x = -\sqrt{\frac{1}{1 + (\partial f / \partial x)^2}} \frac{\partial f}{\partial x}$$
$$N_z = \sqrt{\frac{1}{1 + (\partial f / \partial x)^2}}$$

With, $f(x)$ is the function describing the evolution of the sinusoidal profile following the periodicity axis x .

B.3 Trapezoidal or triangular Profile

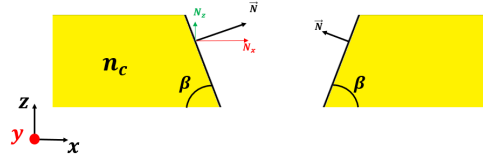


Fig. 2.1 Geometrical profile of the trapezoidal evolution.

In case of the trapezoidal or triangular evolution (Fig.2.1, the components of the normal of the surface are described following the internal angle β as:

$$\begin{aligned}
 N_x &= -\sin(\beta), \text{ for } x \in [0, \frac{\Lambda}{2}], \\
 &= +\sin(\beta), \text{ for } x \in [\frac{\Lambda}{2}, \Lambda] \\
 N_z &= \cos(\beta), \text{ for } x \in [0, \Lambda]
 \end{aligned}$$

B.4 Curvilinear profile

The normal N_x and N_z are depicted in Eq.(B5) and B(6) of ref.[95]. For the aim of clarity, we present the normal to the cylindrical rod used in the reflector structure and the microdisks.

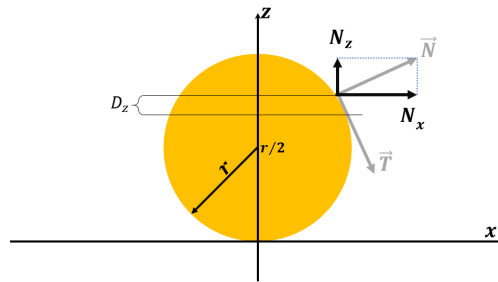


Fig. 2.2 Geometrical parameters of the cylindrical rod.

With r the radius of the cylinder, the normal outside the modulated region is null. Thereupon, $|x| > r$, $N_z = 0$ and $N_x = 0$.

Nevertheless, for $x \in [-r, +r]$, N_z and N_x , depicted in Fig.2.2, are represented as follows,

$$N_z = \sqrt{1 - \frac{x^2}{r^2}}$$
$$N_x = \pm \frac{\sqrt{N_z^2 [1 - N_z^2]}}{N_z}$$

Appendix C

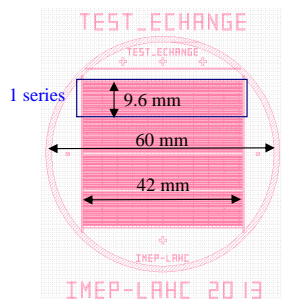
Test ECH mask datasheet

Description of the photolithography mask "TEST_ECH"

The mask is intended for process testing, since it allows cutting the wafer in several pieces (normally 4), all containing the same waveguides.

General view of the mask

The mask is divided in 4 series, each containing 6 patterns of 11 waveguides.



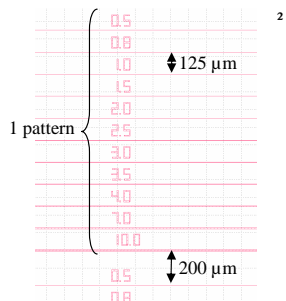
The circle corresponds to the 6 cm diameter standard wafer size. "Standard" alignment crosses are located on top, bottom, left and right of the waveguides.

There are 4 identical series, separated by 100 μm wide dicing lines.

1 series is constituted of (from top to bottom):

- One 100 μm wide dicing line
- A ruler (graduations every 100 μm , number every 1 mm)
- 3 waveguides patterns (see description below)
- 2 Y junctions (1 \rightarrow 2 and 2 \rightarrow 1), width = 2 μm
- 3 waveguide patterns.

Description of one waveguide pattern



- A pattern contains 11 waveguides: 0.5 - 0.8 - 1 - 1.5 - 2 - 2.5 - 3 - 3.5 - 4 - 7 - 10 μm apertures.
- The waveguides are separated by 125 μm (center to center). They are 42 mm long.
- The aperture width is written on top of each waveguide every 4 mm.
- There is a 200 μm spacing between 2 patterns

Conclusion

One series contains 6 patterns of 11 waveguides and 2 Y junctions, so it can be used as an individual sample. Thus with one wafer, 4 samples can be realized. One sample is 9.6 mm wide.

Appendix D

List of Publications

D.1 Journal Publications

A1- **Habib Mohamad**, et al. "Aperiodic differential method associated with FFF: an efficient electromagnetic computational tool for integrated optical waveguides modelization." JOSA A 37.6 (2020): 1014-1024. DOI: 10.1364/JOSAA.387823

A2- **Mohamad Habib**, Essaidi Soukaina, Blaize Sylvain, Macias Demetrio, Benech Pierre and Morand Alain, 2020. Fast Fourier factorization for differential method and RCWA: a powerful tool for the modeling of non-lamellar metallic diffraction gratings. Optical and Quantum Electronics, 52(2), p.127. DOI: 10.1007/s11082-020-2240-y

A3- González-Alcalde, A.K., Salas-Montiel, R., **Mohamad, H.**, Morand, A., Blaize, S. and Macías, D., 2018. Optimization of all-dielectric structures for color generation. Applied optics, 57(14), pp.3959-3967. DOI: 10.1364/AO.57.003959

D.2 Oral contributions in international conferences

B1- **Habib Mohamad**, Sylvain Blaize, Pierre Benech, and Alain Morand. The Aperiodic DM-FFF compared to the AFMM: A Rigorous Method for the Modeling of Guided Optical Structures. Conference ECIO 2020, July 2020, Paris, France.

B2- **Habib Mohamad**, Sylvain Blaize, Pierre Benech, and Alain Morand. An aperiodic differential method associated with the FFF: a numerical tool for integrated optic waveguide

modelization. Conference TNTN 2020, February 2020, Berlin, Germany.

B3- **Habib Mohamad**, Alain Morand, Pierre Benech, Demetrio Macias, Sylvain Blaize. DM-FFF: A Powerful Computational Electromagnetic Method for the Modelization of Complex-Shaped Diffraction Gratings. Conference OWTNM 2019, May 2019, Malaga, Spain.

B4- Alma González-Alcalde, Rafael Salas-Montiel, **Habib Mohamad**, Alain Morand, Sylvain Blaize, et al.. Design of subwavelength structures with a prescribed chromatic response. European Optical Society Biennial Meeting 2018 of the European Optical Society (EOS), EOSAM2018, Oct 2018, Delft, Netherlands.

D.3 Oral Contributions in French National conferences

C1- **Habib Mohamad**, Alain Morand, Pierre Benech et Sylvain Blaize, La FFF appliquée à la méthode différentielle : de l'optique diffractive vers l'optique guidée. Conference GDR Ondes, June 2019, Marseille, France.

C2- **Mohamad, H.**, Morand, A., Blaize, S., Macias, D. and Benech, P., Efficacité de la FFF sur la RCWA et la méthode différentielle appliquée à la diffraction d'un réseau métallique sinusoïdal. In JNOG 2018, Toulouse, France.

Résumé

Introduction

Pour concevoir au mieux des dispositifs photoniques, il est important d'avoir des outils de modélisation fiables et efficaces. En effet si le quadrillage de paramètres technologiques est envisageable pour des dispositifs simples, son coût en nombre de tests devient rapidement un frein à l'optimisation de structures. Il devient donc indispensable de disposer de simulations totalement vectorielles, avec des matériaux à indices de réfraction complexes, de garantir la prise en compte de l'ensemble des modes de propagation (modes guidés, rayonnés et évanescents), bidirectionnelles . . .

La simulation de structures à fort contraste d'indice de réfraction (photonique sur silicium) ou les structures utilisant des motifs métalliques générant des modes plasmoniques ou des motifs sub-longueur d'onde comme les métamatériaux . . . est un ensemble d'exemples qui nécessite l'utilisation de ces outils. Ces derniers se différencient par leur méthode de calcul utilisée : calcul dans le domaine fréquentiel par différences finies ou éléments finis, méthode temporelle par la méthode des différences finies . . . Par exemple, la FDTD est devenue ces dernières années un outil de référence dans le milieu de la photonique sur silicium. Cependant, ces méthodes ne sont pas forcément optimales. Elles diffèrent par les ressources numériques nécessaires notamment sur la mémoire utilisée, le temps de calcul, la prise en compte des conditions de continuité, la discrétisation de la structure qui peut se faire soit dans le domaine spectral ou spatial . . . Néanmoins, certaine méthode comme la FDTD peut générer des approximations induisant des imprécisions ou une augmentation des ressources numériques utilisées dans certaines configurations. Ces quinze dernières années au sein du laboratoire (IMEP-Lahc), des outils basés sur la RCWA ont été développés pour simuler des structures très différentes allant de l'optique diffractive à l'optique guidée en essayant d'optimiser au mieux ces ressources numériques.

L'objectif de cette thèse est de développer un outil plus général dans le but de réduire ces imperfections tout en gardant la possibilité de l'utiliser sur une multitude d'applications de la photonique (optique diffractive, optique guidée . . .). Mon choix s'est porté sur la méthode

différentielle largement utilisée pour l'étude des réseaux de diffraction. Cette méthode peut être plus efficace que la RCWA mais peut avoir aussi des limites pour la simulation de structures à profil complexe notamment en polarisation TM. Depuis les années 2000, l'ajout d'un nouveau module dénommé FFF (Fast Fourier Factorisation ou Factorisation Rapide de Fourier), permet de résoudre cette problématique et ouvrir de nouvelles potentialités à cette méthode. Après une introduction générale, la méthode différentielle associée à la FFF est présentée en détails. Ensuite, une solution simple et rapide qui permet de résoudre le problème des divergences numériques dans le cas des métaux ayant une permittivité purement réelle et négative est proposée. Puis, l'étude complète d'une structure diffractive diélectrique utilisée pour des applications de sécurité visuelle est proposée. La simulation de la structure diffractive est associée à un module utilisant un réseau de neurones pour le design et la modélisation optimale de ces structures. Finalement, pour adapter la méthode aux structures photoniques guidées, une transformée de coordonnées inspirée par la FMM a périodique a été implémentée dans l'algorithme de la MD-FFF transformant cette dernière en une méthode a périodique pour la simulation 2D de structures optiques intégrées utilisant des matériaux à indice de réfraction complexe, non-isotropes et non-magnétiques. La décomposition de la propagation sur une base de modes propres peut permettre d'accéder à des informations non directement accessibles avec la FDTD par exemple. Des résultats plus précis, plus rapides et plus rigoureux ont été obtenus par rapport à la FMM notamment en polarisation TM avec des profils curvilignes comme dans le cas des structures cylindriques.

Ce manuscrit est composé de trois grandes parties, après une introduction générale et la présentation des équations de Maxwell dans le régime temporel et le domaine de Fourier. La première partie décrit la méthode différentielle associée à la Factorisation Rapide de Fourier (DM-FFF). Cette méthode est connue depuis les années 2000 dans la communauté de l'optique diffractive. Elle est notamment utilisée pour la conception et la modélisation des réseaux diffractifs périodiques complexes. La deuxième partie porte sur l'association des PML (Perfectly Matched Layers) à l'algorithme de cette méthode. Avec les modifications apportées (mode d'excitation, matrice spécifique de passage entre sections, ...), j'ai réussi à adapter cette méthode en un outil a périodique pour la modélisation et la conception de structures optiques guidées. Cette méthode est alors plus rigoureuse que l'a-FMM (a périodique Fourier Modale Méthode) au niveau des efficacités des résultats et la convergence en fonction du nombre d'harmoniques utilisées notamment pour des structures non-rectangulaires. Dans la troisième partie, on propose d'associer deux technologies pour des applications en optique intégrée. J'ai essayé d'exploiter la combinaison de la technologie de guides optiques intégrés sur verre de l'IMEP-Lahc avec la technologie de moulage d'un

partenaire industriel SURYS-Hologram. Le but est de réaliser des filtres de Bragg intégrés pour des applications dans le domaine des longueurs d'onde visible et proche infra-rouge.

DM-FFF pour la modélisation de structures diffractives arbitraires

Une structure diffractive peut se résumer comme une cascade de 3 zones : une première zone homogène (milieu où se propage le signal incident et le signal réfléchi), une zone intermédiaire dite modulée (milieu où se trouve le réseau diffractif) et une dernière zone homogène (milieu où se propage le signal transmis). On peut prendre comme exemple un réseau 1D. Dans ce cas, (Ox) représente l'axe de la périodisation du réseau, (Oz) est l'axe de la propagation et (Oy) est un axe invariant. La diffraction d'un réseau peut être définie par la résolution d'un système d'équations différentielles couplées issues des équations de Maxwell. Ce système relie respectivement les composantes transverses du champ électrique E_y et H_x en polarisation TE et les composantes H_y et E_x en polarisation TM. Ce système peut alors se résoudre en décomposant les paramètres opto-géométriques de la structure (permittivité, perméabilité, champs électriques et magnétiques) sur une base de séries de Fourier. On retrouve alors la représentation simplifiée qui relie la variation du vecteur constitué des harmoniques des champs électriques et magnétiques transverses suivant z et une matrice variant selon l'axe de propagation $M(z)$. La propagation ou le passage d'une interface à l'autre est défini par l'obtention d'une matrice S qui relie les ondes entrantes aux ondes sortantes de la couche. Ce formalisme est plus stable numériquement que la matrice T qui relie les ondes d'une interface de la couche aux ondes de l'autre interface. Pour cela, il est donc nécessaire de déterminer des matrices de conversion permettant de définir à chaque interface une conversion entre les vecteurs harmoniques précédents et les pondérations des vecteurs propagatifs ou contra-propagatifs nécessaires pour la mise en cascade des couches. Dans le cas des couches extérieures homogènes, les vecteurs propres sont des ondes planes. La pondération précédente est alors reliée à l'amplitude complexe de ces ondes planes. Cette conversion est alors possible via une matrice de passage Ψ .

Avec la méthode différentielle, la zone modulée est discrétisée en sous-couches j en utilisant la matrice $M(z)$ dépendante en z . Une méthode numérique du type Runge-Kutta d'ordre 4 dans un format matriciel permet alors de définir l'évolution des champs magnétiques et électriques dans la zone modulée. L'épaisseur de chaque couche j doit être suffisamment fine pour que la fonction caractérisant l'évolution des vecteurs harmoniques des champs électromagnétiques transverses soit proche de son développement limité à l'ordre 4 sur

l'intervalle du pas d'intégration. Cette méthode peut donc s'appliquer à un nombre plus important de formes de réseau comparé à la RCWA. Il faut au moins 4 sous couches pour appliquer la méthode numérique Runge-Kutta. Cet ensemble de 4 sous-couches peut être simplifié par une couche M_i avec la RCWA. Ce formalisme permet une convergence à priori plus rapide nécessitant moins d'harmoniques. Mais le nombre de sous-couches est limité. Pour des valeurs trop grandes on retrouve les problèmes de divergence numérique de la matrice T . Elle utilise aussi la FFF pour appliquer à chaque sous couche les règles de Li. La FFF a été introduite par Popov et permet de prendre en compte le profil continu de la surface. L'objectif est de connaître les composantes tangentielles des champs électromagnétiques sur la surface de ce profil continu. Pour cela, on doit déterminer les composantes de la tangente et de la normale à cette même surface. Il sera alors possible de projeter les champs électromagnétiques sur ces deux précédents vecteurs. Dans une couche i , on aura un nombre discret de positions x_s définissant la position de la surface du profil continu dans cette même couche i . Il est important de connaître la tangente et la normale de la surface seulement à ces positions pour cette couche i située à une position z donnée. A ces positions, la connaissance des champs électromagnétiques tangents et normaux nous permettra d'utiliser correctement les règles de Li. Pour $x \neq x_s$ et pour la même position z , le vecteur normal ou tangent peut être quelconque. Après l'implémentation de l'algorithme en Python, j'ai comparé mes résultats aux résultats des différentes méthodes à base de Fourier (RCWA, C-Méthode) pour montrer l'efficacité de la DM-FFF notamment en polarisation TM. En prenant en compte différents profils du réseau (rectangulaire, sinusoïdale, trapézoïdale, etc...), La MD-FFF permet d'avoir une convergence plus stable suivant le nombre d'harmoniques N . En revanche, on peut observer des problèmes de convergence lorsque le métal utilisé a un indice de réfraction réel proche de 0. La valeur nulle correspond à un métal sans pertes. Dans ce cas, la permittivité est quasiment réelle et négative. Si on a une discontinuité du type air métal, on va avoir un saut de permittivité d'une valeur quasi négative à une valeur positive. Ce type de discontinuité ne respecte pas les règles de Li. Il est donc compliqué de modéliser des structures diffractives avec cet indice de réfraction. Pour résoudre ce problème, j'ai proposé d'ajouter une couche nanométrique de gradient d'indice de réfraction sur la face en contact avec le milieu incident. La partie réelle de l'indice de réfraction passe linéairement de l'indice de réfraction réel du diélectrique jusqu'à l'indice de réfraction réel du métal. Il en est de même pour la partie imaginaire. Cette solution nous permet d'éliminer le problème de divergence et rendre la DM-FFF plus efficace et plus rigoureuse pour une grande plage de profils de réseau de diffraction que les autres méthodes connues. Finalement, une étude détaillée d'une structure de sécurité visuelle de réflexion a été étudiée. La structure correspond à un réseau diélectrique associé à un guide optique qui donne un effet visuel

intéressant. Les deux effets physiques (effet du réseau et effet du guide) qui sont présents dans ce type de structure donnent une large gamme de liberté pour manipuler les couleurs diffractés. Suite aux différentes interprétations, nous avons constaté que le paramètre le plus important pour changer le couleur sous incidence normale est la période Λ . Les autres paramètres peuvent affecter le contraste de la couleur réfléchi. De plus, la résonance du mode guidé peut être optimisée en changeant l'épaisseur du guide d'ondes (couche tampon) par le couplage d'un ou plusieurs modes guidés. Par conséquent, des réseaux de diffraction plus complexes peuvent être étudiés. Par exemple, des réseaux métalliques induisant des effets plasmoniques, des réseaux avec des profils continu, discontinu ou / et des structures ayant des parties continues et autres discontinues. Cependant, notre collaborateur industriel, SURYS, utilise la technologie roll to roll pour la production à grande échelle de structures de sécurité visuelle. Avec cette technique, le changement de l'épaisseur de la structure est difficile sur le même échantillon. Mais, différents réseaux avec des périodes différentes Λ peuvent être réalisés sur le même wafer.

Méthode différentielle pour l'analyse de structures guidées

La méthode différentielle présentée est essentiellement appliquée sur les réseaux de diffraction. On peut utiliser cette méthode et l'associer avec des PMLs (Perfect Matching Layers) pour simuler des structures guidées comme l'a déjà proposé Lalanne et al. en combinant la RCWA avec des PMLs. La structure guidée représente une zone guidée entourée de deux zones homogènes (le substrat et le superstrat) selon l'axe x . La propagation se fait toujours selon l'axe z . Les parties à gauche et à droite de la partie guidée sont considérées infinies dans la direction parallèle à l'axe x . On parle de structure ouverte. Il est possible de fixer une largeur pour ces deux couches et de les terminer par une couche absorbante et non réfléchissante d'une largeur donnée. Ces couches peuvent être obtenues grâce à des PMLs. L'empilement de ces couches selon l'axe x peut définir la cellule élémentaire d'un réseau de diffraction que l'on peut périodiser. L'intérêt des PMLs est multiple : premièrement elles permettent d'isoler les cellules élémentaires en absorbant le signal rayonné et en éliminant les réflexions à l'entrée des PMLs. Deuxièmement, elles permettent de convertir une structure ouverte en une structure périodique. Ainsi, les algorithmes basés sur une expansion de Fourier peuvent alors être appliqués sur ce type de guides. Les PMLs sont en fait définies à partir d'une transformée de coordonnées complexes pour simuler le cas précédent. Dans ce cas, la transformée de coordonnées s'applique toujours sur l'axe x mais elle est ici complexe. Elle va agir à la fois sur la partie réelle et imaginaire. Elle est identique à celle proposée par Lalanne et al [36]. Cette transformée de coordonnées est imposée dans toutes les couches.

Il n'y a donc pas de changement de base à faire entre deux couches. On évite donc cette projection qui peut apporter des divergences suivant le nombre d'harmoniques utilisé. La difficulté à implanter ce type de transformée de coordonnées complexes dans la méthode différentielle avec la FFF réside dans le choix de la matrice de passage pour passer des vecteurs harmoniques stationnaires aux vecteurs propres du guide droit afin d'accéder aux ondes propagatives et régressives. Dans ce cas, les zones homogènes utilisées dans le cas du réseau diffractif sont maintenant des guides d'entrée et de sortie entourant une zone modulée qui caractérise la zone guidée à modéliser. La propagation dans ces guides d'extrémités est caractérisée par une pondération de modes propres au lieu d'une pondération d'ondes planes pour les réseaux diffractifs. Mais, la matrice de vecteurs propres de la structure doit être convenablement réorganisée pour répondre à cette propriété. On nommera par la suite la méthode l'a-DM-FFF avec la lettre a qui désigne aperiodique. On a d'abord validé la méthode en l'appliquant sur une structure lamellaire où les matrices S issues de l'a-DM-FFF et de l'a-FMM sont similaires (Fig.7.4). On a ensuite utilisé la structure précédente avec un pilier central qui va faire apparaître des marches d'escalier ou "staircase" sur sa surface avec l'a-FMM. La FFF va permettre de mieux prendre en compte les conditions de continuité sur l'interface du pilier (Fig.8.1). Une structure avec un pilier diélectrique à fort contraste d'indice de réfraction et une autre structure avec pilier métallique sont considérées. On montre alors une convergence plus rapide, et des résultats plus rigoureux que l'a-FMM. En addition, des comparaisons entre l'a-FMM et notre nouvelle méthode ont été faites sur des micro résonateurs (micro-disques). On montre qu'avec notre méthode, les résultats s'approchent des résultats analytiques et on peut atteindre des coefficients de qualité plus élevés. Également, on peut diminuer l'effet de séparation spectrale des deux modes qui caractérisent le résonateur par un facteur de 10. Pour conclure, on montre une nouvelle méthode pour modéliser la propagation de la lumière des structures photoniques en deux dimensions. Grâce à l'apport de la FFF, on montre que l'on a des résultats qui convergent plus rapidement en respectant d'une manière plus rigoureuse les conditions de continuité de la structure idéale que l'on cherche à simuler. On peut avoir des résultats assez similaires pour un même pas de discrétisation en utilisant la RCWA au lieu de l'algorithme Runge-Kutta tout en gardant la FFF. Ces résultats ont abouti à deux posters en conférence internationale et à la publication d'un article dans une revue internationale.

Fabrication de réseau de Bragg par hybridation de couche holographiée et des guides surfaces sur substrat de verre

Les filtres à réseaux de Bragg sont des composants importants dans le domaine de l'optique. Ils sont principalement utilisés dans les domaines des télécommunications ou des capteurs. Si on associe un réseau de Bragg avec un guide d'onde, un filtre passe-bande à bande étroite est obtenu en réflexion au niveau du spectre optique du signal. En transmission, on obtiendra au contraire un filtre réjecteur de bande étroite, le complémentaire du précédent aux pertes près. Donc si on injecte dans le guide une source large bande, on peut sélectionner ou éliminer une bande étroite autour d'une longueur d'onde centrale λ_B . Cette dernière dépend de l'indice effectif du mode dans la partie corruguée qui peut être approximée à l'indice effectif n_{eff} du guide seul et de la période du réseau Λ . Les filtres de Bragg sont très connus dans les fibres (FBG : Fiber Bragg Grating). On peut obtenir ces filtres sur des guides optiques intégrés avec différentes technologies (Si, Silice ...). On peut les obtenir aussi sur des technologies d'échange d'ions sur verre. Ce concept a été utilisé pour réaliser des lasers intégrés pour sélectionner la longueur d'onde du laser. Néanmoins, le montage utilisé dans le laboratoire ne permet d'atteindre des périodes de réseau suffisamment faibles pour réaliser des filtres en longueurs d'ondes dans le visible. L'IMEP-Lahc est spécialisé par la technologie des guides optiques par échange d'ions. Néanmoins, SURYS a une technologie qui permet d'accéder à des réseaux de surface périodiques sur des polymères transparents déposés initialement sur un substrat en associant des techniques de moulage et d'holographie. L'idée était d'hybrider les deux technologies pour avoir des filtres de Bragg dans le domaine visible. Après la fabrication et la caractérisation des guides par échanges d'ions, j'ai proposé deux solutions d'hybridation. La première se base sur le moulage d'une couche de polymère déposée par spin-coating sur les guides de surface (Fig.9.9). Après les simulations et les tests, cette solution n'est pas favorable et ne donne pas des résultats encourageants suite à l'épaisseur de la couche tampon entre les guides et le réseau. Cette couche interdit l'interaction évanescente du mode guidé avec le réseau empêchant un effet de filtrage. La deuxième solution consiste à hybrider directement la surface des guides avec la surface du réseau périodique en utilisant un adhésif qui crée une couche atomique entre l'échantillon composé du réseau de surface avec l'échantillon composé des guides optiques de surface. Les deux plaques sont toujours solidaires. Mais les mesures faites n'ont pas été fructueuses. Un gap entre les deux structures est toujours présent.
